

Nanocrystals-Related Synthesis, Assembly, and Energy Applications 2012

Guest Editors: Bo Zou, William W. Yu, Jaetae Seo,
Ting Zhu, and Michael Z. Hu





**Nanocrystals-Related Synthesis, Assembly,
and Energy Applications 2012**

Journal of Nanomaterials

**Nanocrystals-Related Synthesis, Assembly,
and Energy Applications 2012**

Guest Editors: Bo Zou, William W. Yu, Jaetae Seo, Ting Zhu,
and Michael Z. Hu



Copyright © 2012 Hindawi Publishing Corporation. All rights reserved.

This is a special issue published in "Journal of Nanomaterials." All articles are open access articles distributed under the Creative Commons Attribution License, which permits unrestricted use, distribution, and reproduction in any medium, provided the original work is properly cited.

Editorial Board

Katerina Aifantis, Greece
Nageh K. Allam, USA
Margarida Amaral, Portugal
Xuedong Bai, China
L. Balan, France
Enrico Bergamaschi, Italy
Theodorian Borca-Tasciuc, USA
C. Jeffrey Brinker, USA
Christian Brosseau, France
Xuebo Cao, China
Shafiul Chowdhury, USA
Kwang-Leong Choy, UK
Cui ChunXiang, China
Miguel A. Correa-Duarte, Spain
Shadi A. Dayeh, USA
Claude Estournes, France
Alan Fuchs, USA
Lian Gao, China
Russell E. Gorga, USA
Hongchen Chen Gu, China
Mustafa O. Guler, Turkey
John Zhanhu Guo, USA
Smrati Gupta, Germany
Michael Harris, USA
Zhongkui Hong, USA
Michael Z. Hu, USA
David Hui, USA
Y.-K. Jeong, Republic of Korea
Sheng-Rui Jian, Taiwan
Wanqin Jin, China
Rakesh K. Joshi, India
Zhenhui Kang, China
Fathallah Karimzadeh, Iran
Alireza Khataee, Iran
Do Kyung Kim, Korea
Kin Tak Lau, Australia
Burtrand Lee, USA
Benxia Li, China
Jun Li, Singapore
Shijun Liao, China
Gong Ru Lin, Taiwan
J.-Y. Liu, USA
Jun Liu, USA
Tianxi Liu, China
Songwei Lu, USA
Daniel Lu, China
Jue Lu, USA
Ed Ma, USA
Gaurav Mago, USA
Santanu K. Maiti, Israel
Sanjay R. Mathur, Germany
A. McCormick, USA
Vikas Mittal, UAE
Weihai Ni, Germany
Sherine Obare, USA
Edward Andrew Payzant, USA
Kui-Qing Peng, China
Anukorn Phuruangrat, Thailand
Ugur Serincan, Turkey
Huaiyu Shao, Japan
Donglu Shi, USA
Suprakas Sinha Ray, South Africa
Vladimir Sivakov, Germany
Marinella Striccoli, Italy
Bohua Sun, South Africa
Saikat Talapatra, USA
Nairong Tao, China
Titipun Thongtem, Thailand
Somchai Thongtem, Thailand
Valeri P. Tolstoy, Russia
Tsung-Yen Tsai, Taiwan
Takuya Tsuzuki, Australia
Raquel Verdejo, Spain
Mat U. Wahit, Malaysia
Shiren Wang, USA
Yong Wang, USA
Ruibing Wang, Canada
Cheng Wang, China
Zhenbo Wang, China
Jinquan Wei, China
Ching Ping Wong, USA
Xingcai Wu, China
Guodong Xia, Hong Kong
Zhi Li Xiao, USA
Ping Xiao, UK
Shuangxi Xing, China
Yangchuan Xing, USA
N. Xu, China
Doron Yadlovker, Israel
Ying-Kui Yang, China
Khaled Youssef, USA
William W. Yu, USA
Kui Yu, Canada
Haibo Zeng, China
Tianyou Zhai, Japan
Renyun Zhang, Sweden
Yanbao Zhao, China
Lianxi Zheng, Singapore
Chunyi Zhi, Japan

Contents

Nanocrystals-Related Synthesis, Assembly, and Energy Applications 2012, Bo Zou, William W. Yu, Jaetae Seo, Ting Zhu, and Michael Z. Hu
Volume 2012, Article ID 820439, 2 pages

The Progress of TiO₂ Nanocrystals Doped with Rare Earth Ions, Hai Liu, Lixin Yu, Weifan Chen, and Yingyi Li
Volume 2012, Article ID 235879, 9 pages

Growth and Structure of Pure ZnO Micro/Nanocombs, Tengfei Xu, Pengfei Ji, Meng He, and Jianye Li
Volume 2012, Article ID 797935, 5 pages

Subwavelength Microstructures Fabrication by Self-Organization Processes in Photopolymerizable Nanocomposite, I. Yu. Denisyuk, N. O. Sobeshuk, J. A. Burunkova, and N. D. Vorzobova
Volume 2012, Article ID 827438, 6 pages

Characterization of Orthorhombic α -MoO₃ Microplates Produced by a Microwave Plasma Process, Arrak Klinbumrung, Titipun Thongtem, and Somchai Thongtem
Volume 2012, Article ID 930763, 5 pages

The Energy-Efficient Processing of Fine Materials by the Micropyretic Synthesis Route, H. P. Li
Volume 2012, Article ID 727656, 8 pages

Synthesis and Characterization of ZnTe Hierarchical Nanostructures, Baohua Zhang, Fuqiang Guo, and Wei Wang
Volume 2012, Article ID 293041, 5 pages

Synthesis of CdSe/ZnS and CdTe/ZnS Quantum Dots: Refined Digestive Ripening, Sreeram Cingarapu, Zhiqiang Yang, Christopher M. Sorensen, and Kenneth J. Klabunde
Volume 2012, Article ID 312087, 12 pages

Effect of Ultrasonic Irradiation on Preparation and Properties of Ionogels, Yogendra Lal Verma, Manish Pratap Singh, and Rajendra Kumar Singh
Volume 2012, Article ID 570719, 6 pages

Quantum Size Effect in ZnO Nanoparticles via Mechanical Milling, Nurul Azri Khalisah Aznan and Mohd Rafie Johan
Volume 2012, Article ID 439010, 4 pages

A Two-Step Method to Synthesize BaSn(OH)₆ Crystalline Nanorods and Their Thermal Decomposition to Barium Stannate, Xiaohong Wu, Gang Lv, Xiaoyan Hu, and Yiwen Tang
Volume 2012, Article ID 912731, 6 pages

Preparation and Characterization of Ni(OH)₂ and NiO Mesoporous Nanosheets, Changyu Li and Shouxin Liu
Volume 2012, Article ID 648012, 6 pages



Electrochemical Fabrication of Shape-Controlled Copper Hierarchical Structures Assisted by Surfactants, Huaping Dong, Yajun Wang, Feifei Tao, and Linxia Wang
Volume 2012, Article ID 901842, 6 pages

Direct Preparation of Nano-Quasicrystals via a Water-Cooled Wedge-Shaped Copper Mould, Zhifeng Wang, Weimin Zhao, Chunling Qin, Yan Cui, Shenglei Fan, and Junqing Jia
Volume 2012, Article ID 708240, 6 pages

Editorial

Nanocrystals-Related Synthesis, Assembly, and Energy Applications 2012

Bo Zou,¹ William W. Yu,² Jaetae Seo,³ Ting Zhu,⁴ and Michael Z. Hu⁵

¹ State Key Laboratory of Superhard Materials, Jilin University, Changchun 130012, China

² College of Electronic Science and Engineering, Jilin University, Changchun 130012, China

³ Department of Physics, Hampton University, Hampton, VA 23668, USA

⁴ Philips Lumileds Lighting Company, San Jose, CA 95131, USA

⁵ Oak Ridge National Laboratory, Nuclear Science and Technology Division, Oak Ridge, TN 37831, USA

Correspondence should be addressed to Bo Zou, zoubo@jlu.edu.cn

Received 23 February 2012; Accepted 23 February 2012

Copyright © 2012 Bo Zou et al. This is an open access article distributed under the Creative Commons Attribution License, which permits unrestricted use, distribution, and reproduction in any medium, provided the original work is properly cited.

During the past decades, nanocrystals have attracted broad attention due to their unique shape- and size-dependent physical and chemical properties that differ drastically from their bulk counterparts. Hitherto, much effort has been dedicated to achieving rational controlling over the morphology, assembly, and related energy applications of the nanomaterials. Therefore, the ability to manipulate the morphology, size, and size distribution of inorganic nanomaterials is still an important goal in modern materials physics and chemistry. Especially, the world's demand for energy supply is causing a dramatic escalation of social and political unrest. Likewise, the environmental impact of the global climate change due to the combustion of fossil fuel is becoming increasingly alarming. These problems compel us to search for effective routes to build devices that can supply sustainable energy, with not only high efficiency but also environmental friendship. One of ways to relieve the energy crisis is to exploit devices based on renewable energy sources, such as solar energy and water power. Aiming at this exploration, the primary stage requires the design of appropriate strategies for the synthesis of high-quality nanocrystals with respect to size uniformity and superior electrochemical performances. As a consequence, we organize the current special issue for *Journal of Nanomaterials* to provide the authors with a platform and readers with the latest achievements of nanocrystals-related synthesis, assembly, and energy applications.

One of the papers presents the synthesis of single crystalline ZnTe hierarchical nanostructures by a simple thermal evaporation technology and discussed the corresponding growth mechanism. Another paper reports the synthesis of CdSe and CdTe quantum dots (QDs) from the bulk CdSe and CdTe material by evaporation/cocondensation using the solvated metal atom dispersion technique and refined digestive ripening. It is found that PL quantum yield of CdSe QDs and CdTe QDs upon covering with a ZnS shell was greatly enhanced. Another paper presents that nanosize TiB whiskers were successfully obtained by micro-pyretic synthesis which is considered as the one of the novel energy-saving processing techniques. The diffusion-controlled reaction mechanism was proposed in this study.

One more paper presents the progress of TiO₂ nanocrystals doped with rare earth ions in the aspect of nano-optic and photocatalytic properties. Another paper presents a search article in which ZnO nanoparticles were successfully synthesized at room temperature via mechanical milling, and the quantum size effect was interpreted in terms of absorption and PL spectra. An additional paper presents that ZnO micro-/nanocombs have been successfully synthesized on Cu substrate using a highly repeatable catalyst-free chemical vapor deposition method. The cathodoluminescence spectrum was also measured on an individual ZnO comb and only a broad strong green emission band was observed. Another paper presents that mesoporous

nanosheets of single-crystalline $\text{Ni}(\text{OH})_2$ were successfully prepared via a facile hydrothermal method. Furthermore, single-crystalline NiO mesoporous nanosheets were also obtained through a thermal decomposition of the obtained $\text{Ni}(\text{OH})_2$. Another paper presents that $\text{BaSn}(\text{OH})_6$ nanorods were synthesized via a novel two-step technique involving the preparation of precursor $\text{Na}_2\text{Sn}(\text{OH})_6$ crystals in aqueous solution via hydrothermal method and the ion-exchange reaction between $\text{Na}_2\text{Sn}(\text{OH})_6$ crystals and Ba^{2+} solution that followed, assisted by ultrasonic treatment. In addition, the powder BaSnO_3 has been obtained by thermal treatment using $\text{BaSn}(\text{OH})_6$ nanorods as precursor. The ninth paper presents a microwave plasma synthesis of orthorhombic α - MoO_3 microplates with photoluminescence in a wavelength range of 430–440 nm.

One more paper presents that various copper hierarchical structures assisted by surfactants were successfully fabricated combined with the electrodeposition technique and the possible formation mechanism of the copper hierarchical structures with various morphologies was discussed. Another paper presents that multicomponent Mg -based nano-quasicrystals were directly prepared through a simple route by using a water-cooled wedge-shaped copper mould.

An additional paper describes the research results on nanometers sizes subwavelength nanostructure fabrication by UV-curing of special nanocomposite material with self-organization and light self-focusing effects. Obtained results will be useful for diffraction limit overcoming in projection lithography as well as for deep lithography technique. Another paper presents that ionogels were prepared by ultrasonic-assisted sol-gel process and it has been found that ultrasonic irradiation affected the gelation dynamics and kinetics in pore parameters and vibrational properties of the IL.

Acknowledgments

The editors would like to thank the authors for their contributions to this special issue, the reviewers for their time and dedication.

Bo Zou
William W. Yu
Jaetae Seo
Ting Zhu
Michael Z. Hu

Review Article

The Progress of TiO₂ Nanocrystals Doped with Rare Earth Ions

Hai Liu, Lixin Yu, Weifan Chen, and Yingyi Li

Department of Materials Science and Engineering, Nanchang University, Nanchang 330031, China

Correspondence should be addressed to Lixin Yu, yulixin72@yahoo.com.cn

Received 29 September 2011; Revised 3 November 2011; Accepted 3 November 2011

Academic Editor: William W. Yu

Copyright © 2012 Hai Liu et al. This is an open access article distributed under the Creative Commons Attribution License, which permits unrestricted use, distribution, and reproduction in any medium, provided the original work is properly cited.

In the past decades, TiO₂ nanocrystals (NCs) have been widely studied in the fields of photoelectric devices, optical communication, and environment for their stability in aqueous solution, being nontoxic, cheapness, and so on. Among the three crystalline phases of TiO₂, anatase TiO₂ NCs are the best crystallized phase of solar energy conversion. However, the disadvantages of high band gap energy (3.2 eV) and the long lifetime of photogenerated electrons and holes limit its photocatalytic activity severely. Therefore, TiO₂ NCs doped with metal ions is available way to inhibit the transformation from anatase to rutile. Besides, these metal ions will concentrate on the surface of TiO₂ NCs. All above can enhance the photoactivity of TiO₂ NCs. In this paper, we mainly outlined the different characterization brought about in the aspect of nanooptics and photocatalytics due to metal ions added in. Also, the paper mainly concentrated on the progress of TiO₂ NCs doped with rare earth (RE) ions.

1. Introduction

As one of the most popular semiconductors, TiO₂ has attracted lots of interest for its high photodegradation efficiency, high photocatalytic activity, high stability, and other advantages [1–4]. Just for these reasons, it has been used to purify polluted water and air, to solve the environmental problems, to be host in the field of solar cell and other relative areas [5, 6]. It is well known that reduction of particle size of crystalline system can result in remarkable modification of their physical and chemical properties which are different from those of micro-sized materials, as called bulk, because of surface effect and quantum confinement effect of nanometer materials. Thus TiO₂ NCs have been one of the research central issues. But TiO₂ NCs have the limits of wide band and the trend to transform to rutile from anatase, which has a negative effect to the photocatalytic activity. Some researchers have reported that they could improve the absorption and photocatalytic activity via dye-sensitizing, surface deposition with metal or doping with metal, nonmetal, or their oxides [7–11]. And many nonmetal ions have been successfully doped, such as S, C, F, N, and B [8, 12–16]. Although doping such additives could change the band gap, they will get the oxidative capacity down. Thus,

it cannot degrade the adsorption on the surface of nano-TiO₂ absolutely. In addition, the structure stability is not that well. Also, doping metal ions to nano-TiO₂ has also been studied extensively, such as Pt and W [17–20]. Particularly, many studies have been focused on doping RE ions into TiO₂ NCs to improve this situation [21–27]. Because of the perfect ability of titanium oxide to form complexes with the f-orbital from RE, it will adsorb foreign ions around the surface, then enhancing the photocatalytic activity or other optoelectronic characteristics [27, 28]. Among all the RE elements, the Eu/Er ions are considered as the best choice for its excellent physical and chemical performance. The RE ions will form complexation with RE–O–Ti bond on the inner-sphere surface. On the one hand, this bond will inhibit the transformation from anatase to rutile, and on the other hand, the formed complexation will strengthen the ability to absorb foreign ions [27]. In addition, the absorption of TiO₂ NCs doped with RE ions may be adjusted from UV to visible light region because the RE ions have large amounts of energy levels. So it is very necessary for researchers to explore the theory and the experimental results on such field. And now it has been widely known that the photocatalytic reactivity of titanium dioxide depends on microstructure, particle size, preparative route, foreign ions, and so forth [29–31].

In this paper, we introduced the recent development of nanocrystalline TiO₂ doped with RE ions or other additives.

2. The Approaches to Fabricate TiO₂ NCs

The synthesis technique can affect nanocrystalline TiO₂ on the structure, purity, morphology, and other qualities. The soft chemical method, such as sol-gel, hydrothermal method, has many advantages, such as easy, cheaper, preparation processes being controlled and has been applied to prepare TiO₂ NCs extensively. The comparison among these methods was listed in Table 1.

2.1. Hydrothermal Method. The hydrothermal growth of TiO₂ nanowires with using TiO₂ powder in a 5–10 M alkali solution has been extensively applied [33, 34]. However, these films fabricated by this method are very thin, and the processing temperature is too high to be large-scale applications. Still, there are two major controversies about the chemical structure and formation mechanism in the hydrothermal process of TiO₂ NCs doped with RE ions [32]. These chemical structures and their lattice parameters are shown in Table 2. The chemical composition of Na_xH_{2-x}Ti₃O₇ and Na_xH_{2-x}Ti₂O₄(OH) groups are more acceptable. The replacement of Na⁺ by H⁺ during acid washing and the existence of [TiO₆] play a very important role in forming the TiO₂ nanotubes. And rutile is thought to have a better ability to rearrange than anatase phase. The TiO₂ NCs doped with RE ions are usually formed during the sol-gel process [35–38]. After annealing at a relatively high temperature, the RE ions are absorbed on the surface of NCs or enter into the vacancies of lattice just for the theory of solid reaction. Doping of RE ions will inhibit the transformation from anatase to rutile, then it maybe have a high affect on the TiO₂ nanotube growing as thin-and-long state. It is important and interesting that Tong et al. reported that the TiO₂ NCs-doped Ce⁴⁺ ions by hydrothermal method could effectively improve the photocatalytic activity of TiO₂ NCs under both UV light irradiation and visible light irradiation due to the important role 4f electron configuration of Ce⁴⁺ ions played in interfacial charge transfer and elimination of electron-hole recombination [39]. Yan et al. thought that the expansion of the lattice that probably results from the formation of RE–O–Ti bonds [35]. Also they found that the percentage of anatase phase in RE-doped TiO₂ decreasing in the order of Nd³⁺ > Pr³⁺ > Y³⁺ > La³⁺, as is shown in Table 3, but the degree of red shift increases in the order of La³⁺ < Pr³⁺ < Nd³⁺ < Y³⁺-doped samples, in contrast with the ion radii of RE. We can conclude, the doping of RE ion will cause the energy transfer with TiO₂ conduction or valence band, which will lead red shift due to the transition of the electrons situated in the inner 4f orbital to the 5d orbital (4f-5d transition) or to other 4s orbital (f-f transition) [40]. The applied temperature, treatment time, the type of alkali solution, and the Ti precursor during the hydrothermal treatment [32] are considered as the predominant factors affecting the fabrication of TiO₂ doped with RE. So the study on how the RE ions affect the formation of TiO₂ associating

with these factors above is very necessary to put the TiO₂ NCs into actual application.

2.2. Sol-Gel Synthesis. Sol-gel approach is one of the most practical manners to prepare inorganic materials for its simpleness and low cost. And we can acquire nanoparticles with dimensions ranging from 5 to 100 nm. The material obtained by this method shows many desirable properties such as high surface area, high homogeneity [41–43]. But because the precursor has a so high reactivity that it is hard to control the structure development during the hydrolysis and condensation, which makes it difficult to fabricate monolithic TiO₂ NCs [44–48]. Chen et al. have reported C-, N-modified porous monolithic TiO₂ NCs through sol-gel technique with average particle size of 7.8 nm [48]. And the reaction rate of decolorization of methyl orange is 0.0026 min⁻¹, which proves that the ratio of the precursors plays an important role in the structure and photo activity. Moreover, Zeng et al. had prepared Eu:TiO₂ with a strong photoluminescence emission with the average particle size of 13 nm [49]. As for the RE ions, it is often doped into the solution of precursor in the form of nitrate or chloride. After several hours of stirring, we can obtain transparent sol with RE. Then the sample must be annealing at a certain temperature for a certain period to ensure Ln(III)-TiO₂ NCs obtained. Stengl et al. studied the affects of RE (La, Ce, Pr, Nd, Sm, Eu, Dy, Gd) on the physical and chemical properties of titania NCs by sol-gel method [50], as is shown in Figure 1. They found that best photocatalytic properties in visible light were the TiO₂ NCs doped with Nd³⁺ ions ($k = 0.0272 \text{ min}^{-1}$ for UV and 0.0143 min^{-1} for visible light). Xu et al. also got the similar result that Gd³⁺-doped TiO₂ showing the highest reaction activity among all concerned RE-doped samples (Sm³⁺-, Ce³⁺-, Er³⁺-, Pr³⁺-, La³⁺-, and Nd³⁺-doped TiO₂ NCs catalyst) because of its specific characteristics [23], which was similar with the result from the study of El-Bahy et al., who also thought that Gd³⁺-doped TiO₂ NCs are more effective than La³⁺, Nd³⁺, Sm³⁺, Eu³⁺, and Yb³⁺ just because Gd³⁺/TiO₂ NCs have the lowest band gap and particle size, and also the highest surface area and pore volume [51]. At the meantime, the conclusion that the synthesized Eu/TiO₂ catalyst exhibits strong red emissions under excitation wavelength at 394 and 464 nm from the comparison Eu/TiO₂ and Gd/TiO₂ by Zhou et al. [52]. As can be concluded that, the relationship between RE and luminescent properties or catalytic efficiency needs further research in the field of TiO₂ NCS synthesized by sol-gel technique.

2.3. Anodic Oxidation Method. Since Grimes and coworkers first reported the fabrication of titania nanotube array via anodic oxidation of titanium foil in a fluoride-based solution in 2001 [53], the studies on precise control and extension of the nanotube morphology, length and pore size, and wall thickness [54, 55] have obtained extensive attention. As is thought that chemical dissolution and electrochemical etching process play an important role in the conformation of nanotubes. And the electrolyte used in this system is

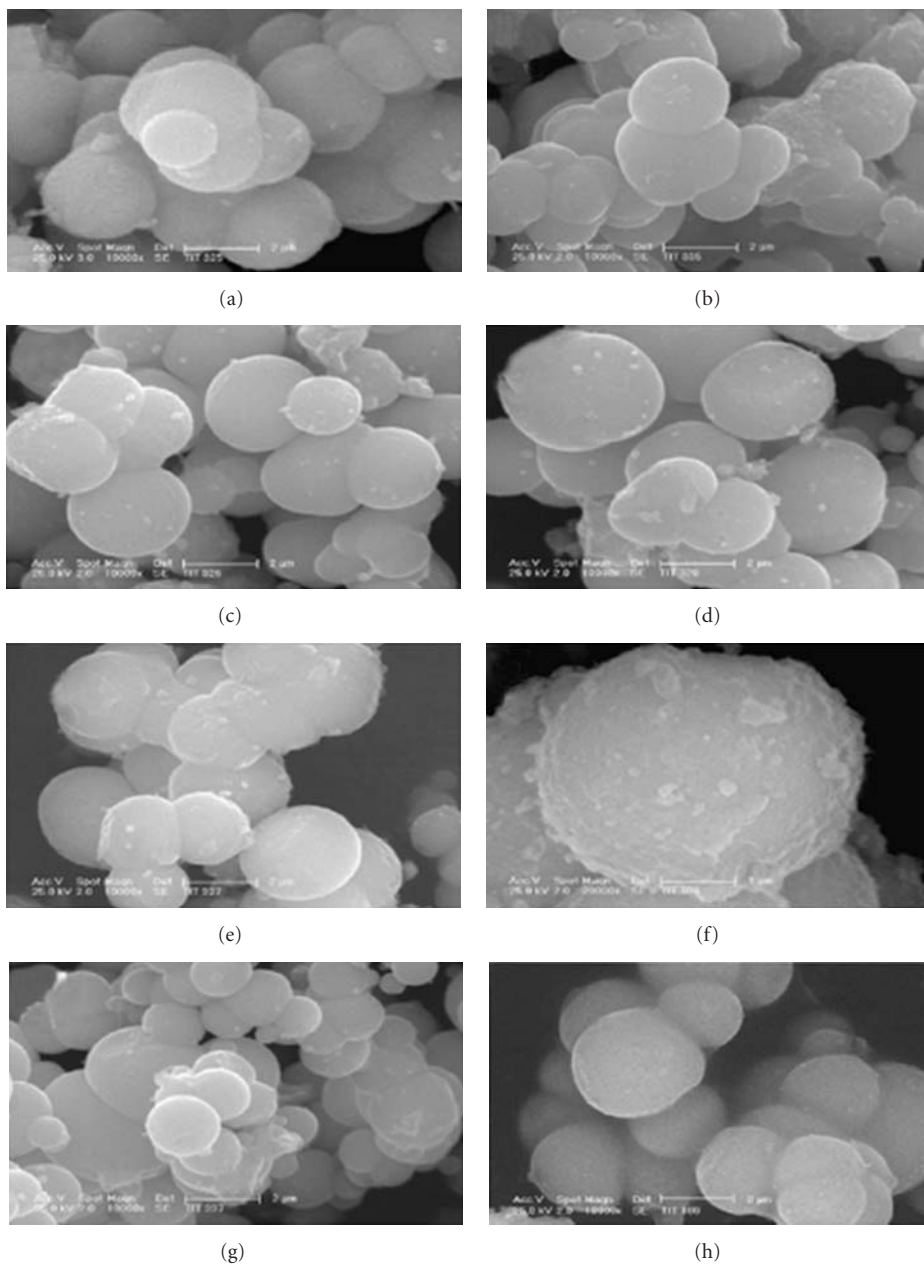


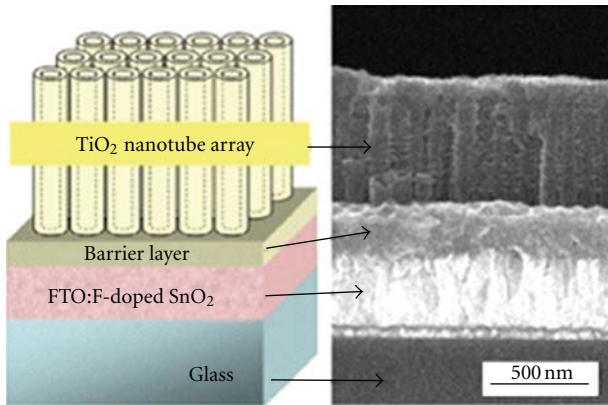
FIGURE 1: SEM images of sample denoted as (a) TiNd₁: 100 g TiOSO₄ + 3.15 g Nd, (b) TiSm₁: 100 g TiOSO₄ + 3 g Sm(NO₃)₃, (c) TiCe₃₁: 100 g TiOSO₄ + 0.25 g Ce₂(SO₄)₃, (d) TiCe₄₁: 100 g TiOSO₄ + 0.25 g Ce(SO₄)₂, (e) TiDy₁: 100 g TiOSO₄ + 3.10 g Dy₂O₃, (f) TiEu₁: 100 g TiOSO₄ + 6.00 g Eu₂O₃, (g) TiPr₁: 100 g TiOSO₄ + 1.50 g Pr(NO₃)₃, and (h) TiLa₁: 100 g TiOSO₄ + 1 g La(NO₃)₃. Reprinted with permission from [50].

always HF or KF, whose concentration has a strong effect on the dimensions and nanotube arrays [56]. Using the anodic potential from 10 to 20 V, self-organized TiO₂ NCs can be produced with diameters between 15 nm and 200 nm under specific electrochemical condition [57, 58]. The pH value of the electrolyte will also affect the thickness of TiO₂ nanotube layers [58, 59]. Yang et al. used anodization method then obtained TiO₂ nanotube arrays with a high surface area [60], as seen in Figure 2. It can be seen that the length and average outer diameter of this nanotube is 680 nm and

80 nm with a length-to-width aspect ratio about 8.5, which raises the conversion efficiencies to 0.31%, improving surface activities largely. RE ions are usually added into TiO₂ NCs during the preparation procedure. After heating at 400°C for a certain time for decomposing the organic compounds brought into during the preparation procedure, the samples are needed to be heated to higher temperature for the insurance of formation of RE compounds in the layers [61]. Graf et al. successfully prepared the TiO₂ doped with cerium and gadolinium ions in the anodic oxidation method, and

TABLE 1: Comparison of current methods in TNT fabrication. Reprinted with permission from [32].

Fabrication method	Advantages	Disadvantages	TNT features
Template-assisted method	(1) The scale of nanotube can be moderately controlled by applied template	(1) Complicated fabrication process (2) Tube morphology may be destroyed during fabrication process	Ordered arrays (powder form)
Electrochemical anodic oxidation method	(1) More desirable for practical applications (2) Ordered alignment with high aspect ratio (3) Feasible for extensive applications	(1) Mass production is limited (2) Rapid formation kinetics is subjected to the utilization of HF (3) Highly expense of fabrication apparatus	Oriented arrays (thin film)
Hydrothermal treatment	(1) Easy route to obtain nanotube morphology (2) A number of modifications can be used to enhance the attributes of titanium nanotubes (3) Feasible for extensive applications	(1) Long reaction duration is needed (2) Highly concentrated NaOH must be added (3) Difficult in achieving uniform size	Random alignment (powder form)

FIGURE 2: Schematic diagram of TiO₂ nanotube photoanode architecture and SEM cross-sectional view of sample fabricated by anodization method. Reprinted with permission from [60].

they found that Gd-doped titanium dioxide showed better photocatalytic activity than cerium-doped sample possibly because Gd³⁺ ions have better stability [62].

2.4. Other Methods. Nowadays, there are also some other routes to fabricate TiO₂ NCs. For example, Liang et al. had studied the effects brought by doping these ions of La, Y, Yb, Eu, Dy into TiO₂ NCs with the plasma way [63]. And they found that the effects of pH, sample flow rate and volume, elution solution, and interfering ions on the separation of analytes all have influence on the photocatalytic activity. Wu et al. systematically explored the effects for lanthanum-ions-doped TiO₂ NCs by plasma spray as well [64].

Template-assisted method is one of the most popular ways to fabricate such material. Attar et al. successfully prepared well-aligned anatase and rutile TiO₂ nanorods and nanotubes with a diameter of about 80–130 nm via sol-gel template method [65]. Also, magnetron sputtering method, electrophoretic deposition (EPD), and many other methods

TABLE 2: Proposed chemical structures of TNTs and their corresponding lattice parameters. Reprinted with permission from [32].

Chemical structure	Lattice parameters
Anatase TiO ₂	Tetragonal; $a = 3.79$ nm, $b = 3.79$, $c = 2.38$
N ₂ Ti ₃ O ₇ , Na ₂ Ti ₃ O ₇ , Na _x H _{2-x} Ti ₃ O ₇	Monoclinic; $a = 1.926$ nm, $b = 0.378$, $c = 0.300$, $\beta = 101.45^\circ$
H ₂ Ti ₂ O ₄ (OH) ₂ , Na ₂ Ti ₂ O ₄ (OH) ₂	Orthorhombic; $a = 1.808$ nm, $b = 0.379$, $c = 0.299$
H _x Ti _{2-x/4} □ _{x/4} O ₄ (H ₂ O)	Orthorhombic; $a = 0.378$ nm, $b = 1.874$, $c = 0.298$
H ₂ Ti ₄ O ₉ (H ₂ O)	Monoclinic; $a = 1.877$ nm, $b = 0.375$, $c = 1.162$, $\beta = 104.6^\circ$

□: Vacancy.

are employed to fabricate TiO₂ NCs doped with RE ions [66–70]. All above methods also could create nanomaterial with perfect morphology and high photocatalytic activity.

3. The Effect Caused by RE Ions

In this section, we mainly discuss the change of optical properties and the morphology caused by the RE ions doped or codoped with RE and other non-RE.

3.1. The Theory of the Effect Caused by RE Ions. The energy transfer from TiO₂ NCs to RE may easily take place since RE ions have a plenty of energy levels. For example, ⁵D₁ → ⁷F₁, ⁵D₀ → ⁷F_{*j*} (*j* = 1, 2, 3, 4) transitions of Eu³⁺ ions will cause visible luminescence peaking at 543, 598, 620, 665, and 694 nm [71]. In addition, the RE-doped TiO₂ NCs almost have the capacity to enhance photocatalytic activity due to

TABLE 3: Structural parameters of rare-earth-doped TiO₂ after template removal. Reprinted with permission from [35].

Sample	Percentage of anatase phase	Specific surface area (m ² /g)	Modal pore diameter (nm)	Total pore volume (cm ³ /g)
TiO ₂ ⁻²	83.17	165	1.6	0.11
[0.3%]	95.18	220	1.4	0.14
Nd-doped TiO ₂				
[0.3%]	90.22	200	1.6	0.15
Pr-doped TiO ₂				
[0.3%]	86.35	289	1.6	0.11
La-doped TiO ₂				
[0.3%]	83.71	175	1.4	0.11
Y-doped TiO ₂				

following properties of as-prepared RE³⁺/TiO₂ composites: (i) quantum size effect; (ii) unique textural properties (mesoporosity with larger BET surface areas and pore sizes); (iii) interesting surface compositions (more hydroxyl oxygen and adsorbed oxygen and some Ti³⁺ species existed at the surface of the products with respect to pure TiO₂) [72], while some thought that the increase in photoactivity is probably due to the higher adsorption, red shifts to a longer wavelength, and the increase in the interfacial electron transfer rate [41, 51].

3.2. The Effect Caused by RE Ions Doped Only. TiO₂ NCs doped with RE ions can concentrate organic pollutants on the semiconductor surface just because lanthanide ions can form complexes with various Lewis bases including organic acids, amines, aldehydes, alcohols, and thiols by the interaction of the functional groups with their f orbital, which can enhance the efficiency of separation between electrons and holes and prohibit the transformation from anatase to rutile [27, 28, 73]. Accordingly, it can prolong the photoresponse in visible region. Du et al. studied the effect of surface OH population on the photocatalytic activity of RE-doped P25-TiO₂ systematically [74], listed in Table 4. It can be seen that Pr, La, Ce, Y, and Sm ions in TiO₂ Ncs have a significant inhibition of phase transformation, especially at 800°C or above. And the anatase fraction follows the decreasing order Pr > La > Ce > Y > Sm. At the meantime, we can also know that the photocatalytic degradation of methylene blue over RE oxide-modified TiO₂ is mainly dependent on the quantity of a specific anatase—OH group. Cacciotti et al. successfully prepared La-, Eu-, and Er-doped TiO₂ NCs via electrospinning technique [75], which also can raise the transformation temperature up to 900°C. Wang et al. also synthesized TiO₂ NCs doped with Eu, Er, Ce, Pr by this method [76]. And the particles obtained had

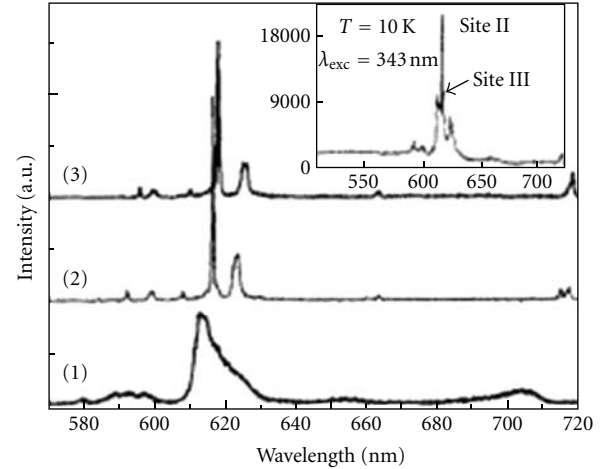


FIGURE 3: Site-selective emission spectra of the Eu_{3n}:TiO₂ nanocrystals at 10 K, with curves (1) $\lambda_{\text{exc}} = 464.7$ nm for Site I; (2) $\lambda_{\text{exc}} = 470.6$ nm for Site II; and (3) $\lambda_{\text{exc}} = 472.0$ nm for Site a, respectively. The inset shows the 10 K emission spectrum under the band gap excitation at 343.1 nm. Reprinted with permission from [81].

an average diameter of 10 nm with remarkable luminescent properties. It can be clearly seen that most of the RE ions have the ability to inhibit the transformation from anatase to rutile. Li et al. reported that the luminescent intensity can be enhanced through energy transfer from Eu³⁺ to TiO₂ NCs [77]. Jeon and Braun synthesized Er³⁺-doped TiO₂ nanoparticles (~50 nm) through a simple hydrothermal method starting from sol-gel precursors with anatase phase [78]. They observed obviously enhanced luminescence from thin films of the nanoparticles by annealing at 500°C. A sharp emission peak at 1532 nm with a full width at half maximum (FWHM) of 5 nm was observed, which excludes the possibility that Er³⁺ ions exist under a free oxide form in the TiO₂ matrix, with contrast with the emission band of erbium oxide nanoclusters synthesized through a microemulsion technique centered at 1540 nm with an FWHM of 22 nm [79]. Patra et al. also studied the upconversion luminescence of Er doped into TiO₂ NCs under 975 nm excitation [80].

However, there are two major controversies still exist [81]. One is whether the lifetime of transition metal or RE ions-doped TiO₂ semiconductor NCs can be shortened by orders of magnitude caused by quantum size effects. The other is that lanthanide ions incorporate into the lattice sites of the host or be adsorbed on the surface because of the different radius and valence between RE ions and cationic of host. Chen et al. prepared TiO₂:Eu anatase NCs (8–12 nm) by a hydrothermal method and proved that Eu³⁺ occupy three sites in NCs host through site selective spectra at 10 K [81], as shown in Figure 3. By means of site selective spectra, at least three kinds of luminescence sites of Eu³⁺ are identified and separated from each other. Two sites (Sites II and IU) exhibit sharp emission and excitation peaks, which are ascribed to the lattice site with ordered crystalline environment (inside). The other site (Site I) associated with

TABLE 4: Characterization of samples. Reprinted with permission from [74].

Sample	Anatase fraction ^a [nm]	Anatase crystal size ^a [nm]	Rutile crystal size ^a [nm]	Band gap energy [eV]	S _{scr} [m ² /g]
P25	0.70	22	37	3.25	51
P25_600	0.70	25	36	3.23	47
P25_0, 2La_600	0.71	28	41	3.23	46
P25_0, 2Ce_600	0.71	27	50	3.19	47
P25_0, 2Y_600	0.72	28	39	3.16	46
P25_0, 2Pr_600	0.71	27	50	3.14	47
P25_0, 25m_600	0.71	26	47	3.16	46
P25_800	0.05	—	43	3.04	16
P25-0.2La-800	0.22	31	43	3.03	23
P25-0.2Ce-800	0.15	35	45	3.04	19
P25-0.2Y-800	0.13	30	50	3.02	20
P25-0.2Pr-800	0.31	35	47	3.02	24
P25-0.25m-800	0.08	29	50	3.01	17
P25-1La-800	0.31	35	45	3.05	25
P25-1Ce-800	0.48	31	47	3.07	30
P25-1Y-800	0.05	—	50	3.04	16
P25-1Pr-800	0.15	31	45	3.03	21
P25-15m-800	0.37	33	50	3.06	29
P25_2La_800	0.14	34	47		21
P25_2Ce_800	0.15	35	49		18

^a Determined from XRD.

the distorted lattice sites near the surface shows significantly broadened fluorescence lines. very strong Eu^{3+} luminescence from major Sites II and III plus other minor sites can be seen under the band gap excitation at 343.1 nm. The energy transfer from the host to Eu^{3+} confirms that Eu^{3+} ions have been effectively incorporated into the TiO_2 NCs. But it should be noted that there may be some RE ions locating at surface sites. So it always has a long way to explore the function caused by lanthanide ions doped.

3.3. The Effect Caused by Codoped RE Ions and Other Ions. Besides, Xu et al. and Ma et al. had prepared the TiO_2 NCs codoped with RE ions and nonmetal ions by the sol-gel method [82, 83], which had better adsorption activity than those doped with RE ions only. Xu et al. reported that Eu-, N-codoped TiO_2 NCs exhibited a significant red shift to the visible area [82], as shown in Figure 4. It is obvious that Eu-, N-codoped TiO_2 NCs show the highest adsorption activity. And we could also know that Eu-, N-codoped TiO_2 NCs have a smaller particle with a good inhibition from anatase to rutile. Besides, Ma et al. also obtained Sm-, N-codoped TiO_2 NCs by a similar way [83], which was similar to the result of Eu-, N-codoped TiO_2 NCs. Thus, we can conclude the absorption of TiO_2 NCs could be modulated from UV light to visible light because of the addition of RE ions, which can meet the application. It is thought that the metal ions (such as lanthanide ions) doped TiO_2 NCs will expand the photoresponse area. Meantime, the nonmetal ions will inhibit the combination

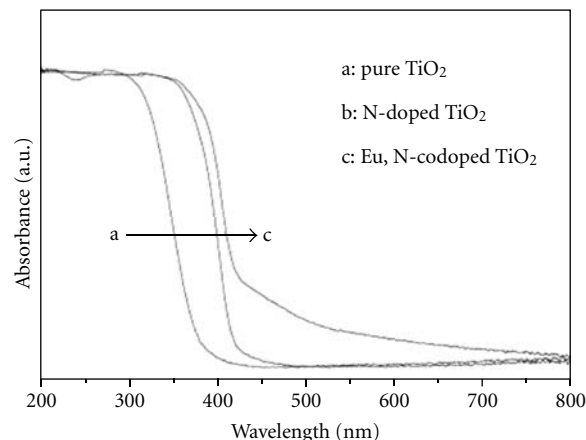


FIGURE 4: DRS spectra of Eu, N-codoped titania, N-doped titania, and pure titania. Reprinted with permission from [82].

of photogenerated electrons and holes. And it also has the ability to suppress the transformation from anatase to rutile. So it is hopeful to improve the photocatalytic activity by adding the metal ions with nonmetal elements.

4. Conclusion

In conclusion, TiO_2 NCs are chosen as one of the most potential candidates to purify polluted water and air, to solve the environmental problems, and to be host in the field of

solar cell and other relative areas for its excellent stability, low cost, and friendliness to environment. Adding RE ions to TiO₂ can suppress the transformation to rutile from anatase, absorb the organic pollutant on the surface of the base, then improving the photocatalytic activity. So RE-doping nano-TiO₂ has been studied extensively, but the application situation is not that affirmative. The author suggested that the development orientation include these aspects below.

- (1) explore the influent theory about the co-doping ions into nano-TiO₂, such as metal and metal, metal and nonmetal, nonmetal and nonmetal, especially the area of metal and nonmetal coexists,
- (2) investigate the way to improve the catalytic properties, without sacrificing the oxidation activity, especially adjusting the absorption range,
- (3) search for the ideal ways to manufacture RE-doped TiO₂ NCs so as to modulate the absorption to visible region and to meet its industrial needs.

References

- [1] P. V. Kamat, "Meeting the clean energy demand: nanostructure architectures for solar energy conversion," *Journal of Physical Chemistry C*, vol. 111, no. 7, pp. 2834–2860, 2007.
- [2] M. Sleiman, C. Ferronato, and J. M. Chovelon, "Photocatalytic removal of pesticide dichlorvos from indoor air: a study of reaction parameters, intermediates and mineralization," *Environmental Science and Technology*, vol. 42, no. 8, pp. 3018–3024, 2008.
- [3] K. Maeda, K. Teramura, D. L. Lu et al., "Photocatalyst releasing hydrogen from water—enhancing catalytic performance holds promise for hydrogen production by water splitting in sunlight," *Nature*, vol. 440, no. 7082, p. 295, 2006.
- [4] X. Chen and S. S. Mao, "Titanium dioxide nanomaterials: synthesis, properties, modifications and applications," *Chemical Reviews*, vol. 107, no. 7, pp. 2891–2959, 2007.
- [5] J. H. Park, S. Kim, and A. J. Bard, "Novel carbon-doped TiO₂ nanotube arrays with high aspect ratios for efficient solar water splitting," *Nano Letters*, vol. 6, no. 1, pp. 24–28, 2006.
- [6] Y. Li, G. Lu, and S. Li, "Photocatalytic transformation of rhodamine B and its effect on hydrogen evolution over Pt/TiO₂ in the presence of electron donors," *Journal of Photochemistry and Photobiology A*, vol. 152, no. 1–3, pp. 219–228, 2002.
- [7] Z. Wang, C. Chen, F. Wu et al., "Photodegradation of rhodamine B under visible light by bimetal codoped TiO₂ nanocrystals," *Journal of Hazardous Materials*, vol. 164, no. 2–3, pp. 615–620, 2009.
- [8] R. Asahi, T. Morikawa, T. Ohwaki, K. Aoki, and Y. Taga, "Visible-light photocatalysis in nitrogen-doped titanium oxides," *Science*, vol. 293, no. 5528, pp. 269–271, 2001.
- [9] W. Zhao, W. Ma, C. Chen, J. Zhao, and Z. Shuai, "Efficient degradation of toxic organic pollutants with Ni₂O₃/TiO₂-xBx under visible irradiation," *Journal of the American Chemical Society*, vol. 126, no. 15, pp. 4782–4783, 2004.
- [10] C. Chen, M. Long, H. Zeng et al., "Preparation, characterization and visible-light activity of carbon modified TiO₂ with two kinds of carbonaceous species," *Journal of Molecular Catalysis A*, vol. 314, no. 1–2, pp. 35–41, 2009.
- [11] H. Li, D. Wang, P. Wang, H. Fan, and T. Xie, "Synthesis and studies of the visible-light photocatalytic properties of near-monodisperse Bi-doped TiO₂ nanospheres," *Chemistry—A European Journal*, vol. 15, no. 45, pp. 12521–12527, 2009.
- [12] T. Ohno, T. Mitsui, and M. Matsumura, "Photocatalytic activity of S-doped TiO₂ photocatalyst under visible light," *Chemistry Letters*, vol. 32, no. 4, pp. 364–365, 2003.
- [13] S. U. M. Khan, M. Al-Shahry, and W. B. Ingler, "Efficient photochemical water splitting by a chemically modified n-TiO₂," *Science*, vol. 297, no. 5590, pp. 2243–2245, 2002.
- [14] J. C. Yu, J. Yu, W. Ho, Z. Jiang, and L. Zhang, "Effects of F-doping on the photocatalytic activity and microstructures of nanocrystalline TiO₂ powders," *Chemistry of Materials*, vol. 14, no. 9, pp. 3808–3816, 2002.
- [15] R. Nakamura, T. Tanaka, and Y. Nakato, "Mechanism for visible light responses in anodic photocurrents at N-doped TiO₂ film electrodes," *Journal of Physical Chemistry B*, vol. 108, no. 30, pp. 10617–10620, 2004.
- [16] S. C. Moon, H. Mametsuka, S. Tabata, and E. Suzuki, "Photocatalytic production of hydrogen from water using TiO₂ and B/TiO₂," *Catalysis Today*, vol. 58, no. 2, pp. 125–132, 2000.
- [17] M. Kang, S. J. Choung, and J. Y. Park, "Photocatalytic performance of nanometer-sized Fe_xO_y/TiO₂ particle synthesized by hydrothermal method," *Catalysis Today*, vol. 87, no. 1–4, pp. 87–97, 2003.
- [18] T. Hathway, E. M. Rockafellow, Y. C. Oh, and W. S. Jenks, "Photocatalytic degradation using tungsten-modified TiO₂ and visible light: kinetic and mechanistic effects using multiple catalyst doping strategies," *Journal of Photochemistry and Photobiology A*, vol. 207, no. 2–3, pp. 197–203, 2009.
- [19] Y. Ishibai, J. Sato, T. Nishikawa, and S. Miyagishi, "Synthesis of visible-light active TiO₂ photocatalyst with Pt-modification: role of TiO₂ substrate for high photocatalytic activity," *Applied Catalysis B*, vol. 79, no. 2, pp. 117–121, 2008.
- [20] T. S. Yang, M. C. Yang, C. B. Shiu, W. K. Chang, and M. S. Wong, "Effect of N₂ ion flux on the photocatalysis of nitrogen-doped titanium oxide films by electron-beam evaporation," *Applied Surface Science*, vol. 252, no. 10, pp. 3729–3736, 2006.
- [21] G. Boschloo and A. Hagfeldt, "Photoinduced absorption spectroscopy of dye-sensitized nanostructured TiO₂," *Chemical Physics Letters*, vol. 370, no. 3–4, pp. 381–386, 2003.
- [22] M. S. P. Francisco and V. R. Mastelaro, "Inhibition of the anatase-rutile phase transformation with addition of CeO₂ to CuO-TiO₂ system: Raman spectroscopy, X-ray diffraction, and textural studies," *Chemistry of Materials*, vol. 14, no. 6, pp. 2514–2518, 2002.
- [23] A. W. Xu, Y. Gao, and H. Q. Liu, "The preparation, characterization, and their photocatalytic activities of rare-earth-doped TiO₂ nanoparticles," *Journal of Catalysis*, vol. 207, no. 2, pp. 151–157, 2002.
- [24] R. Gopalan and Y. S. Lin, "Evolution of pore and phase structure of sol-gel derived lanthana doped titania at high temperatures," *Industrial and Engineering Chemistry Research*, vol. 34, no. 4, pp. 1189–1195, 1995.
- [25] G. Garcia-Martinez, L. G. Martinez-Gonzalez, J. I. Escalante-García, and A. F. Fuentes, "Phase evolution induced by mechanical milling in Ln₂O₃:TiO₂ mixtures (Ln=Gd and Dy)," *Powder Technology*, vol. 152, no. 1–3, pp. 72–78, 2005.
- [26] C. P. Sibu, S. R. Kumar, P. Mukundan, and K. G. K. Warriar, "Structural modifications and associated properties of lanthanum oxide doped sol-gel nanosized titanium oxide," *Chemistry of Materials*, vol. 14, no. 7, pp. 2876–2881, 2002.

- [27] I. Cacciotti, A. Bianco, G. Pezzotti, and G. Gusmano, "Synthesis, thermal behaviour and luminescence properties of rare earth-doped titania nanofibers," *Chemical Engineering Journal*, vol. 166, no. 2, pp. 751–764, 2011.
- [28] D. W. Hwang, J. S. Lee, W. Li, and S. H. Oh, "Electronic band structure and photocatalytic activity of $\text{Ln}_2\text{Ti}_2\text{O}_7$ ($\text{Ln} = \text{La}, \text{Pr}, \text{Nd}$)," *Journal of Physical Chemistry B*, vol. 107, no. 21, pp. 4963–4970, 2003.
- [29] Y. Zhang, A. Weidenkaff, and A. Reller, "Mesoporous structure and phase transition of nanocrystalline TiO_2 ," *Materials Letters*, vol. 54, no. 5–6, pp. 375–381, 2002.
- [30] D. Vorkapic and T. Matsoukas, "Effect of temperature and alcohols in the preparation of titania nanoparticles from alkoxides," *Journal of the American Ceramic Society*, vol. 81, no. 11, pp. 2815–2820, 1998.
- [31] H. Zhang and J. F. Banfield, "Phase transformation of nanocrystalline anatase-to-rutile via combined interface and surface nucleation," *Journal of Materials Research*, vol. 15, no. 2, pp. 437–448, 2000.
- [32] H. H. Ou and S. L. Lo, "Review of titania nanotubes synthesized via the hydrothermal treatment: fabrication, modification, and application," *Separation and Purification Technology*, vol. 58, no. 1, pp. 179–191, 2007.
- [33] T. Kasuga, M. Hiramatsu, A. Hoson, T. Sekino, and K. Niihara, "Formation of titanium oxide nanotube," *Langmuir*, vol. 14, no. 12, pp. 3160–3163, 1998.
- [34] A. Hu, X. Zhang, K. D. Oakes, P. Peng, Y. N. Zhou, and M. R. Servos, "Hydrothermal growth of free standing TiO_2 nanowire membranes for photocatalytic degradation of pharmaceuticals," *Journal of Hazardous Materials*, vol. 189, no. 1–2, pp. 278–285, 2011.
- [35] X. Yan, J. He, D. G. Evans, X. Duan, and Y. Zhu, "Preparation, characterization and photocatalytic activity of Si-doped and rare earth-doped TiO_2 from mesoporous precursors," *Applied Catalysis B*, vol. 55, no. 4, pp. 243–252, 2005.
- [36] K. T. Ranjit, I. Willner, S. H. Bossmann, and A. M. Braun, "Lanthanide oxide doped titanium dioxide photocatalysts: effective photocatalysts for the enhanced degradation of salicylic acid and t-cinnamic acid," *Journal of Catalysis*, vol. 204, no. 2, pp. 305–313, 2001.
- [37] V. Stengl, S. Bakardjieva, J. Šubrt et al., "Sodium titanate nanorods: preparation, microstructure characterization and photocatalytic activity," *Applied Catalysis B*, vol. 63, no. 1–2, pp. 20–30, 2006.
- [38] J. Yu, H. Yu, B. Cheng, X. Zhao, and Q. Zhang, "Preparation and photocatalytic activity of mesoporous anatase TiO_2 nanofibers by a hydrothermal method," *Journal of Photochemistry and Photobiology A*, vol. 182, no. 2, pp. 121–127, 2006.
- [39] T. Tong, J. Zhang, B. Tian, F. Chen, D. He, and M. Anpo, "Preparation of Ce- TiO_2 catalysts by controlled hydrolysis of titanium alkoxide based on esterification reaction and study on its photocatalytic activity," *Journal of Colloid and Interface Science*, vol. 315, no. 1, pp. 382–388, 2007.
- [40] K. Ebitani, Y. Hirano, and A. Morikawa, "Rare-earth ions as heterogeneous photocatalysts for the decomposition of dinitrogen monoxide (N_2O)," *Journal of Catalysis*, vol. 157, no. 1, pp. 262–265, 1995.
- [41] F. B. Li, X. Z. Li, M. F. Hou, K. W. Cheah, and W. C. H. Choy, "Enhanced photocatalytic activity of Ce^{3+} - TiO_2 for 2-mercaptobenzothiazole degradation in aqueous suspension for odour control," *Applied Catalysis A*, vol. 285, no. 1–2, pp. 181–189, 2005.
- [42] Y. Zhang, H. Zhang, Y. Xu, and Y. Wang, "Significant effect of lanthanide doping on the texture and properties of nanocrystalline mesoporous TiO_2 ," *Journal of Solid State Chemistry*, vol. 177, no. 10, pp. 3490–3498, 2004.
- [43] M. Saif and M. S. A. Abdel-Mottaleb, "Titanium dioxide nano-material doped with trivalent lanthanide ions of Tb, Eu and Sm: preparation, characterization and potential applications," *Inorganica Chimica Acta*, vol. 360, no. 9, pp. 2863–2874, 2007.
- [44] J. Konishi, K. Fujita, K. Nakanishi, and K. Hirao, "Monolithic TiO_2 with controlled multiscale porosity via a template-free sol-gel process accompanied by phase separation," *Chemistry of Materials*, vol. 18, no. 25, pp. 6069–6074, 2006.
- [45] S. O. Kucheyev, T. F. Baumann, Y. M. Wang, T. Van Buuren, and J. H. Satcher, "Synthesis and electronic structure of low-density monoliths of nanoporous nanocrystalline anatase TiO_2 ," *Journal of Electron Spectroscopy and Related Phenomena*, vol. 144–147, pp. 609–612, 2005.
- [46] B. Malinowska, J. Walendziewski, D. Robert, J. V. Weber, and M. Stolarski, "The study of photocatalytic activities of titania and titania-silica aerogels," *Applied Catalysis B*, vol. 46, no. 3, pp. 441–451, 2003.
- [47] A. A. Ismail and I. A. Ibrahim, "Impact of supercritical drying and heat treatment on physical properties of titania/silica aerogel monolithic and its applications," *Applied Catalysis A*, vol. 346, no. 1–2, pp. 200–205, 2008.
- [48] C. Chen, W. Cai, M. Long et al., "Template-free sol-gel preparation and characterization of free-standing visible light responsive C,N-modified porous monolithic TiO_2 ," *Journal of Hazardous Materials*, vol. 178, no. 1–3, pp. 560–565, 2010.
- [49] Q. G. Zeng, Z. M. Zhang, Z. J. Ding, Y. Wang, and Y. Q. Sheng, "Strong photoluminescence emission of $\text{Eu}:\text{TiO}_2$ nanotubes," *Scripta Materialia*, vol. 57, no. 10, pp. 897–900, 2007.
- [50] V. Stengl, S. Bakardjieva, and N. Murafa, "Preparation and photocatalytic activity of rare earth doped TiO_2 nanoparticles," *Materials Chemistry and Physics*, vol. 114, no. 1, pp. 217–226, 2009.
- [51] Z. M. El-Bahy, A. A. Ismail, and R. M. Mohamed, "Enhancement of titania by doping rare earth for photodegradation of organic dye (Direct Blue)," *Journal of Hazardous Materials*, vol. 166, no. 1, pp. 138–143, 2009.
- [52] W. Zhou, Y. H. Zheng, and G. H. Wu, "Novel luminescent RE/ TiO_2 (RE = Eu, Gd) catalysts prepared by in-situ sol-gel approach construction of multi-functional precursors and their photo or photocatalytic oxidation properties," *Applied Surface Science*, vol. 253, no. 3, pp. 1387–1392, 2006.
- [53] D. Gong, C. A. Grimes, O. K. Varghese et al., "Titanium oxide nanotube arrays prepared by anodic oxidation," *Journal of Materials Research*, vol. 16, no. 12, pp. 3331–3334, 2001.
- [54] Q. Cai, M. Paulose, O. K. Varghese, and C. A. Grimes, "The effect of electrolyte composition on the fabrication of self-organized titanium oxide nanotube arrays by anodic oxidation," *Journal of Materials Research*, vol. 20, no. 1, pp. 230–236, 2005.
- [55] G. K. Mor, K. Shankar, M. Paulose, O. K. Varghese, and C. A. Grimes, "Enhanced photocleavage of water using titania nanotube arrays," *Nano Letters*, vol. 5, no. 1, pp. 191–195, 2005.
- [56] G. K. Mor, O. K. Varghese, M. Paulose, K. Shankar, and C. A. Grimes, "A review on highly ordered, vertically oriented TiO_2 nanotube arrays: fabrication, material properties, and solar energy applications," *Solar Energy Materials and Solar Cells*, vol. 90, no. 14, pp. 2011–2075, 2006.

- [57] S. Bauer, S. Kleber, and P. Schmuki, "TiO₂ nanotubes: tailoring the geometry in H₃PO₄/HF electrolytes," *Electrochemistry Communications*, vol. 8, no. 8, pp. 1321–1325, 2006.
- [58] J. M. Macák, H. Tsuchiya, and P. Schmuki, "High-aspect-ratio TiO₂ nanotubes by anodization of titanium," *Angewandte Chemie - International Edition*, vol. 44, no. 14, pp. 2100–2102, 2005.
- [59] J. Kunze, L. Müller, J. M. Macak, P. Greil, P. Schmuki, and F. A. Müller, "Time-dependent growth of biomimetic apatite on anodic TiO₂ nanotubes," *Electrochimica Acta*, vol. 53, no. 23, pp. 6995–7003, 2008.
- [60] D. J. Yang, H. Park, S. J. Cho, H. G. Kim, and W. Y. Choi, "TiO₂-nanotube-based dye-sensitized solar cells fabricated by an efficient anodic oxidation for high surface area," *Journal of Physics and Chemistry of Solids*, vol. 69, no. 5-6, pp. 1272–1275, 2008.
- [61] J. M. Macak and P. Schmuki, "Anodic growth of self-organized anodic TiO₂ nanotubes in viscous electrolytes," *Electrochimica Acta*, vol. 52, no. 3, pp. 1258–1264, 2006.
- [62] C. Graf, R. Ohser-Wiedemann, and G. Kreisel, "Preparation and characterization of doped metal-supported TiO₂-layers," *Journal of Photochemistry and Photobiology A*, vol. 188, no. 2-3, pp. 226–234, 2007.
- [63] P. Liang, B. Hu, Z. Jiang, Y. Qin, and T. Peng, "Nanometer-sized titanium dioxide micro-column on-line preconcentration of La, Y, Yb, Eu, Dy and their determination by inductively coupled plasma atomic emission spectrometry," *Journal of Analytical Atomic Spectrometry*, vol. 16, no. 8, pp. 863–866, 2001.
- [64] X. Wu, X. Ding, W. Qin, W. He, and Z. Jiang, "Enhanced photo-catalytic activity of TiO₂ films with doped La prepared by micro-plasma oxidation method," *Journal of Hazardous Materials*, vol. 137, no. 1, pp. 192–197, 2006.
- [65] A. S. Attar, M. S. Ghamsari, F. Hajiesmaeilbaigi, S. Mirdamadi, K. Katagiri, and K. Koumoto, "Synthesis and characterization of anatase and rutile TiO₂ nanorods by template-assisted method," *Journal of Materials Science*, vol. 43, no. 17, pp. 5924–5929, 2008.
- [66] J. Cho, S. Schaab, J. A. Roether, and A. R. Boccacini, "Nanostructured carbon nanotube/TiO₂ composite coatings using electrophoretic deposition (EPD)," *Journal of Nanoparticle Research*, vol. 10, no. 1, pp. 99–105, 2008.
- [67] A. Podhorodecki, G. Zatoryb, J. Misiewicz, J. Domaradzki, D. Kaczmarek, and A. Borkowska, "Influence of annealing on europium photoexcitation doped into nanocrystalline titania film prepared by magnetron sputtering," *Journal of the Electrochemical Society*, vol. 156, no. 3, pp. H214–H219, 2009.
- [68] D. Kaczmarek, J. Domaradzki, A. Borkowska, A. Podhorodecki, J. Misiewicz, and K. Sieradzka, "Optical emission from Eu, Tb, Nd luminescence centers in TiO₂ prepared by magnetron sputtering," *Optica Applicata*, vol. 37, no. 4, pp. 433–438, 2007.
- [69] B. Liu, X. Zhao, and L. Wen, "The structural and photoluminescence studies related to the surface of the TiO₂ sol prepared by wet chemical method," *Materials Science and Engineering B*, vol. 134, no. 1, pp. 27–31, 2006.
- [70] Y. Zhao, C. Li, X. Liu, F. Gu, H. L. Du, and L. Shi, "Surface characteristics and microstructure of dispersed TiO₂ nanoparticles prepared by diffusion flame combustion," *Materials Chemistry and Physics*, vol. 107, no. 2-3, pp. 344–349, 2008.
- [71] C. W. Jia, E. Q. Xie, J. G. Zhao, Z. W. Sun, and A. H. Peng, "Visible and near-infrared photoluminescences of europium-doped titania film," *Journal of Applied Physics*, vol. 100, no. 2, Article ID 023529, 2006.
- [72] J. Li, X. Yang, X. Yu et al., "Rare earth oxide-doped titania nanocomposites with enhanced photocatalytic activity towards the degradation of partially hydrolysis polyacrylamide," *Applied Surface Science*, vol. 255, no. 6, pp. 3731–3738, 2009.
- [73] R. M. Mohamed and I. A. Mkhallid, "The effect of rare earth dopants on the structure, surface texture and photocatalytic properties of TiO₂-SiO₂ prepared by sol-gel method," *Journal of Alloys and Compounds*, vol. 501, no. 1, pp. 143–147, 2010.
- [74] P. Du, A. Bueno-López, M. Verbaas et al., "The effect of surface OH-population on the photocatalytic activity of rare earth-doped P25-TiO₂ in methylene blue degradation," *Journal of Catalysis*, vol. 260, no. 1, pp. 75–80, 2008.
- [75] I. Cacciotti, A. Bianco, G. Pezzotti, and G. Gusmano, "Synthesis, thermal behaviour and luminescence properties of rare earth-doped titania nanofibers," *Chemical Engineering Journal*, vol. 166, no. 2, pp. 751–764, 2011.
- [76] H. Wang, Y. Wang, Y. Yang, X. Li, and C. Wang, "Photoluminescence properties of the rare-earth ions in the TiO₂ host nanofibers prepared via electrospinning," *Materials Research Bulletin*, vol. 44, no. 2, pp. 408–414, 2009.
- [77] L. Li, C. K. Tsung, Z. Yang et al., "Rare-earth-doped nanocrystalline titania microspheres emitting luminescence via energy transfer," *Advanced Materials*, vol. 20, no. 5, pp. 903–908, 2008.
- [78] S. Jeon and P. V. Braun, "Hydrothermal synthesis of Er-doped luminescent TiO₂ nanoparticles," *Chemistry of Materials*, vol. 15, no. 6, pp. 1256–1263, 2003.
- [79] W. Que, Y. Zhou, C. H. Kam et al., "Fluorescence characteristics from microemulsion technique derived erbium (III) oxide nanocrystals," *Materials Research Bulletin*, vol. 36, no. 5-6, pp. 889–895, 2001.
- [80] A. Patra, C. S. Friend, R. Kapoor, and P. N. Prasad, "Fluorescence upconversion properties of Er³⁺-doped TiO₂ and BaTiO₃ nanocrystallites," *Chemistry of Materials*, vol. 15, no. 19, pp. 3650–3655, 2003.
- [81] C. Xueyuan, L. Wenqin, L. Yongsheng, and L. Guokui, "Recent progress on spectroscopy of lanthanide ions incorporated in semiconductor nanocrystals," *Journal of Rare Earths*, vol. 25, no. 5, pp. 515–525, 2007.
- [82] J. Xu, Y. Ao, D. Fu, and C. Yuan, "A simple route for the preparation of Eu, N-codoped TiO₂ nanoparticles with enhanced visible light-induced photocatalytic activity," *Journal of Colloid and Interface Science*, vol. 328, no. 2, pp. 447–451, 2008.
- [83] Y. Ma, J. Zhang, B. Tian, F. Chen, and L. Wang, "Synthesis and characterization of thermally stable Sm,N co-doped TiO₂ with highly visible light activity," *Journal of Hazardous Materials*, vol. 182, no. 1–3, pp. 386–393, 2010.

Research Article

Growth and Structure of Pure ZnO Micro/Nanocombs

Tengfei Xu,^{1,2} Pengfei Ji,² Meng He,² and Jianye Li¹

¹Department of Physical Chemistry, University of Science and Technology Beijing, Beijing 100083, China

²National Center for Nanoscience and Technology, Beijing 100190, China

Correspondence should be addressed to Meng He, mhe@nanoctr.cn and Jianye Li, jyli@ustb.edu.cn

Received 19 September 2011; Revised 16 December 2011; Accepted 18 December 2011

Academic Editor: Ting Zhu

Copyright © 2012 Tengfei Xu et al. This is an open access article distributed under the Creative Commons Attribution License, which permits unrestricted use, distribution, and reproduction in any medium, provided the original work is properly cited.

Comb-shaped ZnO micro/nanostructures were grown on copper substrate using a highly repeatable catalyst-free chemical vapor deposition method. The structure of the ZnO micro/nanocombs was analyzed, and the necking-down phenomena of the comb teeth was explained. The cathodoluminescence (CL) spectrum was measured on an individual ZnO comb, and a strong deep-level emission centered at about 520 nm was observed.

1. Introduction

ZnO, with a wide bandgap of 3.37 eV at room temperature and a high exciton binding energy of 60 meV, is a direct bandgap II–VI semiconductor with good performances. In the past decade, nano-ZnO has attracted considerable attention. A variety of ZnO nanostructures, nanowires [1], nanorods [2], nanoribbons [3], nanocombs [4], nanorings [5], nanohelices [6], and nanotetrapods [7], and have been discovered and reported. Among them, ZnO nanocombs consisting of a ribbon and an array of parallel nanorods perpendicular to the ribbon are of interest for nanocantilever arrays [4], laser arrays [8], nanocomb biosensors [9], and gratings [10].

So far, ZnO nanocombs have been synthesized mainly by thermal evaporation using Zn or ZnO usually mixed with graphite powers as precursors in a wide temperature range (440°C–1350°C) [4, 11–18]. In most cases, Au was also used as the catalyst in the growth. The mechanism involved in generating ZnO nanocombs includes vapor-solid (VS) mechanism without any catalysts and vapor-solid-liquid (VLS) mechanism directed by catalysts. Wang et al. [4] reported that the Zn-terminated (0001) polar surface is chemically active and can initiate a self-catalyzed effect that promotes the growth of comb-like arrays, while the O-terminated (000 $\bar{1}$) polar surface is inert in initiating growth. Chen et al. [16] reported that both VS and VLS mechanisms could explain the growth of ZnO comb-like structures.

Herein, a chemical vapor deposition (CVD) process using a precursor of mixed ZnO and graphite powders is carried out to grow comb-like ZnO micro/nanostructures. In the process, no catalyst is used and as well no catalyst particle is detected at the comb tip, indicating a VS mechanism in the growth of the ZnO comb-like structures. The absence of catalyst particle on the as-grown ZnO micro/nanocombs is an advantage to fabricate ZnO micro/nanodevices without the influence of impurity. This facile way for growing pure ZnO comb-shaped micro/nanostructures on a large scale will facilitate the broad applications of ZnO micro/nanocombs. At last, the structure and growth mechanism of the comb-shaped ZnO structures were discussed, and the CL properties of individual ZnO combs were investigated.

2. Experimental Section

The ZnO micro/nanocombs were synthesized in a tube furnace system [19] through a chemical vapor deposition (CVD) method. At first, a mixture of ZnO and graphite powders (weight ratio 2:1) was grounded and loaded into a quartz boat, which is placed at the center of a horizontal tube furnace. A clean Cu sheet without catalyst was used as a substrate and placed downstream of the source materials to collect the products. Argon, with a flow rate of 30~70 sccm (standard cubic centimeters per minute), was used as the carrier gas. Then, the source materials were heated up to 1000°C with a heating rate of 45°C/min. The substrate

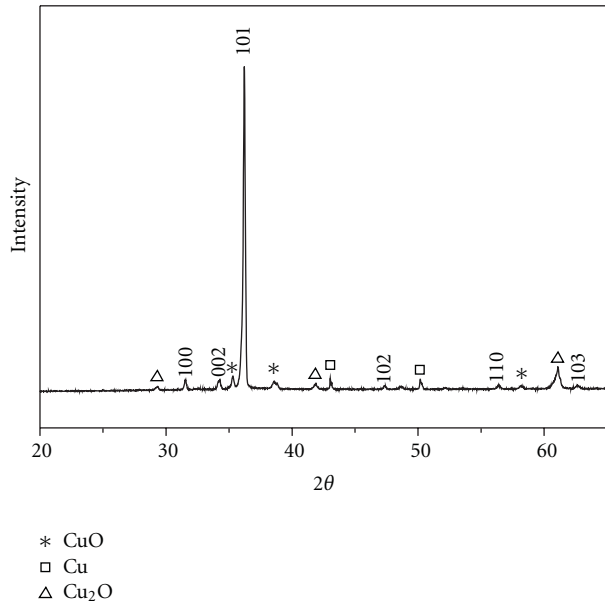


FIGURE 1: XRD pattern of as-prepared ZnO comb-like structures grown on Cu substrate.

temperature is 950°C due to the temperature gradient of the tube-furnace. The pressure was kept at 1 atm during the reaction. The growth was maintained for 90 min. Then, the furnace was cooled down to room temperature, and white products were found covering the Cu substrate.

The as-synthesized products were characterized by X-ray diffraction (XRD, Panalytical X'pert PRO diffractometer), scanning electron microscopy (SEM, Hitachi S-4800), energy-dispersive X-ray (EDX) spectroscopy and transmission electron microscopy (TEM, Tecnai G² F20 U-TWIN). Cathodoluminescence spectrum of an individual comb-like structure was recorded using an in situ optical-electrical measurement system based on a Keithley 4200 semiconductor characterization system and an FEI XL30-SFEG SEM equipped with 4 Kleindiek MM3A nanomanipulators, and the current intensity of electron beam was less than 1nA. More details about the in situ optical-electrical measurement system can be found in [20].

3. Results and Discussion

X-ray powder diffraction pattern of the as-synthesized ZnO micro/nanocombs was shown in Figure 1. Reflections from wurtzitic ZnO could be readily identified and a strong preferred orientation of (101) plane was evidenced. Some weak reflections corresponding to Cu, Cu₂O, and CuO were also observed and ascribed to the Cu substrate.

Figure 2 is an energy-dispersive X-ray spectrum measured on the comb-like structures, and it reveals that only Zn and O can be detected and Cu or other elements are absent. Therefore no particles of Cu, Cu oxides, or Cu alloys contaminate the comb-shaped structures; the Cu, Cu₂O, and CuO identified by XRD should come from the substrate.

Typical SEM images are given in Figures 3(a)–3(c). Some ZnO comb-shaped structures accumulating over the

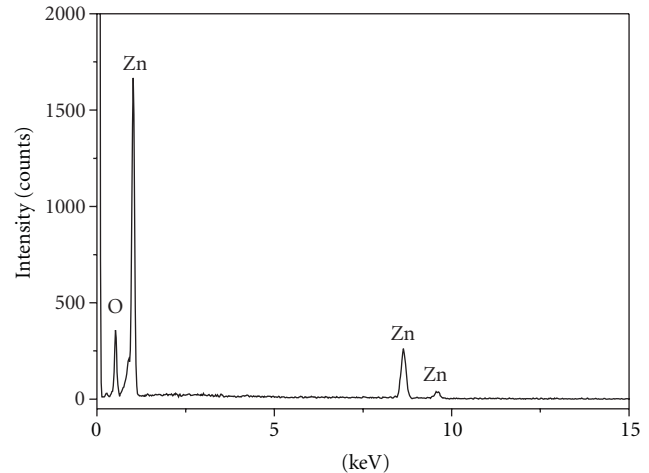


FIGURE 2: EDX spectrum of the ZnO comb-like structures.

substrate can be seen from Figure 3(a). Figure 3(b) presents the details of the morphology of an individual ZnO comb. The comb-like structure has teeth with a length up to 20 μm and a thickness of several hundreds of nanometers. All the teeth stand parallel to one another on one side of ribbon-like stems. The stems are ribbons with a thickness of several hundreds of nanometers and a length of several tens of micrometers. The width of the ribbon is almost the same along the growth direction, which is different from the blade-like structures reported in previous literature [11, 16]. Shown in Figure 3(c) is another kind of ZnO comb-like structures forming on the Cu substrate. The width of the tooth shrinks drastically from several μm at its root to about 300 nm at its sharp tip. The teeth are uniform in length and width in general. The distance between two adjacent teeth is about 2 μm.

The ZnO micro/nanocombs were further characterization by TEM. Shown in Figure 4(a) is a low-magnification image of a comb-like ZnO structure, and the selected area electron diffraction (SAED) pattern obtained from the stem part of the comb-like structure is given as an inset. Presented in Figure 4(b) is an image of the root part of the teeth at higher magnification and SAED pattern taken from a tooth. The identical SAED patterns obtained from different parts of the comb-like structure indicates that the entire particle is a single crystal. SAED patterns agree well with [100] zone axis of wurtzitic ZnO, confirming the results of XRD and EDX analyses. Though [001] cannot be distinguished explicitly from [00 $\bar{1}$] direction with only SAED pattern, we assume that the direction from stem ribbon to the tip of the tooth is [001] in reference to [4]. The teeth of the comb-like structure grow along *c*-axis while the stem ribbon grows along [120] direction with (2 $\bar{1}$ 0) planes as top and bottoms surfaces. Different from the comb structures reported here, the stem ribbons of comb-like structures synthesized by Wang et al. grow along [100] direction with (010) planes as top and bottom surfaces. The necking down of the teeth is frequently observed for our comb-like structures, and interestingly, the positions of necking down are quite uniform for teeth of the

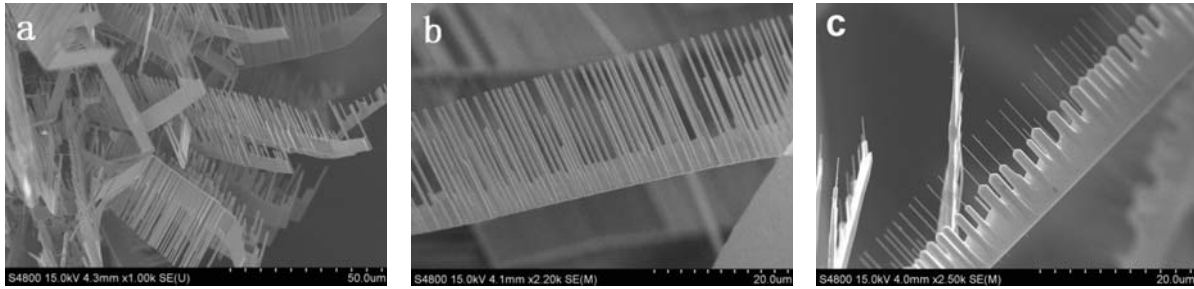


FIGURE 3: Typical SEM images of the comb-like ZnO structures.

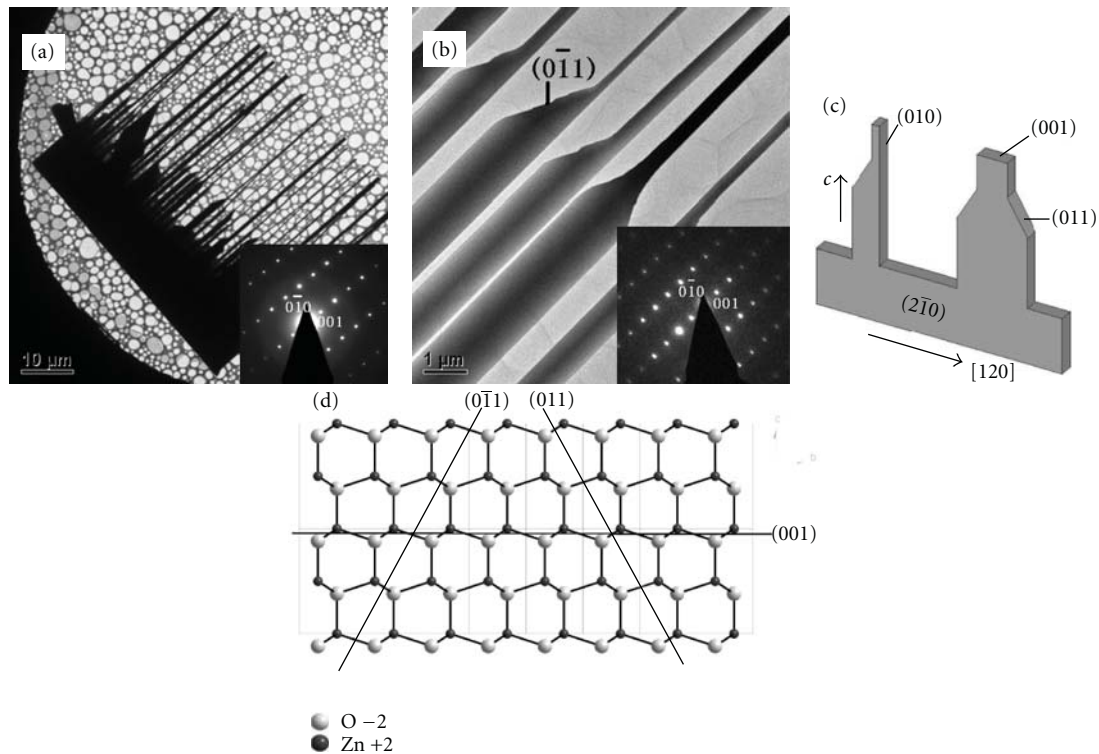


FIGURE 4: (a) TEM image of a ZnO comb, showing the distinct arrays of teeth on one side. The inset is the SAED pattern taken from the stem ribbon. (b) TEM image of the root part of the teeth at higher magnification and the corresponding SAED pattern. (c) Schematic models of the comb-like structure observed by TEM. (d) A projection of wurtzite-type ZnO along [100] direction highlighting its polar planes (001), (011), and (01 $\bar{1}$).

same comb-like structure. The inclined facets occurring at the place where the teeth are necking down are (01 $\bar{1}$) and/or (011), as shown in Figures 4(b) and 4(c). It is noteworthy that (01 $\bar{1}$) and (011) are polar planes, as indicated in Figure 4(d). We suggest that the necking down of the teeth is closely related with the polar planes of wurtzite-type ZnO. Possibly, the surface energy of (01 $\bar{1}$) and (011) polar planes are comparable with that of (001), the most well-known polar planes for wurtzite-type structure. Fluctuation of experimental conditions during the growth can lead to that (01 $\bar{1}$) and (011) surfaces are energy preferred over (001). Then, (01 $\bar{1}$) and/or (011) facets will appear at the tips of the teeth. Clearly, nonpolar surfaces with low indices, such as (010) and (210) as well as their equivalents are more stable than polar ones. Hence, non-polar surfaces are preferred over

polar ones to terminate the single crystalline teeth during the subsequent growth. When such a process happens, a necking down of the teeth will result, and sharper tips will be obtained. So the necking-down phenomena dominated by competition between polar surfaces and non-polar ones can be utilized to synthesize wurtzite-type structures with both sharp tips at nanoscale and thick roots in size of micrometers, which should be very desirable for some applications.

The CL spectrum measured on an individual ZnO comb-like structure is shown in Figure 5. Only a broad and strong green emission band centered at 520 nm is observed, which is commonly seen in ZnO materials synthesized under oxygen-deficient conditions, such as the gas-phase produced nanowires [21]. The chemical and structural origins of the green luminescence from undoped ZnO are

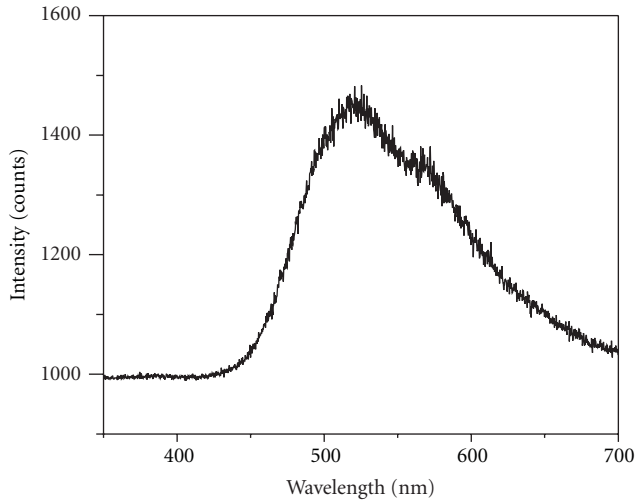


FIGURE 5: CL spectrum measured on an individual ZnO comb-like structure.

still a matter of debate [22, 23]. In what is perhaps the most frequently cited explanation, electrons trapped in singly ionized oxygen vacancies recombine with valence band holes [24]. In another frequently cited explanation, electrons in the conduction band and/or shallow donor states recombine with holes that have been trapped in oxygen vacancies [25]. Compared to the strong green emission centered at 520 nm, no near band edge emission of ZnO was found in Figure 5. The disappearance of the near ultraviolet (UV) band edge emission is due to the low electron beam (1 nA) of the CL measurement. Such a low electron beam generates few electron-hole pairs. Furthermore, a large number of excited electrons are trapped by oxygen vacancies, resulting in little recombination of electron-hole pairs. Thus, the near band edge emission peak of ZnO disappears.

4. Conclusions

In summary, ZnO micro/nanocombs have been successfully synthesized on Cu substrate without catalyst using a simple CVD method. The growth of the comb-like structures can be attributed to a VS mechanism. The structure of the ZnO micro/nanocombs was analyzed and the necking-down phenomena of the comb teeth was explained. The CL spectrum was measured on an individual ZnO comb and only a broad strong green emission band was observed. This facile way for growing pure ZnO micro/nanocombs on a large scale will facilitate the broad applications of ZnO micro/nanocombs.

Authors' Contributions

T. Xu and P. Ji have equally contributed to this paper.

Acknowledgments

The authors thank the financial supports from the National Natural Science Foundation of China (21071016), the Fundamental Research Funds for the Central Universities of

China, Beijing Natural Science Foundation (2093038), and Scientific Research Foundation for the Returned Overseas Chinese Scholars, Ministry of Education of China. Mr. Z. Liu and Dr. M. Gao at Peking University are gratefully acknowledged for help in the CL measurements.

References

- [1] M. H. Huang, S. Mao, H. Feick et al., "Room-temperature ultraviolet nanowire nanolasers," *Science*, vol. 292, no. 5523, pp. 1897–1899, 2001.
- [2] J. Y. Li, X. L. Chen, H. Li, M. He, and Z. Y. Qiao, "Fabrication of zinc oxide nanorods," *Journal of Crystal Growth*, vol. 233, no. 1-2, pp. 5–7, 2001.
- [3] Z. W. Pan, Z. R. Dai, and Z. L. Wang, "Nanobelts of semiconducting oxides," *Science*, vol. 291, no. 5510, pp. 1947–1949, 2001.
- [4] Z. L. Wang, X. Y. Kong, and J. M. Zuo, "Induced growth of asymmetric nanocantilever arrays on polar surfaces," *Physical Review Letters*, vol. 91, no. 18, Article ID 185502, 4 pages, 2003.
- [5] X. Y. Kong, Y. Ding, R. Yang, and Z. L. Wang, "Single-crystal nanorings formed by epitaxial self-coiling of polar nanobelts," *Science*, vol. 303, no. 5662, pp. 1348–1351, 2004.
- [6] P. X. Gao, Y. Ding, W. Mai, W. L. Hughes, C. Lao, and Z. L. Wang, "Conversion of zinc oxide nanobelts into superlattice-structured nanohelices," *Science*, vol. 309, no. 5741, pp. 1700–1704, 2005.
- [7] J. Y. Li, H. Peng, J. Liu, and H. O. Everitt, "Facile gram-scale growth of single-crystalline nanotetrapod-assembled ZnO through a rapid process," *European Journal of Inorganic Chemistry*, no. 20, pp. 3172–3176, 2008.
- [8] H. Yan, R. He, J. Johnson, M. Law, R. J. Saykally, and P. Yang, "Dendritic nanowire ultraviolet laser array," *Journal of the American Chemical Society*, vol. 125, no. 16, pp. 4728–4729, 2003.
- [9] J. X. Wang, X. W. Sun, A. Wei et al., "Zinc oxide nanocomb biosensor for glucose detection," *Applied Physics Letters*, vol. 88, no. 23, Article ID 233106, 2006.
- [10] Z. W. Pan, S. M. Mahurin, S. Dai, and D. H. Lowndes, "Nanowire array gratings with ZnO combs," *Nano Letters*, vol. 5, no. 4, pp. 723–727, 2005.
- [11] C. X. Xu, X. W. Sun, Z. L. Dong, and M. B. Yu, "Self-organized nanocomb of ZnO fabricated by Au-catalyzed vapor-phase transport," *Journal of Crystal Growth*, vol. 270, no. 3-4, pp. 498–504, 2004.
- [12] Y. H. Zhang, J. Liu, T. Liu, L. P. You, and X. G. Li, "Supersaturation-controlled synthesis of two types of single-sided ZnO comb-like nanostructures by thermal evaporation at low temperature," *Journal of Crystal Growth*, vol. 285, no. 4, pp. 541–548, 2005.
- [13] Y. Zhang, X. Song, J. Zheng, H. Liu, X. Li, and L. You, "Symmetric and asymmetric growth of ZnO hierarchical nanostructures: nanocombs and their optical properties," *Nanotechnology*, vol. 17, no. 8, pp. 1916–1921, 2006.
- [14] X. Li, C.-X. Xu, G.-P. Zhu et al., "Disc-capped ZnO nanocombs," *Chinese Physics Letters*, vol. 24, no. 12, pp. 3495–3498, 2007.
- [15] U. Manzoor and D. K. Kim, "Synthesis and enhancement of ultraviolet emission by post-thermal treatment of unique zinc oxide comb-shaped dendritic nanostructures," *Scripta Materialia*, vol. 54, no. 5, pp. 807–811, 2006.

- [16] Y. X. Chen, M. Lewis, and W. L. Zhou, "Zno nanostructures fabricated through a double-tube vapor-phase transport synthesis," *Journal of Crystal Growth*, vol. 282, no. 1-2, pp. 85–93, 2005.
- [17] Y. S. Lim, J. W. Park, S.-T. Hong, and J. Kim, "Carbothermal synthesis of ZnO nanocomb structure," *Materials Science and Engineering B*, vol. 129, no. 1–3, pp. 100–103, 2006.
- [18] R. F. Zhuo, H. T. Feng, Q. Liang et al., "Morphology-controlled synthesis, growth mechanism, optical and microwave absorption properties of ZnO nanocombs," *Journal of Physics D*, vol. 41, no. 18, Article ID 185405, 2008.
- [19] J. Y. Li, L. S. Wang, D. B. Buchholz, and R. P. H. Chang, "Simultaneous growth of pure hyperbranched Zn₃As₂ structures and long Ga₂O₃ nanowires," *Nano Letters*, vol. 9, no. 5, pp. 1764–1769, 2009.
- [20] C. Li, M. Gao, C. Ding et al., "In situ comprehensive characterization of optoelectronic nanomaterials for device purposes," *Nanotechnology*, vol. 20, no. 17, Article ID 175703, 2009.
- [21] L. E. Greene, M. Law, J. Goldberger et al., "Low-temperature wafer-scale production of ZnO nanowire arrays," *Angewandte Chemie*, vol. 42, no. 26, pp. 3031–3034, 2003.
- [22] J. V. Foreman, J. Li, H. Peng, S. Choi, H. O. Everitt, and J. Liu, "Time-resolved investigation of bright visible wavelength luminescence from sulfur-doped ZnO nanowires and micropowders," *Nano Letters*, vol. 6, no. 6, pp. 1126–1130, 2006.
- [23] J. Y. Li, Q. Zhang, H. Peng, H. O. Everitt, L. Qin, and J. Liu, "Diameter-controlled vapor-solid epitaxial growth and properties of aligned ZnO nanowire arrays," *Journal of Physical Chemistry C*, vol. 113, no. 10, pp. 3950–3954, 2009.
- [24] K. Vanheusden, W. L. Warren, C. H. Seager, D. R. Tallant, J. A. Voigt, and B. E. Gnade, "Mechanisms behind green photoluminescence in ZnO phosphor powders," *Journal of Applied Physics*, vol. 79, no. 10, pp. 7983–7990, 1996.
- [25] A. Van Dijken, E. A. Meulenkaamp, D. Vanmaekelbergh, and A. Meijerink, "The kinetics of the radiative and nonradiative processes in nanocrystalline ZnO particles upon photoexcitation," *Journal of Physical Chemistry B*, vol. 104, no. 8, pp. 1715–1723, 2000.

Research Article

Subwavelength Microstructures Fabrication by Self-Organization Processes in Photopolymerizable Nanocomposite

I. Yu. Denisyuk, N. O. Sobeshuk, J. A. Burunkova, and N. D. Vorzobova

Saint-Petersburg National Research University of Information Technologies, Mechanics and Optics, Street Kronverskii 49, Saint-Petersburg 197101, Russia

Correspondence should be addressed to I. Yu. Denisyuk, denisiuk@mail.ifmo.ru

Received 11 October 2011; Revised 11 December 2011; Accepted 2 January 2012

Academic Editor: Jaetae Seo

Copyright © 2012 I. Yu. Denisyuk et al. This is an open access article distributed under the Creative Commons Attribution License, which permits unrestricted use, distribution, and reproduction in any medium, provided the original work is properly cited.

This paper describes our research results on nanometers sizes subwavelength nanostructure fabrication by UV curing of special nanocomposite material with self-organization and light self-focusing effects. For this purpose, special UV curable nanocomposite material with a set of effects was developing: light self-focusing in the photopolymer with positive refractive index change, self-organization based on photo-induced nanoparticles transportation, and oxygen-based polymerization threshold. Both holographic and projection lithography writing methods application for microstructure making shows geometrical optical laws perturbation as result of nanocomposite self-organization effects with formation of nanometers-sized high-aspect-ratio structures. Obtained results will be useful for diffraction limit overcoming in projection lithography as well as for deep lithography technique.

1. Introduction

The main problem of current photolithography is diminishing of minimal feature sizes up to subwavelength value. The smallest feature size X_{\min} that can be projected by a coherent imaging system is $X_{\min} = \lambda/2NA$, and the depth of focus DOF is $DOF = \lambda/[2NA^2]$, where λ is the wavelength of the illumination, and NA is the numerical aperture. The most ordinary way to attain smaller feature sizes is to reduce the wavelength up to excimer laser wavelengths (248 or 193 nm). The NA is typically between 0,5 and 0,8, so the feature size is on the order of the exposure wavelength. State-of-the-art semiconductor fabrication facilities in the year 2010 are forecated to use a 32 nm process, at which point the resolution and depth of focus constraints of optical lithography become difficult.

Figure 1 plots the resolution against the film stack's minimum refractive index. Note that the calculation includes 0.90 as the practical optics limit for $\sin(\theta)$. This requires that the refractive index of the immersion fluids be at least 10% higher than the theoretical minimum value. It is also assumed that all other refractive indices in the stack are higher than the fluid's refractive index. To overcome pitch

size of 32 nm, it is needed to use fluid with refractive index higher than 2,0 that is impossible.

Therefore, techniques to enhance the performance of optical lithography are very important now. As the fundamental limits of optical lithography are approached, the non-linear optical properties of the photoresist become increasingly important. This nonlinearity arises from the change in the complex index of refraction of the photoresist under UV exposure. A common nonlinear optical phenomenon is the light-induced change in the imaginary part of the index of refraction \sim , that is, absorption upon exposure. For instance, contrast enhancement layers composed of a photobleachable dye are often overcoated on a photoresist [1, 2] to introduce exposure thresholding.

For the same reason, special UV-curable nanocomposite with strong non-linear and self-writing effects overcoated on photoresist to improve light distribution in the spot can be used.

The same proposed technique is applicable for deep lithography based on 365 nm UV light with high scattering to improve the shape of small feature in results of geometrical optical laws perturbation at use of light self-focusing in materials.

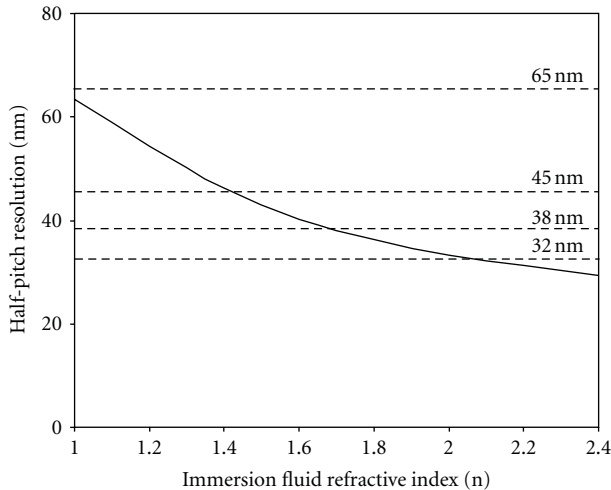


FIGURE 1: Half-pitch resolution plotted against immersion fluid refractive index according to the work [3].

If we make nanocomposite system with self-writing effects and place it as a topcoat, we will obtain self-writing subwavelength artificial waveguide that will guide the light to small subwavelength spot on photoresist surface.

So to make it, it is necessary to develop special material with self-writing effects.

2. Experimental Conditions

UV-curable composition has been developed previously and was described in our works [5, 6]. Acrylic monomers were used such as composition of 2-carboxyethyl acrylate, bisphenol A glycerolate diacrylate, 1,6-gexanediol diacrylate, and trimethylolpropane ethoxylate (1 EO/OH) methyl ether diacrylate (in ratio 5:2:1:2 accordingly) from Aldrich—liquid composition and 2-carboxyethyl acrylate, RSX 51027 (from USB) (in ratio 1:3 accordingly)—solid composition, as initiator was used 2,2-dimethoxy-2-phenylacetophenone (from Aldrich). Initiator type and concentration (0,2 wt %) were chosen according to light source $\lambda = 320 - 365$ nm. Concentration of initiator allows light penetration in monomer material on 1 mm.

For projection lithography were used two monomer compositions: 2-carboxyethyl acrylate and bisphenol A glycerolate in ratio 70:30 and bisphenol A glycerolate diacrylate, 2-carboxyethyl acrylate, and phenoxyethyl acrylate in ratio 25:55:20 with nanoparticles.

Nanocomposites used in this work were based on ZnO nanoparticles dispersed in monomers. The concentration of nanocrystals in the composite which is about 10 wt% and their size (20 nm) will ensure low light scattering by the nanocomposite. ZnO nanocrystals were purchased from Russian local supplier. Prepared nanoparticles were mixed with UV curable monomers mixture. Nanocomposite preparation method and its properties were described previously [6–8].

All experiments were accomplished at room temperature in air without special inert atmosphere (argon). To reduce inhibition effect of oxygen, nanocomposite was cured between two substrates—glass and polyester film.

Process of microstructural element formation was made as follows: drop of composition was placed on substrate (in our case glass processed by NaOH) having chemical interaction with acid groups of composition and covered by polyester film with thin layer of release coating (siloxane). Thickness of composition layer was determined by spacers. UV curing took place at UV irradiation of composition by use of holographic technique or by projection lithography. After curing polyester was removed, and substrate was washed by isopropyl alcohol to remove noncured composition. Holographic method based on interferometer with 320 nm He-Cd CW laser source. In current experiment angle between two laser beams was 10 degrees, and writing lattice period was—2 μ m.

Projection lithography was carried out based on DPSS laser source (355 nm) and quartz lens with aperture 0,4.

SEM photos as well as ion etching of the materials were made by ion beam tool—CrossBeam Neon 40 EsB (Carl Zeiss).

3. Results and Discussion

Light self-focusing and self-organization effects at UV curing of acrylate-based nanocomposites were investigated previously [9]. There are a few effects as follows.

3.1. Self-Focusing of the Light in Material with Positive Refractive Index Change at Photopolymerization. Effect of light self-focusing in optical material having proprieties of positive change of refractive index (RI) at light action is widely investigated recently. For example, in cited work, the results of light self-focusing and self-written waveguide preparation process obtained on glass light-sensitive material are summarized [10].

Self-written waveguides can be evolved if a Gaussian laser beam is focused onto and allowed to propagate through a photosensitive material that shows positive refractive index change in response to laser exposure. Since the refractive index increases with intensity, the initially diffracting beam causes the refractive index to build up along the propagation axis, which is reflected by narrowing and increasing peak intensity of the outcoming beam. In the early stages, an adiabatic taper forms, and over time, a channel waveguide can be created throughout the sample. These are called self-written waveguides as the same light that induced the waveguide is also guided by it [10]. Our experiments show important influence of the well-known oxygen inhibition action on reinforcement of self-focusing light in photopolymer. Oxygen inhibition action to acrylate photopolymerization is described previously [11].

3.2. Short-Distance Nanoparticles Transportation. Effect of light-induced nanoparticles redistribution in nanocomposite is a new effect discovered recently. It takes place at

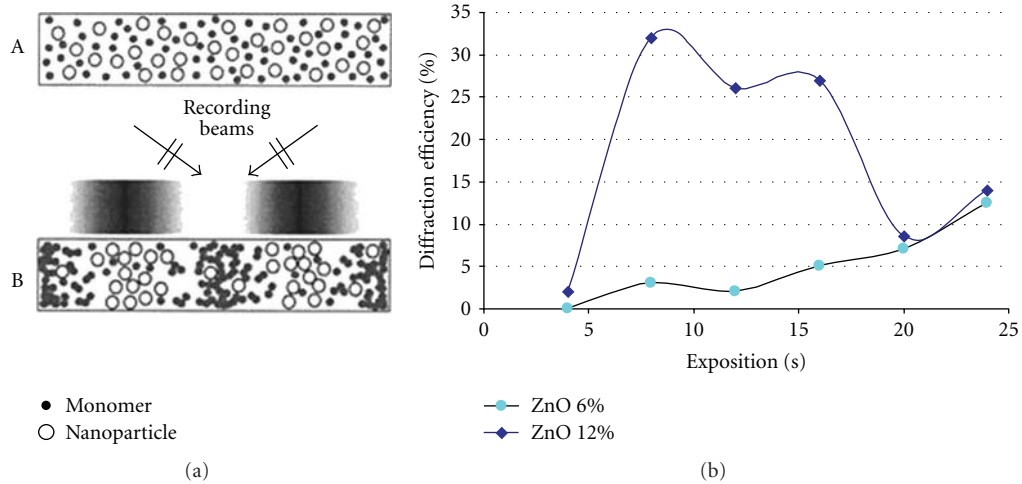


FIGURE 2: (a) Nanoparticles transportation in photopolymer according to the work in [4], (b) our experimental diffraction efficiency dependence on exposition and nanoparticles concentration.

photopolymeric nanocomposite irradiation by periodic light distribution, for example, by lattice made by interference of two laser beams.

The first time these processes were found by Suzuki and coworkers in 2005 on organic-inorganic nanocomposite photopolymer system in which inorganic nanoparticles with a larger refractive index differ from photopolymerized monomers are dispersed in uncured monomers [12]. Inorganic materials possess a wide variety of refractive indices that give us the opportunity to obtain much higher refractive index changes Δn than conventional photopolymers with low scattering loss [13].

Explanation of effects was made in the work of [4]. For monomers with radical photopolymerization, spatially non-uniform light illumination will produce free radicals by dissociation of initiators and subsequent reaction of free radicals with monomers, which leads to chain polymerization of individual monomers in the bright regions.

This polymerization process lowers the chemical potential of monomers in the bright regions, leading to diffusion (short-distance transportation) of monomers from the dark to the bright regions. On the other hand, photoinert inorganic nanoparticles have diffusion from the bright to the dark regions, as illustrated in Figure 2(a), since the particles are not consumed, and their chemical potential increases in the bright regions as a result of the monomer consumption. Such a mutual diffusion process continues until the monomers are consumed completely by polymerization processes and until the high viscosity of cured material makes monomers and nanoparticles immobile. As a result, the spatial distribution of nanoparticles is also fixed, and a refractive-index grating is created as a result of compositional and density differences between the bright and the dark regions.

Figure 2 shows diffraction efficiency dependence of photopolymerizable nanocomposite material from exposition time and nanoparticles concentration. Unlike classic holographic photopolymer in our material, unpolymerized

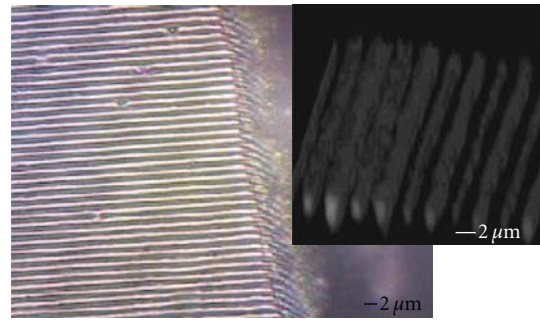


FIGURE 3: Microphotos of cut of obtained 3D structure (left—optical and right—confocal microscopy), lattice period— $2\ \mu\text{m}$.

materials were dissolved by alcohol and removed after exposition. According to schema (Figure 2(a)), unpolymerized monomer in dark areas was removed by dissolution. High augmentation of diffraction efficiency at 12% nanoparticles concentration is a result of nanoparticles redistribution.

As a result, we will obtain 3D parallel plates of polymerized material with nanoparticles divided by the same plate without nanoparticles. Our measurement of the plate was made by transmission optical microscopy on micro-cut of structure and the same obtained by confocal microscopy shown in Figure 3. According to Figure 2(b) there takes place short-distance nanoparticles transportation to the bright regions with change of solubility of material and reinforcement of polymerized 3D lattice formation.

So the process of nanoparticles displacement is a self-writing process or reinforcement of self-focusing process as discussed above.

After that the first experiments on nanoparticles redistribution in nanocomposite transformation on high aspect ratio nanosized structures were made. Figure 4 shows result of ion etching of previously made holographic micropatterns in nanocomposite.

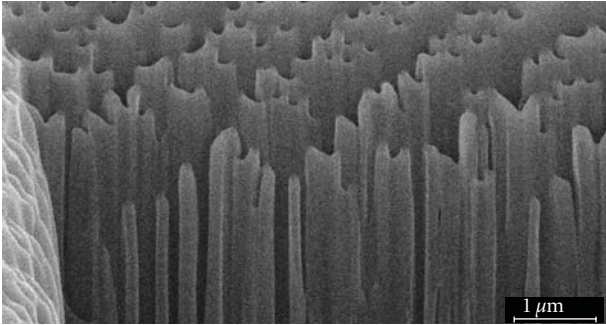


FIGURE 4: The result of ion beam etching: nanocomposite areas with formation of vertical 100 nm width elements.

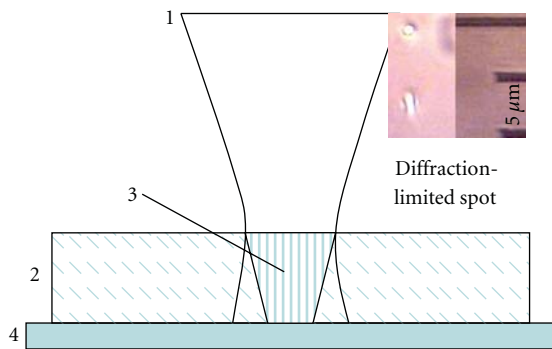
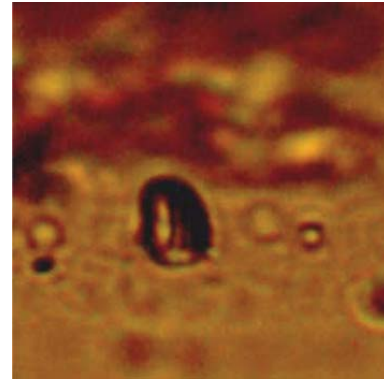


FIGURE 5: Model of light redistribution behind the lens spot as a result of self-writing processes. (1) UV light beam, (2) nanocomposite, (3) Tip self-writing, and (4) photoresist. Polymerized small one-micron-sized cylinder with vertical borders made by this process (insert).

We think that ion beam etches nanoparticles-free polymer plates and does not touch nanoparticles enriched plates. As a result, after polymer evaporation nanoparticles redistribution becomes visual, etching forms subwavelength nano-sized columns with high aspect ratio.

3.3. Microstructure Writing by Projection Lithography. Self-writing and self-focusing effects discussed above are applicable for diminishing polymerized area initially corresponding to light distribution in objective spot as well as to overcome geometric distribution of the light in focus. The main effect is light self-focusing that can be reinforced by oxygen inhibition [14, 15] and nanoparticles redistribution at photopolymerization. Figure 5 shows proposed application of self-writing processes in projection photolithography: using nanocomposite with self-writing effects overcoated on photoresist to improve light distribution in the spot on the photoresist surface.

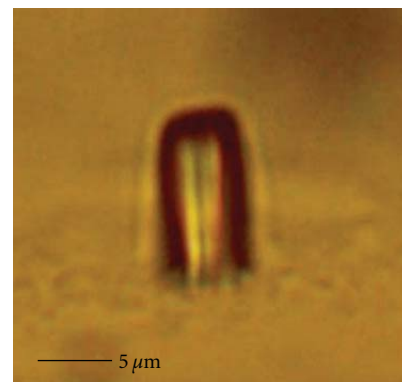
For comparison, two monomer compositions (with and without nanoparticles) were used, and results of them are different. In Figure 6 are represented polymer microstructures obtained in case of 2-carboxyethyl acrylate and bisphenol A glycerolate composition (without nanoparticles). Relation between dimensions/structure shape and exposition is observed. In this experiment was used projection of spot



(a)



(b)



(c)

FIGURE 6: Structures obtained from photopolymer without nanoparticles: (a) diameter 3 μm (spot size 2 μm); (b) diameter 4 μm (spot size 4 μm); (c) diameter 6.5 μm (spot size 6 μm).

expected diameter 1, 2, 4, and 6 mm. Composition without nanoparticles does not allow to obtain structures with all expected diameters. All cylinders based on this composition were at least 3-4 μm diameter; in case of 1 μm expected spot size formation of elements did not take place.

Elements form tends to the cone that corresponds to energy distribution in spot.

In contrast with this series, experiments with nanocomposite gave different results—we made structures with expected diameters 1 mm and obtained diameter less than 1 μm with a form near to cylinder in Figure 7.

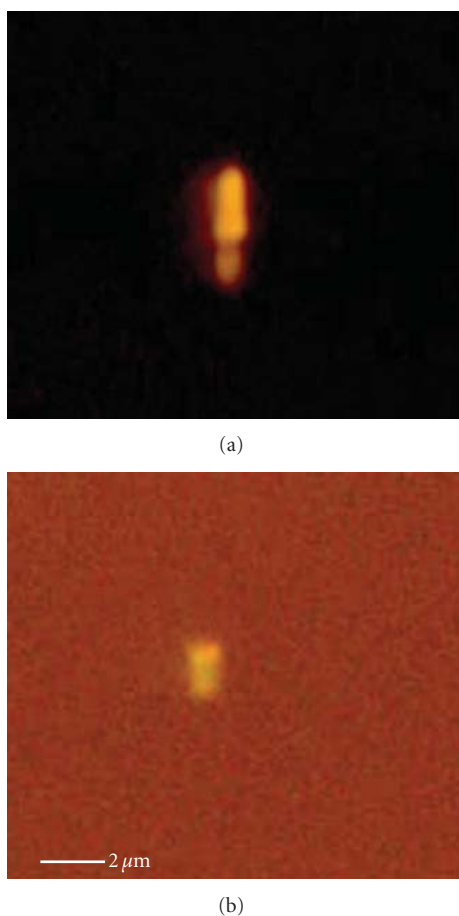


FIGURE 7: $2\ \mu\text{m}$ height structures obtained from nanocomposite: (a) diameter $0.7\ \mu\text{m}$ (spot size $1.5\ \mu\text{m}$), (b) diameter $0.6\ \mu\text{m}$ (spot size $1.5\ \mu\text{m}$).

Figure 7 shows that the use of nanocomposite gives formation of subwavelength elements formed with geometric optics law violation (formation of self-writing cylinder in dispute to cone).

In fact, used lens should form cone 20 degrees, but as a result of nanocomposite self-organization, it is the form of cylinders with vertical borders that confirms our guess-work on self-organization effects in photolithography.

4. Conclusion

Nanocomposite photopolymerizable material shows a set of self-writing effects due to the light beam redistribution as a result of self-focusing in non-linear photopolymer (positive refractive index change at photopolymerization) and effects of photopolymerization inhibition by oxygen and short-distance nanoparticles displacement. UV curing of nanocomposite will result in reinforcement of light self-focusing and grasping of polymerized area. The process is applicable for photolithography. The experiment made at use of 0,4 aperture lens shows possibility of transformation of initial conical light distribution to cylindrical one as a result of investigated processes in nanocomposite UV-curable material and formation of subwavelength-sized elements.

Acknowledgment

The work was made under support of Grant of Russian Ministry of Education no. RNP.2.1.1.3937, "Investigation of possible way for overcoming diffraction limit in photolithography by use of self-organization and non-linear proprieties of photopolymerizable nanocomposite materials," 2009–2011.

References

- [1] B. F. Griffing and P. R. West, "Contrast enhanced lithography," *Solid State Technology*, vol. 28, no. 5, pp. 152–157, 1985.
- [2] C. Rosilio, A. Rosilio, and B. Serre, "Charge-transfer complexes applied to photolithography by formation of a portable conformable mask and as a contrast-enhancement layer," *Microelectronic Engineering*, vol. 8, no. 1-2, pp. 37–54, 1988.
- [3] H. Sewell, D. McCafferty, L. Markoya, E. Hendrickx, J. Hermans, and K. Ronse, "32nm node technology development Using interference immersion lithography," in *Advances in Resist Technology and Processing XXII*, vol. 5753 of *Proceedings of SPIE*, pp. 491–501, 2005.
- [4] Y. Tomita, N. Suzuki, and K. Chikama, "Holographic manipulation of nanoparticle distribution morphology in nanoparticle-dispersed photopolymers," *Optics Letters*, vol. 30, no. 8, pp. 839–841, 2005.
- [5] T. V. Smirnova, Y. E. Burunkova, and I. Y. Denisyuk, "Measuring the shrinkage of UV-hardenable composites based on acrylates and diacrylates," *Journal of Optical Technology*, vol. 73, no. 5, pp. 352–355, 2006.
- [6] J. A. Burunkova, I. Yu. Denisyuk, N. N. Arefieva, and S. A. Semina, "Influence of SiO_2 nanoaddition on the self-organization via UV-polymerization of acrylate nanocomposites," *Molecular Crystals and Liquid Crystals*, vol. 536, pp. 242–248, 2011.
- [7] T. R. Williams, I. Yu. Denisyuk, and J. E. Burunkova, "Hybrid optical material based on high nanoparticles concentration in UV-curable polymers—technology and proprieties," *Molecular Crystals & Liquid Crystals*, vol. 497, no. 1, pp. 142–153, 2008.
- [8] J. E. Burunkova, I. Y. Denisyuk, and T. R. Williams, "Filled polymers with high nanoparticles concentration-synthesis and properties," *Journal of Applied Polymer Science*, vol. 116, no. 4, pp. 1857–1866, 2010.
- [9] I. Yu. Denisyuk, N. D. Vorzobova, J. E. Burunkova, N. N. Arefieva, and M. I. Fokina, "Self-organization effects in photopolymerizable nanocomposite," *Molecular Crystals and Liquid Crystals*, vol. 536, no. 1, pp. 233–241, 2011.
- [10] T. M. Monro, D. Moss, M. Bazylenko, C. Martijn De Sterke, and L. Poladian, "Observation of self-trapping of light in a self-written channel in a photosensitive glass," *Physical Review Letters*, vol. 80, no. 18, pp. 4072–4075, 1998.
- [11] E. Andrzejewska, "Photopolymerization kinetics of multifunctional monomers," *Progress in Polymer Science (Oxford)*, vol. 26, no. 4, pp. 605–665, 2001.
- [12] N. Suzuki, Y. Tomita, and T. Kojima, "Holographic recording in TiO_2 nanoparticle-dispersed methacrylate photopolymer films," *Applied Physics Letters*, vol. 81, no. 22, pp. 4121–4123, 2002.
- [13] N. Suzuki, Y. Tomita, K. Ohmori, M. Hidaka, and K. Chikama, "Highly transparent ZrO_2 nanoparticle-dispersed acrylate photopolymers for volume holographic recording," *Optics Express*, vol. 14, no. 26, pp. 12712–12719, 2006.

- [14] I. Y. Denisyuk, M. I. Fokina, N. D. Vorzobova, Y. E. Burunkova, and V. G. Bulgakova, "Microelements with high aspect ratio prepared by self-focusing of light at UV-curing," *Molecular Crystals and Liquid Crystals*, vol. 497, pp. 228–235, 2008.
- [15] M. I. Fokina, N. O. Sobeshuk, and I. U. Denisyuk, "Polymeric microelement on the top of the fiber formation and optical loss in this element analysis," *Natural Science*, vol. 2, no. 8, pp. 868–872, 2010.

Research Article

Characterization of Orthorhombic α - MoO_3 Microplates Produced by a Microwave Plasma Process

Arrak Klinbumrung,¹ Titipun Thongtem,^{2,3} and Somchai Thongtem^{1,3}

¹Department of Physics and Materials Science, Faculty of Science, Chiang Mai University, Chiang Mai 50200, Thailand

²Department of Chemistry, Faculty of Science, Chiang Mai University, Chiang Mai 50200, Thailand

³Materials Science Research Center, Faculty of Science, Chiang Mai University, Chiang Mai 50200, Thailand

Correspondence should be addressed to Somchai Thongtem, schthongtem@yahoo.com

Received 1 October 2011; Accepted 8 November 2011

Academic Editor: William W. Yu

Copyright © 2012 Arrak Klinbumrung et al. This is an open access article distributed under the Creative Commons Attribution License, which permits unrestricted use, distribution, and reproduction in any medium, provided the original work is properly cited.

Orthorhombic α - MoO_3 microplates were produced from $(\text{NH}_4)_6\text{Mo}_7\text{O}_{24}\cdot 4\text{H}_2\text{O}$ solid powder by a 900 W microwave plasma for 40, 50, and 60 min. Phase, morphologies, and vibration modes were characterized by X-ray diffraction (XRD), selected area electron diffraction (SAED), scanning electron microscopy (SEM), and Raman and Fourier transform infrared (FTIR) spectroscopy. Sixty min processing resulted in the best crystallization of the α - MoO_3 phase, with photoluminescence (PL) in a wavelength range of 430–440 nm.

1. Introduction

Basically, molybdenum oxides are classified into two types: the thermodynamically stable orthorhombic α - MoO_3 phase, and the metastable monoclinic β - MoO_3 phase with ReO_3 -type structure. Orthorhombic α - MoO_3 phase is a promising oxide, with structural anisotropy [1]. It is a wide bandgap n-type semiconductor, which is very attractive for different technological applications such as photochromic materials (changing from colorless to blue by UV irradiation) [2–4], smart windows [5], self-developing photography [2], conductive gas sensors [3], lubricants [6], and catalysts [7]. Orthorhombic α - MoO_3 was composed of MoO_6 octahedral corner-sharing chains, with edge sharing of two similar chains to form layers bonded by the weak van der Waals attraction [2]. Different methods were used to produce the oxide, which led to achieving products with different properties: evaporation of Mo foil by IR in 1 atm synthetic air to produce a uniformly semitransparent film on alumina substrate [3], direct oxidation of a Mo spiral coil in ambient atmosphere to produce film on Si (001) substrate [8], flash evaporation of molybdenum oxide powder on silica glass

substrate, and (111)-oriented silicon wafer in vacuum [9], precipitation [10], and hydrothermal method [11].

In the present research, α - MoO_3 microplates were produced by exposing a solid powder to microwave plasma. This very simple and rapid process, which is also benign to the environment, may lead to large-scale industrial production.

2. Experiment

To produce MoO_3 , $(\text{NH}_4)_6\text{Mo}_7\text{O}_{24}\cdot 4\text{H}_2\text{O}$ powder was used as a starting material without further purification. Each 0.5 g powder was loaded into three 14 mm I.D. \times 100 mm long silica boats. Each was placed in a horizontal quart tube, which was tightly closed and evacuated until its absolute pressure was 3.7 ± 0.1 kPa. The powder was heated in batches by a 900 W microwave plasma; each batch was irradiated for 5 min. After the processing of each batch, the powder was thoroughly mixed and repeatedly heated for a total of 40, 50, or 60 min. During processing, the horizontal quart tube was continuously evacuated to drain the evolved gases out of the system.

The products were characterized using X-ray diffractometer (XRD, SIEMENS D500) operating at 20 kV, 15 mA, and

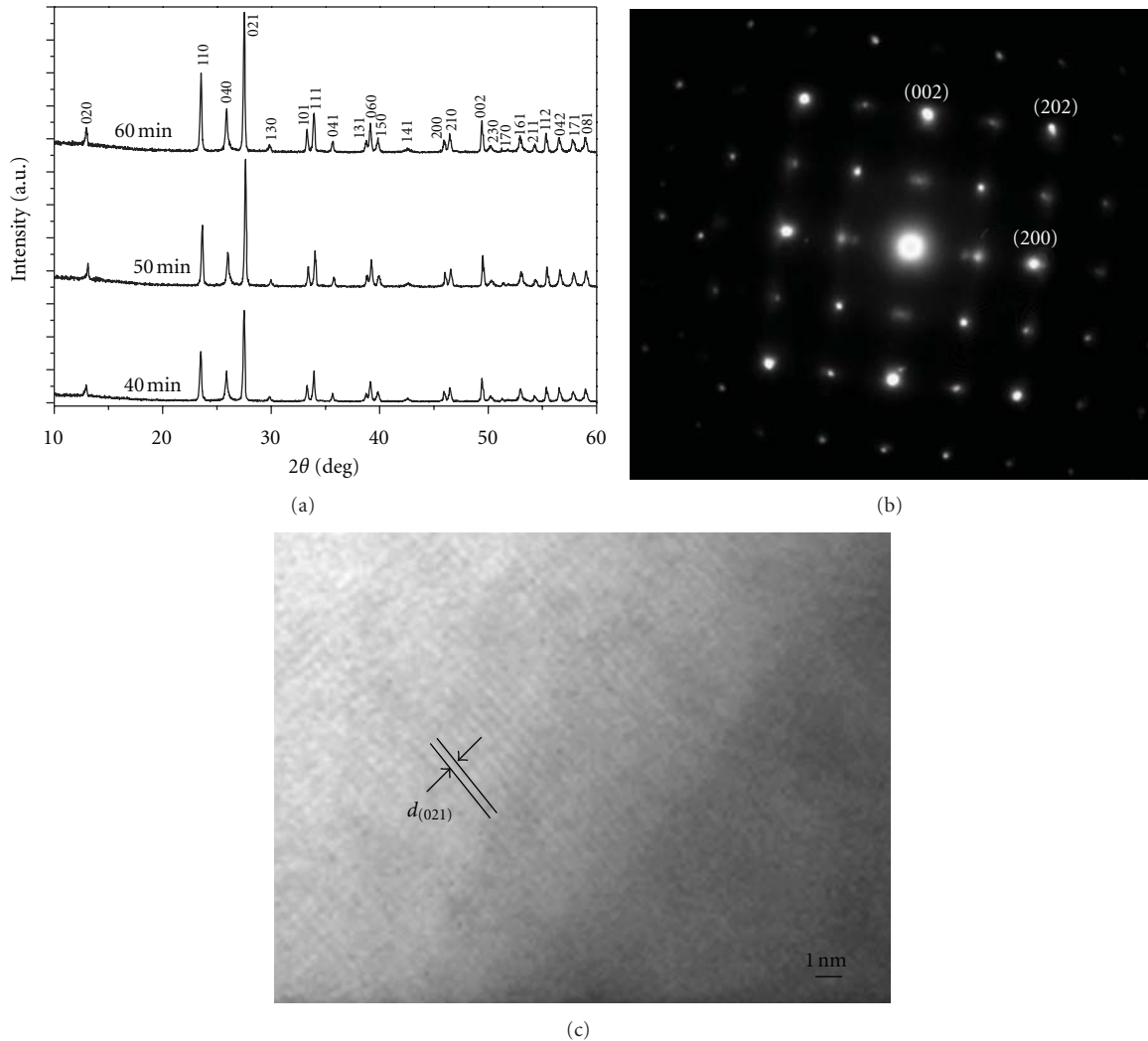


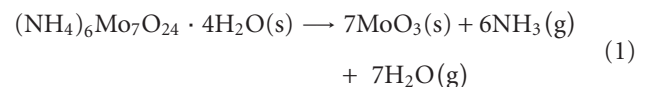
FIGURE 1: (a) XRD patterns of α -MoO₃ processed for 40, 50, and 60 min. (b, c) SAED pattern and HRTEM image of α -MoO₃ processed for 60 min.

using Cu-K α line, in combination with the database of the Joint Committee on Powder Diffraction Standards (JCPDS) [12]; scanning electron microscope (SEM, JEOL JSM-6335F) operating at 15 kV, transmission electron microscope (TEM, JEOL JEM-2010), and selected area electron diffractometer (SAED) operating at 200 kV; Fourier transform infrared spectrometer (FTIR, Bruker Tensor 27) with KBr as a diluting agent and operated in the range of 2000–400 cm⁻¹, Raman spectrometer (T64000 HORIBA Jobin Yvon) using a 50 mW and 514.5 nm wavelength Ar green laser, and photoluminescence (PL) spectrometer (LS 50B PerkinElmer) using a 380 nm excitation wavelength at room temperature.

3. Results and Discussion

3.1. XRD, SAED, and HRTEM. XRD patterns of the products processed for 40, 50, and 60 min are shown in Figure 1(a). Their peaks were specified as orthorhombic MoO₃ of JCPDS database number 05–0508 [12], with no impurity detection. The (020) peaks at 2θ of 12.8° were clearly detected, and

they indicated the presence of orthorhombic phase instead of monoclinic [13]. It should be noted that their intensities were slightly increased with the increase of processing time. The XRD peaks for 60 min processing time were the strongest, reflecting the product with the best degree of crystallinity. During processing, (NH₄)₆Mo₇O₂₄·4H₂O decomposed as follows:



MoO₃(s) was left as the final solid products. Two gases (NH₃ and H₂O) diffused out of the system, and evacuated out of the horizontal quartz tube. It should be noted that some reactant could remain, and was mixed with the final product if the processing time was less than 40 min. Longer processing times resulted in greater purification of the final product.

Calculated lattice parameters (Å) using the plane spacing equation for orthorhombic phase [14] were $a = 3.96$,

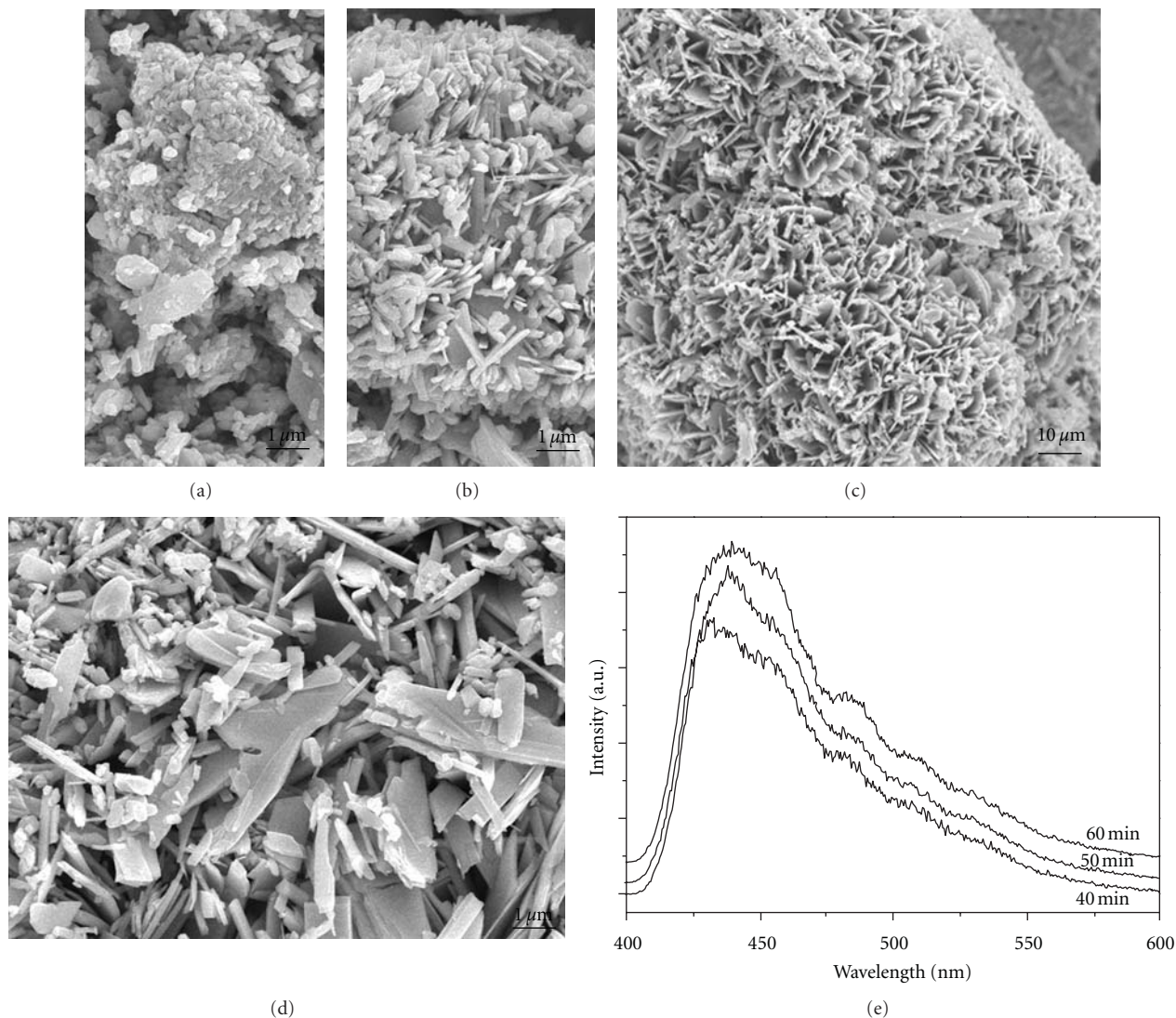


FIGURE 2: SEM images of α - MoO_3 processed for (a) 40 min, (b) 50 min, and (c, d) 60 min, and (e) PL emissions of α - MoO_3 processed for 40, 50, and 60 min.

$b = 13.86$, and $c = 3.70$, in accordance with those of the JCPDS database [12]. Figure 1(b) shows the SAED pattern of a single crystal processed for 60 min. It was indexed [15] to correspond with the (002), (202), and (200) crystallographic planes, which were specified as orthorhombic α - MoO_3 [2, 12, 16]. In the present analysis, an electron beam was sent to the crystal along the [010] direction. The (021) crystallographic plane with 0.33 nm spacing was detected by HRTEM (Figure 1(c)), implying that the product was crystalline in nature. These last two analyses were in accordance with that of the above XRD.

3.2. SEM. SEM images of MoO_3 crystals processed for 40, 50, and 60 min are shown in Figures 2(a)–2(d). Clusters of spheres ranging from 100 nm to a few hundred nm, as well as a small fraction of plates, were produced by 40 min processing. When the processing time was 50 min, more plates—about 100 nm thick and a few μm long—were produced,

growing perpendicular to the cluster surface. Sixty min processing resulted in a further increase in the number of plates produced, as well as their sizes: 100–200 nm thick and a few μm long. During processing, some plates could be broken due to the internal stress developed inside.

3.3. Raman and FTIR Analyses. Raman spectra (Figure 3(a)) of MoO_3 crystals processed for 40, 50 and 60 min were studied in the range of 150–1050 cm^{-1} . During the analysis, a low-intensity laser was used to avoid crystallization. The product of 60 min processing was a highly ordered crystalline structure, and its Raman peaks were the highest. The heights were reduced when the processing time was shortened. In the present research, 12 typical Raman peaks were detected. The peaks at 990 cm^{-1} were specified as the $\text{Mo}=\text{O}$ asymmetric stretching modes of terminal (unshared) oxygen [16]. The strongest peaks were at 813 cm^{-1} , and were specified as the doubly connected bridge-oxygen Mo_2-O stretching modes

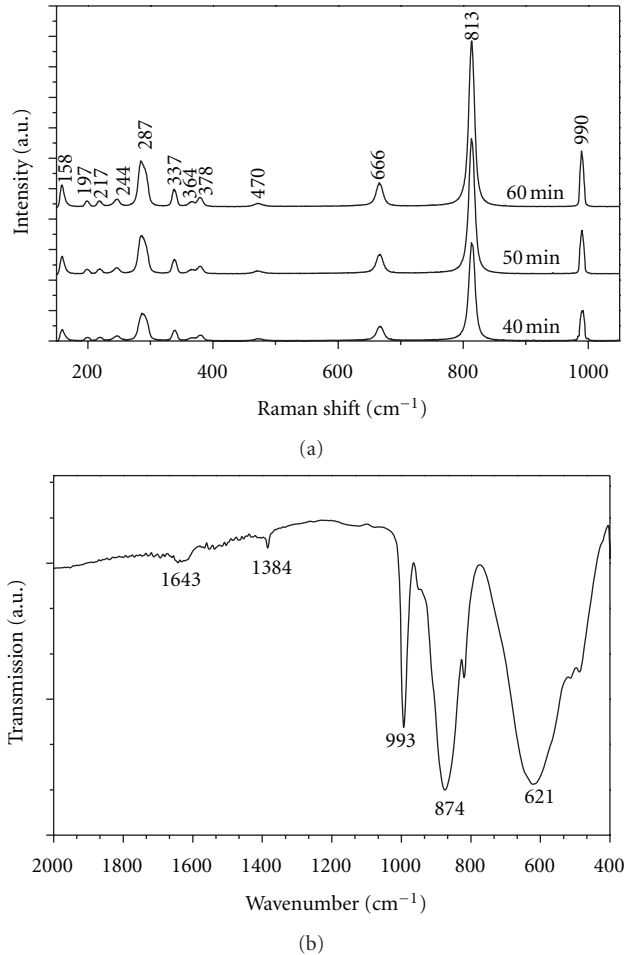


FIGURE 3: (a) Raman analysis of α - MoO_3 processed for 40, 50, and 60 min. (b) FTIR spectrum of α - MoO_3 processed for 60 min.

[2] of doubly coordinated oxygen, caused by corner-shared oxygen atoms in common to two MoO_6 octahedrons [16]. The peaks at 666 cm^{-1} were the $\text{Mo}_3\text{-O}$ stretching modes of triply coordinated bridge-oxygen, caused by edge-shared oxygen atoms in common to three octahedrons [2, 16]. Their remains were the O-Mo-O asymmetric stretching/bending modes at 470 cm^{-1} , O-Mo-O scissoring modes at 378 and 364 cm^{-1} , O-Mo-O bending modes at 337 cm^{-1} , O=Mo=O wagging modes at 287 cm^{-1} , O=Mo=O twisting modes at 244 cm^{-1} , R_c modes at 217 cm^{-1} , O=Mo=O twisting modes at 197 cm^{-1} , and T_b modes at 158 cm^{-1} [16]. Sometimes the Raman peaks were positively/negatively shifted, due to the increase or decrease in the vibration constant of the products [2]. In the present research, the vibrations were the same values, although the processing time and degree of crystallinity were different.

Figure 3(b) shows the FTIR spectrum of α - MoO_3 over the $400\text{--}2000\text{ cm}^{-1}$ range. Three strong vibrations were detected at 621 , 874 and 993 cm^{-1} , associated respectively with the stretching mode of oxygen linked with three metal atoms, the stretching mode of oxygen in the Mo-O-Mo units, and the Mo=O stretching mode—the specification of a layered

orthorhombic α - MoO_3 phase [17]. Two weak vibrations were also detected at 1384 and 1643 cm^{-1} , associated with the vibration mode of the Mo-OH bond and the bending mode of adsorbed water, respectively [17, 18].

3.4. PL Emission. PL emission of orthorhombic α - MoO_3 processed for 40, 50, and 60 min was studied using 380 nm excitation wavelength at room temperature. The PL spectra (Figure 2(e)) presented broad peaks over the $400\text{--}600\text{ nm}$ range with a strong indigo emission centered at $430\text{--}440\text{ nm}$ —in accordance with the report of Song et al. [4]. These emissions were caused by the band-to-band transition. In the present research, very weak shoulders, caused by the electron-hole recombination between the conduction band and the sublevel of adsorbed oxygen acceptors, were also detected; these were able to be reduced by calcination at high temperatures [4]. The luminescence intensity increased with the increase of processing times, in accordance with the improvement of the degree of crystallinity characterized by the above XRD analysis.

4. Conclusions

Orthorhombic α - MoO_3 was successfully produced by a 900 W microwave plasma process for 40, 50, and 60 min. The product processed for 60 min was α - MoO_3 microplates with three main Raman peaks (666 , 813 , and 990 cm^{-1}), three main FTIR vibration modes (621 , 874 , and 993 cm^{-1}), and $430\text{--}440\text{ nm}$ indigo emission—a promising material for different applications.

Acknowledgments

The authors wish to thank the National Nanotechnology Center (NANOTEC), National Science and Technology Development Agency, Thailand, for providing financial support through the project code: P-10-11345, the Thailand's Office of the Higher Education Commission through the National Research University Project, and the Scholarships for Thai Ph.D. Program, and the Thailand Research Fund (TRF) through the TRF Research Grant, including the Graduate School of Chiang Mai University through the general support.

References

- [1] X. W. Lou and H. C. Zeng, "Hydrothermal synthesis of α - MoO_3 nanorods via acidification of ammonium heptamolybdate tetrahydrate," *Chemistry of Materials*, vol. 14, no. 11, pp. 4781–4789, 2002.
- [2] T. He and J. Yao, "Photochromism of molybdenum oxide," *Journal of Photochemistry and Photobiology C*, vol. 4, no. 2, pp. 125–143, 2003.
- [3] E. Comini, L. Yubao, Y. Brando, and G. Sberveglieri, "Gas sensing properties of MoO_3 nanorods to CO and CH_3OH ," *Chemical Physics Letters*, vol. 407, no. 4–6, pp. 368–371, 2005.
- [4] J. Song, X. Ni, D. Zhang, and H. Zheng, "Fabrication and photoluminescence properties of hexagonal MoO_3 rods," *Solid State Sciences*, vol. 8, no. 10, pp. 1164–1167, 2006.

- [5] T. He, Y. Ma, Y. Cao, Y. Yin, W. Yang, and J. Yao, "Enhanced visible-light coloration and its mechanism of MoO₃ thin films by Au nanoparticles," *Applied Surface Science*, vol. 180, no. 3-4, pp. 336–340, 2001.
- [6] J. Wang, K. C. Rose, and C. M. Lieber, "Load-independent friction: MoO₃ nanocrystal lubricants," *The Journal of Physical Chemistry B*, vol. 103, no. 40, pp. 8405–8409, 1999.
- [7] K. R. Reddy, K. Ramesh, K. K. Seela, V. V. Rao, and K. V. R. Chary, "Alkylation of phenol with methanol over molybdenum oxide supported on NaY zeolite," *Catalysis Communications*, vol. 4, no. 3, pp. 112–117, 2003.
- [8] Y. Zhao, J. Liu, Y. Zhou et al., "Preparation of MoO₃ nanostructures and their optical properties," *Journal of Physics: Condensed Matter*, vol. 15, no. 35, pp. L547–L552, 2003.
- [9] C. Julien, A. Khelifa, O. M. Hussain, and G. A. Nazri, "Synthesis and characterization of flash-evaporated MoO₃ thin films," *Journal of Crystal Growth*, vol. 156, no. 3, pp. 235–244, 1995.
- [10] H. X. Bai, X. H. Liu, and Y. C. Zhang, "Synthesis of MoO₃ nanoplates from a metallorganic molecular precursor," *Materials Letters*, vol. 63, no. 1, pp. 100–102, 2009.
- [11] T. Xia, Q. Li, X. Liu, J. Meng, and X. Cao, "Morphology-controllable synthesis and characterization of single-crystal molybdenum trioxide," *The Journal of Physical Chemistry B*, vol. 110, no. 5, pp. 2006–2012, 2006.
- [12] Powder Diffract, File, JCPDS-ICDD, 12 Campus Boulevard, Newtown Square, P.A. 19073-3273, USA, 2001.
- [13] T. Mizushima, K. Fukushima, H. Ohkita, and N. Kakuta, "Synthesis of β -MoO₃ through evaporation of HNO₃-added molybdic acid solution and its catalytic performance in partial oxidation of methanol," *Applied Catalysis A*, vol. 326, no. 1, pp. 106–112, 2007.
- [14] C. Suryanarayana and M. G. Norton, *X-Ray Diffract*, Plenum Press, New York, USA, 1998.
- [15] K. W. Andrews, D. J. Dyson, and S. R. Keown, *Interpretation of Electron Diffraction Patterns*, Plenum Press, New York, USA, 1971.
- [16] T. Siciliano, A. Tepore, E. Filippo, G. Micocci, and M. Tepore, "Characteristics of molybdenum trioxide nanobelts prepared by thermal evaporation technique," *Materials Chemistry and Physics*, vol. 114, no. 2-3, pp. 687–691, 2009.
- [17] G. S. Zakharova, C. Täschner, V. L. Volkov et al., "MoO_{3- δ} nanorods: synthesis, characterization and magnetic properties," *Solid State Sciences*, vol. 9, no. 11, pp. 1028–1032, 2007.
- [18] M. Dhanasankar, K. K. Purushothaman, and G. Muralidharan, "Effect of temperature of annealing on optical, structural and electrochromic properties of sol-gel dip coated molybdenum oxide films," *Applied Surface Science*, vol. 257, no. 6, pp. 2074–2079, 2011.

Research Article

The Energy-Efficient Processing of Fine Materials by the Micropyretic Synthesis Route

H. P. Li

Jinwen University of Science and Technology, New Taipei City 23154, Taiwan

Correspondence should be addressed to H. P. Li, hli@just.edu.tw

Received 26 September 2011; Revised 28 November 2011; Accepted 2 December 2011

Academic Editor: William W. Yu

Copyright © 2012 H. P. Li. This is an open access article distributed under the Creative Commons Attribution License, which permits unrestricted use, distribution, and reproduction in any medium, provided the original work is properly cited.

Energy-efficient processing of TiB compound with nanowhiskers by micropyretic synthesis is investigated in this paper. Micropyretic synthesis not only offers shorter processing time but also excludes the requirement for high-temperature sintering and it is considered as the one of the novel energy-saving processing techniques. Experimental study and numerical simulation are both carried out to investigate the correlation of the processing parameters on the microstructures of the micropyretically synthesized products. The diffusion-controlled reaction mechanism is proposed in this study. It is noted that nanosize TiB whiskers only occurred when the combustion temperature is lower than the melting point of TiB but higher than the extinguished temperature. The results generated in the numerical calculation can be used as a helpful reference to select the proper route of processing nanosize materials. The Arrhenius-type plot of size and temperature is used to calculate the activation energy of TiB reaction. In addition to verifying the accuracy of the experimental measures, the reaction temperature for producing the micropyretically synthesized products with nanostructures can be predicted.

1. Introduction

The micropyretic synthesis, or so-called combustion synthesis (CS) or self-propagating high-temperature synthesis (SHS), employs exothermic reaction processing, which circumvents difficulties associated with conventional methods of time- and energy-intensive sinter processing [1–17]. Two basic micropyretic synthesis modes are commonly employed, namely, the wave propagation mode and the thermal explosion mode. In the wave propagation mode, the compacted powders are ignited at a point by a heat source. After ignition, the heat to propagate the combustion wave is obtained from the heat released by the formation of the synthesized product. The unreacted portion in front of the combustion wave is heated by this exothermic heat, undergoes synthesis, the wave propagates, thus causing further reaction and synthesis, as shown in Figure 1. In the thermal explosion mode, the specimen is heated in a furnace. The furnace may be kept at the ignition temperature or the specimen may be heated in the furnace at a predetermined heating rate to the ignition temperature. The micropyretic reaction in this mode may occur more or less simultaneously at all points in the

specimen. Although the synthesized product phases obtained by both techniques are similar [1], there may be differences in the amount of residual porosity, final dimensions, and the thermal gradient during the processing.

The advantages of micropyretic synthesis techniques include rapid net shape processing and clean products. When compared with conventional powder metallurgy operations, micropyretic synthesis not only offers shorter processing time but also excludes the requirement for high-temperature sintering. Volatile contaminants or impurities may be eliminated as the high temperature combustion wave propagates through the sample, and thus the synthesized products have the higher purity [2, 3]. The steep temperature gradient also gives rise to the occurrence of metastable, nonequilibrium phases or nanosize features, which are not available in the conventional processing [2, 3].

In the past decades, the conventional powder processing routes or other techniques are used to synthesize the materials with the nanostructures [18–22]. During the nanomaterial processing, there are three main difficulties for making reliable, uniform, nanostructure bulk alloys, including the following (1) The microstructural nonuniform-

mity often occurred in the synthesized product. (2) Energy wastage impacts the cost of production. (3) Human safety is encountered when nanoparticles are processed during the synthesis. Micropyretic synthesis offers the rapid net-shape processing and clean homogeneous product and is thus considered as one of novel processing candidates to process the nano materials [10]. In this study, the micropyretic synthesis is used to process the nanosize materials.

Metal borides are a group of ceramic materials with outstanding and attractive properties for technological applications [8]. Among these materials, Ti-B compound differs with high electrical conductivity, and superconductivity at cryogenic temperatures. The formation of nanosize phase in the Ti-B brittle synthesize product can aid to enhance the mechanical properties dramatically and increase its application. In addition, Ti-B materials can also be synthesized in a net shape by micropyretic synthesis due to the higher exothermic heat. In the previous studies [15–17], we have found that the changes in the processing parameters have the significant impact on the properties of micropyretically synthesized products, including the formation of the nanosize features. Thus, the understanding of the processing parameters is important and can help to select the proper processing nanomaterial route during micropyretic synthesis. In this study, Ti+B micropyretic reaction is chosen to study the effects of the processing parameters on the formation of nano size material. The experimental investigation and numerical calculation are both carried out to study the effects of processing parameters on the formation of nanosize TiB whisker in the micropyretically synthesized products.

1.1. Experimental Procedure. Ti+B micropyretic reaction is chosen to study the effect of processing parameters. Samples are obtained by mixing powders, pressing them into shape and finally combusting the shape by ignition from one end. The particle sizes of titanium and amorphous boron powders are both –325 mesh ($<44\ \mu\text{m}$). In order to retard the propagation velocity and further study the sequential reaction of Ti-B combustion, the larger B particle (-60 mesh, $<250\ \mu\text{m}$) is also chosen in this study. The powders are first tumble mixed for ~ 10 minutes without the addition of any liquid medium. Subsequently, the well-mixed powders are pressed at 15000 psi ($-100\ \text{MPa}$), using a double-acting press and die to form an ASTM-ESM [23] standard specimen. The thickness and longitudinal length of the unreacted green compact are 5 mm and 90 mm, respectively. For obtaining unidirectional wave propagation combustion, the compacted specimen is ignited from one end with an external heating source, which is held against the sample until combustion initiates. The heat source is then removed as the combustion front begins to propagate.

Microstructures are taken by scanning electron microscopy (SEM). For some of the microstructures, energy-dispersive analysis of X-ray (EDAX) is performed to obtain compositional data. X-ray diffraction (XRD) work is carried out in a Siemens diffractometer (model: D500) employing a Cu tube (wavelength: 0.15406 nm) operating at 40 KV and 30 mA. Extremely fine ($\sim 100\ \mu\text{m}$) tungsten-rhenium

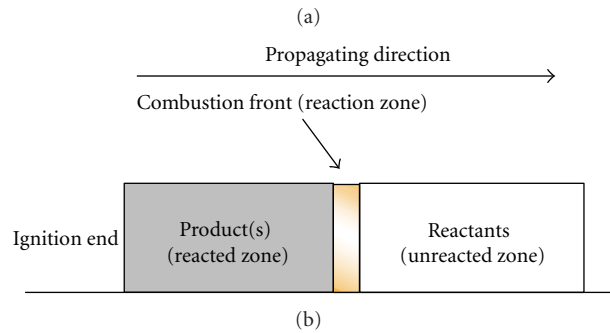
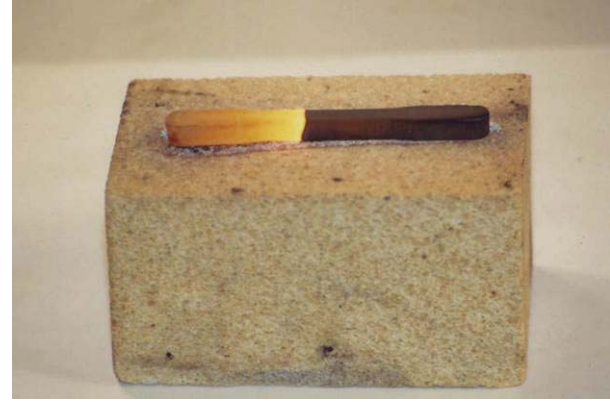


FIGURE 1: (a) The combustion front of the Ti-B reaction (with small Cu) propagates from left to right after the ignition. (b) The schematic of the propagation of the combustion front in Figure 1(a). During the propagation, the sample can be divided into three different zones, including reacted zone, reaction melting zone, and unreacted zone.

(W- 5% Re and W-26% Re) thermocouples are used to measure combustion temperature and propagation velocity during the combustion reaction. The thermocouples are embedded in the central area of a sample, at a depth of half the sample height. A data acquisition system is used to record the temperature at every 0.1-second interval. The combustion temperature is defined as the highest temperature during the combustion reaction. The average propagation velocity is calculated from the known distance between the thermocouples and the time lapse between the first signs of propagation of each thermocouple.

1.2. Numerical Simulation. During the passage of a combustion front in the micropyretic reaction, the energy equation for transient heat conduction, including the source term, containing heat release due to the exothermic reaction is given as [6, 12, 13]

$$\rho C_p \left(\frac{\partial T}{\partial t} \right) = \frac{\partial}{\partial z} \left(\kappa \left(\frac{\partial T}{\partial z} \right) \right) - \frac{4h(T - T_o)}{d} + \rho Q \Phi(T, \eta). \quad (1)$$

Each symbol in the equation is explained in the nomenclature section. The reaction rate, (T, η) , in (1) is given as

$$\Phi(T, \eta) = \frac{\partial \eta}{\partial t} = K_o(1 - \eta) \exp\left(-\frac{E}{RT}\right). \quad (2)$$

TABLE 1: The thermophysical/chemical parameters for the reactants and product at solid state (300 K) and liquid state [24].

Thermophysical/chemical parameters	Ti	B	TiB ₂
Heat capacity (300 K) (J/(kgK))	528	118	950
Heat capacity (liquid) (J/(kgK))	700	2800	2055
Thermal conductivity (300 K) (J/(msK))	21.6	27	25
Thermal conductivity (liquid) (J/(msK))	11	15	13
Density (300 K) (kg/m ³)	4500	2450	4400
Density (liquid) (kg/m ³)	4110	2080	4100

TABLE 2: The values of various parameters used in the numerical calculation [25, 26].

Parameters	TiB ₂
Combustion temperature (K)	3190
Activation energy (kJ/mole)	318 [25]
Exothermic heat (kJ/mole)	4214 [26]
Preexponential factor (1/second)	1×10^{10}

In this study, a numerical calculation for (1) is carried out with the assumption of the first-order kinetics. In (1), the energy required for heating the synthesized product from the initial temperature to the adiabatic combustion temperature is shown on the left-hand side. The terms on the right-hand side are the conduction heat transfer term, the surface heat loss parameter, and the heat release due to the exothermic micropyretic reaction, respectively. The previous two-dimension study [12] has indicated that the conduction heat transfer and surface heat loss are so small as compared with the exothermic heat. Thus, the surface heat loss is assumed to be radically Newtonian and is taken to be zero in this study.

A middle-difference approximation and an enthalpy-temperature method coupled with Gauss-Seidel iteration procedure are used to solve the equations of the micropyretic synthesis problems. In the computational simulation, a one-dimensional sample of 1 cm long is divided into 1201 nodes (regions) to calculate the local temperature. This one-dimensional numerical model assumes the following sequence of events: (1) the specimen is gradually heated by a surface heat source; (2) the reaction is ignited and the combustion front propagates along the specimen; (3) there is a cooling source at one end. The choice of 1 cm sample length is only for computational purpose, and the simulation results are applicable to practical experimental conditions. The proper initial conditions are used to initialize the temperatures and enthalpies at all nodes. At time $t = 0$, the temperatures are taken to be the same as the substrate temperature ($T = T_0$ (300 K) and $\eta = 0$). The energy is gradually added at the ignition node in very small time steps until the combustion front starts to propagate.

The various microscale events, that is, local processes such as warming of the sample, melting of lower refractory reactant, formation of product, and cooling of the sample at one end, are included in this calculation procedure. Depend-

ing on the values of the temperature and enthalpy occurring in the reaction, the proper thermophysical/chemical parameters are considered and the limits of the reaction zone are determined for each node in the numerical calculation. At any given time, the fraction reacted and enthalpy of the current iteration are calculated from the previous fraction reacted and enthalpy of the earlier iteration. The range of the enthalpy as well as the molar ratio among each material for each node is thus determined, and the values of temperature, density, and thermal conductivity at each node can be further calculated in appropriate zone.

The various thermophysical/chemical parameters, such as thermal conductivity, density, and heat capacity of the reactants and product, are assumed to be independent of temperature, but they are different in each state. The average values of these parameters vary as the reaction proceeds, depending upon the degree of reaction. The parameter values used in the computational calculation are shown in Table 1 [24] and Table 2 [25, 26]. In this study, the combustion temperature is defined as the highest reaction temperature during micropyretic synthesis, and the propagation velocity is the velocity of the combustion front propagation. In addition, the higher preexponential factor (K_0) value, 1.0×10^{10} 1/s, is used to be capable of illustrating the variation of the propagation velocity for the Ti-B micropyretic reaction.

2. Results and Discussion

2.1. Ti-B Micropyretic Reaction. It has been proposed that the micropyretic/combustion synthesis includes the diffusion and the capillary-controlled reaction mechanisms, which are dependent on the size of the reactant particle [27–29]. Following the study of Nekrasov et al. [29], the diffusion control is dominant when

$$d_i^2 \ll \frac{2\sigma\lambda d_h}{\mu\nu^2} * \ln\left[\frac{T_c - T_0}{T_m - T_0}\right], \quad (3)$$

where d_i and d_h are the diameters of the particle sizes for the low melting point component and high melting point component, respectively. The other symbols and the values of the variables used for calculating (3) are shown in Table 3 [24–26, 30]. The Ti particle (low melting component) size threshold between the diffusion-controlled and the capillary-controlled combustion propagation may be thus calculated using (3). Employing (3), we note that the diffusion control can take place when the B size (diameter) should be higher

TABLE 3: The thermophysical/chemical parameters for the molten Ti (at 1933 K) used in the calculation of (3) [24–26, 30].

Σ	Surface tension	1.46 N/m
Λ	Thermal diffusivity, [= K/(D·C _p)]	4.4×10^{-6} m ² /s
K	Thermal conductivity	13 J/(m·s·K)
D	Density	4300 Kg/m ³
C_p	Heat capacity	682 J/(Kg·K)
μ	Viscosity	0.002 s(N/m ²)
T_m	Melting point	1933 K
ν	Propagation velocity	0.02 m/s
T_o	Initial temperature	300 K
T_c	Combustion temperature	2700 K

than 0.14 nm for 30 μ m Ti. The boron sizes we used in this study are in the microscale (–60 mesh and –325 mesh, <250 μ m and <44 μ m) and are much higher than the correspondingly calculated critical size. Thus the studied mixtures are expected to be all in the range of diffusion-controlled combustion.

For investigating the possible titanium boride reaction mechanism in the Ti-B binary system, a sample with larger B particles (–60 mesh (<250 μ m)), which propagates at a lower velocity, is intentionally extinguished during the propagation. It is inferred from microstructures that as the combustion starts, the unreacted portion in front of the combustion front is preheated by the released energy. The temperature of the unreacted portion is increased to a high level, melting the less refractory phase (Ti). The molten Ti encapsulates the nonmelting B particles (Figure 2). The resultant increase in the contact area between Ti and B significantly increases the reaction kinetics. The reacted product subsequently forms a layer on the surface of the nonmelting B particle. The exothermic heat of the product formation is released and conducts to unreacted materials, which in turn react, continuing the chain reaction.

From the diffusion-control mechanism theory and the observed microstructures (Figure 2), we propose the following reaction sequences for Ti-B reaction. (1) The Ti particles first melt and flow around the B particles. (2) The contact efficiency of B particles with the Ti liquid is now increased and the molten Ti ignites the rapid reaction. (3) An intermediate complex forms. (4) The Ti atoms diffuse from the melt, across the complex, to readily react with the B particle at its surface. (5) The intermediate complex of reaction is dissolved on the Ti-liquid side. Fresh new intermediate complex phase is formed between the intermediate complex phase and B particle at such a rate that the thickness of the complex is a constant. (6) The final Ti-B stoichiometric product is then precipitated from the molten liquid.

Figures 3(a) and 3(b) show the microstructures for the Ti-B reactions with the different compositions. Note from Figure 3 that microstructures are significantly changed when the composition is varied from 10 wt.% B to 25 wt.% B. The formation of the nanosize feature is only observed in the composition with 10 wt.% B. The average measured propagation velocity for the composition with 25 wt.%

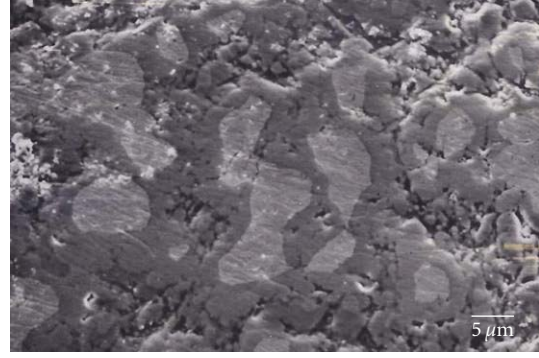


FIGURE 2: SEM morphologies of the Ti-B reacted zone. As the combustion commences, when the temperature of the unreacted portion is increased to a high level, the less refractory phase (Ti) is first melted. The molten Ti then encapsulates the nonmelting B particles and the resultant increase in the contact area between Ti and B dramatically increases the reaction kinetics. The reacted product subsequently forms on the surface of the nonmelting B particle.

B (>20 cm/s) is much higher than that for composition 10 wt.% B (0.96 ± 0.32 cm/s). The combustion temperature for the composition with 25 wt.% B exceeds the upper limit of thermocouples, and the combustion temperature is increased with the increase in the propagation velocity, as shown in Table 3. These experimental demonstrations show that the changes in the processing parameters influence the combustion temperature and propagation velocity, further altering the microstructures and properties of the synthesized products. To understand the processing parameters as nanosize structures form, the computer simulation is then used to aim towards an understanding.

2.2. Numerical Study Is Used to Forecast the Formation of Nanosize Structures. The previous experimental and numerical studies [12, 15, 16] have shown that the processing parameters, including the initial temperature, reactant particle size, diluents, compact density, compositions, exothermic heat, and activation energy have a significant impact on the reaction parameters, like propagation velocity and combustion temperature. A change in the reaction parameters has significantly influenced the properties of the synthesized products. It is noted that the combustion temperature and propagation velocity are increased as increasing the initial temperature or exothermic heat or are decreased as increasing the reactant size, activation energy, or amount of the diluents.

Figure 4 shows the numerical calculating results for the temperature-time plots for the compositions with the different processing parameters (different values of activation energy). The micropyretic reactions are ignited by ignition power (per gram) of 175 Joule/(ms·g) at the position 0 cm, and the heating sources are removed immediately after the combustion front has been ignited. The interval time between two consecutive time steps (profiles) in Figure 4 is 0.001 s. It is found from Figure 4(b) that the combustion

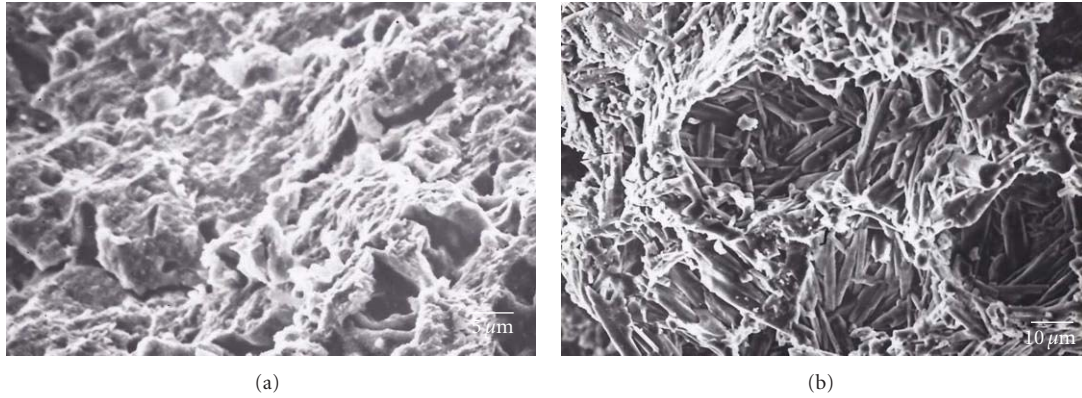


FIGURE 3: SEM morphologies of the Ti-B reacted zone. (a) Ti + 25 wt.% B combustion and (b) Ti + 10 wt.% B combustion.

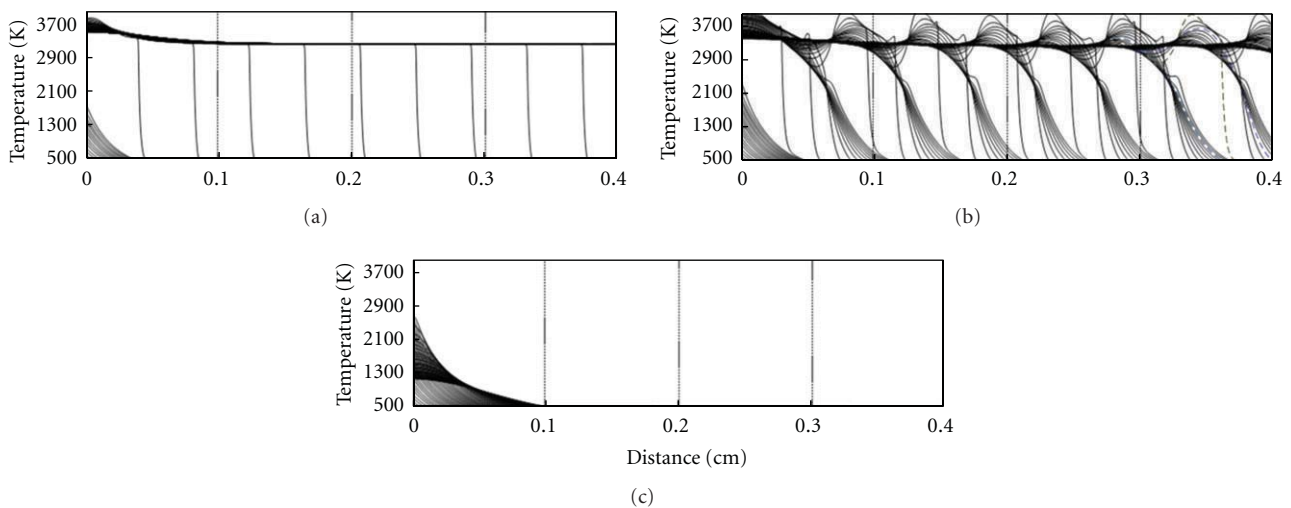


FIGURE 4: Time variations of the combustion front temperature along the TiB_2 specimen with the preexponential factor of $1 \times 10^{10} \text{ s}^{-1}$. The interval time between two consecutive time steps (profiles) is 1.0 ms. The ignition power is taken as 175 Joule/(ms·g) in the numerical calculation. The activation energy in (a), (b), and (c) are taken as 254.4 KJ/mole (80% of reported experimental value) [27], 318.0 KJ/mole (reported experimental value), and 381.6 KJ/mole (120% of reported experimental value), respectively.

front takes 21.04 ms to start propagating for the Ti-B micropyretic reaction with the reported experimental activation energy (318 KJ/mole) [27]. This ignition time interval corresponds to the ignition energy of 3682.0 Joule/g. Figure 4(b) also displays an alternating increase and decrease in the temperature and propagation velocity during the combustion front propagation, indicating that the combustion front for Ti-B micropyretic reaction propagates in an unstable oscillatory manner. When 80% of reported experimental activation energy value is taken in the numerical calculation, the propagation manner is noted to change from unstable manner to stable manner; in addition, the ignition time is reduced from 21.04 ms to 16.38 ms, which corresponds to the ignition energy of 2866.5 Joule/g (Figure 4(a)). When 120% of reported experimental activation energy is taken in the calculation, the ignition time is increased to 25.66 ms (corresponding to the ignition energy of 4490.5 Joule/g) and the combustion front extinguishes immediately after the start of propagation (Figure 4(c)).

It is known that the decrease in the propagation velocity reduces the oscillating combustion temperature. A further decrease in the velocity may extinguish the propagation of the combustion front. The study of Borovinskaya et al. [8] also shows the oscillating patterns for Ti- (and Ta-, Nb-, Zr-) B reaction. Thus, the above results generated from the above numerical demonstrations indicate that the nanowhisker formation can be acquired only at the low reaction temperature but without stopping the chain reaction. This study next tries to select the proper reaction temperature to synthesize the nanosize material by changing the reactant compositions.

2.3. Selection of the Proper Processing Parameters to Synthesize Nanosize Products. Figure 5 shows the SEM morphologies of the synthesized products with different boron content. It is noted from Figure 5 and Table 4 that the sizes of the whiskers are decreased with the decrease in the combustion

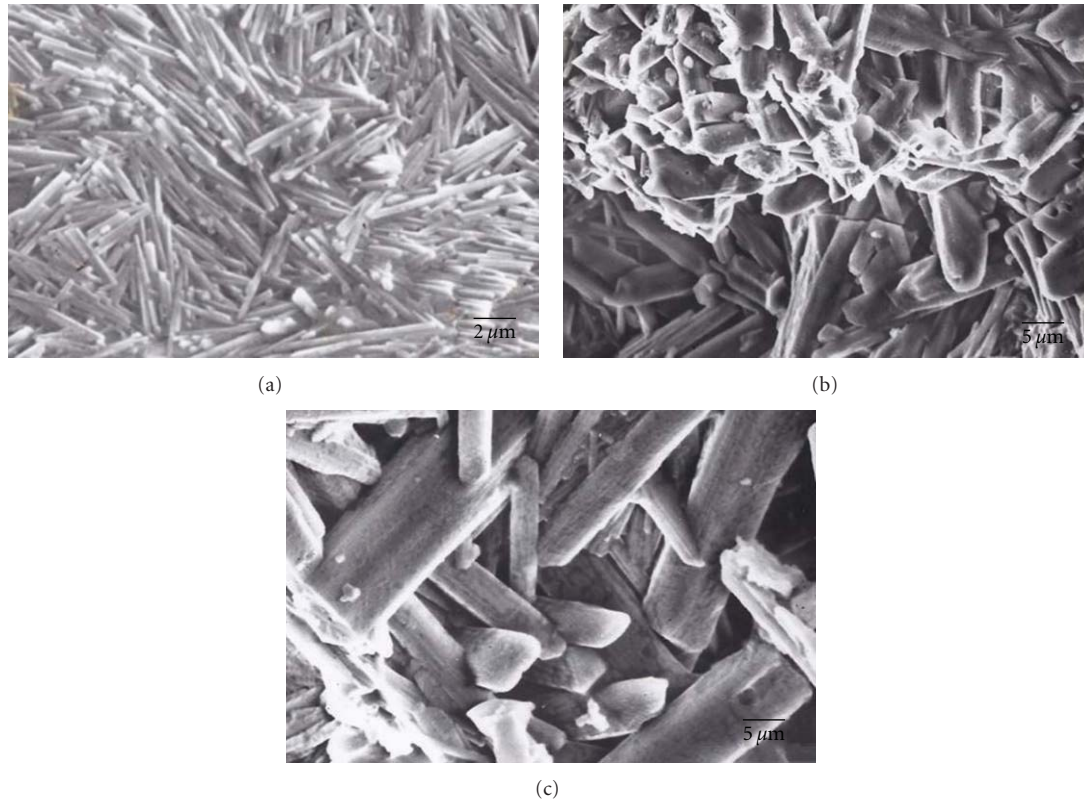


FIGURE 5: SEM morphologies of the Ti-B whiskers. (a) Ti + 10 wt.% B combustion and (b) Ti + 17.5 wt.% B (b) Ti + 20 wt.% B combustion.

TABLE 4: The combustion temperature, propagation velocity, and the diameter of whisker for the compositions with different boron contents.

Boron content (wt.%)	Combustion temperature (K)	Propagation velocity (cm/s)	Diameter of whisker (μm)
25.0	>2100	>20	NA
20.0	1980 ± 26	8.52 ± 1.52	6.96 ± 2.18
17.5	1845 ± 18	7.12 ± 1.46	3.96 ± 1.57
15.0	1672 ± 11	1.92 ± 0.84	1.65 ± 0.46
10.0	1513 ± 15	0.96 ± 0.32	0.64 ± 0.35

temperature. The new nonwhisker structures are observed when the combustion temperature exceeds 2100 K. It is expected that the average measured combustion temperature of composition with 25 wt.% B is much higher than the melting point of TiB phase. The TiB whiskers may be melted and then solidified. The nonwhisker microstructure is thus formed.

The whisker structures are further analyzed by XRD. The X-ray patterns show that the whisker structures tend to be the TiB phase. Similar Ti-B whisker morphologies have also been observed in several studies [31–34]. In the study of Andrievskii et al. [31], it was shown that TiB₂ (hexagonal type) and TiB (orthorhombic type) are probably characterized by anisotropy of surface energy, and consequently the grains are expected to be faceted. Hashimoto et al. [32] found that at sintering temperatures of 1373 K, and 1473 K the needle- or fiber-type TiB₂ precipitates when the coarse B powder ($\sim 150 \mu\text{m}$) is chosen. Hyman et al. [33] performed extensive as-cast-binary as well as TEM studies on the formation of TiB and TiB₂ in the ternary Ti-Al-B system.

It was shown that the crystal structures of both TiB and TiB₂ are based on the same building block and have the same needle-like morphology [33]. Similar whisker-like structures are also observed on the Ti-B compounds by micropyretic synthesis [34]. Yang et al. [34] show that the morphologies of the combustion synthesized Ti-B compounds varied from flake type to whisker type, depending on boron content.

2.4. Robust Check of the Error of the Measured Sizes and Temperatures. Arrhenius-type plot of size and temperature is used to calculate the activation energy of Ti-B reaction. As compared with the reported experimental value, the calculated activation energy can be used to verify the accuracy of the measured size and temperature in this study. The diameters of the TiB whisker-type structures are noted to increase when the combustion temperature is raised by changing the composition. The correlation of the whisker diameter with the temperature is thus used to calculate

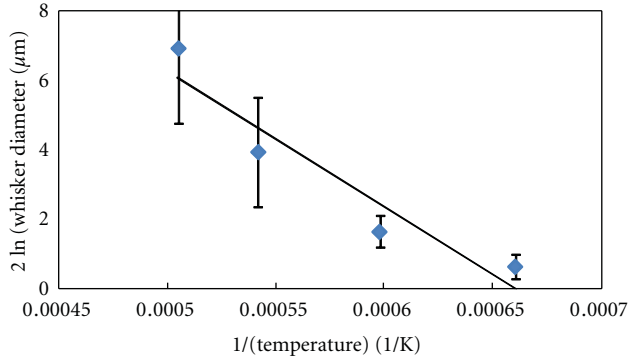


FIGURE 6: Arrhenius-type plot of the TiB whisker diameter and combustion temperature.

the activation energy [35–38]. The general relation between the whisker/grain size and the temperature is expressed as [35, 36]

$$2 \ln(D) = -\frac{E}{RT} + \text{constant}, \quad (4)$$

where D is the grain size or whisker diameter, E is the activation energy for the whisker growth, T is the combustion temperature, and R is the universal constant ($= 8.314 \text{ J/mole/K}$). As employing (4), the activation energy for TiB whisker growth is determined from the plot of $2 \ln(D)$ and $1/T$. From an Arrhenius-type plot in Figure 6, the activation energy for the whisker growth is calculated to be 231 KJ/mole. As compared with the reported values for TiB combustion, 230 KJ/mole [39] or 251 KJ/mole [40], which was approached from the combustion wave velocity and temperature profile investigation, respectively, the calculated value for the whisker growth is in good agreement with the reported values for the Ti-B combustion, verifying the accuracy of the measured size and temperature in this study.

In addition, from the Arrhenius-type plot of diameter and measure combustion temperature, we can also forecast the reaction temperature for the nanosize whisker. Note from the calculated results that the $<10 \text{ nm}$ TiB whisker starts to form when the combustion temperature is decreased to 1500 K.

3. Summary and Conclusions

Processing of TiB compound by micro-pyretic synthesis is carried out in this study. Experimental study and numerical simulation are both used to investigate the correlation of the processing parameters on the microstructure of the synthesized products. It is noted that nanosize TiB whisker is expected to occur when the combustion temperature is lower but higher than the extinguish temperature. The results generated in the numerical calculation can be used as a helpful reference to select properly the processing route of producing nanosize features product. The Arrhenius-type plot of size and temperature is also used to calculate the activation energy of TiB reaction. The calculation activation energy is in a good appointment with the reported value,

verifying that the accuracy of the experimental measures of the grain size in this study. In addition, the Arrhenius-type plot can be used to forecast the combustion temperature for producing nanosize TiB whisker.

Nomenclature

- C_p : Heat capacity, $\text{Jkg}^{-1} \text{K}^{-1}$
 E : Activation energy, Jmole^{-1}
 h : Surface heat transfer coefficient, $\text{Jm}^{-2} \text{K}^{-1} \text{s}^{-1}$
 K_0 : Preexponential factor, s^{-1}
 Q : Exothermic heat of reaction, Jmole^{-1}
 R : Universal gas constant, $\text{Jmole}^{-1} \text{K}^{-1}$
 T : Temperature, K
 T_0 : Initial temperature of the unreacted compact, K
 t : Time, s
 z : Dimensional coordinate, m
 d : Diameter of the specimen, m.

Greek Letters

- κ : Thermal conductivity, $\text{Jm}^{-1} \text{s}^{-1} \text{K}^{-1}$
 Φ : Reaction rate, s^{-1}
 ρ : Density, km^{-3}
 η : Reacted fraction.

References

- [1] Y. S. Naiborodenko, V. I. Itin, and K. V. Savitskii, "Use of combustion and thermal explosion for the synthesis of intermetallic compounds and their alloys," *Powder Metallurgy and Metal Ceramics*, vol. 7, no. 91, pp. 562–567, 1970.
- [2] Z. A. Munir and J. B. Holt, "The combustion synthesis of refractory nitrides—part 1. Theoretical analysis," *Journal of Materials Science*, vol. 22, no. 2, pp. 710–714, 1987.
- [3] Z. A. Munir, "Synthesis of high temperature materials by self-propagating high-temperature combustion methods," *American Ceramic Society Bulletin*, vol. 67, no. 2, pp. 342–349, 1988.
- [4] H. P. Li and J. A. Sekhar, "Influence of the reactant size on the micro-pyretic synthesis of NiAl intermetallic compounds," *Journal of Materials Research*, vol. 10, no. 10, pp. 2471–2480, 1995.
- [5] Y. S. Naiborodenko and V. I. Itin, "Gasless combustion of metal powder mixtures—1. Mechanism and details," *Combustion, Explosion, and Shock Waves*, vol. 11, no. 3, pp. 293–300, 1975.
- [6] A. G. Merzhanov and B. I. Khaikin, "Theory of combustion waves in homogeneous media," *Progress in Energy and Combustion Science*, vol. 14, no. 1, pp. 1–98, 1988.
- [7] V. M. Shkiro and G. A. Nersisyan, "Structure offluctuations occurring in the burning of tantalum-carbon mixtures," *Combustion, Explosion, and Shock Waves*, vol. 14, no. 1, pp. 121–122, 1978.
- [8] I. P. Borovinskaya, A. G. Merzhanov, N. P. Novikov, and A. K. Filonenko, "Gasless combustion of mixtures of powdered transition metals with boron," *Combustion, Explosion, and Shock Waves*, vol. 10, no. 1, pp. 2–10, 1974.
- [9] S. Hwang, A. S. Mukasyan, A. S. Rogachev, and A. Varma, "Combustion wave microstructure in gas-solid reaction systems: experiments and theory," *Combustion Science and Technology*, vol. 123, no. 1–6, pp. 165–184, 1997.

- [10] J. A. Sekhar, H. P. Li, and G. K. Dey, "Decay-dissipative Belousov-Zhabotinsky nanobands and nanoparticles in NiAl," *Acta Materialia*, vol. 58, no. 3, pp. 1056–1073, 2010.
- [11] H. P. Li and J. A. Sekhar, "Belousov-Zhabotinsky dissipative reactions in Ti-B and Ni-Al alloy systems," *Acta Materialia*, vol. 57, no. 18, pp. 5430–5444, 2009.
- [12] M. G. Lakshmikantha and J. A. Sekhar, "Influence of multi-dimensional oscillating combustion fronts on thermal profiles," *Journal of Materials Science*, vol. 28, no. 23, pp. 6403–6408, 1993.
- [13] M. Lakshmikantha and J. A. Sekhar, "Analytical modeling of the propagation of a thermal reaction front in condensed systems," *Journal of the American Ceramic Society*, vol. 77, no. 1, pp. 202–210, 1994.
- [14] H. P. Li, S. B. Bhaduri, and J. A. Sekhar, "Metal-ceramic composites based on the Ti-B-Cu porosity system," *Metallurgical Transactions A*, vol. 23, no. 1, pp. 251–261, 1992.
- [15] H. P. Li and J. A. Sekhar, "Processing maps for the micropyretic synthesis of structural composites and intermetallics," in *Proceedings of the 1st International Conference on Advanced Synthesis of Engineered Materials*, J. J. Moore, E. J. Lavernia, and F. H. Froes, Eds., pp. 25–31, 1993.
- [16] H. P. Li and J. A. Sekhar, "Rapid solidification by unstable combustion synthesis," *Journal of Materials Research*, vol. 8, no. 10, pp. 2515–2523, 1993.
- [17] O. K. Dey and J. A. Sekhar, "Micropyretic synthesis of tough nial alloys," *Metallurgical and Materials Transactions B*, vol. 28, no. 5, pp. 905–918, 1997.
- [18] G. He, J. Eckert, W. Löser, and L. Schultz, "Novel Ti-base nanostructure-dendrite composite with enhanced plasticity," *Nature Materials*, vol. 2, no. 1, pp. 33–37, 2003.
- [19] J. Ning, G. Xiao, L. Wang, B. Zou, B. Liu, and G. Zou, "Facile synthesis of magnetic metal (Mn, Fe, Co, and Ni) oxide nanocrystals via Cation-exchange reaction," *Nanoscale*, vol. 3, no. 2, pp. 741–745, 2011.
- [20] H. A. Lee, M. Imran, N. A. Monteiro-Riviere, V. L. Colvin, W. W. Yu, and J. E. Riviere, "Biodistribution of quantum dot nanoparticles in perfused skin: evidence of coating dependency and periodicity in arterial extraction," *Nano Letters*, vol. 7, no. 9, pp. 2865–2870, 2007.
- [21] H. H. Huang, F. B. Wu, J. W. Lee, and L. C. Chang, "Microstructure and corrosion behavior of Ni-Alloy/CrN nanolayered coatings," *Journal of Nanomaterials*, vol. 2011, Article ID 137498, 6 pages, 2011.
- [22] N. Lin, J. Huang, P. R. Chang, D. P. Anderson, and J. Yu, "Preparation, modification, and application of starch nanocrystals in nanomaterials: a review," *Journal of Nanomaterials*, vol. 2011, Article ID 573687, 13 pages, 2011.
- [23] *Annual Book of ASTM Standard*, ASTM, Philadelphia, PA, USA, 1989.
- [24] E. A. Brandes and G. B. Brook, *Smithells Metals Reference Book*, Butterworth-Heinemann, 1992.
- [25] T. S. Azatyan, V. M. Mal'tsev, A. G. Merzhanov, and V. A. Seleznev, "Combustion wave propagation mechanism in titanium-boron mixtures," *Combustion, Explosion, and Shock Waves*, vol. 16, no. 2, pp. 163–167, 1980.
- [26] G. V. Samsonov and I. M. Vinitkii, *Handbook of Refractory Compounds*, IFI/Plenum, New York, NY, USA, 1980.
- [27] Z. A. Munir and U. Anselmi-Tamburini, "Self-propagating exothermic reactions: the synthesis of high-temperature materials by combustion," *Materials Science Reports*, vol. 3, no. 7–8, pp. 277–365, 1989.
- [28] V. M. Shkiro, V. N. Doroshin, and I. P. Borovinskaya, "Concentration structure of the combustion wave in the titanium-carbon system," *Combustion, Explosion, and Shock Waves*, vol. 16, no. 4, pp. 370–374, 1980.
- [29] E. A. Nekrasov, Y. M. Maksimov, M. K. Ziatdinov, and A. S. Shteinberg, "Effect of capillary spreading on combustion-wave propagation in gas-free system," *Combustion, Explosion, and Shock Waves*, vol. 14, no. 5, pp. 575–581, 1978.
- [30] J. Zhu, A. Kamiya, T. Yamada, W. Shi, K. Naganuma, and K. Mukai, "Surface tension, wettability and reactivity of molten titanium in Ti/yttria-stabilized zirconia system," *Materials Science and Engineering A*, vol. 327, no. 2, pp. 117–127, 2002.
- [31] R. A. Andrievskii, A. T. Pak, and I. F. Baiman, "Some features of structure formation and density variation in thermally reactive titanium-boron powder mixtures," *Soviet Powder Metallurgy and Metal Ceramics*, vol. 28, no. 9, pp. 669–671, 1989.
- [32] Y. Hashimoto, S. Ohrnori, and K. Koyama, "Reaction-sintering of Cu-Ti-B alloys," *Journal of the Japan Society of Powder and Powder Metallurgy*, vol. 33, no. 6, pp. 302–305, 1986.
- [33] M. E. Hyman, C. McCullough, J. J. Valencia, C. G. Levi, and R. Mehrabian, "Microstructure evolution in tial alloys with b additions: conventional solidification," *Metallurgical Transactions A*, vol. 20, no. 9, pp. 1847–1859, 1989.
- [34] W. Y. Yang, H. C. Yi, and A. Petric, "Microstructure of the Ti3Al(Nb)/TiB composite produced by combustion synthesis," *Metallurgical and Materials Transactions A*, vol. 26, no. 11, pp. 3037–3043, 1995.
- [35] C. P. Cameron and R. Raj, "Grain-growth transition sintering of colloiddally prepared alumina powder compacts," *Journal of the American Ceramic Society*, vol. 71, no. 12, pp. 1031–1035, 1988.
- [36] R. E. Read-Hill, *Physical Metallurgy Principle*, 1992.
- [37] R. M. German, *Powder Metallurgy Science*, 1984.
- [38] Y. M. Chiang and W. D. Kingery, "Grain-boundary migration in nonstoichiometric solid solutions of magnesium aluminate spinel: I. Grain growth studies," *Journal of the American Ceramic Society*, vol. 72, no. 2, pp. 271–277, 1989.
- [39] T. S. Azatyan, V. M. Mal'tsev, A. G. Merzhanov, and V. A. Seleznev, "Combustion wave propagation mechanism in titanium-boron mixtures," *Combustion, Explosion, and Shock Waves*, vol. 16, no. 2, pp. 163–167, 1980.
- [40] A. A. Zenin, A. G. Merzhanov, and G. A. Nersisyan, "Thermal wave structure in SHS processes, using the example of boron synthesis," *Combustion, Explosion, and Shock Waves*, vol. 17, pp. 63–71, 1931.

Research Article

Synthesis and Characterization of ZnTe Hierarchical Nanostructures

Baohua Zhang, Fuqiang Guo, and Wei Wang

Department of Physics, Changji College, Changji 831100, China

Correspondence should be addressed to Fuqiang Guo, flowerforever@yahoo.cn

Received 20 September 2011; Revised 14 November 2011; Accepted 14 November 2011

Academic Editor: William W. Yu

Copyright © 2012 Baohua Zhang et al. This is an open access article distributed under the Creative Commons Attribution License, which permits unrestricted use, distribution, and reproduction in any medium, provided the original work is properly cited.

Single-crystalline ZnTe hierarchical nanostructures have been successfully synthesized by a simple thermal evaporation technology. The as-prepared products were characterized with X-ray diffraction (XRD), scanning electron microscopy (SEM), transmission electron microscope (TEM), and photoluminescence spectrum (PL). These results showed that the ZnTe hierarchical nanostructures consisted of nanowires and nanolumps. The room temperature PL spectrum exhibited a pure green luminescence centered at 545nm. The growth mechanism of hierarchical nanostructure was also discussed.

1. Introduction

As an important member of groups II–VI semiconductors, ZnTe (band gap 2.26 eV) [1] has attracted much attention due to outstanding optoelectronic and thermoelectric properties [2, 3], and it is now widely used for nanometer-scale electronics and optoelectronics [4–9]. Several methods have been explored to grow ZnTe-based nanostructures [10–12]. Li [13] and coworkers reported that the semiconductor ZnTe nanowire arrays have been synthesized by the pulsed electrochemical deposition from aqueous solutions into porous anodic alumina membranes. Jun [14] and coworkers reported that the synthesis of spherical and rod-like nanocrystals using a single molecular precursor ($[\text{Zn}(\text{TePh})_2][\text{TMEDA}]$). Recently, the synthesis of ZnTe/CdSe core/shell spherical NCs with varied core sizes and shell thicknesses, as well as their widely tuned emission from the visible to near-infrared regions, was reported by Xie' and coworkers [15]. Conversely, ZnTe nanorods were preferentially synthesized using autoclave reactions [16, 17]. Compared with the sample nanostructures, the hierarchical nanostructures have attracted a great deal of attentions over the past few years due to their improved light absorption efficiency and carrier transport. However, the ZnTe with hierarchical nanostructures has not been reported so far.

In this paper, highly crystallized ZnTe hierarchical nanostructures are synthesized on graphite wafers using a simple thermal evaporation technology. The as-prepared samples are characterized by scanning electron microscopy (SEM), transmission electron microscopy (TEM), and X-ray diffraction (XRD). These results showed that the ZnTe hierarchical nanostructures consist of nanowires and nanolumps. The possible growth mechanism has also been discussed.

2. Experimental Section

The thermal evaporation apparatus for sample fabrication is illustrated in Figure 1.

Source materials of high pure ZnTe (99.99%) powder were placed in an alumina boat which is in the heating center of a horizontal alumina tube furnace. After a piece of graphite wafer was cleaned in piranha solution (30% H_2O_2 /20% H_2SO_4) and rinsed with deionized water, it was placed downstream to act as deposition substrates for materials growth. The distance between the graphite substrate and the source material is 15 cm. Prior to heating, the system was evacuated and flushed with high pure Ar for 1 h to eliminate oxygen. Then the furnace was heated to 1000°C in 120 min and held at this temperature for

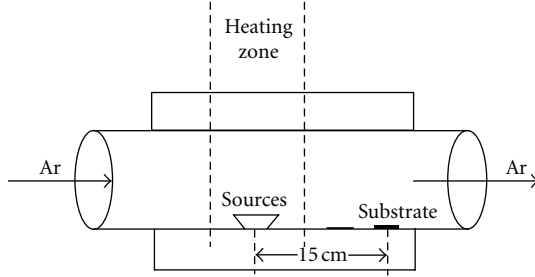


FIGURE 1: Schematic illustration of the furnace used in the experiment.

60 minutes, and subsequently cooled to room temperature under a constant flow rate of 300 SCCM (standard cubic centimeters/minute) Ar.

A Philips XL 30 FEG scanning electron microscope (SEM) with an energy-dispersive X-ray spectroscopy (EDS) was used to observe the morphologies and elemental compositions of the samples. An X-ray diffractometer (XRD) (Japan Mac science) with Cu $K\alpha$ radiation was used to obtain phase compositions of the samples. A JEOL 2010 transmission electron microscope (TEM) with selected-area electron diffraction (SAED) was used to analyze the morphology and microstructure. A Hitachi F-7000FL spectrophotometer was used to measure the room-temperature photoluminescence (PL).

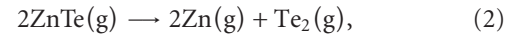
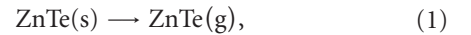
3. Results and Discussion

The large amount of hierarchical nanostructures obtained in such experiments is demonstrated in Figure 2(a). It indicates that high-density nanowires are grown homogeneously on a large area of the graphite wafer. The diameters of the main nanowires range from 300 to 500 nm, and their lengths are in the range of several ten micrometers. The SEM images of the typical 1-fold nanostructure where the nanoparticles grow on one side of the primary nanowires are shown in Figures 2(b) and 2(c). It can be clearly observed that the nanowires are lumpy on the surface, and the nanoparticles have diameter of about 200–1000 nm. The corresponding EDS spectrum inserted in Figure 2(b) indicates that the hierarchical nanostructure is composed of 51% Zn and 49% Te atoms, close to 1:1 stoichiometry of ZnTe. The crystal structure and phase composition of the obtained products were characterized by powder X-ray diffraction (XRD) in Figure 2(d). All the diffraction peaks match well with the standard powder diffraction data (JCPDS no. 65-0385), the four strongest peaks of the product could be indexed to the (111), (200), (220), and (311) planes of the cubic zincblende-structured ZnTe with a lattice constant of $a = 6.10 \text{ \AA}$. XRD diffraction peaks from Te, Zn, or other impurities are not observed in the products.

The morphology and microstructure of the products are further checked using TEM. Figure 3(a) is the morphology TEM image of the lumpy nanowires. It can be seen that

a typical feature of ZnTe hierarchical nanowire consists of nanowires and nanolumps. The nanowires have a diameter of about 200–250 nm, and the height of the “lumpy hills” ranges from 100 to 300 nm. The area marked with 1 and 2 is magnified to get the high-resolution TEM images, as shown in Figures 3(b) and 3(c), respectively. It is shown that both the trunk and the edge have the uniform crystal structure, showing the lattice fringes of the $\{-220\}$ and $\{-1-11\}$ planes with a d spacing of 0.21 nm and 0.35 nm, respectively. Electron diffraction (Figure 3(d)) shows that the growth direction of the ZnTe hierarchical nanowire is $[-220]$.

Vapor-solid (VS) and vapor-liquid-solid (VLS) mechanisms have been widely used to explain the formation of one-dimensional structures [18, 19]. In our work, we considered that the formation of ZnTe hierarchical structures could be explained by the VS mechanism. The process is shown in Figure 4, and four steps are present. Firstly, with the increasing temperature of source, the ZnTe powders start evaporating. Secondly, the Zn and Te_2 gas flows with the Ar carrier gas to the low-temperature area, and react with each other. The ZnTe nanowires grew by means of a self-catalyst vapor solid (VS) mechanism. Thirdly, when the temperature is lower, some ZnTe nanodroplets are formed in the atmosphere and adhered to the surface of newly formed ZnTe nanowires. Finally, Zn and Te_2 vapor species dissolve in ZnTe droplets continually and ZnTe hierarchical structures were obtained. These chemical processes are expressed as (1), (2), and (3):



Room-temperature PL properties of the ZnTe hierarchical structure was also investigated using a He–Cd laser line at 325 nm as the excitation source (Figure 5). Previous reports have shown that the PL properties of ZnTe are sensitive to the morphologies which are influenced by synthetic conditions. For example, Tooru and coworkers reported that PL spectra of ZnTe homoepitaxial layers exhibited a sharp excitonic emission at 2.375 eV [20]. In our experiment, the spectrum exhibits a green emission centered at 545 nm (2.277 eV), which is higher than the band gap of bulk Zinc blende ($E_g = 2.26 \text{ eV}$). We believe that the small blue shift of the PL peak is caused by anti-Stoke’s shift.

4. Conclusion

In summary, ZnTe hierarchical structures were successfully synthesized via a simple thermal evaporation technology. SEM, EDS, and TEM show that the ZnTe hierarchical nanostructures consist of nanowires and nanolumps. Vapor-solid (VS) growth mechanism was proposed for the formation of ZnTe hierarchical structures. Photoluminescence (PL) measurements at room temperature also demonstrate that the synthesized ZnTe hierarchical structures emit a strong

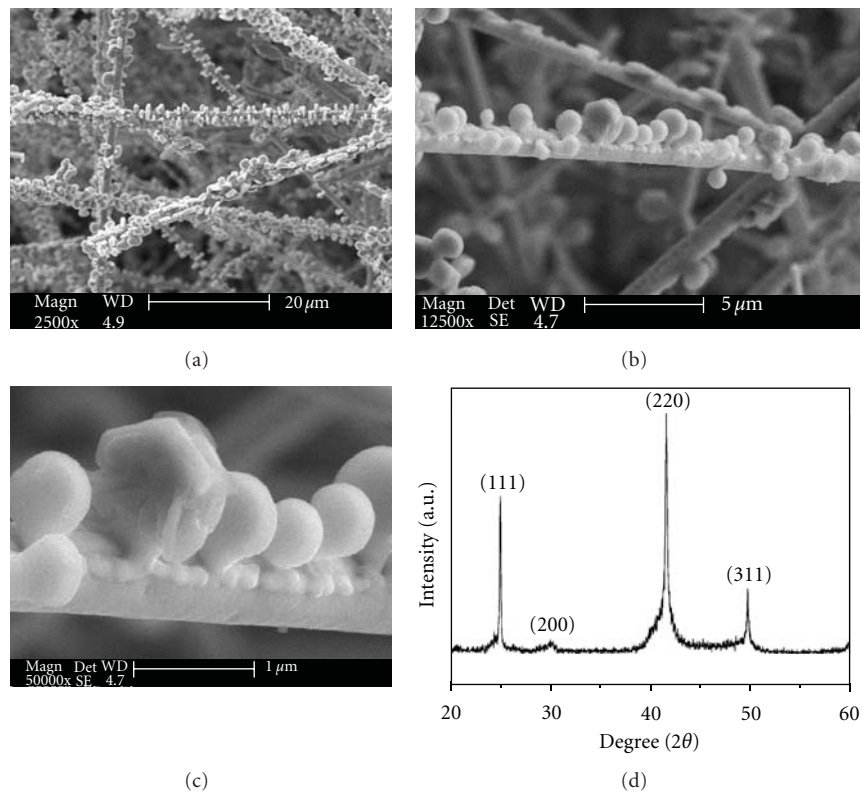


FIGURE 2: Low magnification (a) and high magnification SEM images and corresponding EDS spectrum of the sample (b and c), and XRD spectrum of the sample (d).

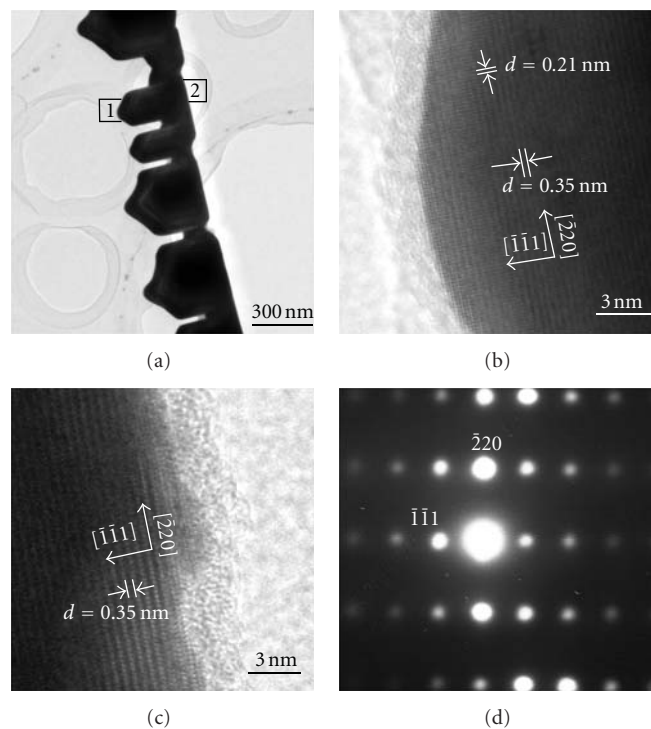


FIGURE 3: TEM image of an individual ZnTe nanowire (a and b), HRTEM image (c), and SAED pattern (d).

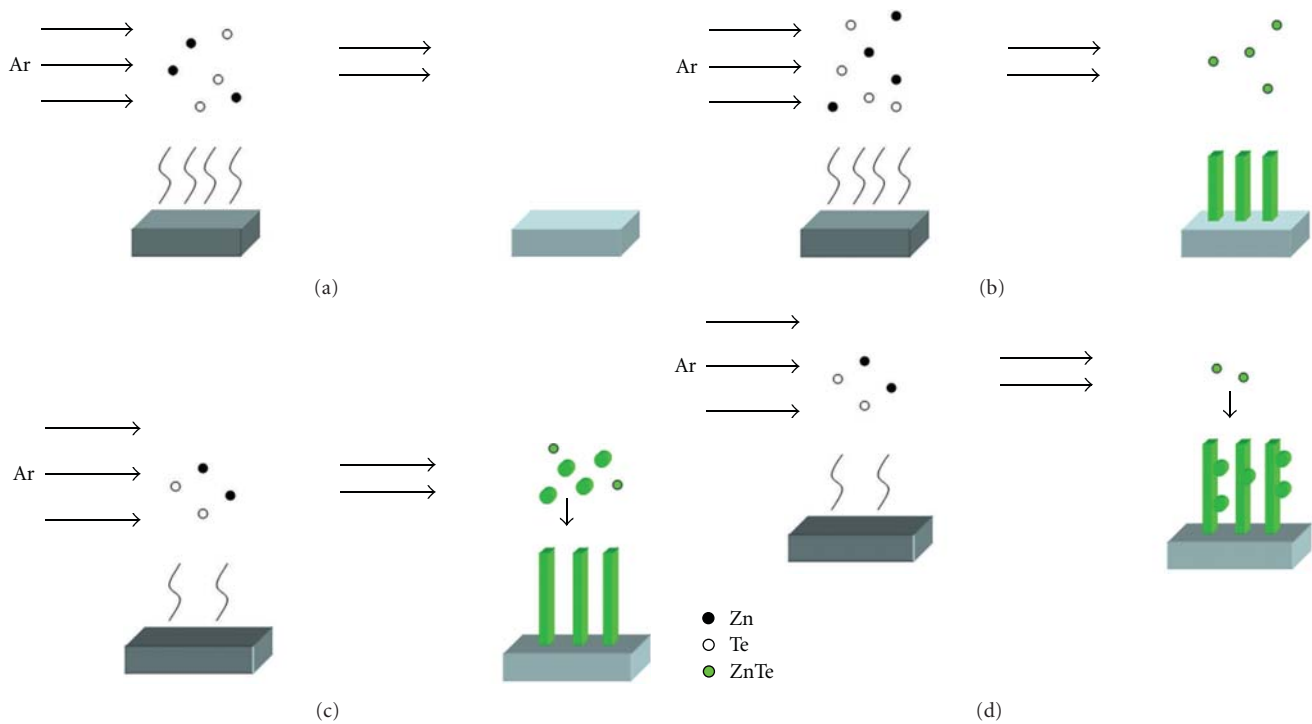


FIGURE 4: Schematic illustration of the formation process of ZnTe hierarchical nanostructures.

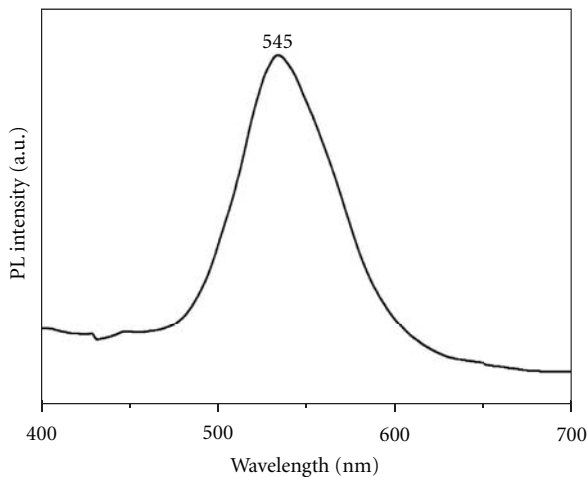


FIGURE 5: PL spectrum of the nanowire arrays at an excitement wavelength of 325 nm.

and stable green light and that their luminescent peak is at about 545 nm.

Acknowledgment

This work is supported financially by Scientific Research Program of the Higher Education Institution of XinJiang (XJEDU2010S46).

References

- [1] K. Yoshino, M. Yoneta, T. Yabe, K. Ohmori, H. Saito, and M. Ohishi, "Optical and electrical characterization of high-quality P-doped ZnTe substrates," *Physica B*, vol. 340–342, pp. 254–257, 2003.
- [2] N. Mingo, "Thermoelectric figure of merit of II-VI semiconductor nanowires," *Applied Physics Letters*, vol. 85, no. 24, pp. 5986–5988, 2004.
- [3] B. Wan, C. Hu, B. Feng, J. Xu, Y. Zhang, and Y. Tian, "Optical properties of ZnTe nanorods synthesized via a facile low-temperature solvothermal route," *Materials Science and Engineering B*, vol. 171, no. 1–3, pp. 11–15, 2010.
- [4] J. A. Zapien, Y. Jiang, X. M. Meng et al., "Room-temperature single nanoribbon lasers," *Applied Physics Letters*, vol. 84, no. 7, pp. 1189–1191, 2004.
- [5] M. S. Gudiksen, L. J. Lauhon, J. Wang, D. C. Smith, and C. M. Lieber, "Growth of nanowire superlattice structures for nanoscale photonics and electronics," *Nature*, vol. 415, no. 6872, pp. 617–620, 2002.
- [6] J. C. Johnson, H. Yan, P. Yang, and R. J. Saykally, "Optical cavity effects in ZnO nanowire lasers and waveguides," *Journal of Physical Chemistry B*, vol. 107, no. 34, pp. 8816–8828, 2003.
- [7] W. Zhou, D. Tang, A. Pan, Q. Zhang, Q. Wan, and B. Zou, "Structure and photoluminescence of pure and indium-doped ZnTe microstructures," *Journal of Physical Chemistry C*, vol. 115, no. 5, pp. 1415–1421, 2011.
- [8] H. Yan, J. Johnson, M. Law et al., "ZnO nanoribbon microcavity lasers," *Advanced Materials*, vol. 15, no. 22, pp. 1907–1911, 2003.
- [9] J. C. Johnson, K. P. Knutsen, H. Yan et al., "Ultrafast carrier dynamics in single ZnO nanowire and nanoribbon lasers," *Nano Letters*, vol. 4, no. 2, pp. 197–204, 2004.

- [10] F. Wang, A. Dong, J. Sun, R. Tang, H. Yu, and W. E. Buhro, "Solution-liquid-solid growth of semiconductor nanowires," *Inorganic Chemistry*, vol. 45, no. 19, pp. 7511–7521, 2006.
- [11] Y. W. Jun, J. E. Koo, and J. Cheon, "One-step synthesis of size tuned zinc selenide quantum dots via a temperature controlled molecular precursor approach," *Chemical Communications*, no. 14, pp. 1243–1244, 2000.
- [12] Y. Xia, P. Yang, Y. Sun et al., "One-dimensional nanostructures: synthesis, characterization, and applications," *Advanced Materials*, vol. 15, no. 5, pp. 353–389, 2003.
- [13] L. Li, Y. Yang, X. Huang, G. Li, and L. Zhang, "Fabrication and characterization of single-crystalline ZnTe nanowire arrays," *Journal of Physical Chemistry B*, vol. 109, no. 25, pp. 12394–12398, 2005.
- [14] Y. W. Jun, C. S. Choi, and J. Cheon, "Size and shape controlled ZnTe nanocrystals with quantum confinement effect," *Chemical Communications*, no. 1, pp. 101–102, 2001.
- [15] R. Xie, X. Zhong, and T. Basche, "Synthesis, characterization, and spectroscopy of type-II core/shell semiconductor nanocrystals with ZnTe cores," *Advanced Materials*, vol. 17, no. 22, pp. 2741–2745, 2005.
- [16] Y. Li, Y. Ding, and Z. Wang, "A novel chemical route to ZnTe semiconductor nanorods," *Advanced Materials*, vol. 11, no. 10, pp. 847–850, 1999.
- [17] J. Du, L. Xu, G. Zou, L. Chai, and Y. Qian, "Solvothermal synthesis of single crystalline ZnTe nanorod bundles in a mixed solvent of ethylenediamine and hydrazine hydrate," *Journal of Crystal Growth*, vol. 291, no. 1, pp. 183–186, 2006.
- [18] R. S. Wagner and W. C. Ellis, "Vapor-liquid-solid mechanism of single crystal growth," *Applied Physics Letters*, vol. 4, no. 5, pp. 89–90, 1964.
- [19] X. Duan and C. M. Lieber, "Laser-assisted catalytic growth of single crystal GaN nanowires," *Journal of the American Chemical Society*, vol. 122, no. 1, pp. 188–189, 2000.
- [20] T. Tanaka, K. Hayashida, S. Wang, Q. Guo, M. Nishio, and H. Ogawa, "Photoluminescence properties of ZnTe homoepitaxial layers grown by synchrotron-radiation-excited growth using nitrogen carrier gas," *Nuclear Instruments and Methods in Physics Research, Section B*, vol. 199, pp. 356–360, 2003.

Research Article

Synthesis of CdSe/ZnS and CdTe/ZnS Quantum Dots: Refined Digestive Ripening

Sreeram Cingarapu,¹ Zhiqiang Yang,² Christopher M. Sorensen,³ and Kenneth J. Klabunde¹

¹Department of Chemistry, Kansas State University, Manhattan, KS 66506, USA

²Department of Chemistry, Clemson University, Clemson, SC 29634, USA

³Department of Physics, Kansas State University, Manhattan, KS 66506, USA

Correspondence should be addressed to Kenneth J. Klabunde, kenjk@ksu.edu

Received 27 September 2011; Accepted 4 November 2011

Academic Editor: Bo Zou

Copyright © 2012 Sreeram Cingarapu et al. This is an open access article distributed under the Creative Commons Attribution License, which permits unrestricted use, distribution, and reproduction in any medium, provided the original work is properly cited.

We report synthesis of CdSe and CdTe quantum dots (QDs) from the bulk CdSe and CdTe material by evaporation/co-condensation using the solvated metal atom dispersion (SMAD) technique and refined digestive ripening. The outcomes of this new process are (1) the reduction of digestive ripening time by employing ligands (trioctylphosphine oxide (TOPO) and oleylamine (OA)) as capping agent as well as digestive ripening solvent, (2) ability to tune the photoluminescence (PL) from 410 nm to 670 nm, (3) demonstrate the ability of SMAD synthesis technique for other semiconductors (CdTe), (4) direct comparison of CdSe QDs growth with CdTe QDs growth based on digestive ripening times, and (5) enhanced PL quantum yield (QY) of CdSe QDs and CdTe QDs upon covering with a ZnS shell. Further, the merit of this synthesis is the use of bulk CdSe and CdTe as the starting materials, which avoids usage of toxic organometallic compounds, eliminates the hot injection procedure, and size selective precipitation processes. It also allows the possibility of scale up. These QDs were characterized by UV-vis, photoluminescence (PL), transmission electron microscopy (TEM), high-resolution transmission electron microscopy (HRTEM), X-ray photoelectron spectroscopy (XPS), and powder XRD.

1. Introduction

The solvated metal atom dispersion (SMAD) technique allows the synthesis of nanomaterial from the bulk material by vaporization and cocondensation [1–8]. The as-prepared poly-dispersed SMAD colloid products were made monodispersed in size by a unique process known as digestive ripening [9]. Digestive ripening involves the heating of polydispersed colloidal material at or near the boiling point (BP) of solvent in the presence of excess surface active ligand [1–11]. In the present work, we employed trioctylphosphine oxide (TOPO) and oleylamine (OA), which served both as capping agent as well as digestive ripening solvent. The general procedure for the synthesis of high-quality crystalline II-VI semiconductor material is by the hot injection method, where cadmium precursor $(\text{CH}_3)_2\text{Cd}$ or CdO is dissolved in coordination ligands like trioctylphosphine oxide, hexylphosphonic acid, or tetradecylphosphonic acids,

and then the selenium precursor (Se dissolved in TOP) quickly injected into the hot coordination reaction mixture, which initiated the nucleation process, and subsequent growth was carried out at a relatively lower temperature, and this process was initially reported by Murray et al. [12], and later, Peng et al. and Talapin et al. have developed the hot injection procedure [13–19]. One of the advancements in this process was selecting an injection temperature and a growth temperature. This high reaction temperature (>150–350°C) facilitates the removal of crystalline defects and allows enhancement in the photoluminescence. In semiconductor QDs, high emission efficiency from a band-edge state is required especially when these are used in lasers or imaging. In general, a high band gap inorganic material coating over the QD core has been proven to enhance the QY by passivating surface nonradiative recombination sites. Typically, II-VI semiconductor QDs are covered with a high band gap ZnS shell, which was initially developed

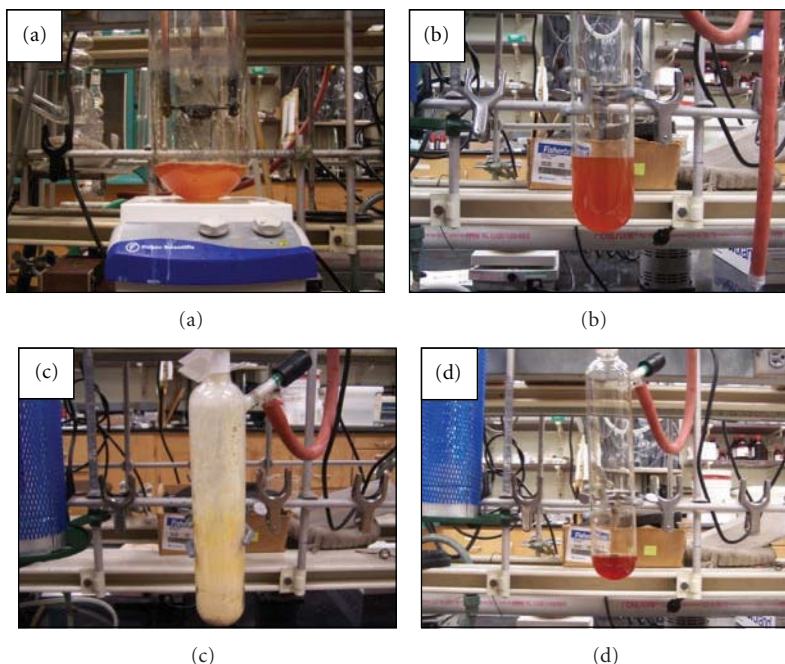


FIGURE 1: (a) as-prepared SMAD CdSe-THF-TOPO-OA colloidal solution after vigorous stirring for a period of 45 minutes (b) as-prepared siphoned CdSe-THF-TOPO-OA colloidal solution (c) semi-solid CdSe-TOPO-OA after complete vacuum evaporation of THF solvent (d) CdSe-TOPO-OA colloid after gentle warming.

by Hines and Guyot-Sionnest [20]. These two methods (hot injection and ZnS shell covering) have been widely used to achieve narrow-size particle distribution and enhance QY. In addition to the above method, other routes like layer by layer ZnS passivation [21], CO₂ gas-expanded liquids [22], surface treatments with polymers [23], and sonochemical processes [24] were used. In the current work, we adopted the sonochemical procedure for the growth of ZnS shell over CdSe and CdTe QD core.

2. Experimental Section

2.1. Chemicals. Bulk cadmium selenide (CdSe) and bulk cadmium telluride (CdTe) (99.9%, Strem Chemicals Inc), oleylamine (98%) from ACROS Organic chemicals, trioctylphosphine oxide (TOPO) (Reagent Plus 99%), trioctylphosphine (TOP), tributyl phosphine (PBU₃), zinc nitrate hexahydrate, and potassium ethylxanthate were purchased from Sigma-Aldrich and used without further purification. Tetrahydrofuran (THF), acetone, and methanol were purchased from Fisher Scientific. Tetrahydrofuran solvents were distilled and degassed four times by the standard freeze-thaw procedure prior to use. Oleyl amine was purged with argon for 2 hrs prior to use.

2.2. Synthesis of as-Prepared SMAD Colloid. A stationary reactor [25] was used for the evaporation and cocondensation of bulk CdSe or CdTe. Briefly, 1 g of either bulk CdSe or bulk CdTe was evaporated using water cooled copper electrodes and the generated heat during the evaporation was

dissipated by water cooled copper electrodes and insulating packing material (Zircar product, Inc.) around the crucible and metal basket. The optimum temperature required for the evaporation of bulk CdSe is $\sim 900^\circ\text{C}$, whereas, for bulk CdTe, it is less than 900°C . Initially the bulk material was charged in C9 boron nitride crucible (R.D. Mathis # C9-BN) resting in a metal basket (R. D. Mathis # B8B # x.030 w), and the ligands were placed at the bottom of the SMAD reactor and the entire setup was then vacuum sealed. After complete evacuation, a liquid N₂ Dewar was placed around the sealed SMAD reactor. Once the vacuum attains 4×10^{-3} torr, initially 50 mL of distilled and degassed THF was evaporated through a solvent shower head, which was inserted into the reactor. The evaporated solvent was condensed on the wall of SMAD reactor by external liquid nitrogen cooling. After the formation of condensed solvent matrix on the walls, the metal crucible was heated by water cooled copper electrode, and the heat was ramped slowly and the evaporated material was cocondensed along with the solvent on to the walls of reactor. Cocondensation of evaporate material along with the solvent restricts aggregation and allows formation of small crystallites. It took nearly 3 hrs for the complete evaporation of 1 g of bulk material. The frozen matrix appears reddish brown (Figure 1). Upon warming up of the frozen matrix with a heat gun, the matrix melts and slowly reaches the bottom of the reactor and mixes well with the coordinating ligands (TOPO with OA). To ensure homogeneous colloid formation, the system was vigorously stirred for 45 minutes with a magnetic stirrer. Figure 1(a) shows the as-prepared CdSe-THF-TOPO-OA colloidal solution after vigorous stirring. The as-prepared SMAD product was then siphoned

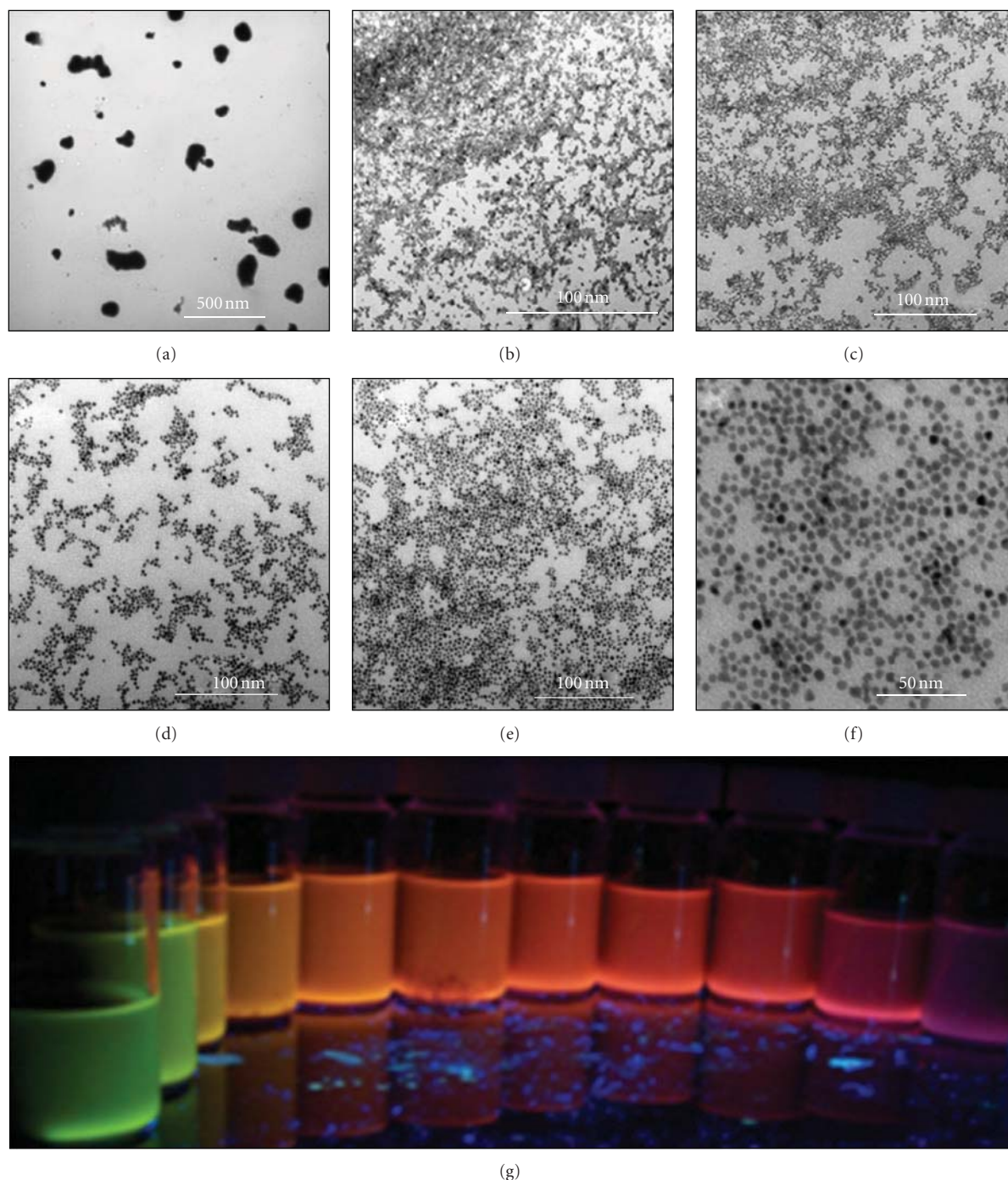


FIGURE 2: The TEM images of (a) as-prepared SMAD product, (b) after 10 min (c) after 20 min and (d) after 40 min of digestive ripening. (e) after 60 min, and (f) after 90 min of digestive ripening (g) CdSe QDS samples collected at various intervals of digestive ripening time upon exposure to UV-Vis illuminator.

into a Schlenk glass tube under the protection of argon (Figure 1(b)). Safety and cleanliness: prior to synthesis, the SMAD reactor was cleaned with aqua regia, base bath, acid bath, and finally with copious amount of water. While working with vacuum lines it's a must to wear protective eye glasses. Both CdSe and CdTe are carcinogenic so, proper protection is necessary while handling these chemicals. Also, the acid and base bath used in cleaning may cause severe

burns, so proper acid proof gloves and protecting clothing are necessary.

2.3. Preparation of CdSe-TOPO-OA Colloid. The THF from the as-prepared CdSe-THF-TOPO-OA colloidal solution was vacuum evaporated, leaving a THF solvent free semisolid CdSe-TOPO-OA colloid (Figure 1(c)). Upon gentle warming, CdSe-TOPO-OA colloid was obtained (Figure 1(d)).

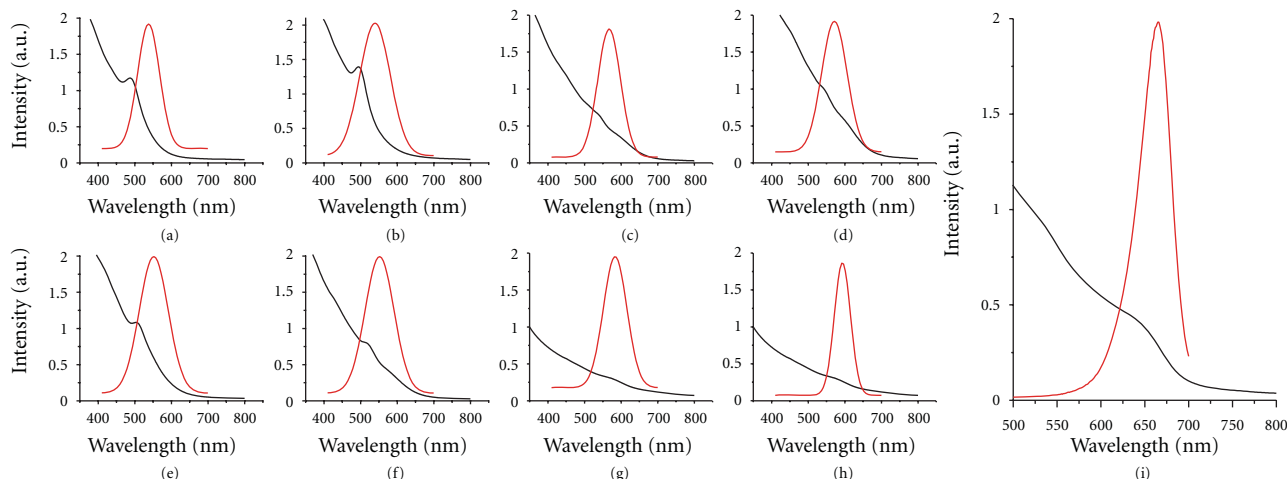


FIGURE 3: (a)–(i) UV-vis absorption spectra and corresponding PL of CdSe QD samples collected at 10, 20, 30, 40, 50, 60, 70, 80, and 90 minutes of digestive ripening.

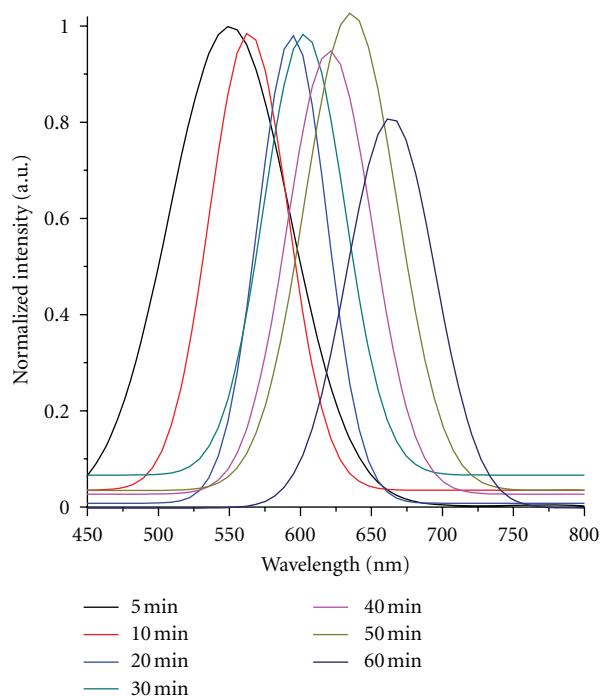


FIGURE 4: Photoluminescence spectrum of CdTe QD samples collected at 5, 10, 20, 30, 40, 50, and 60 minutes of digestive ripening.

This as-prepared product was then subjected to digestive ripening. The same procedure was adopted for the synthesis of the as-prepared CdTe-TOPO-OA system.

2.4. Refined Digestive Ripening. Digestive ripening is the key step for the formation of quasimonodispersed core QDs. In previous work, we used toluene and *t*-butyl toluene as a digestive ripening solvent for the CdSe-TOPO-HDA system. However, for the current work TOPO and OA were used as digestive ripening solvent, as well as capping ligands.

2.5. ZnS Shell Formation on Core Quantum Dots. ZnS shell formation over a core QD (CdSe or CdTe) was carried out by a reported sonochemical procedure using zinc ethylxanthate as precursor [24, 26]. In a typical ZnS shell growth, aliquots (5 mL) of freshly synthesized core QDs were placed in a reaction vessel and then it was placed in 100 W sonicator (Fisher Scientifics), to which freshly prepared zinc ethylxanthate (0.15 g) in tributylphosphine (3 mL) (PBu_3) solution was mixed when the sonication temperature was 60°C . The sonication was continued until the temperature of the reaction mixture reached to 120°C to ensure complete passivation of the QD core with the ZnS shell. During this process, aliquots of reaction mixture were collected to monitor the shell growth and no purification steps were involved on the core solution before use. Isolation of core-shell QDs was carried out by precipitation with anhydrous methanol, followed by washing with acetone and methanol. This process was repeated to remove any unreacted zinc ethylxanthate and excess ligands. The core-shell QDs were then vacuum dried and redispersed in toluene for transmission electron microscope (TEM) sample preparation. No size selective precipitation step was carried out. The yield of core QDs is about ~ 78 – 80% .

3. Characterization

3.1. UV-vis Spectroscopy. UV-vis absorption spectra were obtained using an in situ UV-vis optical fiber, assisted by a DH-2000 UV-vis optical spectrophotometer instrument (Ocean Optics Inc) for core QDs. The absorption spectra of core-shell QDs were obtained using a Cary 500 Scan UV-vis-NIR spectrophotometer. All samples were washed with absolute ethanol, acetone, and were dried under vacuum. The dried samples were then redissolved in toluene for analysis.

3.2. Photoluminescence Spectroscopy. Fluorescence spectra of both core QDs (CdSe and CdTe) and core-shell QDs (CdSe-ZnS and CdTe-ZnS) were measured by using a Fluoro Max-2

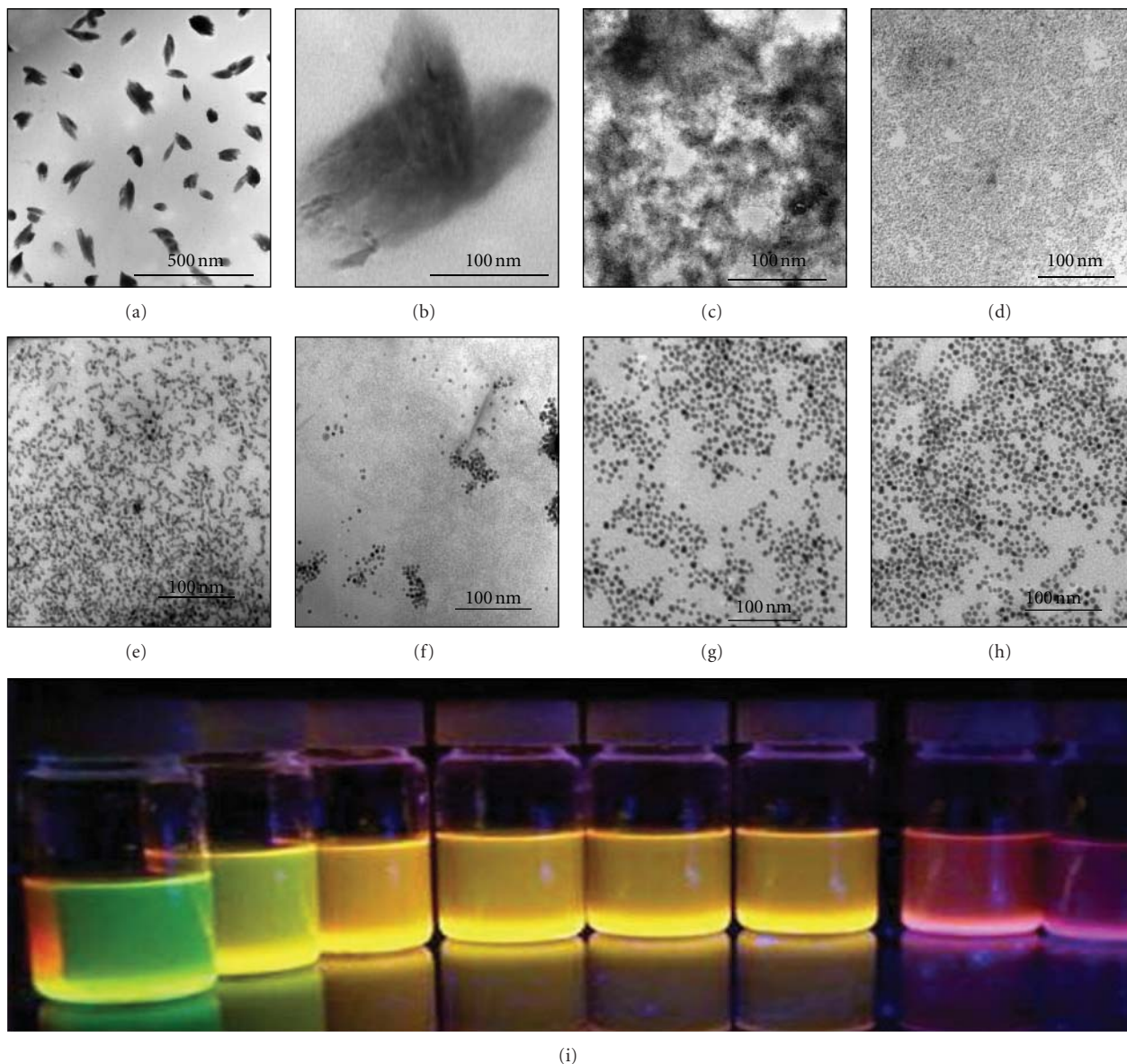


FIGURE 5: TEM images of CdTe QDs, (a, b) as-prepared SMAD product before digestive ripening, (c) after 10 min of digestive ripening, (d) after 20 min, (e) after 30 min (f) after 40 min of digestive ripening, (g) after 50 min and (h) after 60 min of digestive ripening, (i) samples collected at various intervals of digestive ripening time under UV-vis illuminator.

instrument from HORIBA Jobin Yvon Company. These samples were all excited at 400 nm. Photoluminescence quantum yields (QY) value (Φ_{em}) of QDs (CdSe and CdTe) and core-shell QDs (CdSe-ZnS and CdTe-ZnS) were measured relative to Rhodamine 6G in methanol, assuming its PL QYs as 95% [27, 28], and the % yield were calculated by using (1).

$$\Phi_{em} = \Phi_S \left(\frac{I}{IS} \right) \left(\frac{AS}{A} \right) \left(\frac{n_2}{n_1 S_2} \right). \quad (1)$$

In 1, I (sample) and IS (standard) are the integrated emission peak areas, up to 480 nm excitation. A (sample) and AS (standard) are the absorption (<0.1) at 480 nm; n (sample) and nS (standard) are the refractive indices of the solvents;

and the Φ_{em} and Φ_S are the PL QYs for the sample and the standard, respectively.

3.3. Transmission Electron Microscopy (TEM). TEM Studies were Performed on a Philips CM100 operating at 100 kV. The TEM Samples were Prepared by placing a few micro liters of precipitated, washed, vacuum dried and redissolved sample in toluene onto a carbon-coated formvar copper grid and the grids were allowed to dry overnight.

3.4. High Resolution Transmission Electron Microscopy/Energy Dispersive X-Ray Spectroscopy. High-resolution images were performed with a FEI Tecnai F20 XT field emission transmission electron microscopy operated at 300 kV. The energy

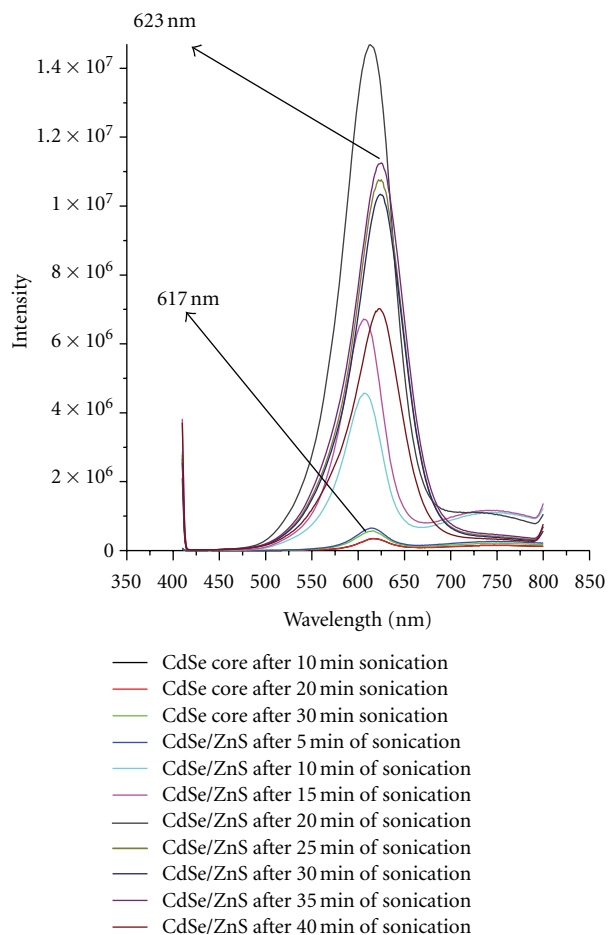


FIGURE 6: Shell coating on digestively ripened CdSe QDs. The broad emission band from 625–700 nm wavelength in core CdSe QDs is due to surface traps. But upon ZnS shell growth, the emission due to surface traps was reduced and simultaneously enhanced PL can be seen. The PL shift from 540 nm to 545 nm and then to 555 nm indicates the growth of shell material on the CdSe Core.

dispersive X-ray (EDX) analysis was carried out in a scanning electron microscope (SEM) mode, which is an integral part of FEI Tecnai F20 XT. The experimental conditions are as follow: energy resolution: 134 eV, reference energy: 5.9 keV, minimum energy: 100 eV, detector thickness: 3 mm, detector distance: 11.8 mm, and detector angle: 14.6°. The facilities were provided by the Microscopy and Analytical Imaging Laboratory at the University of Kansas. Washing procedures were the same as described above. However, a Lacey-carbon-coated TEM grid was used.

3.5. Powder X-Ray Diffraction (PXRD). Powder X-ray diffraction patterns were recorded by a Bruker D8 X-ray diffractometer with $\text{CuK}\alpha$ radiation. PXRD samples were prepared by the evaporation of toluene from the core or core-shell QDs/toluene dispersion loaded on XRD glass plates. The samples were scanned from $20 < 2\theta < 80^\circ$ at an increment of $0.01^\circ/\text{min}$, and the total acquisition time period was more than 7 hrs.

3.6. X-Ray Photoelectron Spectroscopy. XPS data were collected on a Kratos Axis 165 X-ray photoelectron spectrometer operating in the hybrid mode using $\text{Al K}\alpha$ (1486.6 eV) radiation at 300 W. Charge neutralization was used to minimize sample charging, and the charge neutralizer settings were 2.0 amps, 1.7 V charge balance, and 1.1 V bias. Survey spectra were collected with pass energy of 160 eV, while high-resolution spectra were collected with a pass energy of 20 eV. Peak fitting was performed using CASA XPS software, using peaks with a 50% Gaussian, and 50% Lorentzian line shape on a Shirley background. The facilities were provided by the shared experimental facilities (SEF) at the University of Maryland.

4. Results and Discussion

4.1. Cadmium Selenide-Oleylamine-Trioctylphosphine Oxide.

The as-prepared SMAD product generally yields polydispersed colloid material due to little control over the particle size during vaporization and cocondensation [1, 2, 5–7]. In previous work [1], we reported synthesis of CdSe QD from bulk by vaporization/cocondensation, followed by digestive ripening in toluene for 24 hrs and 16 hrs in *t*-butyl toluene. In the current refined digestive ripening, we used TOPO and OA in 30:20 ratio to the bulk starting material, which act as both digestive ripening solvent as well as capping agent. The as-prepared CdSe-TOPO-OA-THF (Figure 1(a)) colloid material is a homogeneous single phase. In order to obtain CdSe-TOPO-OA colloid, the THF solvent was vacuum evaporated resulting a semisolid CdSe-TOPO-OA (Figure 1(b)) and the semi-solid nature (Figure 1(c)) of the CdSe-TOPO-OA can be explained by the fact that TOPO exists as a solid at room temperature, whereas OA is liquid. The yield of CdSe QD is nearly $\sim 80\%$ with variations in batch to batch synthesis and the 20% loss was due to either condensation of vaporized material onto copper electrodes, or possibly to losses in handling. In this work, we also employed OA as a solvent, as others have done [15, 29]. Compared to TOPO, OA is a weaker ligand and binds less strongly to the CdSe, and thereby affects the growth process [27, 30]. The as-prepared CdSe exhibited a broad fluorescence, but within 90 minutes of digestive ripening, the PL becomes sharper and can be tuned to 670 nm. The reduction of digestive ripening time is attributed to the higher boiling point of these ligands/Solvents. The poor-fluorescence behavior of the as-prepared CdSe is due to aggregation of small crystallites, which is evident from the TEM image (Figure 2(a)).

During digestive ripening these aggregates of small crystallites (Figure 2(a)), breakdown completely to form small particles (Figure 2(b)) and grow into quasimonodispersed particles (Figure 2(b)–2(f)), Figure 2(g) is the samples (collected at various intervals of digestive ripening time) under UV-vis illuminator.

It is important to note that in digestive ripening bigger particles will break down into smaller particles and the smaller particles will tend to grow bigger and finally the system will reach a thermodynamic equilibrium size, and

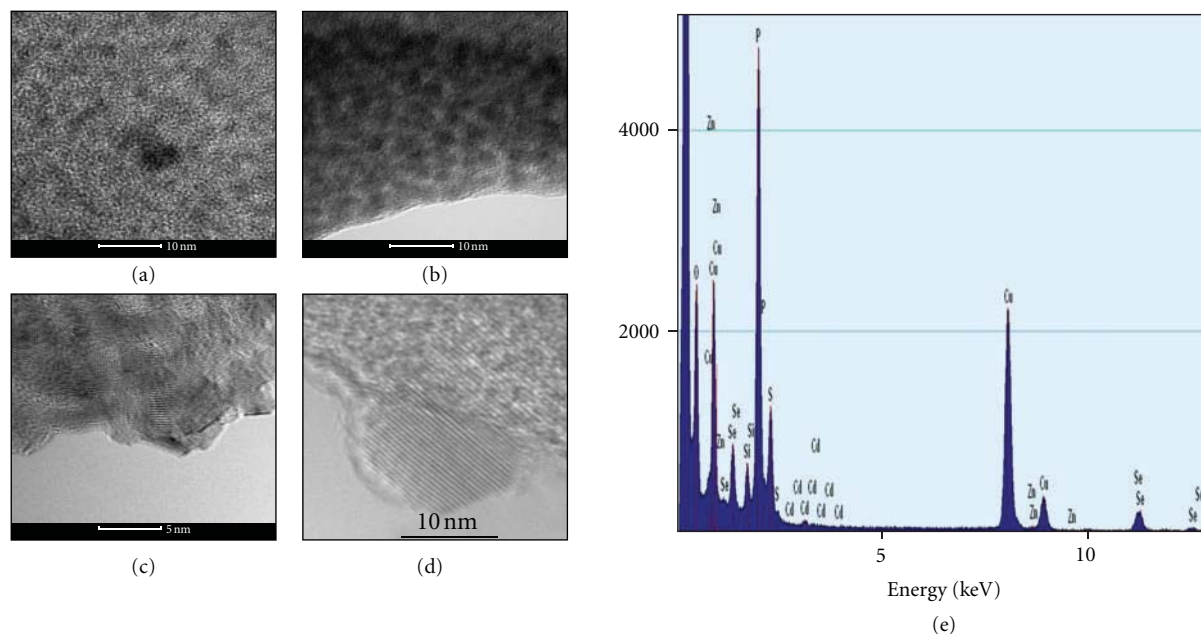


FIGURE 7: (a)–(b) HRTEM image of CdSe QD obtained after 30 and 90 minutes of digestive ripening, (c–d) CdSe/ZnS Core-Shell QDs showing the crystalline lattice and (e) energy dispersion spectroscopy (EDX) spectrum of CdSe-ZnS core-shell QDs showing characteristic peaks of cadmium, selenide, zinc and sulfur. Copper is from the lacy-carbon-coated copper TEM grid.

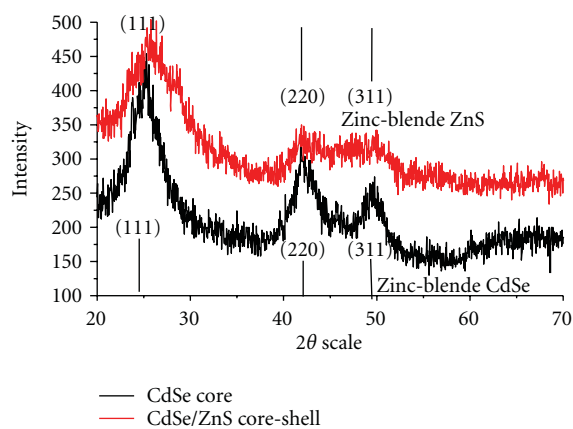


FIGURE 8: The XRD patterns of CdSe (black lines) showing the characteristic features of zinc blend crystalline structure and CdSe/ZnS (red lines) showing the characteristic features of zinc blend structure, and the vertical bars (bottom) correspond to JCPDS file No. 77–2100 and (top) JCPDS file No. 19–0191.

the PL data of CdSe can be correlated with the digestive ripening phenomenon. With digestive ripening time, the UV-Vis spectra shifts to longer wavelength and the PL peaks sharpen (Figure 3(a)–3(i)) indicating the formation of quantum confined quasimonodispersed quantum dots. A more description about digestive ripening phenomenon can be found in latest review article and the reference therein [31].

4.2. *Cadmium Telluride–Oleylamine–Trioctyl Phosphine Oxide*. In case of CdTe, a similar trend was observed where;

the as-prepared SMAD product has broad fluorescence peak but upon digestive ripening the fluorescence peak narrows and shifts in wavelength. Under similar (250°C) digestive ripening temperature, the PL of CdTe can be tuned to 667 nm but compared to CdSe it took only 60 minutes. The as-prepared SMAD product is light yellow and turns brighter yellow color, then red and finally to dark red, which indicates rapid breakdown of aggregated crystallites and dramatic growth of CdTe nanocrystals in the first 30 minutes of digestive ripening. After 30 minutes, the growth rate decreased, indicating the formation of larger particles. Figure 4 shows the PL of CdTe QDs with the progress of digestive ripening time. As observed with CdSe, CdTe also reaches an equilibrium size; where the initial FWHM was broad but as digestive ripening time progresses the FWHM has narrowed.

Figure 5(a) shows the as-prepared SMAD product TEM images. Note the aggregated small crystallites in Figure 5(b), but upon digestive ripening, these aggregates breakdown into smaller particles and then grow in size (Figure 5(c)–5(h)). Figure 5(i) shows the corresponding samples collected at various time intervals from the same batch and these samples were exposed to the UV-Vis illuminator.

4.3. *Cadmium Selenide Core–Zinc Sulfide Shell QDs*. Over coating of semiconductor QDs with a high band gap inorganic material enhances the photoluminescence QY by passivating surface recombination sites [20]. Surface coating not only protects the core nanomaterial from photooxidation but also from physical and chemical stress. The evolution of the PL from the CdSe-ZnS is depicted in Figure 6. It is clearly shown that the PL peak becomes sharp and the red

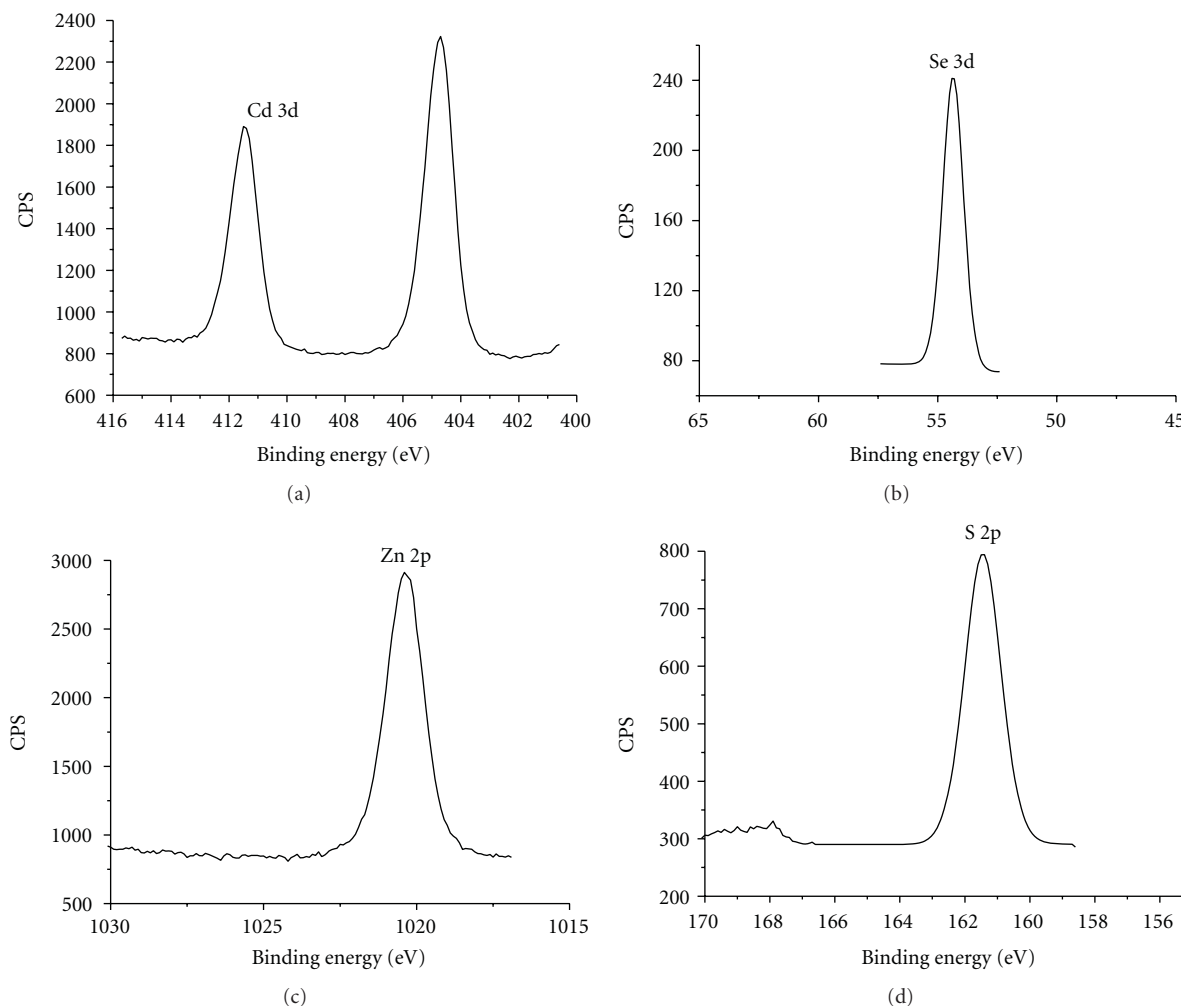


FIGURE 9: (a) XPS spectra of Cd, (b) Se, (c) Zn, and (d) S binding energy (eV) of CdSe-ZnS QDs, respectively.

shift is due to the further growth in the shell thickness. The initial broadening in PL is obviously from the growth of shell material, which is due to increase in particle size and further shell growth resulting in a red-shift (from 568 nm to 577 nm) of PL [32].

Figure 7 is the HRTEM images of (a-b) CdSe and (c-d) CdSe/ZnS core shell quantum dots. The lattice mismatch between the CdSe and ZnS is 12%, and resolving this by using TEM is challenging [28, 32–34], but by measuring the average particle size on the HRTEM images of core, and by subtracting the average particle size measured on the HRTEM images of the core-shell will give an estimated shell thickness.

The average diameter of particle size measured on HRTEM image of CdSe/ZnS core-shell (Figure 7(b)) is 4.8 nm and the average diameter measured on the core (Figure 7(a)) is 3.6 nm. Therefore, the average shell thickness on these particles is 1.2 nm. Core-shell QDs were also characterized by energy dispersion spectroscopy (EDX) as show in Figure 7(e), and the EDX measurements were recorded in the scanning transmission electron microscopy (STEM) mode, which shows both core and shell material.

After ZnS shell growth, the XRD patterns of CdSe core were slightly shifted to higher 2-theta angle (Figure 8), which supports the formation of ZnS shell over the CdSe core. Further, broadening in XRD patterns represents the finite crystalline size of the core. It is interesting to note that in our previous study, when lower boiling point solvents (toluene (BP 110°C), t-butyl toluene (BP 190°C)) were used to digest as-prepared SMAD product, the particles retain the crystalline nature of the bulk starting material, that is, wurtzite (hexagonal) crystalline structure [1].

However, when digestive ripening was carried out at an elevated temperature (250°C) in presence of phosphine and amine ligands, the particles attained a zinc blend (cubic) crystal structure. This transformation is most likely due to the reduction in growth rate [35] in presence of amine ligand [36]. Further, at elevated temperature, the crystalline defects are minimized resulting in enhanced quantum yield. Addition of inorganic high bang gap ZnS shell further enhanced the quantum yield from 36% to 60%.

It is also important to note that when toluene was used as digestive ripening solvent, the measured QY was 11% and

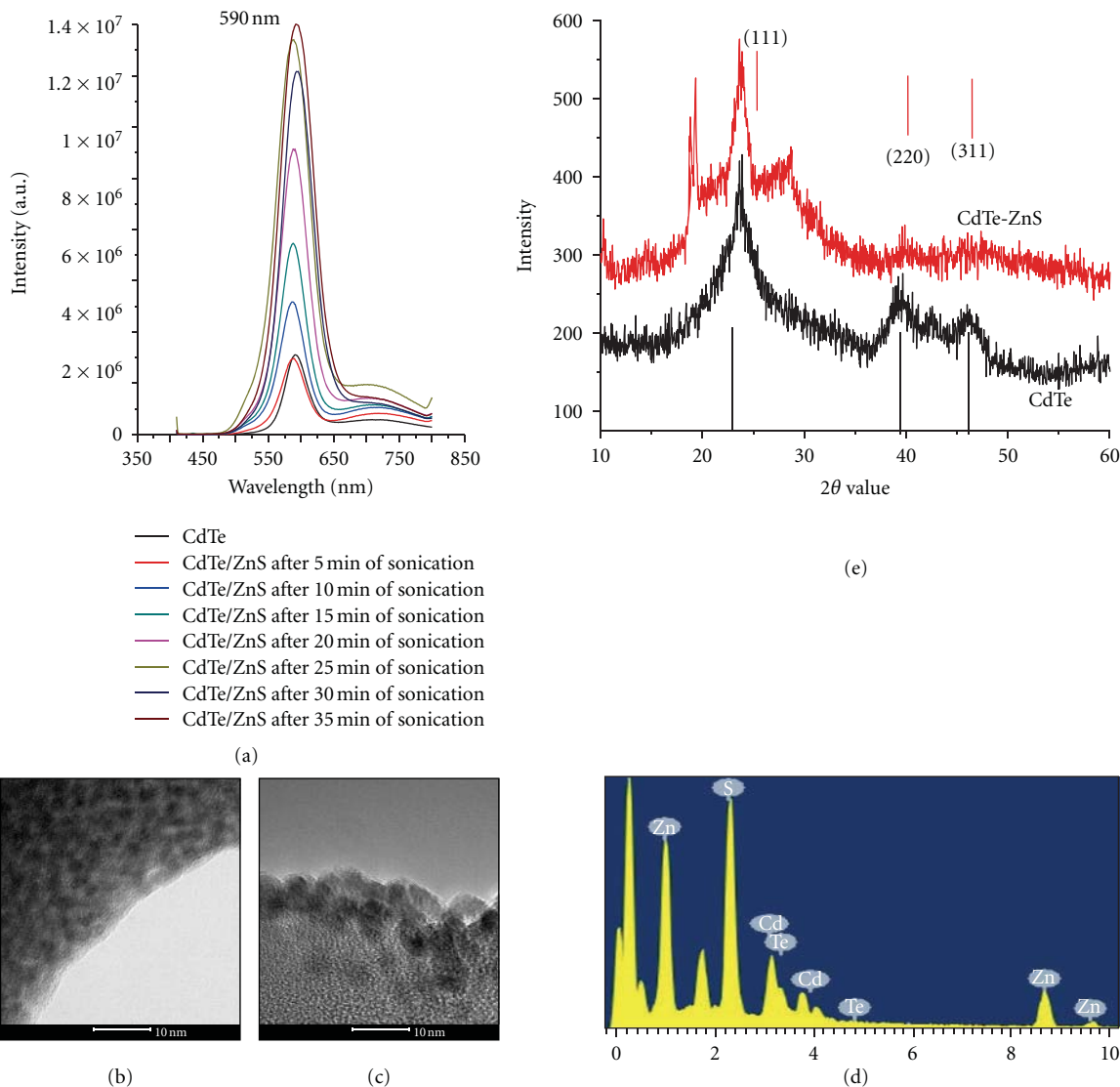


FIGURE 10: (a) Photoluminescence spectrum of CdTe/ZnS shell with sonication time, (b) HRTEM image of CdTeQDs after 30 min of digestive ripening, (c) after ZnS shell, (d) the characteristic zinc blend planes of 111, 220, and 311 locating at 24.40° , 41.60° , and 47.90° for CdTe core and at 24.94° , 41.72° , and 48.76° for CdTe/ZnS in the $10\text{--}60^\circ$ 2θ range and (e) the energy dispersive X-ray spectroscopy (EDS) measurement showing the existence of cadmium, tellurium, zinc and sulfur.

a 28% QY was achieved with t-butyltoluene [1]. With the higher digestive ripening temperature, the higher QY must be due to removal of crystalline defects. The HRTEM images (Figure 7) do show that the particles have good crystalline nature of both core and core-shell particles.

Surface composition of CdSe and CdSe/ZnS QDs was investigated with XPS. In Figure 9(a), the two strong peaks located at 405.2 and 412 eV correspond to Cd 3d binding energy of CdSe, and the peak at 54.3 eV in Figure 9(b), corresponds to Se 3d binding energy of CdSe [28, 37]. The XPS spectrum of CdSe/ZnS core/shell NCs shows typical peaks for ZnS, with Zn $2p_{3/2}$ and S $2p_{3/2}$ located at 1022 (Figure 9(c)) and 161.5 eV (Figure 9(d)), respectively. Based on XPS data, the growth of ZnS shell on CdSe core is confirmed.

4.4. Cadmium Telluride Core–Zinc Sulfide Shell QDs.

Figure 10(a) is the PL of the CdTe/ZnS core shell. The measured QY of CdTe and CdTe/ZnS is 38% and 60% respectively. The lattice parameters for CdTe $c = 6.477 \text{ \AA}$ and for ZnS $c = 6.257 \text{ \AA}$ [38] and the lattice mismatch CdTe core and ZnS shell are 19.8% [38]. Figure 10(b) and 10(c) are the HRTEM image of CdTe QDs before and after addition of ZnS shell. In order to confirm the formation of ZnS shell on CdTe, energy dispersive X-ray spectroscopy (EDX) and the powder XRD measurements were made. The EDX spectrum in Figure 10(d) shows the existence of Te, Cd, Zn, and S in the CdTe/ZnS sample. The sulfur peak at 2.3 keV and the Zn peak at 8.9 keV in EDX spectrum indicate the existence of a ZnS shell layer on the CdTe core. These results of the EDX spectrum further confirm the formation of the core/shell QDs.

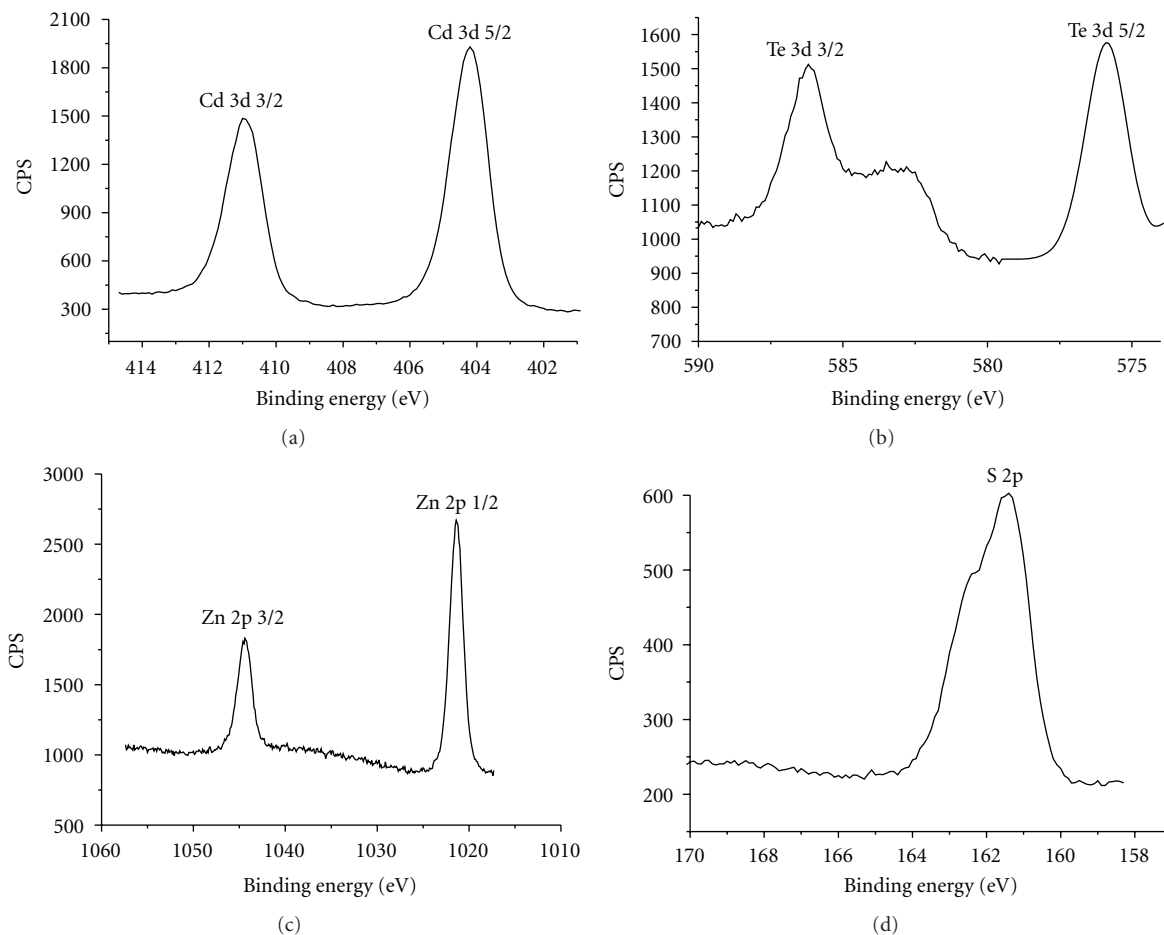


FIGURE 11: (a) XPS spectra of Cd, (b) Te, (c) Zn, and, (d) S-binding energy (eV) of CdTe-ZnS QDs, respectively.

The powder XRD patterns of CdTe and CdTe/ZnS core shell are shown in Figure 10(e). The characteristic zinc blend planes of 111, 220, and 311 located at 24.40° , 41.60° , and 47.90° for CdTe core and at 24.94° , 41.72° , and 48.76° for CdTe/ZnS in $10\text{--}60^\circ$ 2θ range are observed. The position of the XRD peaks of CdTe cores matched well with those of bulk CdTe cubic structure (JCPDS No. 15-0770). After growth of ZnS shell on the CdTe core, the peak position shifted to higher angles towards the positions of bulk ZnS cubic structure peaks (JCPDS No. 05-0566), which substantiates the formation of CdTe/ZnS core shell.

In Figure 11(a), the two strong peaks located at 404.9 and 412 eV correspond to Cd 3d-binding energy of CdTe QD, and the peak at 571.8, 581.9 eV in Figure 11(b) corresponds to Te 3d binding energy of CdTe. In Figure 11(c), the strong peaks 1021, 1044 eV correspond to Zn 2p and 161.5 eV in Figure 11(d), correspond to S binding energy of CdTe/ZnS QDs. These data of XPS provide the direct evidence of the formation of CdTe/ZnS QDs.

5. Conclusions

We demonstrated the ability of the SMAD technique for the synthesis of semiconductor cadmium selenide and

cadmium telluride quantum dots. Digestive ripening at high-temperature (250°C) was achieved by employing TOPO and OA as digestive ripening solvents. Compared to CdSe (90 min), the digestive ripening of CdTe was much faster (60 min). High temperature digestive ripening facilitated the removal of crystalline defects and allows enhancement in the photoluminescence of both CdSe and CdTe. Further enhancement of QY (40 to 60%) was achieved by coating with a high band gap inorganic ZnS shell by sonochemical procedure. Formation of ZnS over the core is evident from enhanced PL, XRD, EDX, and XPS analysis.

Acknowledgment

The support of Department of Energy (DE-FG 02-10 ER16202) is gratefully acknowledged.

References

- [1] S. Cingarapu, Z. Yang, C. M. Sorensen, and K. J. Klabunde, "Synthesis of CdSe quantum dots by evaporation of bulk CdSe using SMAD and digestive ripening processes," *Chemistry of Materials*, vol. 21, no. 7, pp. 1248-1252, 2009.
- [2] S. Cingarapu, Z. Yang, C. M. Sorensen, and K. J. Klabunde, "Synthesis of indium nanoparticles: digestive ripening under

- mild conditions,” *Inorganic Chemistry*, vol. 50, no. 11, pp. 5000–5005, 2011.
- [3] D. Heroux, A. Ponce, S. Cingarapu, and K. J. Klabunde, “Nanoparticles prepared by salt vapor-solvent vapor cocondensation and controlled nucleation: metal sulfides (ZnS, CdS, CdSe, PbS), and metal halide (LiF). Size, aggregates, structures, digestive ripening, superlattices, and impregnations,” *Advanced Functional Materials*, vol. 17, no. 17, pp. 3562–3568, 2007.
- [4] A. A. Ponce and K. J. Klabunde, “Chemical and catalytic activity of copper nanoparticles prepared via metal vapor synthesis,” *Journal of Molecular Catalysis A*, vol. 225, no. 1, pp. 1–6, 2005.
- [5] A. B. Smetana, K. J. Klabunde, and C. M. Sorensen, “Synthesis of spherical silver nanoparticles by digestive ripening, stabilization with various agents, and their 3-D and 2-D superlattice formation,” *Journal of Colloid and Interface Science*, vol. 284, no. 2, pp. 521–526, 2005.
- [6] S. Stoeva, K. J. Klabunde, C. M. Sorensen, and I. Dragieva, “Gram-scale synthesis of monodisperse gold colloids by the solvated metal atom dispersion method and digestive ripening and their organization into two- and three-dimensional structures,” *Journal of the American Chemical Society*, vol. 124, no. 10, pp. 2305–2311, 2002.
- [7] S. I. Stoeva, A. B. Smetana, C. M. Sorensen, and K. J. Klabunde, “Gram-scale synthesis of aqueous gold colloids stabilized by various ligands,” *Journal of Colloid and Interface Science*, vol. 309, no. 1, pp. 94–98, 2007.
- [8] S. B. Kalidindi and B. R. Jagirdar, “Highly monodisperse colloidal magnesium nanoparticles by room temperature digestive ripening,” *Inorganic Chemistry*, vol. 48, no. 10, pp. 4524–4529, 2009.
- [9] X. M. Lin, C. M. Sorensen, and K. J. Klabunde, “Digestive ripening, nanophase segregation and superlattice formation in gold nanocrystal colloids,” *Journal of Nanoparticle Research*, vol. 2, no. 2, pp. 157–164, 2000.
- [10] K. J. Klabunde, C. M. Sorensen, S. I. Stoeva, B. L. V. Prasad, A. B. Smetana, and X. M. Lin, “Digestive ripening, or “nanomachining,” to achieve nanocrystal size control,” in *Metal Clusters in Catalysis and Materials Science: The Issue of Size Control, Part II Methodologies*, C. Corrain, G. Schmid, and N. Toshima, Eds., chapter 11, pp. 233–252, Elsevier Science, Amsterdam, Holland, 2008.
- [11] D. S. Sidhaye and B. L. V. Prasad, “Many manifestations of digestive ripening: monodispersity, superlattices and nanomachining,” *New Journal of Chemistry*, vol. 35, no. 4, pp. 755–763, 2011.
- [12] C. B. Murray, D. J. Norris, and M. G. Bawendi, “Synthesis and characterization of nearly monodisperse CdE (E = sulfur, selenium, tellurium) semiconductor nanocrystallites,” *Journal of the American Chemical Society*, vol. 115, no. 19, pp. 8706–8715, 1993.
- [13] D. Battaglia, J. J. Li, Y. Wang, and X. Peng, “Colloidal two-dimensional systems: CdSe quantum shells and wells,” *Angewandte Chemie—International Edition*, vol. 42, no. 41, pp. 5035–5039, 2003.
- [14] X. Peng, L. Manna, W. Yang et al., “Shape control of CdSe nanocrystals,” *Nature*, vol. 404, no. 6773, pp. 59–61, 2000.
- [15] Z. A. Peng and X. Peng, “Formation of high-quality CdTe, CdSe, and CdS nanocrystals using CdO as precursor,” *Journal of the American Chemical Society*, vol. 123, no. 1, pp. 183–184, 2001.
- [16] L. Qu, Z. A. Peng, and X. Peng, “Alternative routes toward high quality CdSe nanocrystals,” *Nano Letters*, vol. 1, no. 6, pp. 333–337, 2001.
- [17] D. V. Talapin, A. L. Rogach, A. Kornowski, M. Haase, and H. Weller, “Highly luminescent monodisperse CdSe and CdSe/ZnS nanocrystals synthesized in a hexadecylamine-triethylphosphine oxide-triethylphosphine mixture,” *Nano Letters*, vol. 1, no. 4, pp. 207–211, 2001.
- [18] H. Yang, N. Fan, W. Luan, and S. T. Tu, “Synthesis of monodisperse nanocrystals via microreaction: open-to-air synthesis with oleylamine as a coligand,” *Nanoscale Research Letters*, vol. 4, no. 4, pp. 344–352, 2009.
- [19] W. W. Yu and X. Peng, “Formation of high-quality CdS and other II–VI semiconductor nanocrystals in noncoordinating solvents: tunable reactivity of monomers,” *Angewandte Chemie—International Edition*, vol. 41, no. 13, pp. 2368–2371, 2002.
- [20] M. A. Hines and P. Guyot-Sionnest, “Synthesis and characterization of strongly luminescing ZnS-capped CdSe nanocrystals,” *Journal of Physical Chemistry*, vol. 100, no. 2, pp. 468–471, 1996.
- [21] D. V. Talapin, I. Mekis, S. Gotzinger, A. Kornowski, O. Benson, and H. Weller, “CdSe/CdS/ZnS and CdSe/ZnSe/ZnS core-shell-shell nanocrystals,” *Journal of Physical Chemistry B*, vol. 108, no. 49, pp. 18826–18831, 2004.
- [22] B. R. Dorvel, H. M. Keizer, D. Fine, J. Vuorinen, A. Dodabalapur, and R. S. Duran, “Formation of tethered bilayer lipid membranes on gold surfaces: QCM-Z and AFM study,” *Langmuir*, vol. 23, no. 13, pp. 7344–7355, 2007.
- [23] X. S. Wang, T. E. Dykstra, M. R. Salvador, I. Manners, G. D. Scholes, and M. A. Winnik, “Surface passivation of luminescent colloidal quantum dots with poly(dimethylaminoethyl methacrylate) through a ligand exchange process,” *Journal of the American Chemical Society*, vol. 126, no. 25, pp. 7784–7785, 2004.
- [24] M. J. Murcia, D. L. Shaw, H. Woodruff, C. A. Naumann, B. A. Young, and E. C. Long, “Facile sonochemical synthesis of highly luminescent ZnS-shelled CdSe quantum dots,” *Chemistry of Materials*, vol. 18, no. 9, pp. 2219–2225, 2006.
- [25] J. K. Klabunde, P. L. Timms, P. S. Skell, and S. Ittel, “Introduction to metal atom syntheses,” in *Inorganic Syntheses*, D. Shriver, Ed., vol. 19, pp. 59–86, John Wiley & Sons, New York, NY, USA, 1979.
- [26] P. S. Nair, T. Radhakrishnan, N. Revaprasadu, G. Kolawole, and P. O’Brien, “Cadmium ethylxanthate: a novel single-source precursor for the preparation of CdS nanoparticles,” *Journal of Materials Chemistry*, vol. 12, no. 9, pp. 2722–2725, 2002.
- [27] S. L. Cumberland, K. M. Hanif, A. Javier et al., “Inorganic clusters as single-source precursors for preparation of CdSe, ZnSe, and CdSe/ZnS nanomaterials,” *Chemistry of Materials*, vol. 14, no. 4, pp. 1576–1584, 2002.
- [28] C. Q. Zhu, P. Wang, X. Wang, and Y. Li, “Facile phosphine-free synthesis of CdSe/ZnS core/shell nanocrystals without precursor injection,” *Nanoscale Research Letters*, vol. 3, no. 6, pp. 213–220, 2008.
- [29] X. Zhong, Y. Feng, and Y. Zhang, “Facile and reproducible synthesis of red-emitting CdSe nanocrystals in amine with long-term fixation of particle size and size distribution,” *The Journal of Physical Chemistry C*, vol. 111, no. 2, pp. 526–531, 2006.
- [30] Y. M. Sung, K. S. Park, Y. J. Lee, and T. G. Kim, “Ripening kinetics of CdSe/ZnSe core/shell nanocrystals,” *The Journal of Physical Chemistry C*, vol. 111, no. 3, pp. 1239–1242, 2007.

- [31] D. S. Sidhaye and B. L. V. Prasad, "Many manifestations of digestive ripening: monodispersity, superlattices and nanomachining," *New Journal of Chemistry*, vol. 124, no. 9, pp. 2049–2055, 2011.
- [32] L. Qu and X. Peng, "Control of photoluminescence properties of CdSe nanocrystals in growth," *Journal of the American Chemical Society*, vol. 124, no. 9, pp. 2049–2055, 2002.
- [33] B. O. Dabbousi, J. Rodriguez-Viejo, F. V. Mikulec et al., "(CdSe)ZnS core-shell quantum dots: synthesis and characterization of a size series of highly luminescent nanocrystallites," *The Journal of Physical Chemistry B*, vol. 101, no. 46, pp. 9463–9475, 1997.
- [34] M. A. Hines and P. Guyot-Sionnest, "Bright UV-blue luminescent colloidal ZnSe nanocrystals," *The Journal of Physical Chemistry B*, vol. 102, no. 19, pp. 3655–3657, 1998.
- [35] M. B. Mohamed, D. Tonti, A. Al-Salman, A. Chemseddine, and M. Chergui, "Synthesis of high quality zinc blende CdSe nanocrystals," *The Journal of Physical Chemistry B*, vol. 109, no. 21, pp. 10533–10537, 2005.
- [36] L. Wang, X. Sun, W. Liu, and X. Yu, "Phosphine-free synthesis of high quality zinc-blende CdSe nanocrystals in air," *Colloids and Surfaces A*, vol. 353, no. 2-3, pp. 232–237, 2010.
- [37] Z. Quan, Z. Wang, P. Yang, J. Lin, and J. Fang, "Synthesis and characterization of high-quality ZnS, ZnS:Mn²⁺, and ZnS:Mn²⁺/ZnS (core/shell) luminescent nanocrystals," *Inorganic Chemistry*, vol. 46, no. 4, pp. 1354–1360, 2007.
- [38] T. Trindade, P. O'Brien, and N. L. Pickett, "Nanocrystalline semiconductors: synthesis, properties, and perspectives," *Chemistry of Materials*, vol. 13, no. 11, pp. 3843–3858, 2001.

Research Article

Effect of Ultrasonic Irradiation on Preparation and Properties of Ionogels

Yogendra Lal Verma, Manish Pratap Singh, and Rajendra Kumar Singh

Ionic Liquid and Solid State Ionics Laboratory, Department of Physics, Banaras Hindu University, Varanasi 221005, India

Correspondence should be addressed to Rajendra Kumar Singh, rksingh_17@rediffmail.com

Received 22 August 2011; Revised 25 October 2011; Accepted 29 October 2011

Academic Editor: Jaetae Seo

Copyright © 2012 Yogendra Lal Verma et al. This is an open access article distributed under the Creative Commons Attribution License, which permits unrestricted use, distribution, and reproduction in any medium, provided the original work is properly cited.

Silica-gel matrices containing ionic liquid (IL) 1-butyl-3-methylimidazolium hexafluorophosphate viz. ionogels have been synthesized using one-pot nonhydrolytic sol-gel method and taking tetraethyl orthosilicate (TEOS) as starting precursor. Effect of ultrasonic irradiation on pore parameters of ionogels and vibrational properties of the IL upon confinement in the porous matrix has been investigated. The synthesized gels have been characterized by BET, DSC, TGA, and FTIR. BET analysis shows some changes in the pore parameters due to ultrasonic irradiation. DSC results indicate shift in glass transition temperature upon confinement of the IL. The FTIR spectra show changes in vibrational bands on confinement, particularly, the bands related to the imidazolium ring; aliphatic chain and anion PF_6^- of the IL are found to shift upon confinement in porous silica matrix obtained due to ultrasonic irradiation. Ultrasonic irradiation has been found to affect the gelation dynamics and kinetics and pore parameters.

1. Introduction

Ionic liquids are novel materials, which are self-dissociating and composed of organic cations and inorganic/organic anions of varying size [1–7]. Due to dissociated ionic species, ILs have high ionic conductivity. Besides high ionic conductivity, ILs have low vapour pressure, large electrochemical window, high thermal stability, high chemical stability, wide liquidus range and good capability of dissolving various organic/inorganic materials. Low vapour pressure of ILs attracted the attention of chemists in order to develop less polluting chemical processes for synthesis. Recently, high ionic conductivity is attractive from the point of view of its application in electrochemical devices (like batteries, fuel cells, super capacitors, electrochemical solar cells, and electrochromic devices [8–12], etc.). However, its use gets limited due to liquidus nature which results in difficulties such as packaging, leakage and portability. Dai et al. [13] for the first time introduced ionic liquid in porous silica gels. Subsequently, these materials were termed as “ionogel”. Now, the ionogels are being extensively investigated by many researchers [14, 15]. The ionogels are suitable candidates

for applications in many devices such as fuel cell, electrochemical sensor, biosensor, and catalysis, and as optical solvent, biocatalysis [15]. The very nature of ionogels involves entrapment of IL in nanopores. According to IUPAC classification, based on pore diameter (d), porous materials are grouped into three classes: (a) microporous, $d < 2$ nm; (b) mesoporous, 2 nm $< d < 50$ nm; (c) macroporous, $d > 50$ nm [16]. When IL goes into confined geometry of matrix pore, since IL molecules are big, if the size of the IL ≈ 9 Å (estimated from gauss-view) is of the order of pore size [14], confinement is likely to change their properties significantly. Therefore, many attempts have been made to study IL in confined geometry. The confinement involves the following. (i) Matrix pore size [17]. (ii) Pore wall surface decoration/functionalization [18]. (iii) Type of matrix: like oxide matrices SiO_2 , SnO_2 , and so forth, or mesoporous conducting matrices of silver, single wall carbon nanotubes, multiwall carbon nanotubes, and so forth [19]. The properties in oxide and conducting porous matrices change differently because of the difference in the nature and extent of IL-pore wall interaction. (iv) Some common ILs with imidazolium and pyridinium cations with different

anions. Most studies of ILs in confined geometry are focused on the imidazolium-based cations [19–24]. In our earlier experimental and theoretical studies on [BMIM][PF₆], we found that the cation ring gets weakly attached to the silica gel surface oxygen leading to changes in melting point, fluorescence, and vibrational bands [25]. It may be noted that all the studies listed above including our study [18–25] were on ILs with small anions. More recently, we have studied the IL with large anion size [BMIM][OcSO₄] and have proposed a phenomenological model to qualitatively account for the anion size dependence of melting point depression [14]. Pore parameters are found to be the function of IL loading. We feel that, apart from these factors, ultrasonic irradiation may affect the pore parameters and other parameters of the matrix. With this view in mind, we have studied the effect of ultrasonic irradiation on pore parameters of the silica-gel matrix containing IL. We have monitored the effect of ultrasound irradiation on changes in the following properties of IL in confined geometry: pore parameters (namely, porosity, pore size distribution, nitrogen sorption characteristic, surface area and pore volume), cation ring related vibrations, aliphatic chain C–H vibrations, and vibrations of anion.

Since the rates of chemical reactions such as hydrolysis and condensation in the sol-gel processes are very important to synthesize the different microstructure of gels, different methods have been used to control sol-gel processes. Ultrasonic irradiation can be used to control the gelation dynamics and kinetics of gelation process. The effect of ultrasound on chemical reaction in the sol-gel process is mainly due to acoustic cavitation, which includes three discrete stages: nucleation, bubble growth, and implosive collapse. If ultrasound wave is used, rapid compression of gas during cavitation collapse leads to nearly adiabatic heating due to slow thermal transport, thereby forming localized hot-spot and bond cleavage or rearrangement cause, followed by atomic and radical recombination and thermal and chemical quenching [26–28].

The gels prepared by ultrasonic treatment are also called “sonogels”. The sonogels have properties which differ from those of the gels prepared without ultrasonic irradiation. However, no study of the effect of ultrasound on the synthesis of ionic liquid confined in silica matrix (ionogels) has been reported. In the present study, the effect of ultrasound irradiation on gelation and subsequent properties of ionogels has been reported. To the best of our knowledge, this is first study conducted to see the effect of ultrasonic irradiation on pore parameters of ionogels.

2. Materials and Methods

2.1. Chemical. The ionic liquid [BMIM][PF₆] and TEOS were procured from Sigma-Aldrich (numerical prescribed purity) and used as received except for vacuum pre-drying and heating. The other chemical, that is, formic acid (GR grade) was purchased from Merck, Germany.

2.2. Synthesis of IL-Confined Porous Silica Gel. IL-confined porous silica gels (ionogels) have been prepared using

one-pot nonhydrolytic sol-gel method. tetraethyl orthosilicate (TEOS) as sol-gel precursor was mixed with formic acid and IL ([BMIM][PF₆]) at a TEOS/HCOOH/IL molar ratio of 1/8/0.4. Care was taken in handling of IL so that it does not come in contact with ambient humidity (handled under dry nitrogen atmosphere). Further, before use, the samples were heated at a temperature of 100°C for 12 hours and vacuum-dried at a pressure of 10⁻³ Torr for 6 hours to remove traces of water. The gel was finally vacuum-dried. Ionic-liquid-confined silica gel of SiO₂ + 65 wt% IL was prepared. It was observed that the silica gel matrix containing 65 wt% of the IL gets gelled in 40 minute, while upon ultrasonic irradiation, gelation time reduced considerably. Monoliths were aged at casting temperature for 15 days.

We have used low and high power continuous wave sources for the ultrasonic irradiation of the sols. Power output of low power continuous ultrasonic source (frequency 10 MHz) was 10 m watts while the power output of the high power ultrasonic source (frequency 20 KHz) is 120 watts. Ionic liquid, metallic precursor, and formic acid were taken in the specially designed reaction vessel in the proportion mentioned above. Resulting sol was exposed to ultrasonic irradiation. The following three samples have been prepared:

Sample 1# IG: without ultrasonic irradiation,

Sample 2# IG1: low power ultrasonic irradiation,

Sample 3# IG2: high power ultrasonic irradiation.

The reaction vessel used for ultrasonic irradiation consisted of a double-walled metallic (stainless steel) jacket having inlet and outlet assembly for circulating thermostatic fluid. At the bottom of the cylindrical vessel, a quartz crystal of frequency 10 MHz was fitted which, when excited by radio waves of same frequency, generated ultrasonic waves. These waves passed through the sample. The assembly for the high power ultrasonicator consisted of Vibronics Ultrasonicator having 20 KHz transducer.

2.3. Characterization Methods

2.3.1. Pore Analysis. Surface area, pore volume, and pore size were measured by BET (Brunauer-Emmett-Teller) method at 77 K on a Gemini V 2390 t from Micromeritics Instrument Corporation (reproducibility of the system is ±0.01%, and the molecular size of the adsorptive gas (N₂) = 0.162 nm² at 77 K [16]). Before the measurements were carried out, IL was extracted by dissolving the gel ingot in acetone (at 60°C) and washing several times then subjecting to vacuum drying. After drying, samples were degassed under the flow of N₂ at 60°C for 25 hr for BET analysis.

2.3.2. Thermogravimetric Analysis (TGA). The thermogravimetric analysis was done using a Mettler Toledo TGA/DSC 1 (degree of accuracy is ±0.3 K) at heating rate 10°C/min under N₂ atmosphere, and the samples for TGA/DSC measurements were put in Al₂O₃ pans. Each sample was also dried at 80–90°C for 5 h before the TGA measurement.

2.3.3. Differential Scanning Calorimetry (DSC). Measurements of glass transition temperatures of the samples

TABLE 1: Specific surface area, pore volume, pore diameter, and porosity of monolithic silica samples.

Sample name	Average pore diameter (nm)	Pore volume (cm ³ /g)	BET surface area (m ² /g)	% Porosity
#IG	11.8	1.3	299	74
#IG1	14.8	1.4	251	75.5
#IG2	22.6	1.6	182	78

were carried out on a Mettler Toledo DSC-1 (with degree of accuracy ± 0.02 K). The samples were placed in 40 μ L hermetically sealed aluminum pan with pinhole at the top of the pan, the samples inside the DSC furnace were exposed to a flowing N₂ atmosphere. Before the DSC measurement test, each sample was dried at 80°C for 5 hr.

2.3.4. Fourier Transform Infrared (FTIR) Spectra. The FTIR spectra were recorded using Perkin Elmer spectrum 65 FTIR spectrometer with 0.5 cm⁻¹ resolution. The solid SiO₂:IL composite was dispersed in KBr and pelletised for recording the spectra of various SiO₂:IL samples. For recording the spectra of IL (neat), a drop of IL was used to wet the KBr pellet.

3. Results and Discussion

The gelification occurred in 40 minutes when no ultrasonic irradiation was done, in 35 minutes, when sol was irradiated with low power ultrasonic wave, while gelification occurred in 25 minutes upon passage of high power ultrasonic waves in the sol. Possibly, the passage of ultrasound wave allows sol-gel particles to approach each other more easily without large electrostatic barriers which enhances the rate of condensation. Apart from the rate of condensation (or rate of gelation), the size of pores also depends upon ultrasonic irradiation. The sol-gel processes may have improved upon ultrasonic irradiation. Figure 1 shows the radial contraction of gel (without ultrasonication) with time. From the Figure 1, it can be seen that for initial few hours (approx. 50 hrs), radial contraction occurred at a rapid rate, while after 50 hrs the contraction rate slowed down due to slow evaporation of the solvent. Radial contraction shows the exponential decaying trend.

3.1. BET Analysis. The pore sizes (as determined by BET) of silica matrices (IL was extracted from the pores before making N₂-sorption studies) corresponding to 65 wt% of IL (higher loading of IL was used intentionally, so that the effect of ultrasonic irradiation (if any), is significant) in the reaction vessel for #IG, #IG1, and #IG2 are given in Table 1. From Table 1, it can be seen that the pore parameter is maximum for #IG2, that is, high power ultrasonic irradiation produces large pores; large pore size may be attributed to large cavitation bubbles formed due to high power ultrasonic irradiation (resulting a larger pores), while low power ultrasonication produces smaller cavitation bubbles (hence smaller pores). Ultrasonic irradiation increases pore volume as well as porosity, and the highest porosity is observed for sample #IG2. However, ultrasonic irradiation decreases the surface area. IL-confined porous silica matrices were

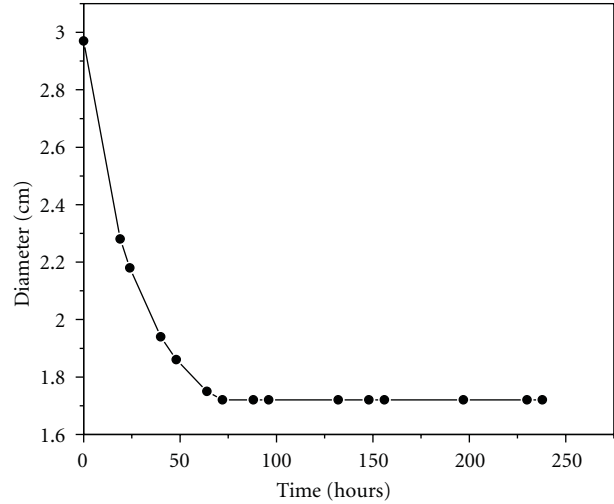


FIGURE 1: Radial contraction of disc shaped silica monolith ionogels (without ultrasonication).

obtained with (low and high power ultrasonic irradiation) and without ultrasonication, and corresponding isotherms and pore size distribution curves are shown in Figure 2. From Figure 2, it can be seen that there is sharp decline in the desorption curve which is indicative of mesoporosity, while the hysteresis between the two curves demonstrates that there is a diffusion bottleneck. Inset of Figure 2 shows pore size distribution curve, and from the curves it can be seen that the low power ultrasonic irradiation resulted in nearly uniform pore size distribution. S_{BET} decreased by about 17% upon US irradiation; there was larger decrease corresponding to high power ultrasonic irradiation. Mass density of disk-shaped monolith was found to decrease upon ultrasonication.

The % porosity of the samples was calculated from BJH data using the following equation (1)

$$\% \text{ porosity, } \varphi = \frac{\text{BJH pore volume}}{\text{BJH pore volume} + 1/\rho}, \quad (1)$$

where ρ is the density of silica, (2.2 g/cm³) [29]. The % porosity of the samples is given in the Table 1. It was found that ultrasonication resulted in change in porosity, high power ultrasonication resulted in larger change in porosity.

3.2. Change in the FTIR Bands of IL on Confinement. The FTIR spectra of unconfined (bulk), confined IL with low as well as high power are shown in Figure 3. Before taking any measurement, we heated the IL-confined samples in order to avoid the spurious peaks arising from residual solvent

TABLE 2: Vibrational bands of IL ([BMIM][PF₆]) and IL-confined samples (#IG, #IG1, and #IG2).

Bulk IL	Vibrational bands (cm ⁻¹)		
	#IG	#IG1	#IG2
1114 (in plane C–H bending of imidazolium ring)	1098	1104	1109
2880, 2941, 2968 (alkyl chain C–H vibration)	2881, 2942, 2969	2881, 2942, 2970	2881, 2942, 2969
3127 (cation ring C–H vibration)	3128	3128	3128
3172 (C ₂ –N ₁ –C ₅ vibration)	3175	3174	3174

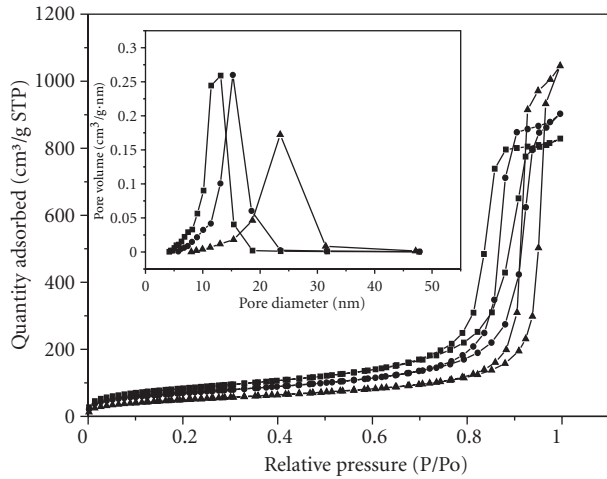
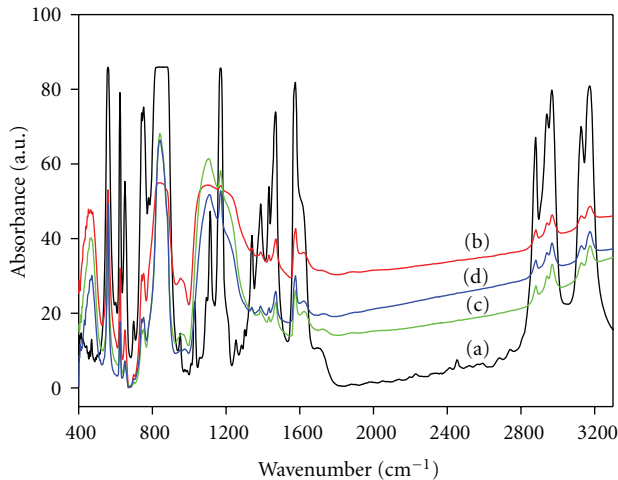
FIGURE 2: N₂ adsorption-desorption isotherms and Pore-size distribution (inset) of silica gel matrices: #IG (■), #IG1 (●), #IG2 (▲).

FIGURE 3: The FTIR spectra of (a) pure IL, (b) #IG, (c) #IG1, and (d) #IG2.

left in the samples. The peaks of unconfined IL shift on confinement as given below.

- (i) The vibrational band related to PF₆ at 837 cm⁻¹ of bulk IL is shifted to 841 cm⁻¹, 840 cm⁻¹, and 841 cm⁻¹ in samples #IG, #IG1, and #IG2, respectively.
- (ii) From Figure 4(a) and Table 2, it can be seen that vibrational bands of bulk IL at 1114 cm⁻¹ related

to in-plane C–H bending of imidazolium ring shift to 1098 cm⁻¹, 1104 cm⁻¹, and 1109 cm⁻¹ in samples #IG, #IG1 #IG2, respectively. There is larger shift corresponding to unconfined sample, while high power ultrasonic irradiation results in the least shift.

- (iii) The alkyl chain C–H vibrations at 2880 cm⁻¹, 2941 cm⁻¹, and 2968 cm⁻¹, {see Figure 4(b) and Table 2} of unconfined IL shift to 2881 cm⁻¹, 2942 cm⁻¹, 2969 cm⁻¹; 2881 cm⁻¹, 2942 cm⁻¹, 2970 cm⁻¹, and 2881 cm⁻¹, 2942 cm⁻¹, 2969 cm⁻¹ in #IG, #IG1, and #IG2, respectively. It is important to see that alkyl chain C–H vibrations in the present study are not changing much.
- (iv) The cation ring C–H vibrations as well as C₂–N₁–C₅ vibrations at 3127 cm⁻¹, 3172 cm⁻¹{see Figure 4(b) and Table 2} shift to 3128 cm⁻¹, 3175 cm⁻¹, 3128 cm⁻¹, 3174 cm⁻¹ and 3128 cm⁻¹, 3174 cm⁻¹, respectively, in #IG, #IG1, and #IG2. The shift in these vibrational bands can be attributed to the interaction of H of the ring with the pore walls.

3.3. Thermal Stability. Figure 5 shows the thermogravimetric analysis curve of the bulk IL, low power ultrasonicated, high power ultrasonicated, and without ultrasonicated samples.

It is clear that thermal stability gets reduced upon ultrasonic irradiation. Thermal degradation starts at approximately 170°C for all the samples having confined IL. Confined ILs exhibits multistep degradation process. Thermal stability gets reduced upon ultrasonic irradiation. For low power ultrasonic irradiation, the onset of decomposition temperature, T_d , is 174°C while high power ultrasonic irradiation onset, T_D , is 177°C.

3.4. Differential Scanning Calorimetry. DSC experiments disclose the effect of confinement on the phase transition of the ionic liquid within the ionogels. From the DSC thermogram (Figure 6) it can be seen that the glass transition temperature (T_g) for the bulk IL ([BMIM][PF₆]) is about -75°C which becomes -76.4°C for #IG2 sample, while there is slight change in T_g for samples #IG1 and #IG in comparison to #IG2. Thus, the decrease in the glass transition temperature upon confinement of IL in sample #IG2 is about 1.4°C while, in samples #IG1 and #IG, is ~1°C. The decrease in the glass transition temperature (T_g) can be explained on the basis of the following equation [14]:

$$\Delta T_g = \frac{V \Delta \alpha T_g \Delta \sigma}{\Delta C_p R}, \quad (2)$$

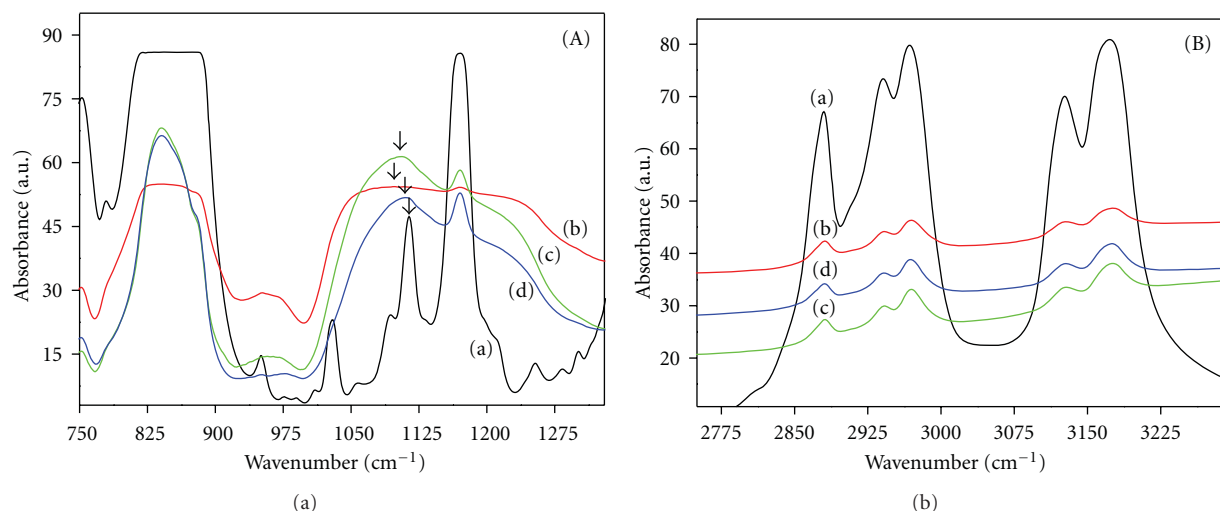


FIGURE 4: The extended FTIR spectra of BMIMPF₆, before and after confinement in the regions (A) 750–1330 cm⁻¹ and (B) 2750–3290 cm⁻¹ for (a) pure IL, (b) #IG, (c) #IG1, and (d) #IG2.

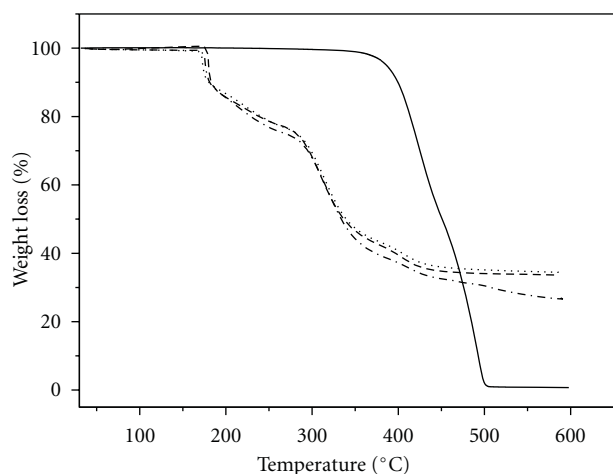


FIGURE 5: TGA thermograms for bulk IL (BMIMPF₆) (—), #IG (---), #IG1 (· · · · ·), and #IG2 (- · - · -).

where $\Delta\alpha$ is the thermal expansion coefficient, V is the molar volume, $\Delta\sigma$ is the difference between gas wall and ionic liquid wall interfacial energies, T_g is the glass transition temperature of unconfined IL, and ΔC_p is the heat capacity at constant pressure. The above equation describes the relation between glass transition temperature and pore diameter ($d = 2R$). However, quantitative explanation is difficult (because of complicated wall particle interaction).

4. Conclusion

Ionogels were prepared by both ultrasonic-assisted sol-gel process and traditional sol-gel process. It has been found that ultrasonic irradiation affects the gelation dynamics and kinetics and results in changes in pore parameters. We have also found a change in the glass transition temperature (T_g) of the IL upon confinement. The result shows that ultrasonic

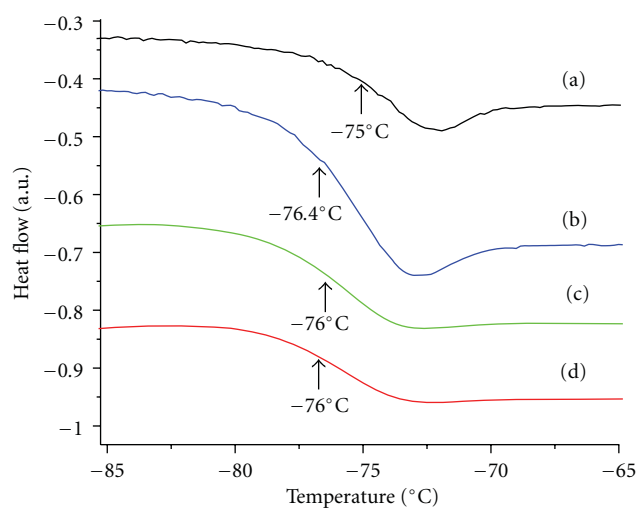


FIGURE 6: Glass transitions of (a) bulk IL (BMIMPF₆), (b) #IG2, (c) #IG1, and (d) #IG.

irradiation produces changes in pore parameters, and pore size distribution becomes uniform.

Acknowledgments

R. K. Singh is grateful to the DST, New Delhi and BRNS-DAE, India for providing financial assistance.

References

- [1] M. Armand, F. Endres, D. R. MacFarlane, H. Ohno, and B. Scrosati, "Ionic-liquid materials for the electrochemical challenges of the future," *Nature Materials*, vol. 8, no. 8, pp. 621–629, 2009.
- [2] N. V. Plechkova and K. R. Seddon, "Applications of ionic liquids in the chemical industry," *Chemical Society Reviews*, vol. 37, no. 1, pp. 123–150, 2008.

- [3] F. Endres and S. Zein El Abedin, "Air and water stable ionic liquids in physical chemistry," *Physical Chemistry Chemical Physics*, vol. 8, no. 18, pp. 2101–2116, 2006.
- [4] J. F. Wishart, "Energy applications of ionic liquids," *Energy and Environmental Science*, vol. 2, no. 9, pp. 956–961, 2009.
- [5] L. A. Blanchard, D. Hancu, E. J. Beckman, and J. F. Brennecke, "Green processing using ionic liquids and CO₂," *Nature*, vol. 398, no. 6731, pp. 28–29, 1999.
- [6] K. R. Seddon, "Ionic liquids: a taste of the future," *Nat Mater*, vol. 2, no. 6, pp. 363–365, 2003.
- [7] J. P. Hallett and T. Welton, "Room-temperature ionic liquids: solvents for synthesis and catalysis," *Chemical Reviews*, vol. 111, no. 5, pp. 3508–3576, 2011.
- [8] S. Seki, Y. Kobayashi, H. Miyashiro et al., "Lithium secondary batteries using modified-imidazolium room-temperature ionic liquid," *Journal of Physical Chemistry B*, vol. 110, no. 21, pp. 10228–10230, 2006.
- [9] R. F. de Souza, J. C. Padilha, R. S. Gonçalves, and J. Dupont, "Room temperature dialkylimidazolium ionic liquid-based fuel cells," *Electrochemistry Communications*, vol. 5, no. 8, pp. 728–731, 2003.
- [10] A. Balducci, U. Bardi, S. Caporali, M. Mastragostino, and F. Soavi, "Ionic liquids for hybrid supercapacitors," *Electrochemistry Communications*, vol. 6, no. 6, pp. 566–570, 2004.
- [11] P. Wang, S. M. Zakeeruddin, J. E. Moser, and M. Grätzel, "A new ionic liquid electrolyte enhances the conversion efficiency of dye-sensitized solar cells," *Journal of Physical Chemistry B*, vol. 107, no. 48, pp. 13280–13285, 2003.
- [12] D. R. Macfarlane, M. Forsyth, P. C. Howlett et al., "Ionic liquids in electrochemical devices and processes: managing interfacial electrochemistry," *Accounts of Chemical Research*, vol. 40, no. 11, pp. 1165–1173, 2007.
- [13] S. Dai, Y. H. Ju, H. J. Gao, J. S. Lin, S. J. Pennycook, and C. E. Barnes, "Preparation of silica aerogel using ionic liquids as solvents," *Chemical Communications*, no. 3, pp. 243–244, 2000.
- [14] M. P. Singh, R. K. Singh, and S. Chandra, "Studies on imidazolium-based ionic liquids having a large anion confined in a nanoporous silica gel matrix," *Journal of Physical Chemistry B*, vol. 115, no. 23, pp. 7505–7514, 2011.
- [15] J. Le Bideau, L. Viau, and A. Vioux, "Ionogels, ionic liquid based hybrid materials," *Chemical Society Reviews*, vol. 40, no. 2, pp. 907–925, 2011.
- [16] K. S. W. Sing, D. H. Everett, R. A. W. Haul et al., "Reporting physisorption data for gas/solid systems with special reference to the determination of surface area and porosity (recommendations 1984)," *Pure and Applied Chemistry*, vol. 57, no. 4, pp. 603–619, 1985.
- [17] M. Davenport, A. Rodriguez, K. J. Shea, and Z. S. Siwy, "Squeezing ionic liquids through nanopores," *Nano Letters*, vol. 9, no. 5, pp. 2125–2128, 2009.
- [18] R. Göbel, A. Friedrich, and A. Taubert, "Tuning the phase behavior of ionic liquids in organically functionalized silica ionogels," *Dalton Transactions*, vol. 39, no. 2, pp. 603–611, 2010.
- [19] S. Chen, K. Kobayashi, Y. Miyata et al., "Morphology and melting behavior of ionic liquids inside single-walled carbon nanotubes," *Journal of the American Chemical Society*, vol. 131, no. 41, pp. 14850–14856, 2009.
- [20] M. P. Singh, R. K. Singh, and S. Chandra, "Thermal stability of ionic liquid in confined geometry," *Journal of Physics D: Applied Physics*, vol. 43, no. 9, Article ID 092001, 2010.
- [21] A. Karout and A. C. Pierre, "Silica xerogels and aerogels synthesized with ionic liquids," *Journal of Non-Crystalline Solids*, vol. 353, no. 30–31, pp. 2900–2909, 2007.
- [22] O. Oter, K. Ertekin, and S. Derinkuyu, "Photophysical and optical oxygen sensing properties of tris(bipyridine)ruthenium(II) in ionic liquid modified sol-gel matrix," *Materials Chemistry and Physics*, vol. 113, no. 1, pp. 322–328, 2009.
- [23] M. Sha, G. Wu, Y. Liu, Z. Tang, and H. Fang, "Drastic phase transition in ionic liquid [dmim][cl] confined between graphite walls: new phase formation," *Journal of Physical Chemistry C*, vol. 113, no. 11, pp. 4618–4622, 2009.
- [24] A. Karout and A. C. Pierre, "Porous texture of silica aerogels made with ionic liquids as gelation catalysts," *Journal of Sol-Gel Science and Technology*, vol. 49, no. 3, pp. 364–372, 2009.
- [25] M. P. Singh, R. K. Singh, and S. Chandra, "Properties of ionic liquid confined in porous silica matrix," *ChemPhysChem*, vol. 11, no. 9, pp. 2036–2043, 2010.
- [26] K. Morita, Y. Hu, and J. D. Mackenzie, "The effects of ultrasonic irradiation on the preparation and properties of Ormosils," *Journal of Sol-Gel Science and Technology*, vol. 3, no. 2, pp. 109–116, 1994.
- [27] E. Blanco, L. Esquivias, R. Litrán, M. Piñero, M. Ramírez-del-Solar, and N. de la Rosa-Fox, "Sonogels and derived materials," *Applied Organometallic Chemistry*, vol. 13, no. 5, pp. 399–418, 1999.
- [28] L. Esquivias, M. Piñero, V. Morales-Flórez, and N. de la Rosa-Fox, "Aerogels synthesis by sonocatalysis: sonogels," in *Aerogels Handbook*, M. A. Aegerter, N. Leventis, and M. M. Koebel, Eds., pp. 419–441, 1st edition, 2011.
- [29] R. K. Iler, *The Chemistry of Silica*, Wiley, New York, NY, USA, 1979.

Research Article

Quantum Size Effect in ZnO Nanoparticles via Mechanical Milling

Nurul Azri Khalisah Aznan and Mohd Rafie Johan

Advanced Materials Research Laboratory, Department of Mechanical Engineering, University of Malaya, Lembah Pantai, 50603 Kuala Lumpur, Malaysia

Correspondence should be addressed to Nurul Azri Khalisah Aznan, nurulazri@siswa.um.edu.my

Received 7 July 2011; Revised 15 September 2011; Accepted 16 September 2011

Academic Editor: William W. Yu

Copyright © 2012 N. A. K. Aznan and M. R. Johan. This is an open access article distributed under the Creative Commons Attribution License, which permits unrestricted use, distribution, and reproduction in any medium, provided the original work is properly cited.

ZnO nanocrystals were successfully produced by mechanical milling. It is shown that mechanical milling is very effective and simple to produce ZnO nanoparticles with the possibility of obtaining large quantities of materials. Size effects in ZnO nanoparticles were probed by XRD and UV-vis and photoluminescence (PL) spectroscopy. Absorption due to free electron was clearly observed, whereas strong PL lines were recorded in the UV and blue region. The absorbance and photoluminescence were found to increase with reduction in particle size. Blueshift of excitonic and emission peaks was observed as a consequence of the size quantization effect. Formation of pure ZnO phase was confirmed from XRD pattern and the optical spectroscopy.

1. Introduction

Compared to bulk materials, nanoscale materials exhibit large specific surface area and size-dependent quantum confinement effects. Nanoscale materials often have distinct electronic, optical, magnetic, catalytic, and thermal properties. They provide a unique opportunity to observe the evolving electronic structure of materials growing from molecules to bulk. The investigations on size-dependent electronic structure have revealed interesting properties including discretization of electron energy levels, concentration of oscillator strength, highly polarizable excited states, and increased electron-electron correlation [1–4]. ZnO nanoparticles are one of the important multifunctional materials due to their unique optical and electronic properties [5–9]. It has a wide band gap semiconductor, having high exciton binding energy of 60 meV and has stable wurtzite structure with lattice spacing $a = 0.325$ nm and $c = 0.521$ nm. Several authors have reported high photoluminescence (PL) efficiencies in ZnO nanostructures [10, 11]. Optical techniques are the most common techniques to study the quantum size effects. Here, we report studies on the optical properties of zinc oxide (ZnO) nanoparticles, synthesized by a mechanical route. We have emphasized UV-vis and PL spectroscopic studies, to examine the size-induced effects.

Various techniques have been used to synthesis ZnO nanoparticles including mechanical milling [12], hydrothermal synthesis [13], sol-gel method [14], and spray pyrolysis [10].

2. Experimental

Commercially obtained ZnO powder with size ~ 200 nm and purity 99% was milled in a zirconia jar with zirconia balls with a ball-to-powder weight ratio of 14. The mechanical milling was performed in a horizontal ball mill operating at 200 rpm for different milling times (5, 10, 15, and 20 h). No solvent was used in this process.

The optical properties were investigated by using Cary, 50-probe UV-vis spectrophotometer, and Perkin Elmer (LS-55) Luminescence Spectrophotometer (PL). X-ray diffraction patterns were performed using SIEMEN D500 X-ray diffractometer equipped with graphite monochromatized Cu $K\alpha$ radiation ($\lambda = 1.5418 \text{ \AA}$) irradiated with a scanning rate of $0.02^\circ \text{ s}^{-1}$. The particle size was calculated from the effective mass equation using data from UV-vis spectroscopy.

3. Results and Discussion

Figure 1 shows the XRD pattern of the ZnO powders before and after milling. All the peaks corresponding to the

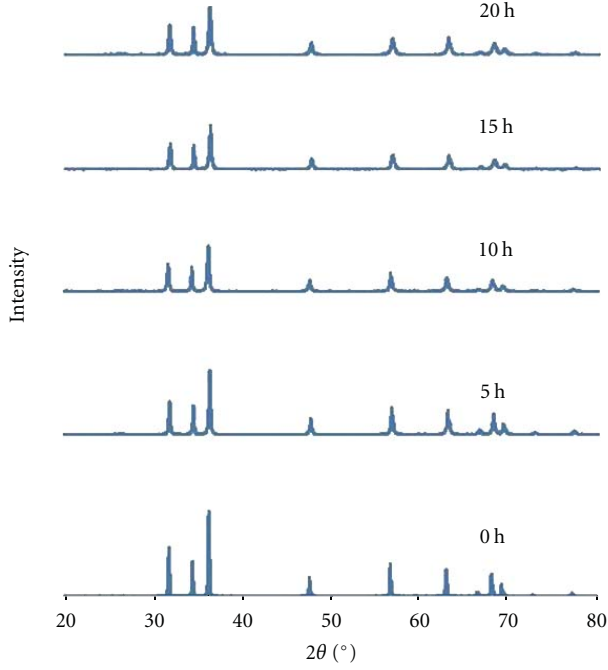


FIGURE 1: XRD pattern for ZnO particles before and after milling.

reflections of hexagonal phase ZnO match well with standard diffraction data (JCPDS card no. 80-0075), as well as with that for high-purity powder. With increasing milling time, the corresponding peaks become less intense and broader. No major change is observed on the lattice parameters. The considerably broad reflections are mainly a consequence of a small grain size with a small contribution from internal strain induced by the severe mechanical deformation.

Figure 2 shows the UV absorption spectra of ZnO powders milled at different milling times. Absorption peaks corresponding to 5, 10, 15, and 20 h are obtained at 284.97, 281.98, 279.94, and 276.95 nm, respectively. As seen from Figure 2, the absorption spectra for all the samples show sharp excitonic peaks and blue shifted due to quantum confinement effect. The absorbance increases as the milling time increases. Therefore, the optical properties get enhanced with the increasing ratio of surface to volume in ZnO powder.

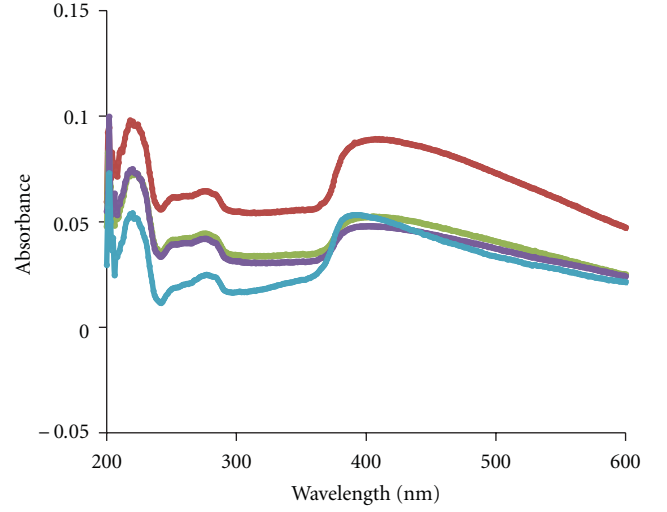
The particle size was determined from the effective mass equation below [13]:

$$E = E_{\text{bulk}} + h^2 \pi^2 \left(\frac{1}{m_e} + \frac{1}{m_h} \right) - \frac{(1.8e^2)}{4\pi\epsilon'\epsilon'_0 R}, \quad (1)$$

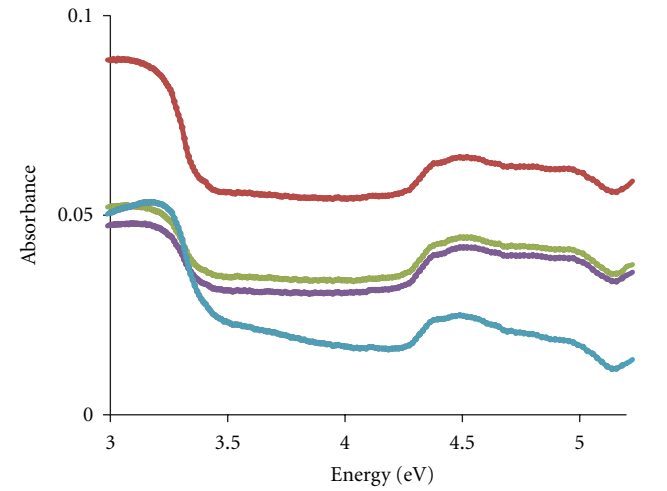
where E and E_{bulk} are the band gap of synthesized and bulk (3.3 eV) ZnO particles, respectively, R is radius of the particle, m_e is the effective mass of electron ($0.28 m_0$), m_h is the effective mass of hole ($0.49 m_0$), ϵ' is the dielectric constant of material (2.1), ϵ'_0 is the permittivity of free space, and h is the Planck's constant.

Table 1 shows the size of ZnO particles are decreases as the milling time increases.

Figure 3 shows the room temperature photoluminescence (PL) spectra of ZnO nanoparticles milled for 5, 10,



(a)



(b)

FIGURE 2: UV-vis spectra of ZnO nanoparticles at various milling times with respect to their (a) wavelength and (b) energy.

TABLE 1: Characteristics of ZnO powders at various milling times.

Milling time (h)	FWHM (eV)	UV emission peak (nm)	BE emission peak (nm)	Particle size from (1) (nm)
5	0.46	309.0	414.0	2.32
10	0.51	308.5	430.0	2.24
15	0.52	306.5	418.0	2.18
20	0.54	307.0	417.5	2.10

15, and 20 h. ZnO nanoparticles exhibited two prominent emission PL bands at around 309 and 418 nm. The PL peak at 309 nm which is intense and sharp is assigned to near-band-edge emission (UV emission) attributed to free electron recombination [15]. This peak intensity is decreased

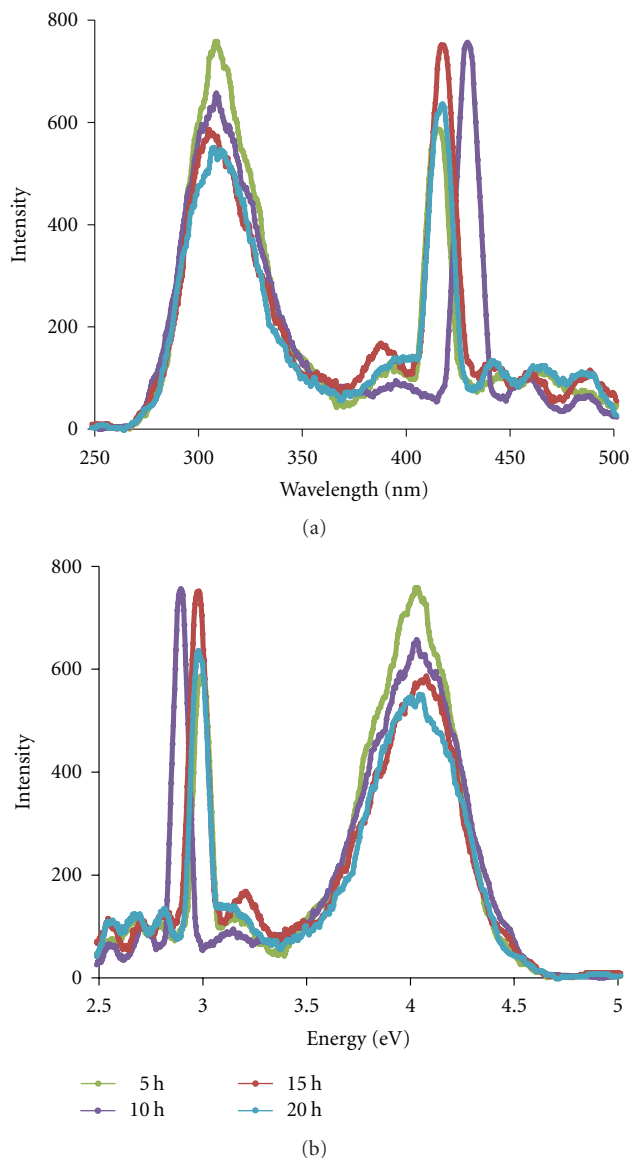


FIGURE 3: Photoluminescence spectra of ZnO powders at various milling time.

and blue shifted as the particle size decreases. Blue shift in the UV emission peak is due to the quantum confinement effect. The peak around 430 nm is blue emission (BE) which is attributed to intrinsic defects such as oxygen and zinc interstitials [16]. It can be observed that only small changes in the parameters are observed for the sample milled 20 h, which is wider and less-quantum efficiency. The mechanical milling produces different kinds of defects in the powders giving place to an increase in the possible recombination mechanisms. Table 1 summarized the UV and PL characteristics of the samples.

4. Conclusion

ZnO nanoparticles were successfully synthesized at room temperature via mechanical milling. Absorption spectra

demonstrate sharp excitonic peaks and blue shifted corresponding to quantum confinement effect. The absorbance was increased as the milling time increases. Strong PL lines were recorded in the UV and blue region. The crystal structure of ZnO nanoparticles is the same as that of bulk ZnO, though some amount of internal strain induced by the severe mechanical deformation.

Acknowledgment

The authors gratefully acknowledge financial support from Ministry of Higher Education of Malaysia under Fundamental Research Grant Scheme FRGS Grant (no. FP015/2008C).

References

- [1] A. D. Yoffe, "Low-dimensional systems: quantum size effects and electronic properties of semiconductor microcrystallites (zero-dimensional systems) and some quasi-two-dimensional systems," *Advances in Physics*, vol. 42, no. 2, pp. 173–266, 1993.
- [2] Y. Kayanuma, "Quantum-size effects of interacting electrons and holes in semiconductor microcrystals with spherical shape," *Physical Review B*, vol. 38, no. 14, pp. 9797–9805, 1988.
- [3] L. E. Brus, "Zero-dimensional "excitons" in semiconductor clusters," *IEEE Journal of Quantum Electronics*, vol. 22, no. 9, pp. 1909–1914, 1986.
- [4] M. V. Rama Krishna and R. A. Friesner, "Exciton spectra of semiconductor clusters," *Physical Review Letters*, vol. 67, no. 5, pp. 629–632, 1991.
- [5] T. Kumpika, W. Thongsuwan, and P. Singjai, "Optical and electrical properties of ZnO nanoparticle thin films deposited on quartz by sparking process," *Thin Solid Films*, vol. 516, no. 16, pp. 5640–5644, 2008.
- [6] H. Yano, J. Sugiyama, A. N. Nakagaito et al., "Optically transparent composites reinforced with networks of bacterial nanofibers," *Advanced Materials*, vol. 17, no. 2, pp. 153–155, 2005.
- [7] R. J. Nussbaumer, W. R. Caseri, P. Smith, and T. Tervoort, "Polymer-TiO₂ nanocomposites: a route towards visually transparent broadband UV filters and high refractive index materials," *Macromolecular Materials and Engineering*, vol. 288, no. 1, pp. 44–49, 2003.
- [8] V. Srikant and D. R. Clarke, "On the optical band gap of zinc oxide," *Journal of Applied Physics*, vol. 83, no. 10, pp. 5447–5451, 1998.
- [9] A. Moballegh, H. R. Shahverdi, R. Aghababazadeh, and A. R. Mirhabibi, "ZnO nanoparticles obtained by mechanochemical technique and the optical properties," *Surface Science*, vol. 601, no. 13, pp. 2850–2854, 2007.
- [10] A. K. Singh, S. B. Patil, and V. C. Janu, "Structural, optical and electrical characterization of nano-structured ZnO thin films deposited by solution growth technique," in *Proceedings of the 8th IEEE Conference on Nanotechnology, (NANO '08)*, vol. 2, pp. 760–763, Arlington, Tex, USA, August 2008.
- [11] L. C. Damonte, L. A. Mendoza Zélis, B. M. Soucase, and M. A. Hernández Fenollosa, "Nanoparticles of ZnO obtained by mechanical milling," *Powder Technology*, vol. 148, no. 1, pp. 15–19, 2004.
- [12] A. Sasaki, W. Hara, A. Mastuda, N. Tateda, K. Saitom, and M. Yoshimoto, "Buffer-enhanced room-temperature growth and characterization of epitaxial ZnO thin films," *Applied Physics Letters*, vol. 86, no. 23, Article ID 231911, 3 pages, 2005.

- [13] A. Z. Sadek, W. Wlodarski, K. Kalantar-Zadeh et al., "H₂ and NO₂ gas sensors with ZnO nanobelt layer on 36° LiTaO₃ and 64° LiNbO₃ SAW transducers," in *Proceedings of the 4th IEEE Conference on Sensors*, pp. 1343–1346, Irvine, Calif, USA, November 2005.
- [14] M. K. Patra, K. Manzoor, M. Manoth, S. R. Vadera, and N. Kumar, "Studies of luminescence properties of ZnO and ZnO: Zn nanorods prepared by solution growth technique," *Journal of Luminescence*, vol. 128, no. 2, pp. 267–272, 2008.
- [15] A. K. Singh, V. Viswanath, and V. C. Janu, "Synthesis, effect of capping agents, structural, optical and photoluminescence properties of ZnO nanoparticles," *Journal of Luminescence*, vol. 129, no. 8, pp. 875–878, 2009.
- [16] A. Ghosh, N. G. Deshpande, Y. G. Gudage et al., "Effect of annealing on structural and optical properties of zinc oxide thin film deposited by successive ionic layer adsorption and reaction technique," *Journal of Alloys and Compounds*, vol. 469, no. 1-2, pp. 56–60, 2009.

Research Article

A Two-Step Method to Synthesize BaSn(OH)₆ Crystalline Nanorods and Their Thermal Decomposition to Barium Stannate

Xiaohong Wu,¹ Gang Lv,² Xiaoyan Hu,² and Yiwen Tang²

¹ College of Electronic Information Engineering, Wuhan Polytechnic, Wuhan 430074, China

² Institute of Nanoscience and Nanotechnology, Central China Normal University, Wuhan 430079, China

Correspondence should be addressed to Gang Lv, ganglv@mail.ccnu.edu.cn

Received 6 August 2011; Accepted 4 October 2011

Academic Editor: Ting Zhu

Copyright © 2012 Xiaohong Wu et al. This is an open access article distributed under the Creative Commons Attribution License, which permits unrestricted use, distribution, and reproduction in any medium, provided the original work is properly cited.

A novel two-step technique is introduced to synthesize BaSn(OH)₆ nanorods. The method involves the preparation of precursor Na₂Sn(OH)₆ crystals in aqueous solution via hydrothermal method and the ion-exchange reaction between Na₂Sn(OH)₆ crystals and Ba²⁺ solution that followed, assisted by ultrasonic treatment. The BaSn(OH)₆ nanorods array are formed due to the split of plate-formed Na₂Sn(OH)₆ during the ion-exchange treatment. The influence of the surfactant on the growth of the one-dimensional (1D) BaSn(OH)₆ nanostructures is investigated. In addition, the powder BaSnO₃ has been obtained by thermal treatment at 450°C for 5 h under inert gas protecting condition using BaSn(OH)₆ nanorods as precursor. The 1D shape of BaSn(OH)₆ was retained after thermal treatment.

1. Introduction

As a perovskite-structured ceramic, BaSnO₃ is becoming more and more important in material technology because of its characteristic dielectric properties. It has been recently considered to be a new material for semiconductor gas sensors because of its high selectivity, sensitivity, and stability toward sensor materials for a lot of gases, including CO, H₂, Cl₂, NO_x, and humidity [1–4]. The mechanism of the gas sensitivity of this semiconducting oxide is a surface reaction process [5]. Thus, a large surface area of the oxide powder is of importance to its characteristic sensor properties. In the recent papers, nanostructures have demonstrated good sensitivity as sensing materials [6–9]. The 1D nanostructure of BaSnO₃ may improve the sensitivity of gas-sensing materials because of their shape and size. The micrometer BaSnO₃ has been synthesized by solid reaction [10], sol-gel method [11], and hydrothermal method [12]. A modified hydrothermal method was used to prepare BaSn(OH)₆ nanoparticle with diameter of 10 nm as precursor from treating SnO₂·xH₂O and Ba(OH)₂ solution at 250°C. Then, BaSnO₃ of 27 nm was obtained by recrystallizing BaSn(OH)₆ at 330°C. In this work, the peptization of precursor BaSn(OH)₆ was strictly

dependent on the pH value of the solution and the particle sizes of the SnO₂·xH₂O sol were necessary to be in the range of less than 20 nm [13]. More recently [14], we reported a new simple two-step technique to synthesize well-defined CdSnO₃·3H₂O nanocubes where their shape and size can be controlled by adjusting the experimental factors. The method involved the preparation of Na₂Sn(OH)₆ as starting materials via a hydrothermal method in solution, followed by the ion-exchange reaction between solid Na₂Sn(OH)₆ and Cd²⁺ solution, assisted by ultrasonic treatment. Our other works that followed revealed that the method could be extended to fabricate other kinds of stannate. In the present work, we applied this method to synthesize BaSn(OH)₆ nanostructure, and the morphology of the obtained product was nanorod array. The influences of reaction conditions, including surfactant and reaction time, on the growth of BaSn(OH)₆ nanorod array were investigated.

2. Experimental

5.0 g of SnCl₄ and 0.5 g of cetyltrimethylammonium bromide (CTAB) were dissolved in 50 mL of deionized water. 30 mL of 12.5 mol/L NaOH aqueous solution was then added

dropwise into the solution under vigorous stirring. The resulting slurry was transferred into a Teflon-lined stainless steel autoclave with a capacity of 100 mL treated under hydrothermal conditions at 180°C for 24 h. After the vessel was cooled to room temperature, the precursor $\text{Na}_2\text{Sn}(\text{OH})_6$ was obtained.

1.5 mmol of BaCl_2 was dissolved in 300 mL of deionized water to obtain an aqueous solution. The precursor obtained in the hydrothermal process was rapidly introduced to the Ba^{2+} aqueous solution. The slurry was ultrasonically treated for 30 min. The resultant $\text{BaSn}(\text{OH})_6$ was filtered, washed with distilled water and ethanol, and then dried at room temperature. The as-prepared $\text{BaSn}(\text{OH})_6$ was subsequently calcined at 450°C for 5 h under inert gas protecting conditions (99.9% Ar).

The crystallinity and phase purity of the product were examined by a Bruker D8 advanced X-ray diffractometer (XRD) with monochromatized $\text{Cu K}\alpha$ radiation ($\lambda = 1.5418 \text{ \AA}$). The morphology and structure of the product were characterized using a JEOL JEM-2010 transmission electron microscope (TEM) operating at 200 kV and a JEOL JSM-6700F scanning electron microscope (SEM).

3. Results and Discussion

Figure 1(a) shows the XRD patterns of the product prepared by hydrothermal method. All the detectable peaks in Figure 1(a) can be assigned by their peak position to the hexagonal structure of $\text{Na}_2\text{Sn}(\text{OH})_6$ with lattice parameters of $a = 5.94 \text{ \AA}$ and $c = 14.1 \text{ \AA}$. These parameters match well with the information for JCPDS file card 24-1143. Figure 1(b) shows the XRD patterns of the sample obtained from the reaction between solid $\text{Na}_2\text{Sn}(\text{OH})_6$ and the BaCl_2 aqueous solution. The peak positions are consistent with the standard diffraction pattern of $\text{BaSn}(\text{OH})_6$ (JCPDS 09-0053), with no other crystalline phase observed.

Scanning electron microscopy (SEM) analyses were used to explore the morphology of the products. Figure 2(a) shows the image of the precursor $\text{Na}_2\text{Sn}(\text{OH})_6$, which clearly displays that the product is composed of sheets in different sizes. The SEM image in Figure 2(b) reveals that the $\text{BaSn}(\text{OH})_6$ consists of nanorod arrays with diameters of 90–110 nm and lengths up to several micrometers. The most of the nanorods are aligned in the same direction. To provide further insight into the nanostructures of the rods, TEM investigations are also performed. As shown in Figure 3(a), the $\text{BaSn}(\text{OH})_6$ nanorods are straight, uniform, and tightly packed as a bundle array. The selective-area electron diffraction (SAED) (Figure 3(b)) reveals that the nanorods are crystalline in structure.

From a great deal of experimental work, we find that the surfactant plays an important role in controlling the morphology of the sample. The use of CTAB is crucial to the formation of $\text{BaSn}(\text{OH})_6$ nanorod arrays. Nanosheets were obtained when CTAB was replaced by polyethylene glycol (PEG), and nondirectional nanorods were obtained in the presence of polyvinylpyrrolidone (PVP), which were shown in Figures 4(a) and 4(b). On the basis of our detailed examination and the information we have gathered [15], a

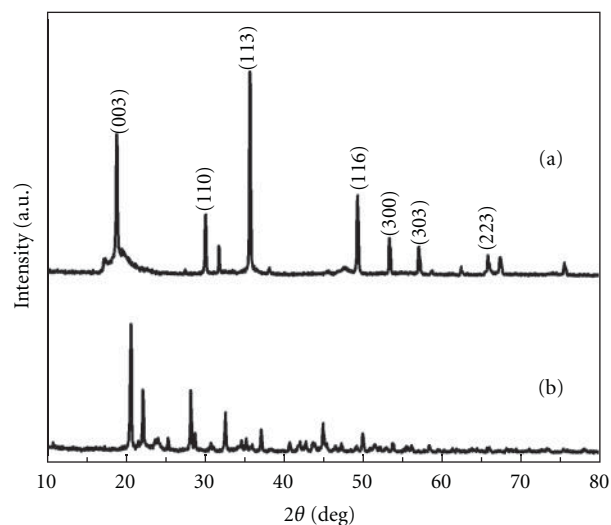
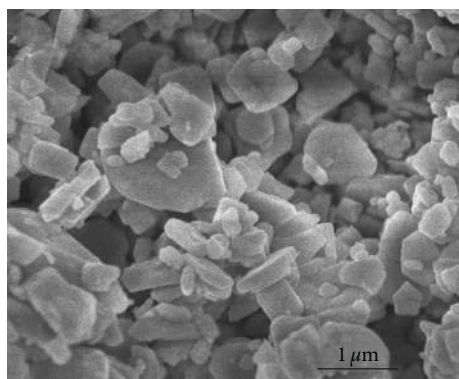


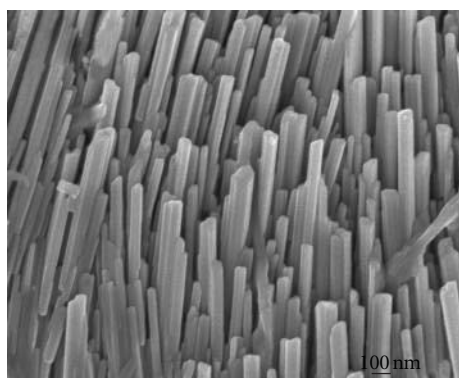
FIGURE 1: XRD patterns of the products: (a) $\text{Na}_2\text{Sn}(\text{OH})_6$ and (b) $\text{BaSn}(\text{OH})_6$.

formation process of the $\text{BaSn}(\text{OH})_6$ nanorods array can be proposed. An illustration of the $\text{Na}_2\text{Sn}(\text{OH})_6$ formation process is shown in Figure 5. When NaOH solution was added dropwise into the SnCl_4 and CTAB mixture solution, the precipitation of $\text{Sn}(\text{OH})_4$ was obtained immediately. By keeping on adding NaOH, the $\text{NaSn}(\text{OH})_6$ was formed (Figure 5(a)). On the other hand, it was reported that the anionic surfactant CTAB can be made to form micelles [16]. In this system, single-chain surfactant molecules CTAB reacted preferentially with $\text{Sn}(\text{OH})_4^{2-}$ polyanions which displace the original surfactant monoanions (Figure 5(b)). Then anionic surfactant CTAB formed sandwich micelles due to the anion charge density and shape requirement (Figure 5(c)). The condensation of $\text{Sn}(\text{OH})_4^{2-}$ absorbed by CTAB is minimal at low temperature according to cooperation interactions of ion-pairs charges and organic Van der Waals forces. After hydrothermal treatment at 180°C for 24 h, the surfactant reorganized the changing interface charge density, so more $\text{Sn}(\text{OH})_4^{2-}$ was absorbed by CTAB. The inorganic surfactant composites $\text{CTAB}^+-\text{Sn}(\text{OH})_4^{2-}-\text{Na}^+-\text{Sn}(\text{OH})_4^{2-}-\text{CTAB}^+$ were formed as shown in Figure 5(d). Finally, when the inorganic surfactant composites were introduced to Ba^{2+} aqueous solution, the Ba^{2+} replaced the Na^+ of these composites assisted by ultrasonic treatment. Accompanying the formation of $\text{BaSn}(\text{OH})_6$, strong stress appeared in the crystal. To release the stress and lower the total energy, the original plates split to nanorods. So the possible function of the surfactant CTAB in the present process is to be a template for the formation of 1D nanostructures.

For a complete view of the formation process of the $\text{BaSn}(\text{OH})_6$ nanorods array and their growth mechanism, a detailed time-dependent morphology evolution study during the ultrasonic process was conducted (Figures 6(a)–6(d)). Most of the product obtained after 5 min treatment exhibited micrometer sheets, and the rodlike structure could



(a)



(b)

FIGURE 2: SEM images of the products: (a) $\text{Na}_2\text{Sn}(\text{OH})_6$ and (b) $\text{BaSn}(\text{OH})_6$.

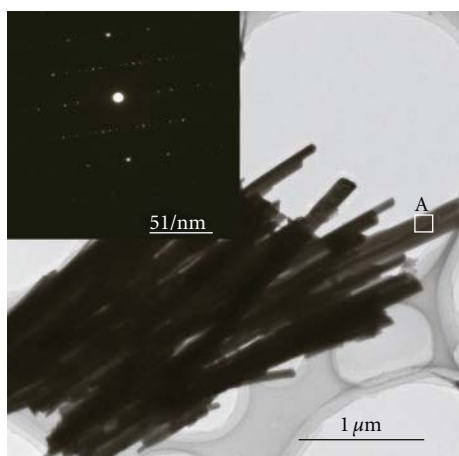
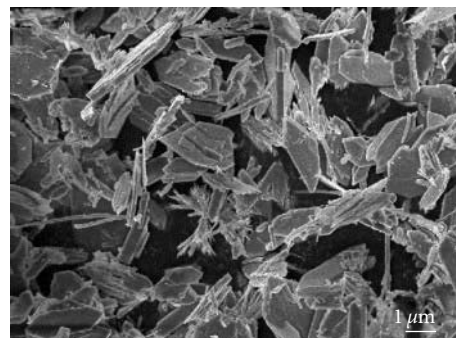
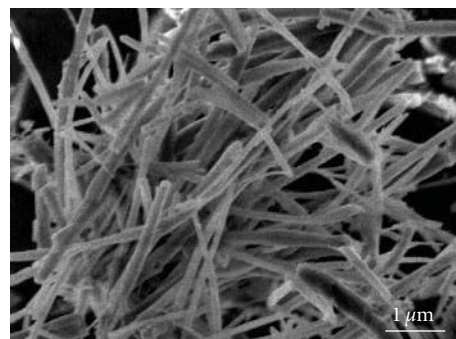


FIGURE 3: TEM and SAED images of the $\text{BaSn}(\text{OH})_6$ nanorods.

be seen on the big sheets (Figure 6(a)). Prolonging the reaction time to 10 min, more and more nanorods were formed as shown in Figure 6(b). For reaction times of 20 min, the product consisted predominantly of nanorods that were adherent to each other (Figure 6(c)). The ion-exchange reaction was complete at 30 min, and the nanorods were separate due to the partial dissolution of the CTAB (Figure 6(d)).



(a)



(b)

FIGURE 4: SEM images of the products in the presence of (a) PEG and (b) PVP.

In order to investigate the thermal stability and its phase transformation, we thermally treated $\text{BaSn}(\text{OH})_6$ at 450°C . The phase of the product was studied by XRD measurement as shown in Figure 7. All of the reflections could be indexed to the BaSnO_3 phase with the cubic structure BaSnO_3 (JCPDS 74-1300). The morphology of the final product BaSnO_3 was investigated with SEM. As shown in Figure 8, the rod shape retained after heat treatment at 450°C , but their feature of unidirection was lost and the size of rod was increased from average 100 nm to about 400 nm due to the recrystallization of nanorods. To get further information of the nanorods, Brunauer-Emmett-Teller (BET) N_2 adsorption-desorption analysis was performed. Figure 9 displays the adsorption-desorption isotherm, from which the BET surface area could be calculated as $22.09\text{ m}^2\text{g}^{-1}$. The value is larger than that of the nanoparticles previously reported in the literature [12], which means that the 1D BaSnO_3 nanorods we prepared may have a potential application in gas sensors or catalysts.

4. Conclusions

It has been found that a two-step technique can be used to synthesize nanocrystalline stannates. Well-defined $\text{BaSn}(\text{OH})_6$ nanorods have been successfully prepared using this novel method in high yields. The formation of the plate-formed precursor $\text{Na}_2\text{Sn}(\text{OH})_6$ plays a very important role in the final morphology of sample. The $\text{BaSn}(\text{OH})_6$ nanorods array were formed due to the split of $\text{Na}_2\text{Sn}(\text{OH})_6$ during

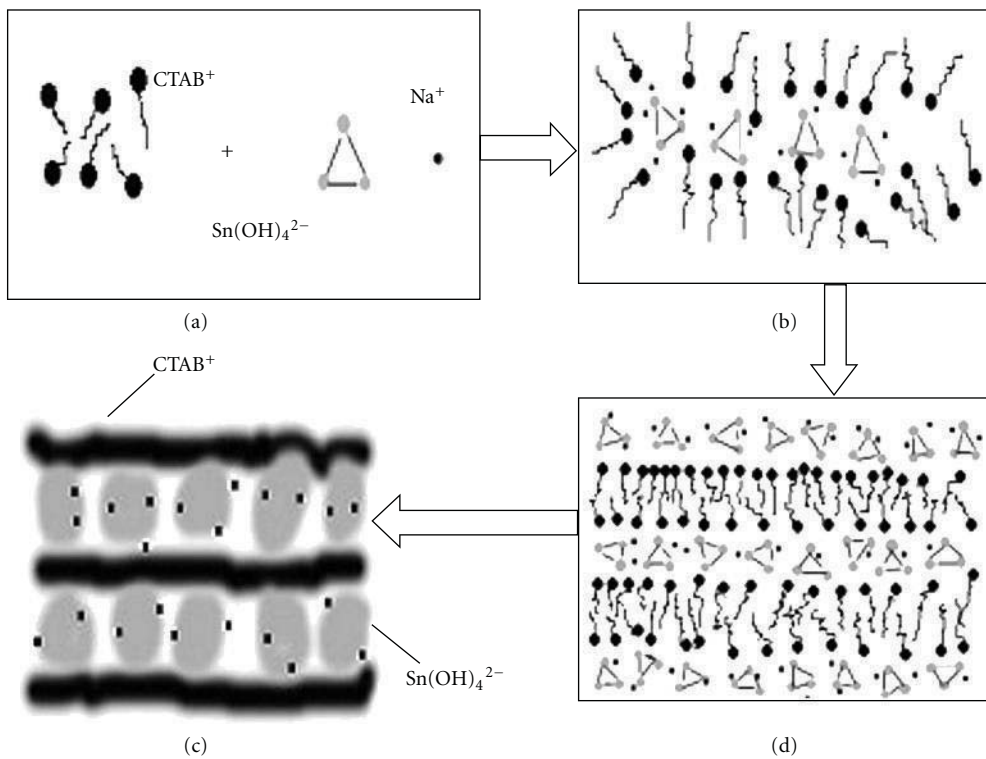


FIGURE 5: Schematic representation of different periods in the CTAB-assisted hydrothermal preparation of $\text{Na}_2\text{Sn(OH)}_6$.

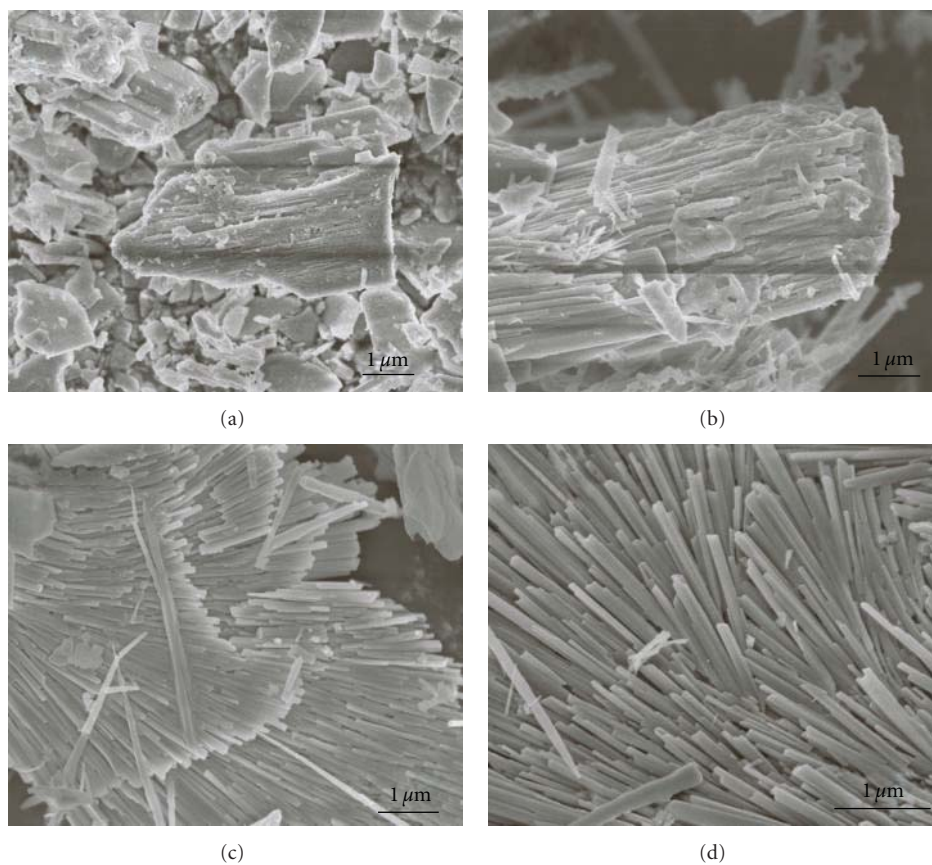


FIGURE 6: SEM images of the BaSn(OH)_6 obtained after an ion-exchange time of (a) 5 min, (b) 10 min, (c) 20 min, and (d) 30 min.

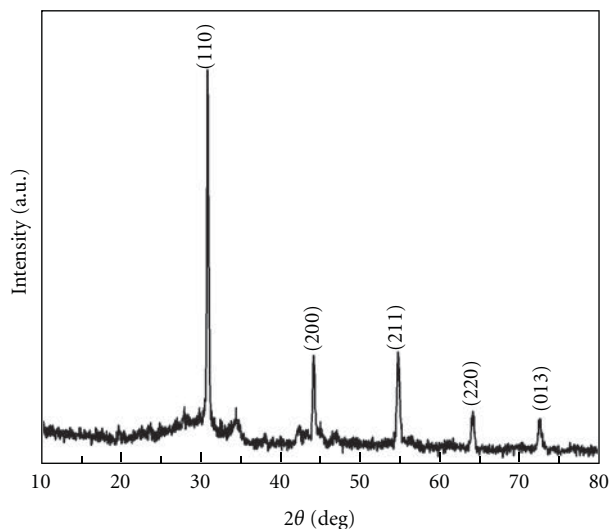


FIGURE 7: XRD pattern of BaSnO₃.

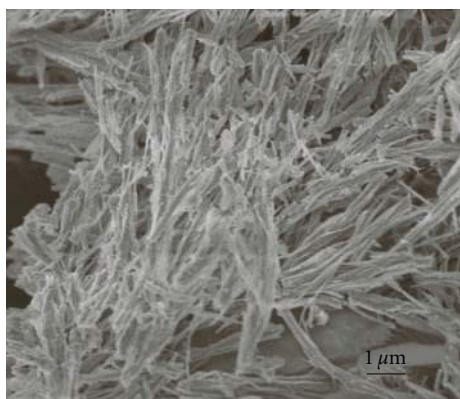


FIGURE 8: SEM image of the BaSnO₃.

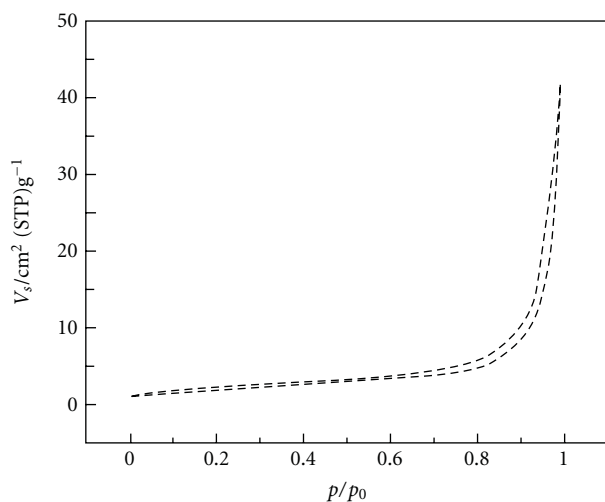


FIGURE 9: N₂ adsorption isotherm of BaSnO₃ nanorods.

the ion-exchange treatment. BaSnO₃ has been obtained by thermally treating BaSn(OH)₆ nanorods at 450°C, for 5 h under an inert gas protecting condition. The rod shape of BaSn(OH)₆ was sustained after thermal decomposition to BaSnO₃.

Acknowledgment

The paper is financially supported by self-determined research funds of CCNU from the colleges' basic research and operation of MOE of China (CCNU09A02011).

References

- [1] J. Cerdà, J. R. Morante, and A. L. Spetz, "BaSnO₃ oxygen sensors without the need of a reference electrode," in *2nd IEEE International Conference on Sensors*, pp. 1164–1165, October 2003.
- [2] X. Chu, "Dilute CH₃SH-sensing characteristics of BaSnO₃ thick film sensor," *Materials Science and Engineering B*, vol. 106, no. 3, pp. 305–307, 2004.
- [3] M. Viviani, M. T. Buscaglia, V. Buscaglia, M. Leoni, and P. Nanni, "Barium perovskites as humidity sensing materials," *Journal of the European Ceramic Society*, vol. 21, no. 10–11, pp. 1981–1984, 2001.
- [4] C. V. G. Reddy, S. V. Manorama, and V. J. Rao, "Preparation and characterization of barium stannate: application as a liquefied petroleum gas sensor," *Journal of Materials Science: Materials in Electronics*, vol. 12, no. 2, pp. 137–142, 2001.
- [5] O. K. Tan, W. Zhu, Q. Yan, and L. B. Kong, "Size effect and gas sensing characteristics of nanocrystalline xSnO₂-(1-x)α-Fe₂O₃ ethanol sensors," *Sensors and Actuators, B*, vol. 65, no. 1, pp. 361–365, 2000.
- [6] X. Wang, J. Zhang, and Z. Zhu, "Ammonia sensing characteristics of ZnO nanowires studied by quartz crystal microbalance," *Applied Surface Science*, vol. 252, no. 6, pp. 2404–2411, 2006.
- [7] G. Xu, Y. W. Zhang, X. Sun, C. L. Xu, and C. H. Yan, "Synthesis, structure, texture, and CO sensing behavior of nanocrystalline tin oxide doped with scandia," *Journal of Physical Chemistry B*, vol. 109, no. 8, pp. 3269–3278, 2005.
- [8] Y. Zhu, J. Shi, Z. Zhang, C. Zhang, and X. Zhang, "Development of a gas sensor utilizing chemiluminescence on nanosized titanium dioxide," *Analytical Chemistry*, vol. 74, no. 1, pp. 120–124, 2002.
- [9] C. J. Martinez, B. Hockey, C. B. Montgomery, and S. Semancik, "Porous tin oxide nanostructured microspheres for sensor applications," *Langmuir*, vol. 21, no. 17, pp. 7937–7944, 2005.
- [10] A. S. Deepa, S. Vidya, P. C. Manu, S. Solomon, A. John, and J. K. Thomas, "Structural and optical characterization of BaSnO₃ nanopowder synthesized through a novel combustion technique," *Journal of Alloys and Compounds*, vol. 509, no. 5, pp. 1830–1835, 2011.
- [11] J. Cerdà, J. Arbiol, R. Diaz, G. Dezanneau, and J. R. Morante, "Synthesis of perovskite-type BaSnO₃ particles obtained by a new simple wet chemical route based on a sol-gel process," *Materials Letters*, vol. 56, no. 3, pp. 131–136, 2002.
- [12] W. Lu and H. Schmidt, "Lyothermal synthesis of nanocrystalline BaSnO₃ powders," *Ceramics International*, vol. 34, no. 3, pp. 645–649, 2008.
- [13] W. Lu and H. Schmidt, "Hydrothermal synthesis of nanocrystalline BaSnO₃ using a SnO₂·xH₂O sol," *Journal of the European Ceramic Society*, vol. 25, no. 6, pp. 919–925, 2005.

- [14] Y. Tang, Y. Jiang, Z. Jia, B. Li, L. Luo, and L. Xu, "Synthesis of $\text{CdSnO}_3 \cdot 3\text{H}_2\text{O}$ nanocubes via ion exchange and their thermal decompositions to cadmium stannate," *Inorganic Chemistry*, vol. 45, no. 26, pp. 10774–10779, 2006.
- [15] Q. Huo, D. I. Margolese, U. Ciesla et al., "Organization of organic molecules with inorganic molecular species into nanocomposite biphasic arrays," *Chemistry of Materials*, vol. 6, no. 8, pp. 1176–1191, 1994.
- [16] C. C. Huang, C. S. Yeh, and C. J. Ho, "Laser ablation synthesis of spindle-like gallium oxide hydroxide nanoparticles with the presence of cationic cetyltrimethylammonium bromide," *Journal of Physical Chemistry B*, vol. 108, no. 16, pp. 4940–4945, 2004.

Research Article

Preparation and Characterization of Ni(OH)₂ and NiO Mesoporous Nanosheets

Changyu Li and Shouxin Liu

College of Material Science and Engineering, Northeast Forestry University, Harbin 150040, China

Correspondence should be addressed to Shouxin Liu, liushouxin@126.com

Received 30 July 2011; Revised 30 September 2011; Accepted 30 September 2011

Academic Editor: Bo Zou

Copyright © 2012 C. Li and S. Liu. This is an open access article distributed under the Creative Commons Attribution License, which permits unrestricted use, distribution, and reproduction in any medium, provided the original work is properly cited.

Mesoporous nanosheets of single-crystalline β -nickel hydroxide (β -Ni(OH)₂) were successfully synthesized via a facile hydrothermal method using Ni(NO₃)₂ · 6H₂O as precursor in a mixed solution of sodium hydroxide (NaOH) and sodium dodecylbenzenesulfonate (SDBS). Single-crystalline nickel oxide (NiO) mesoporous nanosheets can be obtained through a thermal decomposition method using β -Ni(OH)₂ mesoporous nanosheets as precursor. The influences of SDBS and hydrothermal treatment were carefully investigated; the results showed that they played important roles in the formation of β -Ni(OH)₂ mesoporous nanosheets. The as-obtained β -Ni(OH)₂ and NiO were characterized by X-ray diffraction (XRD), transmission electron microscopy (TEM), thermal gravity-differential thermal analysis (TG-DTA), and specific surface area, and pore size test.

1. Introduction

The development of nanomaterials is attracting increasing attentions due to their unique physical and chemical properties that are different from conventional bulk materials. It is well known that the size, morphology, and structure of nanomaterials significantly influence their physical and chemical properties and, therefore, their applications [1–3]. The nanomaterials with mesoporous structures Especially have technical advances in various fields, such as adsorption, separation, catalysis, drug delivery, sensors, photonics, and nanodevices [4, 5].

As reported, nickel hydroxide (Ni(OH)₂) has attracted increasing interests due to its applications in alkaline rechargeable batteries (such as Ni/MH, Ni/Zn, Ni/Cd, and Ni/Fe, [6–8]), which are most widely used in many applications ranging from power tools to portable electronics and electric vehicles [9]. There are two phases of Ni(OH)₂, known as α -Ni(OH)₂ and β -Ni(OH)₂. Single-crystalline β -Ni(OH)₂ nanosheets have been demonstrated taking advantage of its intrinsic lamellar structure [9–11] and widely used due to its high stacking density and stability in alkaline condition compared with α -Ni(OH)₂. Recently, some reports have demonstrated that Ni(OH)₂ with a smaller crystalline

size and more crystalline defects possesses a higher chemical proton diffusion coefficient, and this will diminish the concentration polarization of protons during charge/discharge cycle, leading to a better charge/discharge cycling behavior [12]. Literatures have reported that the activity of Ni(OH)₂ electrode could be significantly improved when nanosized Ni(OH)₂ was added into microsized Ni(OH)₂ [13, 14]; especially, nanosized Ni(OH)₂ with mesoporous structures can enhance the electrochemical performance greatly [15]. Furthermore, NiO is a very important p-type semiconductor with a direct band gap of 3.5 eV and often used as catalyst, electrochemical capacitor, fuel cell electrode, gas sensor, and so forth [16–18]. NiO can be obtained by calcinating the corresponding Ni(OH)₂ simply in air, and the shape of Ni(OH)₂ particles could be maintained [19]. To date, numerous works [20–24] have been developed to synthesize Ni(OH)₂ with different morphologies because the electrochemical performances of Ni(OH)₂ are directly affected by its morphology and size [25–27]. Chen and Gao [10] reported the synthesis of different morphologies of nickel hydroxide through using ethanol as growth media. Meyer et al. [11] synthesized platelet-like nanoparticles of nickel hydroxide. Matsui et al. [28] obtained Ni(OH)₂ nanorods using carbon-coated anodic alumina film in hydrothermal

conditions. However, to obtain well-defined $\text{Ni}(\text{OH})_2$ nanostructures with mesoporous structure is still the challenge in nanochemistry and nanomaterials.

Herein, we demonstrate a facile method for the synthesis of single-crystal $\beta\text{-Ni}(\text{OH})_2$ mesoporous nanosheets, and NiO mesoporous nanosheets can also be obtained through the thermal decomposition using the as-prepared $\beta\text{-Ni}(\text{OH})_2$ as precursor.

2. Experimental

All of the reagents, except SDBS (chemical purity), were of analytical grade and used as received without further purification. In a typical experiment, 0.370 g $\text{Ni}(\text{NO}_3)_2 \cdot 6\text{H}_2\text{O}$ and 0.930 g SDBS were dissolved in 80 mL distilled water under magnetic stirring for 15 min to form a homogeneous solution at room temperature, and then 0.170 g NaOH was added into the solution. Afterward, the solution was transferred into a 100 mL Teflon-lined stainless autoclave, sealed and maintained at 140°C for 24 h, and then cooled to room temperature naturally. The products were collected, washed several times with distilled water and absolute ethanol, and dried at 60°C in air. To study the influences of SDBS and hydrothermal treatment on the formation of $\beta\text{-Ni}(\text{OH})_2$ nanosheets, parallel experiments were carried out with keeping other reaction conditions unchanged.

As-prepared $\beta\text{-Ni}(\text{OH})_2$ was calcined in air at 400°C for 2 h to produce NiO .

X-ray diffraction (XRD) patterns of the prepared samples were recorded on a D/max-r B X-ray diffractometer with graphite-monochromatized $\text{CuK}\alpha$ radiation ($\lambda = 1.5418 \text{ \AA}$), employing a scanning rate of 4°/min in the range from 15° to 90°. The size and morphology of the products were characterized by H-7650 transmission electron microscopy (TEM). High-resolution transmission electron microscopy (HRTEM, Tecnai F30) with the selected area of electron-diffraction (SAED) was employed to investigate the detailed structure of $\beta\text{-Ni}(\text{OH})_2$ microstructures. The N_2 adsorption-desorption isotherms and Barrett-Joyner-Halenda (BJH) pore size distribution were investigated on a Micromeritics ASAP 2020 equipment. TG-DSC (a Pyris Diamond thermogravimetric/DSC apparatus) was used to analyze the thermal behavior of samples with a heating rate of 10°C/min from room temperature to 600°C in air.

3. Results and Discussion

In Figure 1, curve (a) shows the XRD pattern of $\beta\text{-Ni}(\text{OH})_2$ prepared by the typical method. All diffraction peaks can be indexed to the pure hexagonal phase of $\beta\text{-Ni}(\text{OH})_2$ (JCPDS, file No. 14-0117). No peaks from impurities are observed, indicating that the product was pure phase. Curve (b) shows the XRD pattern of the $\beta\text{-Ni}(\text{OH})_2$ sample prepared in the absence of SDBS, from which, it is obvious to see the intensity change of some peaks compared with curve (a). Curve (c) is the XRD pattern of $\text{Ni}(\text{OH})_2$ prepared at room temperature. As shown, the Bragg reflections are broad, indicating that this sample has small size and poor

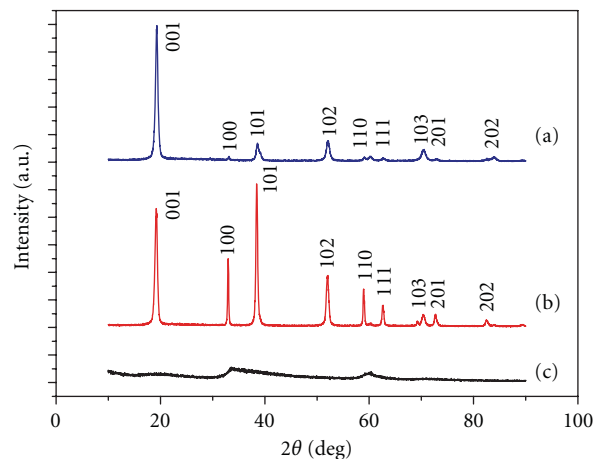


FIGURE 1: XRD patterns of the prepared $\beta\text{-Ni}(\text{OH})_2$ samples: (a) with using SDBS; (b) without using SDBS; (c) without hydrothermal treatment.

crystallinity. According to curve (a) and curve (c), it proves that hydrothermal treatment plays an important role in improving their crystallinity. This result is consistent with the literature [29, 30].

As known, the morphology and size of nanoparticles prepared by hydrothermal methods could be well-controlled by the addition of certain surfactant. Many theories have also been proposed to describe the mechanism of the shape-revolution process; however, they did not carry much conviction. From the difference between curve (a) and (b) in Figure 1, it can be concluded that all diffraction peak directions, except for [001] direction, are suppressed with the addition of SDBS. In other words, the prepared $\beta\text{-Ni}(\text{OH})_2$ has a preferential [001] growth direction in the presence of SDBS. It is well known that the surfactant in solution will aggregate into micelles. During the reaction, the micelles play the roles of “seeds;” the originally produced clusters will aggregate on the micelles, and further grow to nanoproductions, which can be called a special soft template technique to synthesize nanowires [31]. In our case, this process slows down the reaction rate of Ni^{2+} and OH^- and determines the preferential growth direction of $\beta\text{-Ni}(\text{OH})_2$ nanoparticles.

Figure 2 shows the TEM images of the $\beta\text{-Ni}(\text{OH})_2$ products obtained from different reaction conditions. As indicated in Figure 2(a), the obtained $\beta\text{-Ni}(\text{OH})_2$ products are irregular hexagonal shapes with sharp edges and the edge sizes are in the range of 25–160 nm. The rod-like structures are formed because of some sheets being on edge in the grid. Figure 2(b) shows the TEM image of $\beta\text{-Ni}(\text{OH})_2$ nanosheets prepared without the presence of SDBS, indicating the smaller size. Figure 2(c) shows the product obtained without the hydrothermal treatment, from which we can see that the sample has an irregular shape and a poor crystallized structure. The results indicate that hydrothermal treatment plays an important role in the formation of $\beta\text{-Ni}(\text{OH})_2$ nanosheets; coinciding with the literature [32].

Figure 3(a) gives the magnified TEM image of the $\beta\text{-Ni}(\text{OH})_2$ nanosheets, the bright spots on the surface of

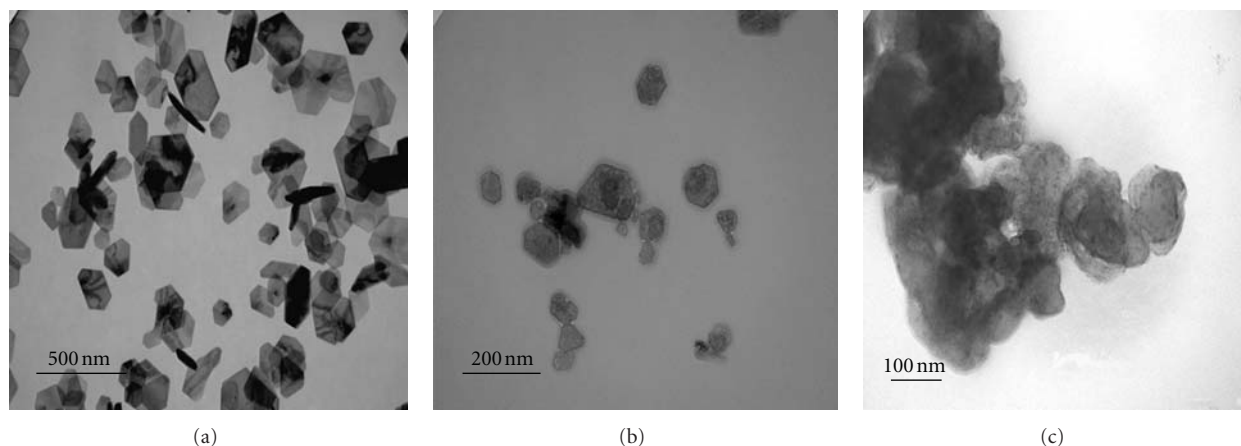


FIGURE 2: TEM images of the β -Ni(OH)₂ nanosheets prepared: (a) in the presence of SDBS, (b) without using SDBS, and (c) without hydrothermal treatment.

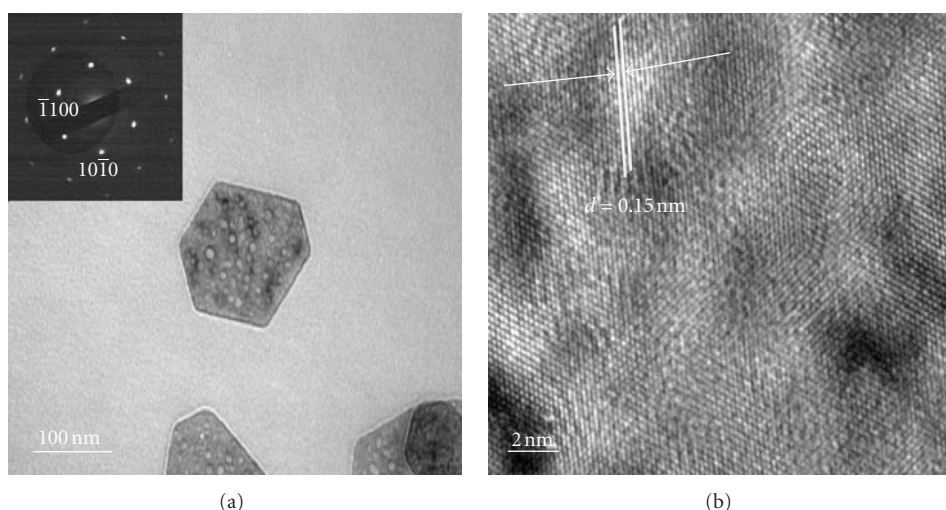


FIGURE 3: (a) TEM and (b) HRTEM images of β -Ni(OH)₂ mesoporous nanosheets. Inset of (a) is the corresponding SAED pattern.

the sheets reveal the porous structure. As shown in SEAD pattern (inset of Figure 3(a)), the as-prepared β -Ni(OH)₂ nanosheets are single crystals of hexagonal phase, and the surfaces of these hexagonal β -Ni(OH)₂ nanosheets are the (001) planes. Figure 3(b) exhibits the HRTEM image of the β -Ni(OH)₂ nanosheets, from which we can see that the crystal lattice planes are perfectly aligned. The lattice space of about 1.50 Å corresponds to the interplanar spacing of (003) planes, indicating that the β -Ni(OH)₂ nanosheets have a preferential [001] growth direction, consistent with the result of XRD as well.

The thermal property of the β -Ni(OH)₂ nanosheets was analyzed by TG-DSC, and the variations of heat and weight while β -Ni(OH)₂ was being sintered are recorded. As shown in Figure 4, there is an endothermic peak at 336.2°C in the DSC curve, accompanied by a weight loss of 18.81% (observed in TG curve at the same temperature), resulting from the thermal decomposition of β -Ni(OH)₂. When β -Ni(OH)₂ sample was heated to above 336.2°C, we can not

observe any obvious endothermic or exothermic peak in the DSC curve. The slight mass change between 336.2 and 500°C is due to the desorption of oxygen from bulk NiO, and we can conclude that β -Ni(OH)₂ precursor could be decomposed to NiO above 336.2°C completely. The observed weight loss of 18.81% is close to the calculated loss value of 19.4%.

Based on the TG and DSC results, in our experiments, the as-prepared β -Ni(OH)₂ nanosheets were calcined at 400°C for 2 h to obtain NiO nanosheets. Figure 5 gives the XRD pattern of NiO powder. All the diffraction peaks can be indexed to a face-centered cubic phase NiO with lattice parameters $a = 4.17$ (JCPDS, file No. 78-0643), and no diffraction peaks of Ni(OH)₂ or other impurities were observed, indicating that β -Ni(OH)₂ has been converted to NiO completely.

The size and morphology of the as-prepared NiO were examined by TEM. Figure 6(a) exhibits the TEM image of NiO, showing that the shape of nanosheets was maintained after the thermal decomposition of β -Ni(OH)₂. The

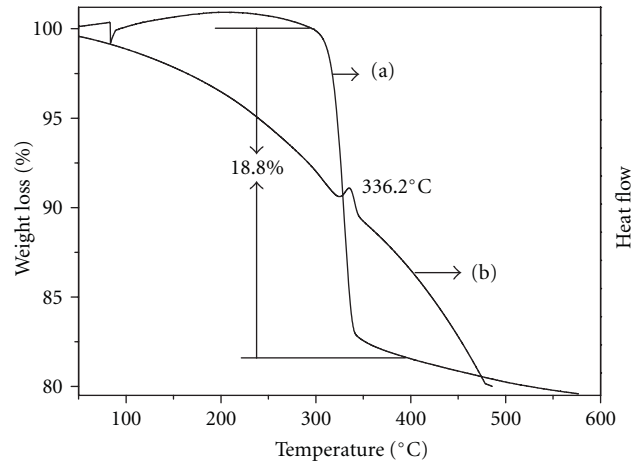


FIGURE 4: TG-DSC curves of β -Ni(OH)₂ mesoporous nanosheets.

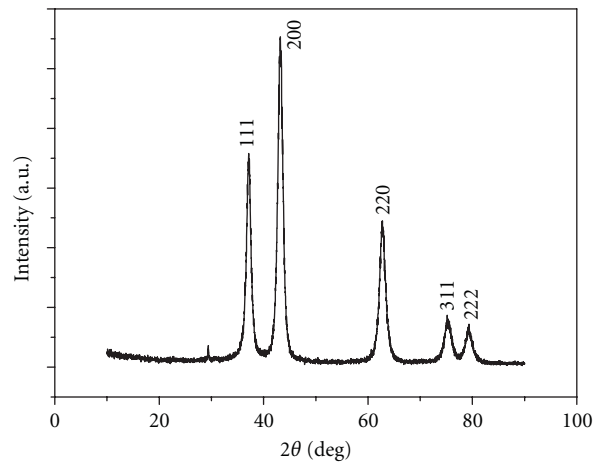


FIGURE 5: XRD pattern of the NiO mesoporous nanosheets.

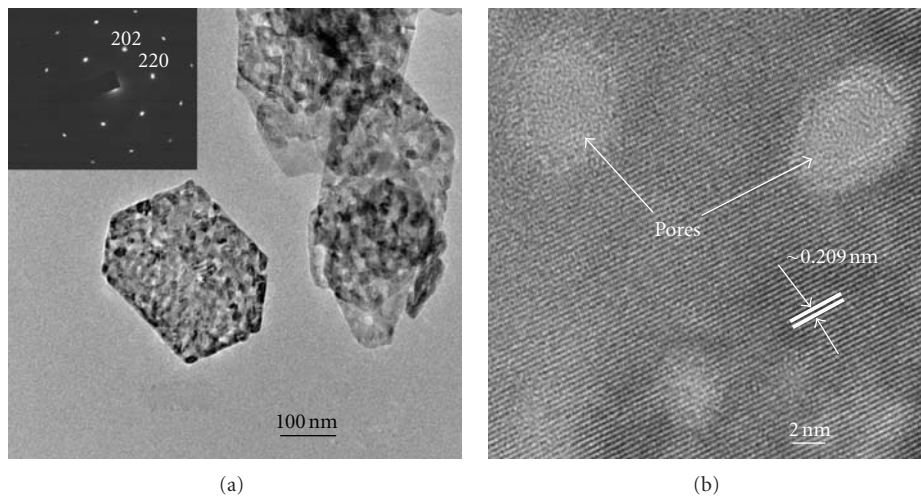


FIGURE 6: (a) TEM and (b) HRTEM images of NiO mesoporous nanosheets. Inset of (a) is the corresponding SAED pattern.

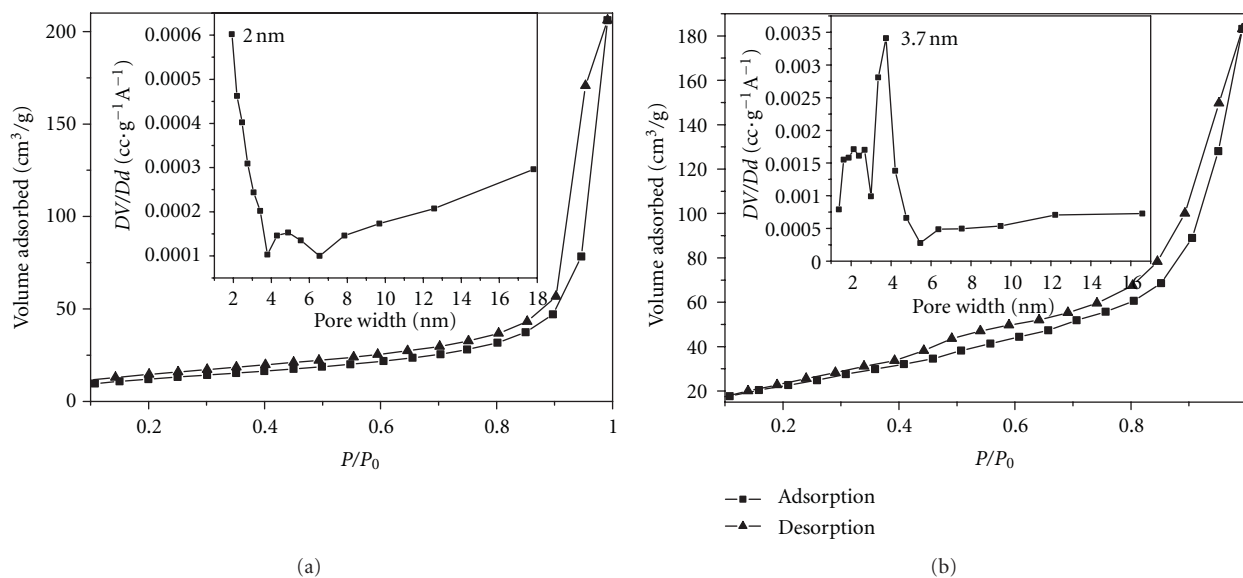


FIGURE 7: N_2 adsorption-desorption isotherm and pore size distribution (insets) of (a) β -Ni(OH) $_2$ and (b) NiO nanosheets.

corresponding SAED pattern of NiO nanosheets (inset in Figure 6(a)) exhibits many spots, indicating the nature of single crystal. The diffraction pattern can be indexed to the face-centered cubic NiO, consistent with the XRD result. Figure 6(b) is the HRTEM image of the as-prepared NiO nanosheets. As shown in it, the crystal lattice planes are perfectly aligned, and the lattice space is about 2.09 Å, corresponding to the interplanar spacing of 200 planes for cubic NiO. This reveals that the growth of the nanosheets follows the 200 direction; in other words, the nanosheets grow along with the a axis.

TEM images of β -Ni(OH) $_2$ and NiO (Figure 3(a) and Figure 6(a)) reveal their mesoporous structure by the wormhole-like porous structure on the surfaces of the sheets, then the mesoporous structures and pore sizes of β -Ni(OH) $_2$ and NiO were investigated by the N_2 adsorption/desorption techniques. The N_2 adsorption-desorption isotherms and BJH pore size distribution profiles (inset in Figures 7(a) and 7(b)) of β -Ni(OH) $_2$ and NiO were shown in Figure 7. It is obvious that these isotherms can be closely related to IV-type isotherm, characteristic of mesoporous materials. The BET surface area of mesoporous β -Ni(OH) $_2$ nanosheets is 46.6 m 2 g $^{-1}$, and the pore size distribution is peaked at around 2 nm (inset in Figure 7(a)). For NiO mesoporous nanosheets (mesoporous Ni(OH) $_2$ calcinated at 400°C for 2 h), the BET surface areas and the pore size distribution increase to 85.98 m 2 g $^{-1}$ and 3.7 nm, respectively.

4. Conclusion

In summary, a progressive production of β -Ni(OH) $_2$ mesoporous nanosheets with single-crystalline structure has been constructed via a one-step SDBS-assisted hydrothermal route. Using the obtained β -Ni(OH) $_2$ nanosheets as precursors, NiO nanosheets could be obtained by the calcination at 400°C for 2 h. The results of some parallel experiments

show that surfactant SDBS and hydrothermal treatment have important effect on the formation of β -Ni(OH) $_2$ nanosheets. The N_2 adsorption/desorption isotherms and BJH pore size distribution profiles of β -Ni(OH) $_2$ and NiO confirm their mesoporous structure.

Disclosure

The paper is original and it has been written by the stated authors who are all aware of its content and approve its submission. It has not been published previously and is not under consideration for publication elsewhere.

Conflict of Interests

There is no conflict of interest exists in our paper.

Acknowledgment

This work is supported by the National Nature Science Fund of China Grant no. 30771692.

References

- [1] Z. H. Kang, E. B. Wang, L. Gao et al., "One-step water-assisted synthesis of high-quality carbon nanotubes directly from graphite," *Journal of the American Chemical Society*, vol. 125, no. 45, pp. 13652–13653, 2003.
- [2] S. Y. Lian, E. B. Wang, Z. H. Kang et al., "Synthesis of magnetite nanorods and porous hematite nanorods," *Solid State Communications*, vol. 129, no. 8, pp. 485–490, 2004.
- [3] Z. B. Lei, G. J. Ma, M. Y. Liu et al., "Sulfur-substituted and zinc-doped in(OH) $_3$: a new class of catalyst for photocatalytic H_2 production from water under visible light illumination," *Journal of Catalysis*, vol. 237, no. 2, pp. 322–329, 2006.

- [4] T. Kresge, M. E. Leonowicz, W. J. Roth, J. C. Vartuli, and J. S. Beck, "Ordered mesoporous molecular sieves synthesized by a liquid-crystal template mechanism," *Nature*, vol. 359, no. 6397, pp. 710–712, 1992.
- [5] A. Navrotsky, O. Trofyrnluk, and A. Andrey, "Thermochemistry of microporous and mesoporous materials," *Chemical Reviews*, vol. 109, no. 9, pp. 3885–3902, 2009.
- [6] W.-K. Hu and D. Noréus, "Alpha nickel hydroxides as lightweight nickel electrode materials for alkaline rechargeable cells," *Chemistry of Materials*, vol. 15, no. 4, pp. 974–978, 2003.
- [7] X. M. He, J. J. Li, H. W. Cheng, C. Y. Jiang, and C. R. Wan, "Controlled crystallization and granulation of nano-scale β -Ni(OH)₂ cathode materials for high power Ni-MH batteries," *Journal of Power Sources*, vol. 152, no. 1-2, pp. 285–290, 2005.
- [8] W. G. Zhang, W. Q. Jiang, L. M. Yu, Z. Z. Fu, W. Xia, and M. L. Yang, "Effect of nickel hydroxide composition on the electrochemical performance of spherical Ni(OH)₂ positive materials for Ni-MH batteries," *International Journal of Hydrogen Energy*, vol. 34, no. 1, pp. 473–480, 2009.
- [9] Z. H. Liang, Y. J. Zhu, and X. L. Hu, " β -nickel hydroxide nanosheets and their thermal decomposition to nickel oxide nanosheets," *Journal of Physical Chemistry B*, vol. 108, no. 11, pp. 3488–3491, 2004.
- [10] D. L. Chen and L. Gao, "A new and facile route to ultrafine nanowires, superthin flakes and uniform nanodisks of nickel hydroxide," *Chemical Physics Letters*, vol. 405, no. 1–3, pp. 159–164, 2005.
- [11] M. Meyer, A. Bée, D. Talbot et al., "Synthesis and dispersion of Ni(OH)₂ platelet-like nanoparticles in water," *Journal of Colloid and Interface Science*, vol. 277, no. 2, pp. 309–315, 2004.
- [12] M. C. Bernard, R. Cortes, M. Keddad, H. Takenouti, P. Bernard, and S. Senyari, "Structural defects and electrochemical reactivity of β -Ni(OH)₂," *Journal of Power Sources*, vol. 63, no. 2, pp. 247–254, 1996.
- [13] X. J. Han, P. Xu, C. Q. Xu, L. Zhao, Z. B. Mo, and T. Liu, "Study of the effects of nanometer β -Ni(OH)₂ in nickel hydroxide electrodes," *Electrochimica Acta*, vol. 50, no. 14, pp. 2763–2769, 2005.
- [14] X. H. Liu and L. Yu, "Influence of nanosized Ni(OH)₂ addition on the electrochemical performance of nickel hydroxide electrode," *Journal of Power Sources*, vol. 128, no. 2, pp. 326–330, 2004.
- [15] B. Li, M. Ai, and Z. Xu, "Mesoporous β -Ni(OH)₂: synthesis and enhanced electrochemical performance," *Chemical Communications*, vol. 46, no. 34, pp. 6267–6269, 2010.
- [16] M. S. Wu and H. H. Hsieh, "Nickel oxide/hydroxide nanoplatelets synthesized by chemical precipitation for electrochemical capacitors," *Electrochimica Acta*, vol. 53, no. 8, pp. 3427–3435, 2008.
- [17] J. J. He, H. Lindström, A. Hagfeldt, and S. E. Lindquist, "Dye-sensitized nanostructured p-type nickel oxide film as a photocathode for a solar cell," *Journal of Physical Chemistry B*, vol. 103, no. 42, pp. 8940–8943, 1999.
- [18] X. F. Song and L. Gao, "Facile synthesis and hierarchical assembly of hollow nickel oxide architectures bearing enhanced photocatalytic properties," *Journal of Physical Chemistry C*, vol. 112, no. 39, pp. 15299–15305, 2008.
- [19] M. H. Cao, X. Y. He, J. Chen, and C. W. Hu, "Self-assembled nickel hydroxide three-dimensional nanostructures: a nanomaterial for alkaline rechargeable batteries," *Crystal Growth & Design*, vol. 7, no. 1, pp. 170–174, 2007.
- [20] D. N. Yang, R. M. Wang, M. S. He, J. Zhang, and Z. F. Liu, "Ribbon—and boardlike nanostructures of nickel hydroxide: synthesis, characterization, and electrochemical properties," *Journal of Physical Chemistry B*, vol. 109, no. 16, pp. 7654–7658, 2005.
- [21] S. M. Zhang and H. Zeng, "Self-assembled hollow spheres of β -Ni(OH)₂ and their derived nanomaterials," *Chemistry of Materials*, vol. 21, no. 5, pp. 871–883, 2009.
- [22] J. T. Sun, J. G. Cheng, C. W. Wang, X. L. Ma, M. Li, and L. J. Yuan, "Synthesis and morphological control of nickel hydroxide for lithium-nickel composite oxide cathode materials by an eddy circulating precipitation method," *Industrial and Engineering Chemistry Research*, vol. 45, no. 6, pp. 2146–2149, 2006.
- [23] L. H. Dong, Y. Chu, and W. D. Sun, "Controllable synthesis of nickel hydroxide and porous nickel oxide nanostructures with different morphologies," *Chemistry—A European Journal*, vol. 14, no. 16, pp. 5064–5072, 2008.
- [24] Q. Y. Li, R. N. Wang, Z. R. Nie, Z. H. Wang, and Q. Wei, "Preparation and characterization of nanostructured Ni(OH)₂ and NiO thin films by a simple solution growth process," *Journal of Colloid and Interface Science*, vol. 320, no. 1, pp. 254–258, 2008.
- [25] X. Han, X. Xie, C. Xu, D. Zhou, and Y. Ma, "Morphology and electrochemical performance of nano-scale nickel hydroxide prepared by supersonic coordination-precipitation method," *Optical Materials*, vol. 23, no. 1-2, pp. 465–470, 2003.
- [26] X. Y. Guan and J. C. Deng, "Preparation and electrochemical performance of nano-scale nickel hydroxide with different shapes," *Materials Letters*, vol. 61, no. 3, pp. 621–625, 2007.
- [27] T. N. Ramesh, "Crystallite size effects in stacking faulted nickel hydroxide and its electrochemical behaviour," *Materials Chemistry and Physics*, vol. 114, no. 2-3, pp. 618–623, 2009.
- [28] K. Matsui, T. Kyotani, and A. Tomita, "Hydrothermal synthesis of single-crystal Ni(OH)₂ nanorods in a carbon-coated anodic alumina film," *Advanced Materials*, vol. 14, no. 17, pp. 1179–1219, 2002.
- [29] M. H. Cao, T. F. Liu, S. Gao et al., "Single-crystal dendritic micro-pines of magnetic α -Fe₂O₃: large-scale synthesis, formation mechanism, and properties," *Angewandte Chemie International Edition*, vol. 44, no. 27, pp. 4197–4201, 2005.
- [30] H. B. Liu, L. Xiang, and Y. Jin, "Hydrothermal modification and characterization of Ni(OH)₂ with high discharge capability," *Crystal Growth and Design*, vol. 6, no. 1, pp. 283–286, 2006.
- [31] Y. K. Liu, Y. Chu, L. K. Yang, D. X. Han, and Z. X. Lü, "A novel solution-phase route for the synthesis of crystalline silver nanowires," *Materials Research Bulletin*, vol. 40, no. 10, pp. 1796–1801, 2005.
- [32] Y. W. Li, Q. X. Yang, J. H. Yao, Z. G. Zhang, and C. J. Liu, "Effect of synthesis temperature on the phase structure and electrochemical performance of nickel hydroxide," *Ionics*, vol. 16, no. 3, pp. 221–225, 2010.

Research Article

Electrochemical Fabrication of Shape-Controlled Copper Hierarchical Structures Assisted by Surfactants

Huaping Dong,¹ Yajun Wang,² Feifei Tao,¹ and Linxia Wang¹

¹Department of Chemistry and Chemical Engineering, Shaoxing University, Shaoxing, Zhejiang 312000, China

²College of Biological and Environmental Engineering, Zhejiang University of Technology, Zhejiang 310014, China

Correspondence should be addressed to Feifei Tao, fingal.tao@gmail.com

Received 1 August 2011; Accepted 21 September 2011

Academic Editor: William W. Yu

Copyright © 2012 Huaping Dong et al. This is an open access article distributed under the Creative Commons Attribution License, which permits unrestricted use, distribution, and reproduction in any medium, provided the original work is properly cited.

Various copper hierarchical structures assisted by surfactants were successfully fabricated combined with the electrodeposition technique. To the best of our knowledge, it is the first report on the controlled synthesis of metal copper hierarchical structures. All of the products synthesized in the presence and absence of surfactants, such as cetyltrimethylammonium bromide (CTAB), sodium dodecyl sulfate (SDS), or polyvinylpyrrolidone (PVP), were face-centered cubic copper, characterized by X-ray diffraction (XRD), indicating the surfactant-independent crystal structure. However, supplementing surfactants is helpful to construct hierarchical structures and exerts an important influence on copper morphologies. The absence of surfactants led to the formation of the nubby structures, while the use of surfactants resulted in the synthesis of the flower, dendrite, and sphere-like hierarchical morphologies. The effect of deposition time on the copper morphologies was investigated by scanning electron microscopy (SEM), and the possible formation mechanism of the copper hierarchical structures with various morphologies was discussed.

1. Introduction

In recent years, nanostructured materials with special morphologies have attracted considerable research interests for their unique magnetic, optical, and electronic properties, and potential applications [1–4]. Hierarchical materials constructed by nanostructures have been the research hotspots due to their size, or shaped-dependent properties, which are mainly determined by their composition, crystallinity, size, and morphology [5]. Therefore, in order to obtain prominent performance, much effort has been made on the composition, size, and morphology control of various materials. In the current stage, metallic hierarchical structures with various morphologies [6, 7] have been attracting extensive attention because of their potential applications in nanoscale devices, sensors, nonlinear optics, and magnetic storage media. So far, many synthetic methods including solvothermal reduction, electrodeposition, and template growth have been developed to prepare metallic hierarchical materials [8–10]. Among them, electrodeposition has received extensive attention due to the rich variation of

growth morphologies and the simplicity of the experimental setup [11–13].

The importance of metal copper for the next-generation on-chip interconnection has been well established since the first discovery that copper wiring has advantages of lower resistance, higher allowable current density, and increased scalability compared with the Ti/Au (Cu) wiring. Increasing efforts have been devoted to the fabrication of metal copper nanostructures with various morphologies in recent years due to the potential applications in biomimetic design [14], sensor [15], and catalysis [16]. However, there are few of the works on the preparation of metal copper nanostructures [14, 16], especially self-assembled hierarchical structures [17]. The lack of a facile method to selectively fabricate copper hierarchical structures assembled by nanomaterials with different morphologies still remains a huge obstacle to the material researchers.

In this paper, we reported a novel and simple method to successfully fabricate the copper hierarchical structures with morphological variety, such as flower-like structures self-assembled by nanosheets, dendrite-like crystals constructed

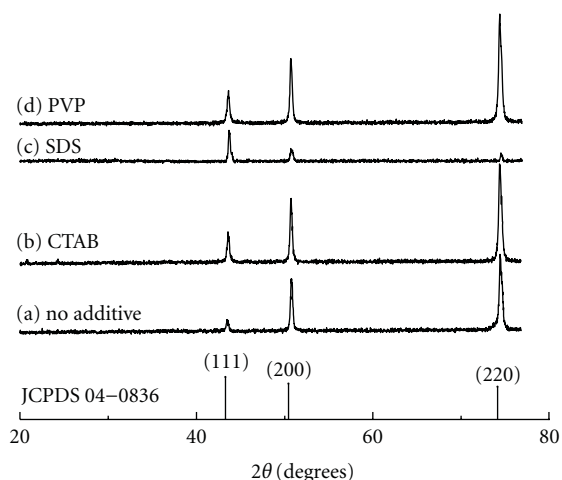


FIGURE 1: XRD patterns of the products fabricated with no additive (a), CTAB (b), SDS (c) and PVP (d) in the electrolyte.

by 1D nanostructures, and the large congeries built by sphere-like structures, by using the electrochemical deposition technology at room temperature. The metal copper materials with self-assembled structures can be selectively fabricated in the presence of surfactants. To the best of our knowledge, it is the first report on the controlled synthesis of various metal copper self-assemblies. This method is very facile, rapid, and effective for preparing the metal copper hierarchical structures with high yields.

In our reaction system, copper chloride is used as copper source, and cetyltrimethylammonium bromide (CTAB), sodium dodecyl sulfate (SDS) or polyvinylpyrrolidone (PVP) as the shape-controllers that could effectively adjust the morphologies of metal copper hierarchical structures. And the copper structures with different morphologies were in detail investigated by X-ray diffraction (XRD) and scanning electron microscopy (SEM). Based on the experimental data, the possible formation process of metal copper hierarchical structures with various morphologies was discussed.

2. Experimental Sections

2.1. Chemical Reagents. Copper chloride dihydrate ($\text{CuCl}_2 \cdot 2\text{H}_2\text{O}$), sulfuric acid (H_2SO_4), cetyltrimethylammonium bromide (CTAB), sodium dodecyl sulfate (SDS), and polyvinylpyrrolidone (PVP) were purchased from Sino-pharm Chemical Reagent Co., Ltd. All chemicals were of analytical grade and used without any further purification. All solutions were prepared using deionized water.

2.2. Preparation of Metal Copper Hierarchical Structures. The electrodeposition solution consisted of CuCl_2 ($0.1 \text{ mol} \cdot \text{L}^{-1}$), H_2SO_4 ($0.1 \text{ mol} \cdot \text{L}^{-1}$), various additives at the same concentration of $40 \text{ g} \cdot \text{L}^{-1}$, such as CTAB, SDS, and PVP, and deionized water. Electrodeposition was carried out in a two-electrode electrochemical cell. Both the anode electrode and cathode electrode were composed of the copper foils with the diameter of 0.8 cm, the length of 1.5 cm, and the thickness

of 0.1 cm. The two electrodes were placed parallel to each other and perpendicularly inserted into the electrodeposition solution. The potentiostatic electrodeposition was carried out at the electric potential of 1.0 V for varying deposition time without heating or stirring.

2.3. Sample Characterization. After reacted for several minutes, the cathode as the working electrode was taken out, and carefully rinsed with deionized water more than five times, then allowed to air-dry before characterization. The samples for scanning electron microscopy (SEM) were directly fixed to a SEM stub and were sputtered with a 5 nm layer of platinum. Images were obtained with a JEOL JSM-5610 LV SEM operating at an accelerating voltage of 15 kV. The specimens for structural characterization were carefully peeled from the foils and subjected to X-ray diffraction (XRD) using a D/Max-RA diffractometer with $\text{Cu K}\alpha$ radiation.

3. Results and Discussion

3.1. XRD of Metal Copper Materials. Figure 1 shows the XRD patterns of the products fabricated at the electric potential of 1.0 V for 10 min in the absence of surfactant and in the presence of CTAB, SDS, and PVP in the electrolyte, respectively. The diffraction peaks in the range of $20^\circ < 2\theta < 80^\circ$ can be indexed as the face-centered cubic (fcc) directions of Cu (111), (200), and (220), in good agreement with Joint Committee on Powder Diffraction Standards (JCPDS) no. 04-0836. No peaks from other phases were found, suggesting the high purity was obtained. Besides, it is further indicated that supplementing surfactants does not change the crystal structure of the products but obviously affects the peak intensities of metal copper materials. Compared with the peak intensity ratio of 100:46:20 in JCPDS no. 04-0836, the ratios of (111), (200), and (220) peak intensities of various copper materials assisted by no additive, CTAB, SDS, and PVP were 100:416:600, 100:210:320, 100:42:29, and 100:195:329, respectively. On the other hand, for the as-prepared product in the presence of SDS (curve c in Figure 1), the diffraction peak strength at about 43° was obviously higher than those at about 50° and 74° , similar to that of JCPDS no. 04-0836. However, these phenomena did not happen on the products fabricated without additive or with other surfactants, attributing to the different growth rate of various directions of metal copper crystals. In contrast with the crystal structure of the products, supplementing surfactants has a notable effect on the growth rate of different direction of the as-prepared products.

3.2. Effect of Surfactants on Metal Copper Hierarchical Structures. To get an insight into the formation process of metal copper hierarchical structures with different morphologies, time-dependent experiments were carried out and the products were inspected by SEM. Figure 2 shows the SEM images of the products with no additive at the varying deposition time. At the beginning of the deposition, the ruleless nubby structures with inconsistent size were first formed after reacted for 5 min (Figure 2(a)). The SEM image

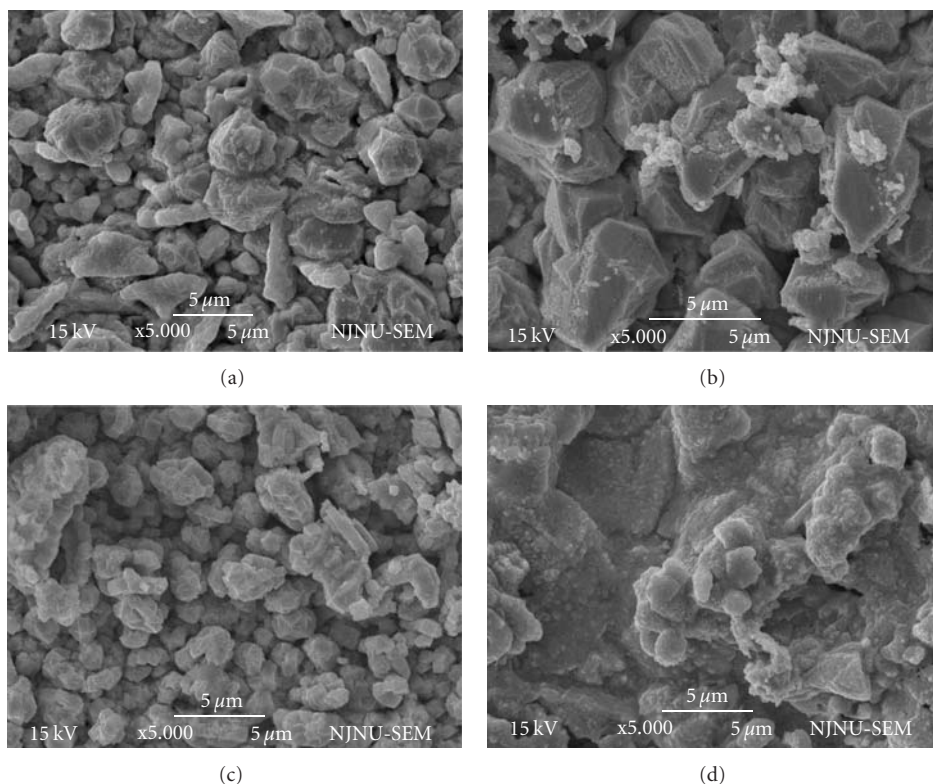


FIGURE 2: SEM images of the products with no additive in the electrolyte at the different deposition times of 5 min (a), 10 min (b), 20 min (c), and 30 min (d).

of the product formed at 10 min showed that the size of nubby structures increased with the increasing deposition time and came up to $5\text{--}8\ \mu\text{m}$ (Figure 2(b)). The crinkles on the surface of nubby structures indicated that the products were constructed by many small blocks. As the reaction time increased to 20 min (Figure 2(c)), the small nubby structures with the size of about $3\ \mu\text{m}$ were observed due to the further splitting of the former larger nubby structures. At the deposition time of 30 min, the ruleless nubby structures further grew up on the foil, piled up each other, and constructed the copper film (Figure 2(d)). The above experimental results show that in the absence of additive the similar growth rates in different directions lead to the formation of the ruleless nubby structures. With the prolonged deposition time, the nubby structures gradually grow up, and then split into many small blocks which further developed, and finally contribute to the formation of the copper film.

Figure 3 shows SEM images of the products by adding CTAB in the electrodeposition solution at varying deposition time. At the beginning of the deposition, the nanosheets with the thickness of about $50\ \text{nm}$ perpendicularly grew up on the foil and interwove each other, shown in Figure 3(a). With the increasing reaction time, taking the old nanosheets as the new growth points, the secondary sheet-like structures gradually matured, which caused the nanosheets with similar thickness to develop in number and to become bushier, forming the nanosheet arrays on the substrate (Figure 3(b)). After reacted for 30 min, the nanosheets further grew up and

some sphere-like structures wrapped in the inner part of nanosheets were observed (Figure 3(c)). When the reaction time lasted for 1 h, there were some flower-like structures self-assembled by nanosheets in high yield with uniform size of about $15\ \mu\text{m}$, shown in Figure 3(d). The above experimental results clearly indicate the formation process of the flower-like hierarchical structures constructed by nanosheets. Assisted by CTAB, the different growth rates of metal copper in each direction promote vertical growth of the copper nanosheets with the uniform thickness on the substrate. With the rapid growth of nanosheets, the growth of the crystal nucleus of the inner part wrapped in nanosheets is easier to be affected by the electrolyte diffusion, leading to the lack of protection of CTAB in the growth process of metal copper. Therefore, the products further develop into the sphere-like structures with micrometer size and come up as shown in the inset of Figure 3(c), similar to the formation of crystal copper without additive. When the sphere-like particles emerged from the nanosheets come into contact with the electrolyte owing to the rapid growth rate, CTAB further promotes the appearance of the sheet-like structures and finally leads to the formation of the flower-like hierarchical structures self-assembled by nanosheets. Based on the above analysis, adjusting the electrodeposition time can effectively control the formation of nanosheet arrays and flower-like hierarchical structures.

Figure 4 shows the SEM images of the products assisted by SDS in the electrolyte at varying deposition time. At

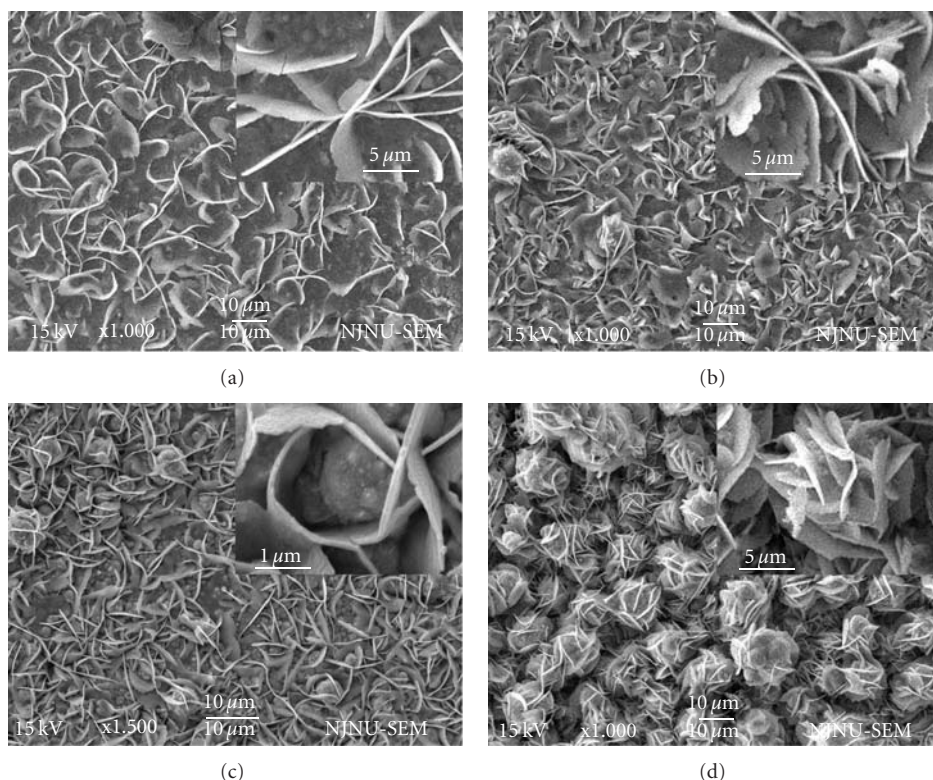


FIGURE 3: SEM images of the products by adding CTAB in the electrolyte at the different deposition times of 10 min (a), 20 min (b), 30 min (c), and 1 h (d). The insets in Figures 3(a)–3(d) show the magnification SEM images of the corresponding photos.

the beginning of the deposition, the prototype of dendrite-like structure with cross-linked branches was first formed and covered the whole substrate after being reacted for 1 min (Figure 4(a)). With the increasing deposition time, the branches of dendrite-like structure gradually developed and independently grew up (Figure 4(b)). The SEM images of the products reacted for 5 min (Figure 4(c)) which indicated that the trunks and branches of the dendrite-like structures further evolved and became thicker. And taking the old branches as the new growth points, the sub-dendrite-like structures occurred on the branches. After being reacted for 10 min, the sub-dendrite-like structures with the uniform length of about $2\ \mu\text{m}$ wove together (Figure 4(d)). The above experimental results clearly show that under the assistant role of SDS, the products first nucleate on the foil and grow at one-dimensional approach, and then the dendrite-like structures are gradually formed. With the increasing deposition time, the instability of the branches promotes the appearance of sub-dendrite-like structures with small size, which further evolve and interweave together, and finally construct the dendrite-like crystals constructed by 1D nanostructures. The formation of dendrite-like copper crystals is a nucleation-growth-regrowth process. It is an effective approach to rapidly fabricating the dendrite-like crystals.

Figure 5 shows the SEM images of the products with PVP in the electrolyte at the varying deposition time. At the beginning of the reaction, only a few protuberances of

approximately $1\ \mu\text{m}$ irregularly were arranged on the foil, shown in Figure 5(a). With the increasing reaction time, the protuberances further developed, and gradually wove together, then became the sphere-like structures with the diameter of about $2\ \mu\text{m}$ (Figure 5(b)). When the reaction time lasted for 20 min, the sphere-like structures assembled each other and became the larger congeries as shown in the inset of Figure 5(c). The above experimental results distinctly display that assisted by PVP, the same growth rates in all directions promote the formation of the sphere-like structures. With the further evolution, the sphere-like structures assemble each other and finally form the large congeries constructed by sphere-like structures.

Based on the above experimental results, it is clearly shown that the copper hierarchical structures with different morphologies, such as flower-like structures self-assembled by nanosheets, dendrite-like crystals constructed by 1D nanostructures, and the large congeries built by sphere-like structures, can be effectively fabricated by using the additives of CTAB, SDS, and PVP. The schematic presentation of the fabrication procedure of metal copper materials fabricated by the assistance of CTAB, SDS, and PVP was shown in Figure 6, clearly illustrating the evolution of various copper hierarchical structures. Due to some reasons, such as the interactions of copper ions and the additives and the selective adsorption of the surfactants on certain crystallographic planes, the difference of the additives has an important effect on the growth rate of the different orientation of

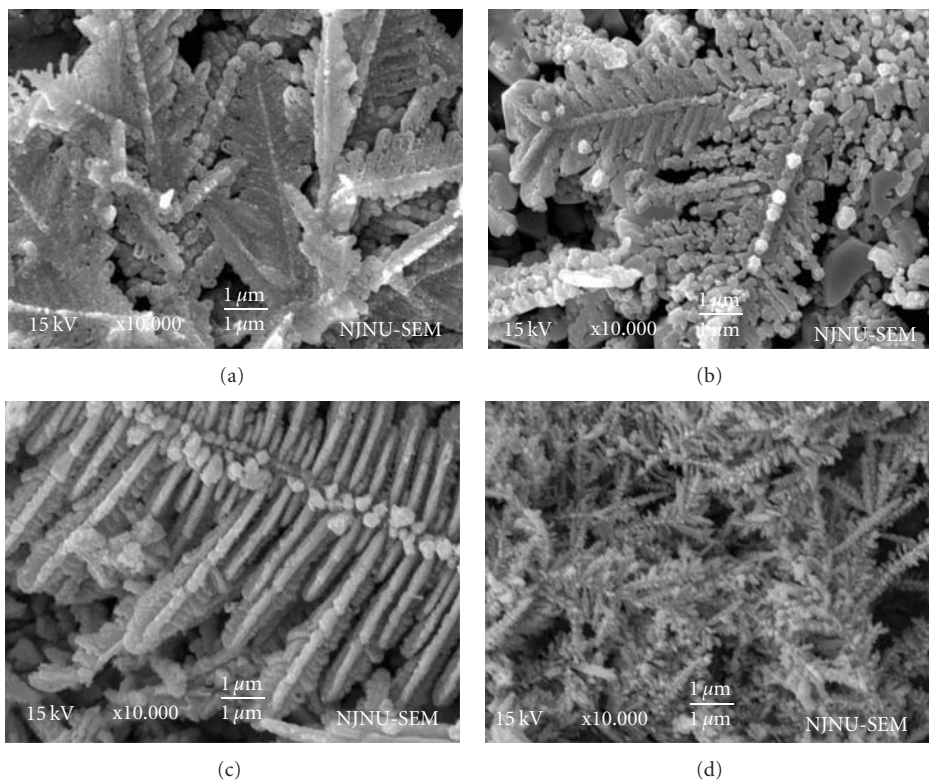


FIGURE 4: SEM images of the products by adding SDS in the electrolyte at the different deposition times of 1 min (a), 3 min (b), 5 min (c), and 10 min (d).

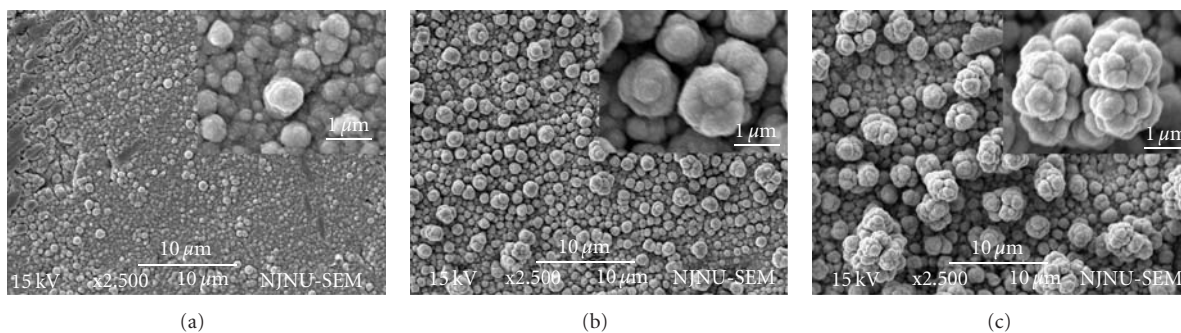


FIGURE 5: SEM images of the products by adding PVP in the electrolyte at the different deposition times of 5 min (a), 10 min (b), and 20 min (c). The insets in Figures 5(a)–5(c) show the magnification SEM images of the corresponding photos.

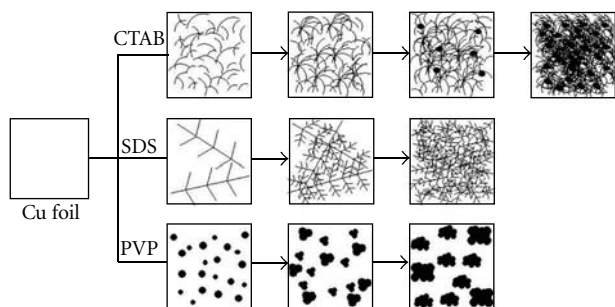


FIGURE 6: Schematic presentation of the process involved in the preparation of various metal copper hierarchical structures assisted by CTAB, SDS, and PVP.

metal copper during the electrodeposition, resulting in the formation of metal copper self-assemblies with various morphologies. The exact role of the additives in the formation of copper hierarchical structures is not clear at this moment and further studies are needed.

4. Conclusion

In this paper, we developed the controlled fabrication of copper hierarchical structures with different morphologies by using the additives, such as CTAB, SDS, and PVP, combined with the electrodeposition technology. The outstanding features of this template-free method are its simplicity, convenience, and effectiveness. It is the first time that the

shape-controlled synthesis of metal copper self-assemblies is reported. All of the products were face-centered cubic copper, and the crystal structure was surfactant independent. In the absence of additives, only ruleless nubby structures are observed; in contrast, in the presence of CTAB, the flower-like hierarchical structures self-assembled by nanosheets with the uniform size are formed. Adjusting the deposition time was efficient to control the formation of the nanosheet arrays and the flower-like hierarchical structures. When the electrolyte was supplemented with SDS, the dendrite-like copper crystals constructed by 1D nanostructures are rapidly synthesized. When the electrolyte was added by PVP, the large congeries built by sphere-like structures was revealed. In summary, a simple and novel way to selectively control the formation of copper hierarchical structures with different morphologies is established by using the different additives.

Acknowledgments

The authors acknowledge financial supports from Foundation of Zhejiang Educational Committee of China (Grant no. Y200805544), Natural Scientific Foundation of Zhejiang (Grant no. Y4090605), the National Science Foundation for Young Scientists of China (Grant no. 20901051), and 973 Program (no. 2011CB710800).

References

- [1] T. Thurn-Albrecht, J. Schotter, G. A. Kastle et al., "Ultrahigh-density nanowire arrays grown in self-assembled diblock copolymer templates," *Science*, vol. 290, no. 5499, pp. 2126–2129, 2000.
- [2] E. C. Lin, J. J. Cole, and H. O. Jacobs, "Gas phase electrodeposition: a programmable multimaterial deposition method for combinatorial nanostructured device discovery," *Nano Letters*, vol. 10, no. 11, pp. 4494–4500, 2010.
- [3] R. Brayner, R. Iglesias, S. Truong et al., "Surface-enhanced Raman scattering on Silver nanostructured films prepared by spray-deposition," *Langmuir*, vol. 26, no. 22, pp. 17465–17469, 2010.
- [4] A. Frömsdorf, A. Kornowski, S. Pütter, H. Stillrich, and L. T. Lee, "Highly ordered nanostructured surfaces obtained with silica-filled diblock-copolymer micelles as templates," *Small*, vol. 3, no. 5, pp. 880–889, 2007.
- [5] Y. Sun and Y. Xia, "Shape-controlled synthesis of gold and silver nanoparticles," *Science*, vol. 298, no. 5601, pp. 2176–2179, 2002.
- [6] Y. Zhao, T. Topping, J. F. Bingert et al., "High tensile ductility and strength in bulk nanostructured nickel," *Advanced Materials*, vol. 20, no. 16, pp. 3028–3033, 2008.
- [7] D. Wei, W. Qian, Y. Shi, S. Ding, and Y. Xia, "Mass synthesis of single-crystal gold nanosheets based on chitosan," *Carbohydrate Research*, vol. 342, no. 16, pp. 2494–2499, 2007.
- [8] M. P. Zach, K. H. Ng, and R. M. Penner, "Molybdenum nanowires by electrodeposition," *Science*, vol. 290, no. 5499, pp. 2120–2123, 2000.
- [9] Y. L. Hou and S. Gao, "Solvochemical reduction synthesis and magnetic properties of polymer protected iron and nickel nanocrystals," *Journal of Alloys and Compounds*, vol. 365, no. 1–2, pp. 112–116, 2004.
- [10] D. Li, R. S. Thompson, G. Bergmann, and J. G. Lu, "Template-based synthesis and magnetic properties of cobalt nanotube arrays," *Advanced Materials*, vol. 20, no. 23, pp. 4575–4578, 2008.
- [11] G. She, W. Shi, X. Zhang, T. Wong, Y. Cai, and N. Wang, "Template-free electrodeposition of one-dimensional nanostructures of tellurium," *Crystal Growth & Design*, vol. 9, no. 2, pp. 663–666, 2009.
- [12] N. Tian, Z. Y. Zhou, N. F. Yu, L. Y. Wang, and S. G. Sun, "Direct electrodeposition of tetrahedral Pd nanocrystals with high-index facets and high catalytic activity for ethanol electrooxidation," *Journal of the American Chemical Society*, vol. 132, no. 22, pp. 7580–7581, 2010.
- [13] B. Zhang, Y. Y. Weng, X. P. Huang et al., "Creating in-plane metallic-nanowire arrays by corner-mediated electrodeposition," *Advanced Materials*, vol. 21, no. 35, pp. 3576–3580, 2009.
- [14] C. R. Kothapalli and A. Ramamurthi, "Copper nanoparticle cues for biomimetic cellular assembly of crosslinked elastin fibers," *Acta Biomaterialia*, vol. 5, no. 2, pp. 541–553, 2009.
- [15] T. R. L. C. Paixão and M. Bertotti, "Development of a breath alcohol sensor using a copper electrode in an alkaline medium," *Journal of Electroanalytical Chemistry*, vol. 571, no. 1, pp. 101–109, 2004.
- [16] E. A. Karakhanov, A. L. Maximov, Y. S. Kardasheva et al., "Copper nanoparticles as active catalysts in hydroxylation of phenol by hydrogen peroxide," *Applied Catalysis A*, vol. 385, no. 1–2, pp. 62–72, 2010.
- [17] C. Jiang, W. Zhang, Y. Liu, and Y. Qian, "Self-assembled copper nanowalls into microstructures with different shapes: a facile aqueous approach," *Crystal Growth & Design*, vol. 6, no. 11, pp. 2603–2606, 2006.

Research Article

Direct Preparation of Nano-Quasicrystals via a Water-Cooled Wedge-Shaped Copper Mould

Zhifeng Wang, Weimin Zhao, Chunling Qin, Yan Cui, Shenglei Fan, and Junqing Jia

School of Materials Science and Engineering, Hebei University of Technology, Tianjin 300130, China

Correspondence should be addressed to Weimin Zhao, wzmzhao@yahoo.com

Received 30 June 2011; Accepted 9 August 2011

Academic Editor: Bo Zou

Copyright © 2012 Zhifeng Wang et al. This is an open access article distributed under the Creative Commons Attribution License, which permits unrestricted use, distribution, and reproduction in any medium, provided the original work is properly cited.

We have successfully synthesized multicomponent Mg-based nano-quasicrystals (nano-QCs) through a simple route by using a water-cooled wedge-shaped copper mould. Nanoscale QCs are prepared directly on tip of wedge-shaped castings. The further study shows that nano-QCs in the $Mg_{71}Zn_{26}Y_2Cu_1$ alloy show well microhardness of greater than HV450. Electrochemical properties of three kinds of quasicrystal alloys are investigated in simulated seawater. The $Mg_{71}Zn_{26}Y_2Cu_1$ nano-QC alloy presents the best corrosion resistance in this study for the formation of well-distributed nano-QC phases (1~5 nm) and polygonal $Mg_2(Cu,Y)$ nanophases (40~50 nm).

1. Introduction

Quasicrystals (QCs) are aperiodic solids whose atomic arrangements have symmetries (typically five- or tenfold) that are forbidden for conventional crystallography [1] and have long been thought forbidden in nature. It brings about a paradigm shift in solid-state physics when the first QC example is obtained in a rapidly solidified Al-Mn alloy [2]. The unexpected discovery of QCs presents scientists with a new, puzzling class of materials and involves hundreds of researchers in this realm. In the past nearly thirty years, QCs in various systems have been synthesized in laboratories [3, 4] and have also been discovered in natural minerals [5]. These QCs possess a host of unusual mechanical and physical properties [6]. Though they cannot be applied directly as structural materials for their innate brittleness, they present high microhardness which makes them used as good strengthening phases for some flexible matrix. Accordingly, diverse QC master alloys have been successfully synthesized and added into different commercial alloys [7, 8].

Usually, nano-quasicrystals (nano-QCs) can be synthesized through two kinds of ways. Nano-QCs are known to form in annealed [9, 10] or ball-milled [11] metallic glasses. Moreover, they can also be fabricated in extruded [12, 13], rolled [14], or wrought [15] Mg-based alloys

at high temperature. These nano-QC alloys exhibit better mechanical properties compared with their corresponding glasses or conventional crystalline alloys [16]. So, the nano-QC alloy is a kind of very promising material. In this study, we have synthesized nano-QC alloys through a new and simple route instead of traditional heat treatment and texturing process. Thus, the forming process of nano-QC alloy can strongly be simplified. At the same time, the costing of manufacture equipment can highly be cut down.

On the other hand, magnesium alloys present poor corrosion resistance. They can easily be eroded either in acid, neutral, or alkali solutions, even in pure water [17]. So, their further applications are restrained. Considering the excellent corrosion resistance of QCs [18], we manage to in situ synthesis Mg-based nano-QCs in Mg-Zn-Y alloys which are hopeful to show their improved corrosion resistance.

In past work, we have synthesized quaternary spherical Mg-Zn-Y-based QC phase [19] by controlling compositions and undercooling conditions of the melts. In order to fabricate nanoscale QCs, we improve the cooling condition in this paper by using a water-cooled wedge-shaped copper mould [20]. Multicomponent spherical nano-QCs are successfully synthesized and their electrochemical properties are investigated in simulated seawater.

TABLE 1: Nominal composition of the experimental alloys.

Alloy No.	Alloy compositions (at. %)				
	Mg	Zn	Y	Cu	Ni
1#	72.0	26.0	2.0	—	—
2#	71.0	26.0	2.0	1.0	—
3#	71.0	26.0	2.0	0.5	0.5

2. Experimental

The experimental alloys (Table 1) were produced by a reformed crucible electric resistance furnace (SG₂-5-10 A, China), melted under the mixture of CO₂/0.5vol.%SF₆ protective atmosphere, using Mg(99.95%) and Zn(99.90%) ingots, Ni(99.99%) and Cu(99.99%) powder, and Mg-29.05%Y master alloy. Stirring for 2 min by impellor at 1073 K and holding for 5 min above 1053 K, the melt was poured and cooled in a water-cooled wedge-shaped copper mould. Samples were taken on tip of castings as shown in Figure 1.

The morphology observation of QCs was conducted using transmission electron microscopy (TEM, DEOL JEM-2010FEE, Japan). Microhardness of QC alloys was examined by microhardness tester (HXD-1000, China). The electrochemical properties of specimens were tested in simulated seawater (2.73% NaCl, 0.24% MgCl₂, 0.34% MgSO₄, 0.11% CaCl₂, 0.08% KCl, and 96.5% deionized water, vol.%) by an electrochemical workstation (Gamry, PCI4-750, USA) with a sweep rate of 10 mV/s. A saturated calomel electrode (SCE) was used for the reference electrode.

3. Results and Discussion

TEM photos of QC alloys in different sample positions are shown in Figure 2. Three kinds of componential micro-/nano-QC phases are synthesized on tip of wedge-shaped castings. Energy-dispersive spectroscopy (EDS) analysis (Figure 3) shows that micro-/nano-QC phases in Position B of Alloy 1~ Alloy 3 are Mg-Zn-Y phase, Mg-Zn-Y-Cu phase, and Mg-Zn-Y-Cu-Ni phase, respectively. The selected area electron-diffraction (SAED) patterns with typical fivefold rotational symmetry identify that these micro-/nano-QC phases are icosahedral QCs. Among all QCs, QCs in Position A of Alloy 1 show petal-like morphology, while others show spherical morphology. From the further analysis in Table 2, we can see that in alloys with same components, QCs in Position B are smaller than those in Position A, while QC microhardness in Position B is greater than that in Position A. After introducing Cu(-Ni) into Mg-Zn-Y alloys, we can see in the same sample position, QC size of Alloy 2 and Alloy 3 is obviously smaller than that of Alloy 1. QC size of Alloy 2 in Position A is close to that of Alloy 1 in Position B. Nano-QC spheres about 8~30 nm and 1~5 nm are synthesized in Position B of Alloy 3 and Alloy 2, respectively. It shows from the microhardness testing that the smaller the QC spheres, the greater their value of microhardness. Furthermore, the microhardness of nano-QC spheres in Position B of Alloy 2 exceeds HV450, which shows fascinating properties.

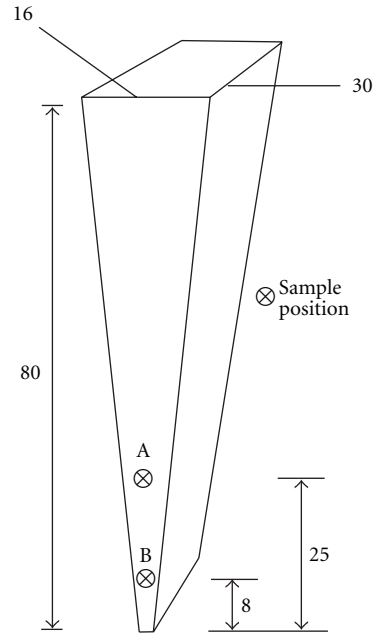


FIGURE 1: Sketch map of a wedge-shaped casting (mm).

Figure 4 shows the potentiodynamic polarization curves of QC alloys (Position B) measured in simulated seawater open to air at room temperature. We can see that Mg₇₁Zn₂₆Y₂Cu₁ nano-QC alloy presents high corrosion resistance in simulated seawater and its corrosion resistance is much better than that of Mg₇₂Zn₂₆Y₂ and Mg₇₁Zn₂₆Y₂Cu_{0.5}Ni_{0.5} QC alloys. The further study shows that this result can be ascribed to the existence of well-distributed nano-QC phases (shown in Figure 5 by red arrows) and polygonal Mg₂(Cu,Y) phases [21]. These high-corrosion resistance phases decrease the anodic passive current density, improve the polarization resistance, cut down the corrosion rate (Table 3), and finally improve the corrosion resistance of the Mg-Zn-Y-based alloy markedly. Cu and Ni have long been considered as harmful elements for improving corrosion resistance of Mg-based alloy [22], however they are used to synthesize nano-QC spheres in this paper. Due to high-corrosion resistance of QC phases, Mg₇₁Zn₂₆Y₂Cu₁ and Mg₇₁Zn₂₆Y₂Cu_{0.5}Ni_{0.5} nano-QC alloys present better corrosion resistance than Mg₇₂Zn₂₆Y₂ QC alloy. Moreover, the corrosion resistance of Mg₇₁Zn₂₆Y₂Cu₁ nano-QC alloys is higher than Mg₇₁Zn₂₆Y₂Cu_{0.5}Ni_{0.5} nano-QC alloys for the higher damage level of Ni to the corrosion resistance of magnesium alloy than that of Cu when they have same contents [22].

It was reported that a large negative enthalpy of mixing and/or existence of Frank-Kasper-type phases appear to be the crucial criteria for the formation of nano-quasicrystalline phase in any system [23]. Meanwhile, Mg-Zn-Y-based QCs just belong to Frank-Kasper-type phases [24] and have a certain negative enthalpy of mixing. So theoretically, Mg-Zn-Y-based nano-QCs can be formed in a proper cooling conditions. The past cooling rate the researchers made to produce QCs was whether too high or too low, and

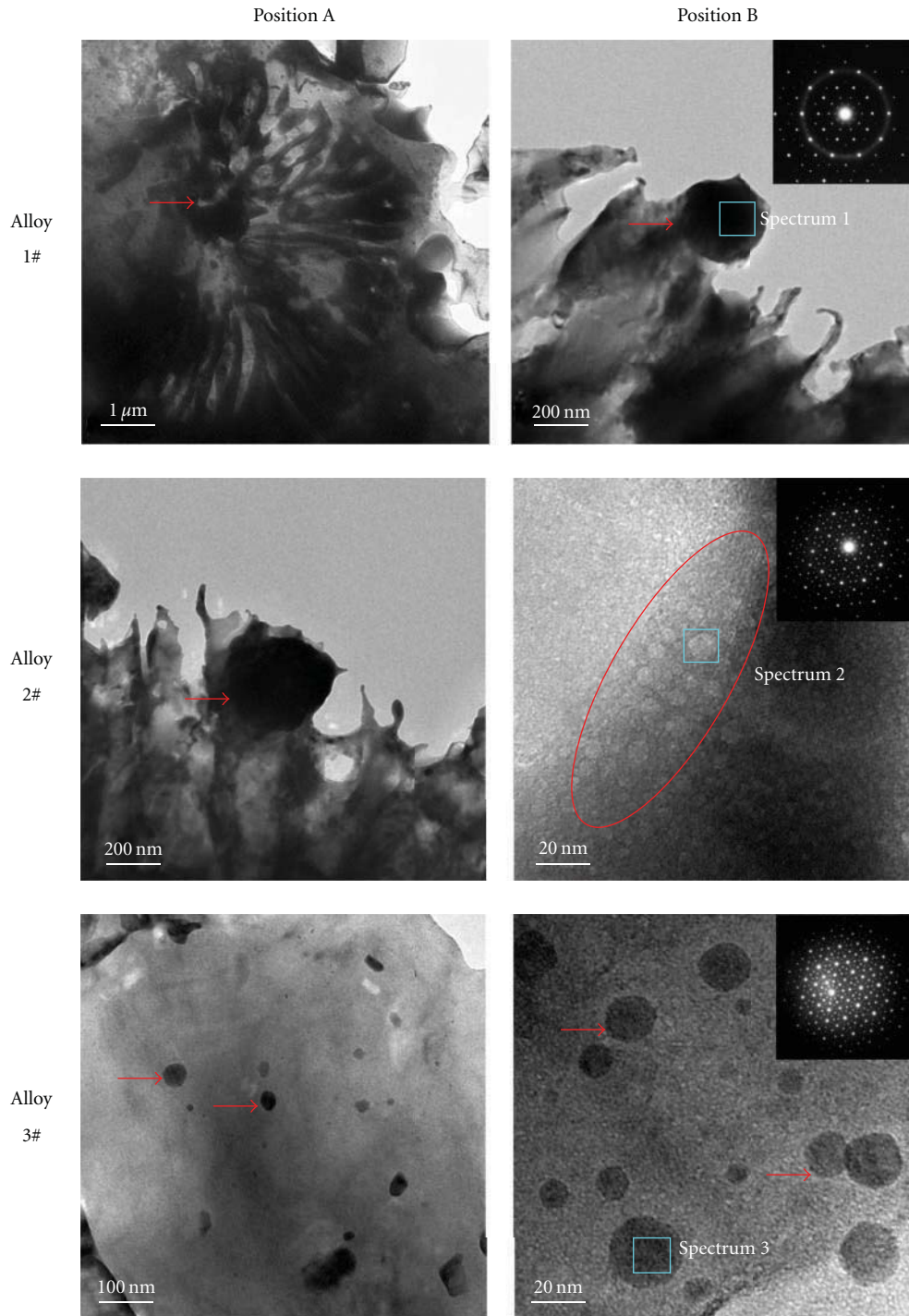


FIGURE 2: TEM photos of micro/nano-QC alloys and QC typical selected area electron-diffraction (SAED) patterns on Position B of different alloys.

was not content with the forming conditions of nano-QCs. This route just meets the demands for forming nanoscale QCs. So, nano-QCs are successfully produced in this paper. Moreover, the additions of Cu and Ni improve the degree of constitutional supercooling of Mg-Zn-Y melts and reduce the crucial criteria radius for forming spherical QCs. However, increasing thermodynamics undercooling coming

from water-cooled wedge-shaped copper mould makes it still possible to form spherical QCs. At the same time, the alloy components designed for this study is based on the three empirical rules [25] for the formation of metallic glass. It has been widely accepted that quasicrystals and at least some metallic glasses are built up with icosahedral clusters [26]. The short-range atomic configuration is very similar

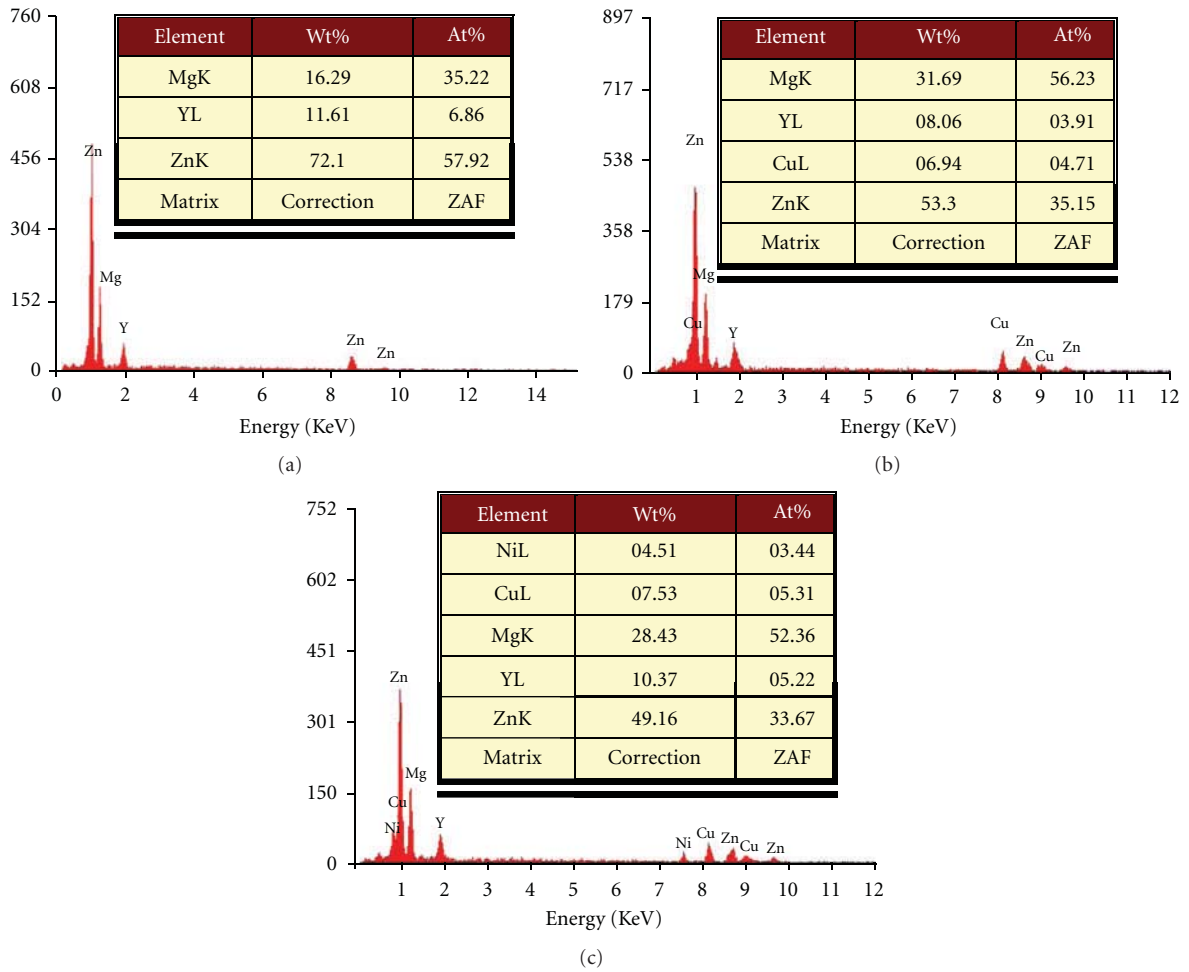


FIGURE 3: Energy-dispersive spectroscopy (EDS) analysis of QCs in Position B.

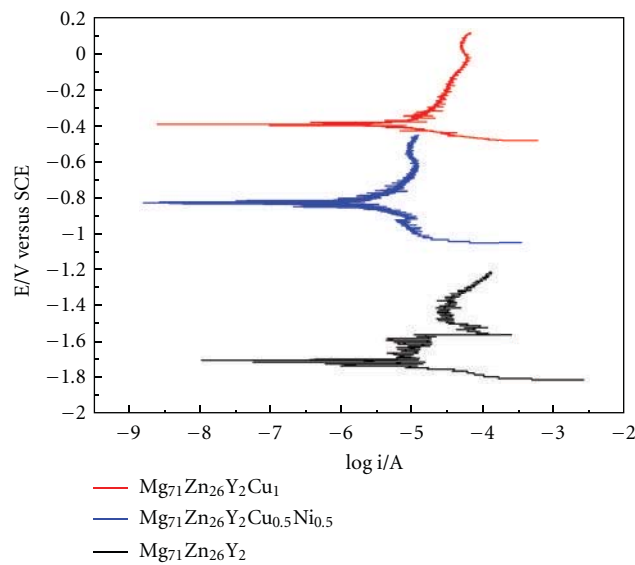


FIGURE 4: Potentiodynamic polarization curves of QC alloys (Position B) measured in simulated seawater open to air at room temperature.

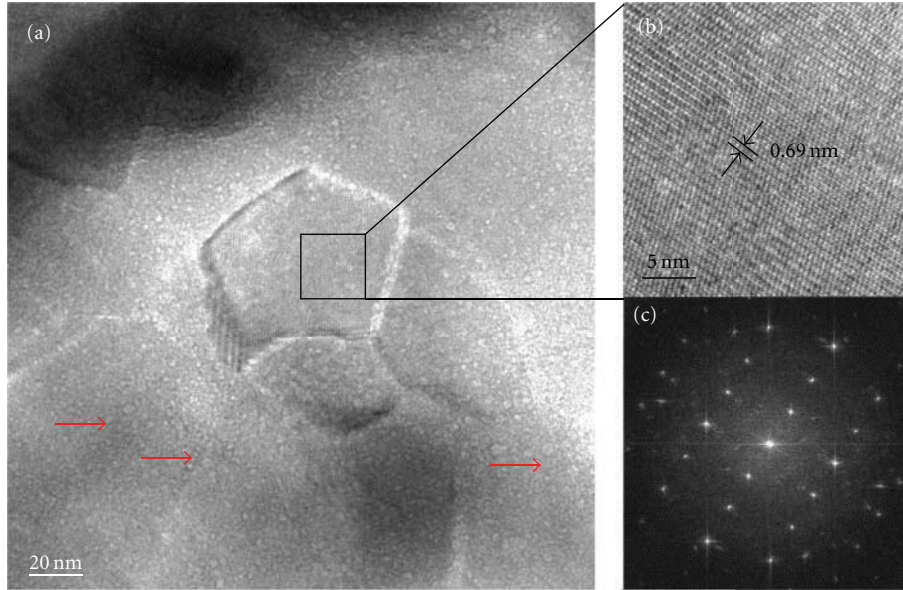


FIGURE 5: Pentagonal nanophase in Alloy 2 (a) TEM photo. (b) Magnifying TEM photo and (c) its fast Fourier transform (FFT) pattern.

TABLE 2: Comparisons of the quasicrystals (QCs).

Alloy	Sample position	QC size(diameter)/nm	QC morphology	Microhardness /HV
1	A	650–900	Petal-like	324
	B	330–340	Spherical	375
2	A	370–400	Spherical	367
	B	1.0–5.0	Spherical	459
3	A	20–55	Spherical	412
	B	8–30	Spherical	438

TABLE 3: Corrosion parameters obtained from potentiodynamic polarization curves for Position B of QC alloys in simulated seawater.

Specimen	$I_{\text{corr}}/\mu\text{A}/\text{cm}^{-2}$	$R_p/\text{k}\Omega$	Corrosion Rate/mpy
1	11.09	6.925	19.298
2	2.035	14.76	1.522
3	3.762	8.105	3.084

I_{corr} : corrosion current; R_p : polarization resistance.

between the quasicrystal and amorphous phases [27]. On the tip of the wedge-shaped ingots, its cooling conditions is just suitable for these icosahedral clusters to be nucleation of QCs. And then, it leaves very short time for quasicrystal growth. So, it is nano-QCs that form in this route instead of metallic glasses.

4. Conclusions

After introducing Cu(-Ni) into Mg-Zn-Y alloys, spherical nano-quasicrystals (nano-QCs) are directly prepared on tip of wedged-shaped castings. Nano-QCs in the $\text{Mg}_{71}\text{Zn}_{26}\text{Y}_2\text{Cu}_1$ alloy show well microhardness of greater

than HV450. At the same time, the $\text{Mg}_{71}\text{Zn}_{26}\text{Y}_2\text{Cu}_1$ nano-QC alloy presents high corrosion resistance in simulated seawater for the formation of well-distributed nano-QC phases (1~5 nm) and polygonal $\text{Mg}_2(\text{Cu},\text{Y})$ nanophases (40~50 nm).

Acknowledgments

The authors would like to thank the financial supports from both Natural Science Foundation of Hebei Province, China (no. E2010000057) and International Science & Technology Cooperation Program of China (no. 2010DFA51850). The technical assistance of TEM testing from Dr. H. T. Fan, China National Academy of Nanotechnology & Engineering is also acknowledged.

References

- [1] P. Thiel, "Quasicrystals: when all pieces fit together," *Nature Materials*, vol. 6, no. 1, pp. 11–12, 2007.
- [2] D. Shechtman, I. Blech, D. Gratias, and J. W. Cahn, "Metallic phase with long-range orientational order and no translational symmetry," *Physical Review Letters*, vol. 53, no. 20, pp. 1951–1953, 1984.

- [3] Z. Luo, S. Zhang, Y. Tang, and D. Zhao, "Quasicrystals in as-cast Mg-Zn-RE alloys," *Scripta Metallurgica et Materiala*, vol. 28, no. 12, pp. 1513–1518, 1993.
- [4] A. P. Tsai, A. Inoue, and T. Masumoto, "A stable quasicrystal in Al-Cu-Fe system," *Japanese Journal of Applied Physics*, vol. 26, no. 9, pp. L1505–L1507, 1987.
- [5] L. Bindi, P. J. Steinhardt, N. Yao, and P. J. Lu, "Natural quasicrystals," *Science*, vol. 324, no. 5932, pp. 1306–1309, 2009.
- [6] A. V. Blaaderen, "Quasicrystals from nanocrystals," *Nature*, vol. 461, no. 7266, pp. 892–893, 2009.
- [7] J. Zhang, L. Pei, H. Du, W. Liang, C. Xu, and B. Lu, "Effect of Mg-based spherical quasicrystals on microstructure and mechanical properties of AZ91 alloys," *Journal of Alloys and Compounds*, vol. 453, no. 1–2, pp. 309–315, 2008.
- [8] Z. Wang, W. Zhao, H. Li, and C. Liang, "Fabrication of quaternary Mg-Zn-Y-Ce quasi-crystal alloys and their strengthening effects on AZ91 magnesium alloys," *China Foundry*, vol. 7, no. 4, pp. 342–348, 2010.
- [9] J. Saida, M. Matsushita, and A. Inoue, "Nano icosahedral quasicrystals in Zr-based glassy alloys," *Intermetallics*, vol. 10, no. 11–12, pp. 1089–1098, 2002.
- [10] M. Galano, F. Audebert, I. C. Stone, and B. Cantor, "Nanoquasicrystalline Al-Fe-Cr-based alloys. Part I: phase transformations," *Acta Materialia*, vol. 57, no. 17, pp. 5107–5119, 2009.
- [11] S. Scudino, U. Kühn, L. Schultz, H. Breitzke, K. Lüders, and J. Eckert, "Formation of quasicrystals in ball-milled amorphous Zr-Ti-Nb-Cu-Ni-Al alloys with different Nb content," *Journal of Materials Science*, vol. 39, no. 16–17, pp. 5483–5486, 2004.
- [12] Y. Liu, G. Yuan, C. Lu, W. Ding, and J. Jiang, "The role of nanoquasicrystals on the ductility enhancement of as-extruded Mg-Zn-Gd alloy at elevated temperature," *Journal of Materials Science*, vol. 43, no. 16, pp. 5527–5533, 2008.
- [13] A. Singh, M. Watanabe, A. Kato, and A. P. Tsai, "Microstructure and strength of quasicrystal containing extruded Mg-Zn-Y alloys for elevated temperature application," *Materials Science and Engineering A*, vol. 385, no. 1–2, pp. 382–396, 2004.
- [14] A. Müller, G. Garcés, P. Pérez, and P. Adeva, "Grain refinement of Mg-Zn-Y alloy reinforced by an icosahedral quasicrystalline phase by severe hot rolling," *Journal of Alloys and Compounds*, vol. 443, no. 1–2, pp. L1–L5, 2007.
- [15] D. H. Kim, J. Y. Lee, H. K. Lim, W. T. Kim, and D. H. Kim, "Effect of Al addition on the elevated temperature deformation behavior of Mg-Zn-Y alloy," *Materials Science and Engineering A*, vol. 487, no. 1–2, pp. 481–487, 2008.
- [16] A. Inoue and A. Takeuchi, "Recent progress in bulk glassy, nanoquasicrystalline and nanocrystalline alloys," *Materials Science and Engineering A*, vol. 375–377, no. 1–2, pp. 16–30, 2004.
- [17] F. Shi, Y. C. Yu, X. F. Guo, Z. M. Zhang, and Y. Y. Li, "Corrosion behavior of as-cast Mg₆₈Zn₂₈Y₄ alloy with I-phase," *Transactions of Nonferrous Metals Society of China*, vol. 19, no. 5, pp. 1093–1097, 2009.
- [18] V. N. Balbyshev, D. J. King, A. N. Khramov, L. S. Kasten, and M. S. Donley, "Investigation of quaternary Al-based quasicrystal thin films for corrosion protection," *Thin Solid Films*, vol. 447–448, pp. 558–563, 2004.
- [19] Z. Wang, W. Zhao, H. Li, J. Ding, Y. Li, and C. Liang, "Effect of titanium, antimony, cerium and carbon nanotubes on the morphology and microhardness of Mg-based icosahedral quasicrystal phase," *Journal of Materials Science & Technology*, vol. 26, no. 1, pp. 27–32, 2010.
- [20] M. A. Suarez, O. Alvarez, M. A. Alvarez, R. A. Rodriguez, S. Valdez, and J. A. Juarez, "Characterization of microstructures obtained in wedge shaped Al-Zn-Mg ingots," *Journal of Alloys and Compounds*, vol. 492, no. 1–2, pp. 373–377, 2010.
- [21] J. Zhang, K. Qiu, A. Wang, H. Zhang, M. Quan, and Z. Hu, "Effects of pressure on the solidification microstructure of Mg₆₅Cu₂₅Y₁₀ alloy," *Journal of Materials Science & Technology*, vol. 20, no. 1, pp. 106–108, 2004.
- [22] G. L. Song, *Corrosion and Protection of Magnesium Alloys*, Chemistry Industry Press, Beijing, China, 2006.
- [23] B. S. Murty and K. Hono, "On the criteria for the formation of nanoquasicrystalline phase," *Applied Physics Letters*, vol. 84, no. 10, pp. 1674–1676, 2004.
- [24] R. Sterzel, E. Dahlmann, A. Langsdorf, and W. Assmus, "Preparation of Zn-Mg-rare earth quasicrystals and related crystalline phases," *Materials Science and Engineering A*, vol. 294–296, pp. 124–126, 2000.
- [25] A. Inoue, "Stabilization of metallic supercooled liquid and bulk amorphous alloys," *Acta Materialia*, vol. 48, no. 1, pp. 279–306, 2000.
- [26] C. Dong, W. Chen, Y. Wang et al., "Formation of quasicrystals and metallic glasses in relation to icosahedral clusters," *Journal of Non-Crystalline Solids*, vol. 353, no. 32–40, pp. 3405–3411, 2007.
- [27] A. Inoue, A. P. Tsai, H. M. Kimura, and T. Masumoto, "Enthalpy relaxation behaviour of Al-Si-Cr quasicrystalline and amorphous alloys upon annealing," *Journal of Materials Science*, vol. 23, no. 2, pp. 429–437, 1988.